Hydrometallurgically Generated Nanostructured Lead(II) Oxide from Depleted Lead-Acid Batteries for Potential Reuse in Next Generation Electrochemical Systems

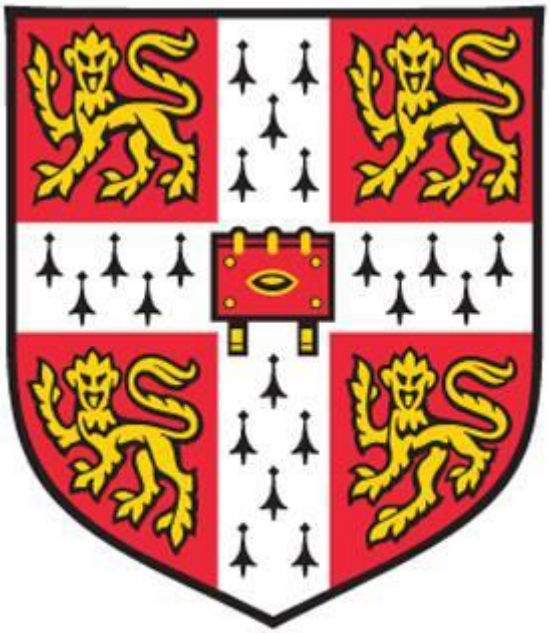

Robert Chi Yung Liu

Fitzwilliam College
University of Cambridge

A dissertation submitted for the degree of
Doctor of Philosophy

September 2016

Preface

This dissertation is the result of my own work and includes nothing which is the outcome of work done in collaboration except as declared in the Preface and specified in the text.

It is not substantially the same as any that I have submitted, or, is being concurrently submitted for a degree or diploma or other qualification at the University of Cambridge or any other University or similar institution except as declared in the Preface and specified in the text.

I further state that no substantial part of my dissertation has already been submitted, or, is being concurrently submitted for any such degree, diploma or other qualification at the University of Cambridge or any other University of similar institution except as declared in the Preface and specified in the text. This dissertation does not exceed 60,000 words in length.

Acknowledgements

I would like to thank Dr Vasant Kumar for his supervision and invaluable feedback and support during this project. To the past and present members of the Materials Chemistry Group, University of Cambridge, thank you for all your help and support. In particular, I would like to thank Dr Carsten Schwandt, Dr Daniel Jewell and Marcel Yiao for being excellent sources of electrochemical and chemistry knowledge.

I am grateful to all the staff at the Department of Materials Science and Metallurgy for their invaluable help and advice over the years, especially Simon Griggs and Zlatko Saracevic for their help with SEM and BET respectively. I am also thankful to Mary Vickers and Andrew Moss for their invaluable assistance with XRD over the years. I would also like to express my gratitude to Rosie Ward for her help and advice over the years.

I am indebted to and grateful to my mother, to whom I dedicate this thesis, for always supporting me and giving me the encouragement to move forward.

I have been blessed to have had so many wonderful people to count on as friends for keeping my spirits up over the course of this journey. Thank you all for being the support, inspiration, distraction and counsel I needed: Wil, Steve, Kent, Adam, Fabrizia, Oksana, Julia, Leszek, Julian, Ellen, Clara, Alex, Juvereya, Xanthe, Nenad, Sylwia, Jaap, Carl, Varun, Amir, Mike, Alan, Omba, Emily, Bruno, Silvia, Alja, Jess, Maggi, Nick, Sean, Niamh, Ola, Seb, Paul, Iris, Jamie, Asaf, Mu, Anup, Elliott, Guy, Zane, Dafina, Morven, Christian, Kim, George and countless others for empathising and encouraging me when I needed it. A special thanks to my housemates Katarzyna and Matheus for their boundless enthusiasm and encouragement. I am very grateful to Dr Paul Coxon for his patience and support in reading and correcting this dissertation. I would also like to thank my girlfriend Harriet for her support and encouragement.

“Live as if you were to die tomorrow. Learn as if you were to live forever”

- Mahatma Gandhi

Abstract

The recycling of lead-acid batteries (LABs) is currently an energy intensive, inefficient and polluting procedure. An alternative hydrometallurgical recycling process is investigated in this study. PbO, PbO_2, and $PbSO_4$ were individually reacted with a mixture of aqueous citric acid and sodium hydroxide solution, with hydrogen peroxide being used as a reducing agent for PbO_2.

Pure lead citrate of either $Pb(C_6H_6O_7)\cdot H_2O$ or $Pb_3(C_6H_5O_7)_2\cdot 3H_2O$ was the product crystallized in each leaching experiment depending on the initial conditions.

Combined spent electroactive paste materials from industry were leached and processed. 2.5 M H_2O_2, 3.2 M $C_6H_8O_7\cdot H_2O$ and 3.5 M NaOH were used for optimal leaching and were successful in synthesising $Pb_3(C_6H_5O_7)_2\cdot 3H_2O$ after less than one hour. These amounts could be reduced by individual leaching of plate materials.

The combustion-calcination of $Pb_3(C_6H_5O_7)_2\cdot 3H_2O$ was successful in generating PbO containing both forms of the polymorph α and β crystal phases together with metallic Pb. A novel method to generate PbO from lead citrate was found through a self-sustaining combustion route where leached waste materials were preheated to 270 °C for ~15 minutes and were found to self-sustain a smouldering reaction to produce PbO with a predominately β phase containing metallic Pb.

Electrochemical analysis of PbO from $Pb_3(C_6H_5O_7)_2\cdot 3H_2O$ demonstrated the viability in the by-product to be used in an electroactive paste and therefore reused in new LABs.

Pure α-PbO was generated from both forms of lead citrate, $Pb(C_6H_6O_7)\cdot H_2O$ and $Pb_3(C_6H_5O_7)_2\cdot 3H_2O$ using NaOH. Pure β-PbO was also generated from $Pb(C_6H_6O_7)\cdot H_2O$ and $Pb_3(C_6H_5O_7)_2\cdot 3H_2O$ using NaOH through dissolution/re-precipitation reactions.

$PbCO_3$ was successfully generated from $Pb(C_6H_6O_7)\cdot H_2O$ and $Pb_3(C_6H_5O_7)_2\cdot 3H_2O$ using NaOH, $NaHCO_3$ and an acid in a series of disassociation and re-precipitation reactions. $PbCO_3$ could be used to thermally generate α and β-PbO as well as Pb_3O_4 by calcination at 350, 600 and 450 °C respectively.

Glycerol was entrained in both $PbCO_3$ and α-PbO as an in-situ reducing agent to generate PbO containing metallic Pb.

Acid reactivity and absorption characteristics of PbO derived from $Pb_3(C_6H_5O_7)_2\cdot 3H_2O$ heated in CO_2 were equal to and greater than those used in industry for both automotive and industrial batteries.

Contents

1 Introduction

The first source of electrochemical power began in 1800 with the invention of the Volta Pile by Italian physicist Alessandro Volta. This was the first device that could convert chemical energy into electrical energy. This was followed by the lead-acid electrochemical cell invented in 1859 by the French physicist Gaston Planté and is one of the oldest types of secondary battery, shown in Figure 1-1. The chemical energy is converted into electrical energy through the use of electrodes and electrolyte, with interconnected single voltaic cells designed to provide electricity. The lead-acid electrochemical system is one of the most successful ever developed and even now no other system is yet able to compete on cost grounds. Despite having the second lowest energy-to-weight ratio of all relevant battery systems, the lead-acid system is able to supply high surge currents and therefore maintain a relatively large power-to-weight ratio. Owing to its comparatively low cost amongst other secondary batteries, such as nickel-cadmium (NiCd) and lithium ion batteries, good stability, reliability and high recoverability derived from well-established recycling infrastructure, the lead-acid battery (LAB) currently holds a significant global market share[(1)].

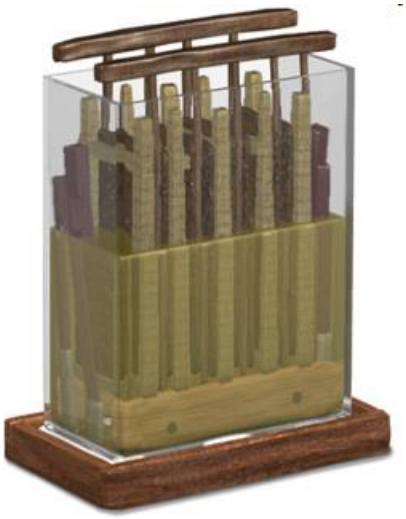

***Figure 1-1**: First lead-acid electrochemical cell, invented in 1859 by French physicist Gaston Planté[(2)]*

The versatility and excellent reversibility of this electrochemical system have enabled it to be deployed extensively as both a mobile power source for vehicle service and traction, for the motor industry in starting, lighting and ignition (SLI) applications, as well as in stationary applications ranging from small emergency supplies, Uninterruptible Power Supplies (UPS), load levelling systems, and solar energy storage. The manufacture of LABs currently account for more than 80% of lead consumption[(3)]. This is approximately mirrored by the market share of the lead supply derived from recycled lead[(4)]. This therefore illustrates how intimately the manufacture of LABs and the recycling of lead are interlinked.

Indeed, lead is the world's most commonly recycled metal with respect to the available obsolete metal value on an industrial scale[5].

The main disadvantages to the lead-acid system are: its weight, which is due to the heavy lead electrode. This is one of the areas where other chemistries such as the lithium (Li) ion system have an advantage. The other is the use of lead and the environmental impact the current method of recovery and recycling of LABs causes. These issues have in part created a greater emphasis on producing Li based batteries for Electrical Vehicles (EVs). Consequently, LABs, which have been the longest established automotive battery for over 100 years, have not been seriously considered for the next generation of EVs and Hybrid Electrical Vehicles (HEVs), despite their successful use in traction and slow-moving vehicles.

If the main drawbacks to the lead-acid system can be overcome, it would be a serious contender for use in the next generation of EVs and HEVs as well as a whole host of other applications. Only a small part of the lead metal is used as the electroactive component, whereas the majority is used in the heavy lead grid in the battery which only serves to hold the lead paste in place and serves as a current collector. This could be replaced by light modern advanced materials. Further, the active material can be made more efficient by using nanoparticles in the paste. Development is continuing worldwide to improve this system to increase the specific power, energy and deep discharge life. At present, conventional LABs such as those designed for SLI or deep-cycle use would not be suitable for HEVs due to the demands of the electrical systems and the nature of operation.

This study aims to develop an improved sustainable method for recovering spent lead paste as a feed for the next generation of low cost and energy efficient lead based electrochemical systems. This is realised through optimising an environmentally sustainable recycling procedure. A number of options for improvements through research will be outlined after an overview of the current state of the art in LAB technology. The primary interest in the current study is to improve the physical properties and morphology of the lead(II) oxide (PbO) recovered product. This, together with improvements from, and incorporation of, other novel LAB research will seek to achieve greater discharge capacity and cycle life compared to the current state of the art.

The research objectives in the current study are as follows:

- To optimise the recycling process of LABs using room temperature methods
- To investigate and control the physical characteristics of the powdered by-products
- To investigate alternative synthesis methods to generate LAB related compounds

2 Background and Principles of Operation

2.1 Electrode Processes

A battery is a device that converts the chemical energy in its active materials directly into electrical energy by means of an electrochemical oxidation-reduction (redox) reaction.
The electrochemical reactions normally take place at the surface of electrodes where the species, after diffusion through the electrolyte accept (reduction) or lose (oxidation) electrons[6]. Generally, it can be expressed by the following:

Anode	$Red_1 - ne \leftrightarrow Ox_1$	Oxidation	**2-1**
Cathode	$Ox_2 + ne \leftrightarrow Red_2$	Reduction	**2-2**

The overall reaction in the cell can be expressed by:

$$Red_1 + Ox_2 \leftrightarrow Ox_1 + Red_2 \qquad \textbf{2-3}$$

For a rechargeable system such as those considered here, the battery is recharged by a reversal of the process. This type of reaction involves the transfer of electrons from one material to another through an electric circuit. During discharge of the battery the anode material is oxidised (electrons are produced), while the cathode material is reduced (electrons are consumed). In the fully charged state, there is a surplus of electrons at the anode (thus making it negative) and a deficit of electrons on the cathode (thus making it positive). During the discharge process, electrons flow from the anode towards the cathode through the external circuit and a current is produced.

The driving force for electrons in the external circuit is the electrical potential difference between two electrodes called the electromotive force (emf). Once all the active materials on the electrodes are used up, the battery cannot provide any more power. The discharged battery can then be either disposed and recycled if it is a primary battery, or recharged if it is a rechargeable (secondary) battery. Charging involves the application of current to the battery in the opposite direction to the flow of current during discharging. Thus, anode in the galvanic cell becomes cathode in the charging cell and cathode becomes anode while the battery is recharged[7]. It is common practice to term the electrodes after their primary use which is discharging current since the convention in electric systems is that electric current flows from the positive pole to the negative one. Consequently, the $PbO_2/PbSO_4$ electrode has been dubbed the positive plate while the $PbSO_4/Pb$ the "negative".

The essential thermodynamic condition enabling a battery to supply electrical energy is negative sign of change of the free energy ΔG of the overall battery reaction that is the requirement for spontaneous electrochemical reactions.

$$\Delta G = - nF\Delta E \quad \textbf{2-4}$$

where:

F = Faraday constant 96 487 (Coulomb)

E = potential (V) of cell equal to $E^0_C - E^0_A$ (for standard potentials)

n = number of electrons exchanged in electrode reaction

When conditions are away from standard condition the cell potential is determined by the Nernst equation:

$$E = E^0 - \frac{RT}{nF} \ln \frac{a_{Red2} a_{Ox1}}{a_{Ox2} a_{Red1}} \quad \textbf{2-5}$$

R = gas constant (J mol^{-1} K^{-1})

T = temperature (K)

a_{Red}, a_{Ox} = activities of reduced/oxidized form of species reacting at electrodes(6).

The charge and discharge reactions that occur in the LAB are facilitated by the unusual feature that the same elements are involved in both the positive and negative electrode reactions. At the positive electrode, which serves as the cathode during discharge, the active material is a mixture of $PbSO_4/PbO_2$. As the battery discharges, PbO_2 is reduced to $PbSO_4$. The reactions can be expressed as follows:

$$PbO_2 + 3H^+ + HSO_4^- + 2e^- \rightarrow PbSO_4 + 2H_2O \quad \textbf{2-6}$$

Reactions that occur on charging are as follows:

$$PbSO_4 + 2H_2O \rightarrow PbO_2 + 3H^+ + HSO_4^- + 2e^- \quad \textbf{2-7}$$

Side reactions that may occur during charging are as follows:

$$2H_2O \rightarrow 4H^+ + O_2 + 4e^- \quad \textbf{2-8}$$

$$Pb + 2H_2O \rightarrow PbO_2 + 4H^+ + 4e^- \quad \textbf{2-9}$$

At the anode, the lead (Pb) (negative active material) reacts with sulphate ions to form $PbSO_4$ during the discharge reaction, as follows:

$$Pb + HSO_4^- \rightarrow H^+ + 2e^- + PbSO_4 \quad \textbf{2-10}$$

Reactions that occur on charging are as follows:

$$PbSO_4 + H^+ + 2e^- \rightarrow Pb + HSO_4^- \quad \textbf{2-11}$$

Side reactions that may occur during charging are as follows:

$$O_2 + 4H^+ + 4e^- \rightarrow 2H_2O \quad \textbf{2-12}$$

$$2H^+ + 2e^- \rightarrow H_2 \quad \textbf{2-13}$$

Giving the net reaction upon discharge thus:

$$Pb + PbO_2 + 2H^+ + 2HSO_4^- \rightarrow 2PbSO_4 + 2H_2O \quad \textbf{2-14}$$

This reaction occurs by a dissolution/precipitation mechanism in which the Pb^{2+} ion dissolves and re-precipitates onto the surface of the electrode. The Pb^{2+} ion is only slightly soluble in H_2SO_4 and therefore allows the product to maintain the porous structure of the plate relatively well during charge and discharge processes[8]. The negative electrode acts as an anode during discharge and a cathode during charge with corresponding electron exchange and chemical oxidation/reduction reactions occurring.

During discharge, there is only one-half reaction at each of the plate polarities, namely **2-6** and **2-10**. The reaction becomes limited by the diffusion of species in solution as the rate of discharge increases which leads to the decrease of the discharge voltage of the cell. During the charging process, the situation becomes somewhat more complicated. In addition to the reverse reactions of the discharge process, as illustrated in reactions **2-7** and **2-11**, there are four other side, or secondary, reactions that occurs; **2-8**, **2-9**, **2-12** and **2-13**, due to favourable thermodynamic conditions, but occur slowly due to kinetic conditions within the system. These secondary reactions, however, are said to proceed only slowly under normal charge regimes and bring the charge reactions **2-7** and **2-11** to completion without much gas evolution[9]. As shown in the equations above, the PbO_2 in the positive plate and the lead in the negative plate are converted to $PbSO_4$ in these processes.

The Nernst equation for the cell potential is as follows:

$$E = E^0 + 2.303\ RT/nF(\log [HSO_4^-] + \log [H^+]) \quad \textbf{2-15}$$

The standard cell potential at 25 °C is 2.01. Based on a cell voltage of 2.60 V for 100% H_2SO_4 going to 100% H_2O, the theoretical energy density of the lead-acid cell is 784.8 kJ/kg (218 Wh kg^{-1}), the weight being that of the whole battery. If 40% H_2SO_4 is assumed and including the weight of H_2O, the practical theoretical specific energy of the lead-acid cell decreases to 442.8 kJ/kg (123 Wh kg^{-1})[8]. This value varies slightly according to different researchers; McAllister et al[10] stated the theoretical specific energy as 633.6 kJ/kg (176 Wh kg^{-1}) and that the practical achievable specific energy depends on the discharge rate and is typically 15-25% of the theoretical value. Although there are slight variations in these values, they give a good indication of what can be achieved, especially since the LAB has a history of poor energy density. Current commercially available traction batteries only generate around 108 kJ/kg (30 Wh kg^{-1})[11] while more advanced designs yield around 180 kJ/kg (50 Wh kg^{-1}). Indeed, the differences in these values underline and highlight the fact that although the overall chemical reaction that occurs in the LAB is well established, some of the mechanisms that limit and enable the reaction under different conditions are still not well understood.

2.2 Manufacture of PbO for Lead-Acid Batteries

The integral parts of the LAB are its electroactive materials derived from PbO as the precursor for making the active anode and cathode paste. There are currently two main methods used for the manufacture of PbO, the Barton Pot and ball mill processes[12]. The oxide produced by these methods contains between 20 and 30 wt. % unoxidized lead and is commonly known in industry as “leady oxide”. A brief overview of the two processes is outlined below:

2.2.1 The Barton Pot Method

George V. Barton first proposed in 1898 a method that yielded partially oxidised lead powder, leady oxide, at a considerably faster rate and in a simpler process compared to its predecessor. This process involved the pumping of molten lead into a large reaction pot and being rapidly rotated by paddles to agitate the lead. The reaction pot is heated to approximately 470 ˚C whilst the molten lead is stirred and continuously pulverised. The lead is then oxidised by a stream of humidified air, the resultant PbO particles are then transported to a classifier where the coarse grains are separated from the fine particles and are then returned to the reactor.

The coarse particles are oxidised, dispersed and returned to the classifier. The temperature of the reaction pot is typically maintained in the range of 460-470 ˚C. The leady oxide produced is conveyed through a series of cyclone separators and a dust collector, to remove the PbO dust from the air stream, and into a silo, once acceptable small particles and phase compositions have been obtained[13]. Table 2-1 outlines typical values for Barton Pot oxide characteristics, widely used in the USA, that are considered to be important for battery manufacturers for automotive and industrial applications.

***Table 2-1**: Characteristics of Barton Pot leady oxide for different battery applications[14]*

Characteristic	**Automotive Batteries**	**Industrial Batteries**
Free Lead (wt. %)	18-24	22-28
Apparent density (g ml^{-1})	7-9.4	9-11.4
Acid absorption (mg/g)	170-210	130-155
Particle size:		
Median (µm)	2.2	2.8
% below 1	10-15	5-10
Alpha:Beta ratio	96:6	96:4

2.2.2 The Ball Mill Method

The Ball Mill method was invented in 1924 by Shimadzu in Japan. Although a variety of variants now exists since its invention, the basic principles applied by Shimadzu remain the same and are based on solid-phase reactions and operate within the temperature range of 70-180 ˚C. The ball mill process involves the oxidation of lead balls or ingots within a large steel drum that is rotated around its horizontal axis. As the steel drum rotates the solid lead pieces collide against each other, generating heat from the friction created. This heat is sufficient to initiate the surface oxidation reaction.

The oxidation temperature is maintained at about 90-100 ˚C, a value at which the surface oxidizes readily, by the removal of excess heat by drawing out cool air through the drum. This air flow both facilitates the oxidation process as well as entraining the PbO powder obtained. This is followed by a separation process whereby coarse PbO grains are returned to the mill for further oxidation and attrition milling, and the PbO powders with the required grain particle size are collected by cyclone separators and dust collectors[13].
The powder characteristics produced and energy requirement by the Barton Pot and the Ball Mill processes are compared in Table 2-2 below.

***Table 2-2**: Comparison of the Barton Pot and ball mill processes[13]*

Characteristic	Barton Pot	Ball Mill
Particle size	3-4 mm average diameter	2-3 mm average diameter
Oxide crystal structures (wt%)	5-30% β-PbO, remaining α-PbO	~100% α-PbO
Surface area (m^2 g^{-1})	0.4-1.8	2-3
Energy use (kWh t^{-1})	Up to 100	100-300

The powders produced by the ball mill process are much more active due to the smaller particle size it generates and subsequently ensures better performance and longer life of the battery. They also have a greater acid absorption value of ~240 mg/g. The Barton Pot process however has the advantage of lower production costs due to the lower energy consumption, and higher production rate.

Due to the difference in the proportion of crystal structures produced by each method, many battery manufacturers use a mixture of ball mill and Barton oxides in their batteries. Despite the differences in surface area and particle size as detailed in Table 2-2, a study conducted by Corino et al.[15] found that the difference in values for total pore volume and median pore diameter were minor. Table 2-3 outlines these differences.

***Table 2-3**: Comparison of total pore volume and median pore diameter between Barton Pot and ball mill processes*

Characteristic	Barton Pot	Ball Mill
Total pore volume (ml/g)	0.19 - 0.26	0.20 - 0.30
Median pore diameter (μm)	1.50 - 2.64	1.67 - 2.67

Given that the performance characteristics of leady oxide manufactured from either of these processes have little perceived differences, the total pore volume and median pore diameter may be better indicators of powder efficacy than surface area and acid absorption. The significance of the type of PbO used will now be discussed.

2.3 Lead Oxides

Lead is able to form a number of oxides due to its four valence electrons in partially filled orbitals; two in the 6s and two in the 6p orbitals. A number of studies have been carried out in an attempt to identify those oxides of lead that may be useful and viable in terms of performance in the operation of LAB. Three have been identified.

2.3.1 Lead(II) Oxide, PbO

There are two polymorphic forms of PbO. The red polymorph of PbO, commonly known as litharge or α-PbO, has a tetragonal crystal structure and is stable at low temperatures. The yellow polymorph, commonly known as massicot or β-PbO, has an orthorhombic structure and is stable at elevated temperatures. The structures of the two polymorphic forms are shown in Figure 2-1. The transition temperature of α-PbO to β-PbO is around 480 ˚C[16].

The battery industry currently uses a mixture of 70 to 80 wt. % PbO and 20 to 30 wt. % lead particles, or free lead. The method of manufacture determines the relative proportions of the two oxide polymorphs present in the final product. This factor is particularly important, as it has been shown that the ratio of the polymorphs moderates the yields of the different basic $PbSO_4$ phases that can be formed during the curing process in the production of battery plates.

It has been shown that α-PbO favours tri-basic $PbSO_4$, $3PbO{\cdot}PbSO_4{\cdot}H_2O$, while β-PbO promotes tetra-basic $PbSO_4$, $4PbO{\cdot}PbSO_4$. This is significant as the basic $PbSO_4$ phases have a direct impact on the plate performance characteristics in terms of capacity and cyclability during charge and discharge cycling[15].

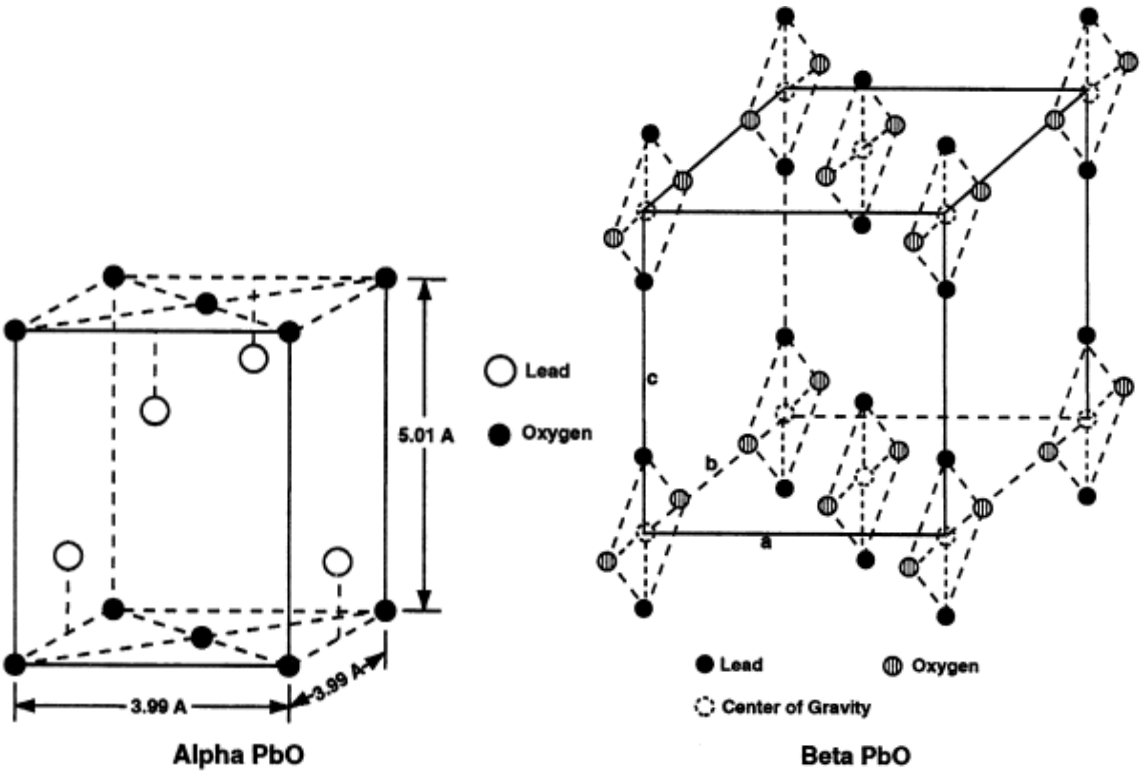

***Figure 2-1**: Crystal structures of α (Tetragonal) and β-PbO (Orthorhombic)[14]*

2.3.2 Lead (II, IV) Oxide, Pb_3O_4

Lead (II, IV) oxide, also known as red lead or lead tetroxide is formed when PbO is heated in a stream of air at around 540 ˚C and has a tetragonal crystal structure at room temperature. A representation of the structure of Pb_3O_4 is shown in Figure 2-2. This form of lead is usually used in battery making due to its ability to facilitate plate formation, contributing to high-rate performance and enhancing initial capacity[14].

Approximately one-third of the oxide is converted directly into PbO_2 before the formation charge is initiated in order to fix the starting compositions of the electrodes.

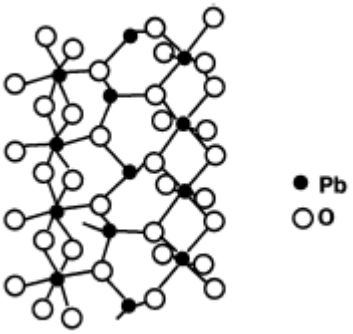

***Figure 2-2**: Crystal structure of Pb_3O_4 (Tetragonal)[14]*

2.3.3 Lead(IV) Oxide, PbO_2

In the LAB, PbO_2 is the product of positive plate formation and constitutes the active mass. PbO_2 exists in two forms, α-PbO_2, which has an orthorhombic crystal structure, and β-PbO_2, which has a tetragonal crystal structure. The lead:oxygen ratio is a nominal 1:2. The properties of PbO_2 are fundamental to battery design; most significantly the morphology of the positive active mass contributes to the overall performance of the electrochemical system. In addition, the strength and elasticity of PbO_2 are determined by its microstructure, making the control of this essential in the current study, given the further complexity that both the shape and the volume of PbO_2 and its product during battery discharge, $PbSO_4$, changes during each charge and discharge cycle. It is generally accepted that the β form of PbO_2 contributes the greatest share of electrochemical capacity out of the two polymorphs[17]. It has been suggested however, that the α form imparts structural durability to the positive active mass[18]. If this is true, the effect would only be temporary as α-PbO_2 is irreversibly converted to β-PbO_2 during the charge/discharge process via $PbSO_4$.

2.3.4 Summary

The effect of PbO with different characteristics on the structure and properties of positive and negative plate of LABs are of principal importance and require thorough investigation. This is especially true when new manufacturing techniques are involved in producing new types of batteries using the same chemistry, which may yield novel results. There are continuous changes involved during the conversion of oxide to the active materials of the plates. These include: shape, apparent density, particle size distribution and BET surface area. It is important to monitor these changes, particularly on the nanoscale. By analysing these characteristics and the interplay between them, including the manner in which they were generated, favourable features can be retained and detrimental ones minimised and an optimum manufacturing process obtained for the production of LABs used for different applications[19].

Together with these materials, the cell consists of an assembly of electrodes, separators and electrolyte housed inside a container with terminals. These components will now be discussed.

2.4 Cell Components

2.4.1 The Cathode

The cathode – the oxidising electrode, where reduction takes place – accepts electrons from the external circuit and is reduced during the electrochemical reaction while discharging. It is also known as the positive electrode in industry due to its state of charge when the battery is fully charged. One of the most important factors that determine the performance of the LAB is the positive active mass. The positive PbO_2 active material is formed by electrochemical oxidation of basic $PbSO_4$ and PbO[20]. The performance of the battery can be significantly improved by making it more electrochemically reactive as the $PbSO_4$ formed during the discharge and charging processes is an insulator which creates a non-conducting coating on the PbO_2[10].

This insulating coating decreases the active utilisation of the battery as it prevents the positive, and thereby also the negative, electrode from fully discharging, thus impeding the ability of the battery to attain its theoretical specific energy. There are four precursor stages to its production that will determine the inherent characteristics of this active mass. The cumulative effect of the type of PbO used, the manner in which the paste is mixed, the curing conditions and the process of formation are all significant in determining the electrochemical reactivity of the cathode and therefore the performance of the cell.

2.4.2 The Anode

The anode or negative electrode – the reducing or fuel electrode – gives up electrons to the external circuit and is oxidised during the electrochemical reaction. It is also known as the negative electrode in industry. The fully charged negative plate consists of a porous mass of lead particles surrounding a lead alloy grid. The initial formation of the lead anode is also based on the PbO precursor. Concurrently with the formation of the positive PbO_2 active material at the cathode by electrochemical oxidation, the anode is formed by electrochemical reduction to form $PbSO_4$ when discharged.

It is standard practice in LAB manufacture to add a small amount (typically 0.2-0.4 wt. %) of barium sulphate ($BaSO_4$) to the negative active material. This provides a large number of nuclei on which $PbSO_4$ crystals are able to grow, which in turn serves to increase the surface area of the discharge product and thus to assist charge acceptance. $BaSO_4$ is believed to be effective in this function because it is isomorphous with $PbSO_4$[21].

It is important to note that for both the anode and cathode, a good mass adhesion to the grid is vital to avoid problems at the grid/mass interface[22].

2.4.3 The Electrolyte

The electrolyte – the ionic conductor – provides the medium for transfer of charge, as ions, inside the cell between the anode and cathode. The electrolyte in the LAB is H_2SO_4, which occupies pores within each plate and the volume in between, which also contains the separator. The typical H_2SO_4 concentration is 5 M (1.28 g cm^{-3}[23, 24]). Ions from the electrolyte take part in the discharge process. H^+ ions are produced at the negative plate and consumed at the positive plate while HSO_4^- ions are drawn from the electrolyte. Therefore, during discharge it is a requirement for there to be a net flux of H^+ ions from the negative plate to the positive while electrons flow round the external circuit.

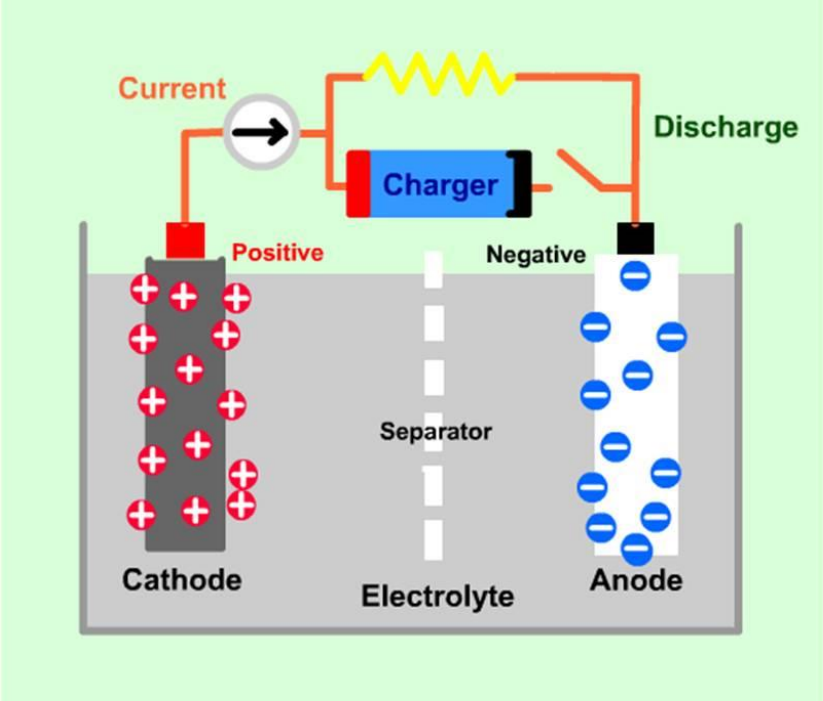

***Figure 2-3**: An illustration of a Lead-acid cell[25] (Note: the distance between the anode and the cathode is exaggerated for clarity, in practice they are both in direct contact with the insulating porous separator to minimise internal resistance.)*

Figure 2-3 shows a basic cell, an electrochemical unit which provides a source of electrical energy by direct conversion of chemical energy with all its major components. A battery consists of one or more electrochemical cells, electrically connected in an appropriate series/parallel arrangement to provide the required operating voltage and current levels.

2.4.4 The Separators

Separators are critical components in a LAB. They are placed in between the positive and negative plates to prevent short circuit through physical contact[26]. Although required, separators lower the efficiency of the cell as they obstruct the flow of ions between the plates and increase the internal electrical resistance. A number of different materials have been used in the past to make separators, they include: glass fibre mat, wood, cellulose, rubber, sintered PVC, microporous PVC/polyethylene.

An effective separator must have a number of mechanical properties, they include: porosity, pore size distribution, permeability, electrical resistance, specific surface area, ionic conductivity, mechanical stability and strength, and chemical compatibility with the electrolyte. While in operation, the separator must have good resistance to acid and oxidation. The area of the separator must be a little larger than the area of the plates to prevent material shorting between the plates. The separators must remain stable over the operating temperature range and anticipated useful life of the battery.

2.5 Types of Lead-acid Batteries

2.5.1 Flooded Batteries

Flooded LABs have been used for more than 140 years in various applications, which include automotive, traction and stationary. Although valve-regulated LABs have gained significant market share over the past few decades, the flooded design is still the major part of all manufactured LABs[27].

The essential components of a LAB are the positive and negative electrodes (grids and active materials), the electrolyte (diluted H_2SO_4), the highly porous separators between the plates, the current collector system (top bars, terminals, and inter-cell connectors for block batteries), and the container with the lid. Flat plate design is used for virtually all negative and most of the positive electrodes. The more electrode material there is in the cell, the greater the capacity of the cell. Thus, a small cell has lower capacity than a larger cell, given the same chemistry. For marine applications, boats, submarines etc., these batteries are usually not sealed so that the electrolyte can be replenished when it is vented while charging. Flooded LABs are mechanically the weakest as the grid is only supported at the edges.

2.5.2 Sealed Valve-Regulated Lead–Acid (VRLA) Batteries

Sealed LABs have been developed over a number of years and for many applications. They have become the system of choice, especially for stationary applications[28]. The main practical requirements for a sealed battery are the high hydrogen overpotential for the negative grid alloy to suppress hydrogen evolution at the negative electrode, the correct balance of active materials and a means by which oxygen can diffuse from the positive electrode to the negative where it is chemically recombined, which usually involves a catalyst. This is termed a recombinant system.

These batteries are designed to prevent electrolyte loss through evaporation, spillage and gassing and consequently, increase the life of the battery. They typically contain lead-calcium or lead-calcium-tin alloy grids with either an absorptive glass mat separator or a conventional microporous polymeric separator and a gelled electrolyte.

The absorptive glass mat separators are designed for operation with the separator only partially saturated with electrolyte and a small amount of connected gas porosity to permit rapid transport of oxygen between the positive and negative electrodes. In gel cells, the electrolyte is mixed with finely divided silica and forms a gel. This becomes fissured on a very fine scale and allows oxygen to diffuse rapidly between the plates.

This therefore allows the cells to operate fully sealed without the need for routine maintenance. This type of cell is seen as the main contender for future motive power applications and much research has gone into developing it further for EVs and HEVs[29].

2.5.2.1 Gelled-electrolyte cells

Gelled-electrolyte cells have become important for both stationary and traction service. These cells use a thickening agent such as fumed silica to immobilise the electrolyte. This enables the battery to continue to function even if the container is breached, unlike the flooded design. However, because they cannot be re-filled, controlling the rate of charge is very important.

They are an alternative recombinant technology used in VRLA batteries to facilitate recombination of gases produced during charging. When in use for stationary applications, they are complementary to other types of VRLA cell. For traction applications, they form part of a range of alternatives for reduced maintenance but maintenance-free operation will increasingly become the standard requirement. They have a disadvantage in that they must be charged at a slower rate as any gassing will result in damage to the cell. For EV and HEV applications, sealed operation is a definite requirement and the enormous level of interest in this area has and will continue to stimulate rapid technological improvements which must be directed in part to improving the cyclability of VRLA batteries and their tolerance to operating conditions[28].

2.5.2.2 Absorbed Glass Mat battery, AGM

This type of battery is also known as an Absorptive Glass Micro-Fibre battery. They represent the latest evolution of commercialised LABs. This is a type of VRLA battery where the boron silicate fibreglass mat acts as the separator between the electrodes, which also absorbs the free electrolyte, acting like a sponge immobilising the electrolyte and additionally providing physical bond between the lead plates and the container. This allows it to be both vibration and impact resistant, as well as being spill proof with a very high degree of porosity of more than 90%[22]. This high degree of porosity gives rise to poor mechanical properties and therefore requires reinforcement, which can be achieved with synthetic fibres to improve the strength[30]. Its purpose is to promote recombination of the hydrogen and oxygen given off during the charging process. No silica gel is necessary.

The fibreglass mat absorbs and immobilises the acid in the mat but keeps it in a liquid rather than a gel form. The high porosity and the pore structure of the glass mat results in a very low electrical resistance. In this way, the acid is more readily available to the plates allowing faster reactions between the acid and the plate material, permitting higher charge/discharge rates as well as deep cycling. This construction is very robust and is able to withstand severe shock and vibration and the cells will not leak even if the case is cracked.

AGM batteries are also sometimes called "starved electrolyte" or "dry", because the fibreglass mat is only 95% saturated with H_2SO_4 and there is no excess liquid. Nearly all AGM batteries are VRLA AGMs and have a very low self-discharge rate of from 1 to 3% per month and can have a life time of 12 years at 20 ˚C[22].

2.5.3 SLI Batteries (Starting, Lighting and Ignition)

This is the typical automotive battery application. Automotive batteries are designed to be fully charged when starting the vehicle; after starting the vehicle, the used charge, typically 2 to 5% of the charge, is replaced by the alternator and the battery returns to full charge. These batteries are not designed to be discharged below 50% Depth of Discharge (DOD) and discharging below these levels can damage the plates and shorten battery life.

2.5.4 Deep Cycle Batteries

This type of battery is used in a variety of applications such as in submarines, forklift trucks, powering golf carts and for some EVs, which are designed to be completely discharged before recharging. The charging process can generate excessive heat, which can warp the plates; therefore, deep cycle batteries need thicker and stronger or more solid plate grids. This differs from standard automotive batteries which are not designed for repeated deep cycling and use thinner plates with a greater surface area to achieve high current carrying capacity.

Automotive batteries will generally fail after 30-150 deep cycles, while they may last for thousands of cycles in normal starting use. If batteries designed for deep cycling are used for automotive applications they must be made larger, by about 20%, to compensate for their lower current carrying capacity. A typical labelled layout of a LAB is shown in Figure 2-4.

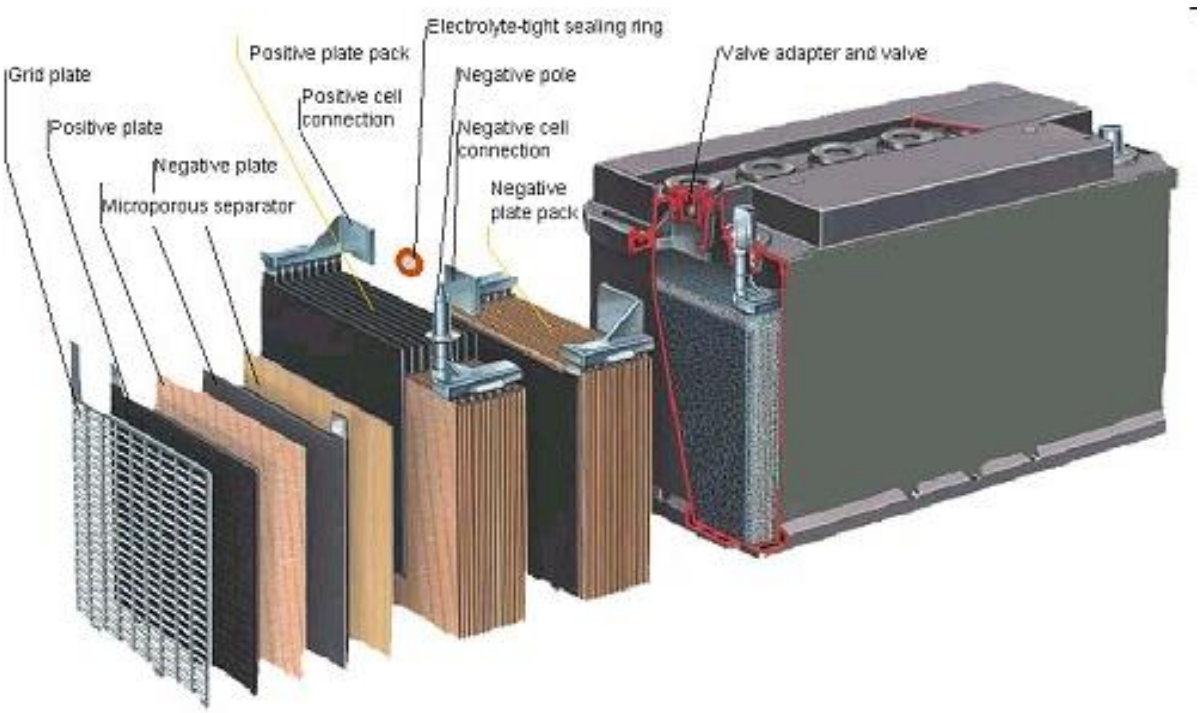

***Figure 2-4**: Typical layout of a lead-acid battery*[31]

2.6 Overview of Lead-Acid Batteries

Conventional lead-acid traction cells require frequent servicing in the form of water addition. There are however, various methods of reducing the need for maintenance. These methods all have their advantages and disadvantages, both in initial cost and total life cost. Table 2-4 summarises the methods that are employed to reduce the need for maintenance. For flooded batteries, the use of either mechanical or pneumatic pumps to re-circulate the electrolyte or short high-current electrical pulses for the same purpose can be coupled with lower levels of overcharge to increase the maintenance interval.

Overcharge can be described as the continual charging of the battery beyond its fully charged state. Changes in the alloy composition are used to further reduce water losses and as a result, maintenance intervals of up to a year are achievable. In addition, automatic watering systems are available to make maintenance more convenient and more accurate. For many applications, however, water addition is neither desirable nor practical and as a result there is a preference towards VRLA cells for traction service[28].

***Table 2-4**: Methods to achieve reduced maintenance for lead-acid batteries for traction applications*

Battery type	Maintenance interval (cycles)	Degree of overcharge (%)	Recharge time (h)
Flooded, conventional charger	15-20	15-20	8-13
Electrolyte agitation, reduced overcharge	50-75	5	6
Electrolyte agitation, low-maintenance alloys, reduced overcharge	200-250	5	8-13
Gel	Never	<5	11-13
Absorption glass mat separator	Never	<5	6-8

There are however, disadvantages of such maintenance-free gel traction cells. The battery and charger are coupled together in a system and so replacement of existing batteries must always include the charger. The recharge time also tends to be longer than flooded batteries and cycle life for regular deep cycling is lower.

These drawbacks, however, are not considered too serious for many applications, especially in a variety of industrial applications such as sweeper trucks, automatically-guided vehicles and pallet trucks where the sealed battery can be taken full advantage of and in many practical situations more frequent charging is not a major issue.

The LAB faces many new challenges from other electrochemical systems as an automotive battery which must be overcome if it is to remain the dominant system in industry. Many improvements can be made to the system to allow it to remain highly competitive, likely through major redesign and scientific research, in order to modernise the system to meet new demands from industry.

Future automotive service requires, in addition to cold-cranking performance, the combination of high power capability, very good charge-acceptance and an excellent cycle life. Such applications include stop-start, regenerative braking and soft, mild and full hybrid vehicles[22]. The electrical systems in future electric and hybrid electric vehicles are expected to undergo significant changes and are to become far more extensive than current vehicles in production. This is mainly due to the requirement for a greater degree of electrical functionality in order to improve fuel economy and in addition, to replace mechanical functions in the vehicles such as steering, braking and air-conditioning by electrical equivalents to provide greater safety, comfort and cost[32]. These advanced electrical systems are said to require the electrical storage element to operate at a partial-state-of-charge for most of its life and at significantly high rates, termed ‘HRPSoC’ duty[9].

The battery failure modes observed in such operations are quite different from those seen in standard electric vehicles which require deep-cycling, which can currently be satisfied by VRLA batteries. Some of the changes require systems to operate at a higher voltage which means that more cells are required, increasing the overall weight of the battery. In the case of lead-acid systems, this represents a significant increase in weight which will prove unattractive for future electrical vehicles. Clearly, this would suggest that any future new design and research into a new improved LAB will require significant research into making the battery lighter while maintaining its voltage output.

At present, around three-quarters of LAB manufactured in the world are for conventional automotive use. These batteries are unsuitable for providing adequate performance in any of the electrical systems outlined earlier, primarily due to the mode of operation of having to be at a partial-state-of-charge and having to discharge and charge at far higher rates than they are designed for in their current role. A comparison of some of the key parameters for a typical automotive (SLI) battery, a deep-cycle battery and a battery undergoing HRPSoC duty is shown in Table 2-5.

***Table 2-5**: Typical duty and performance characteristics for VRLA batteries in different categories of present and new-generation vehicles*

[a] This is the normal operating range for the Honda Insight, but the battery-management system of this vehicle will allow a wider range of operation between 30 and 80% state-of-charge if so required by the driving pattern

[b] In multiples of 1 h rate

[c] These are two forms of premature capacity loss(9)

Parameter	**Application**		
	SLI, 12 V	Electrical vehicle	Future automotive
Duty	High-rate start	Deep-cycle	High-rate PSoC
State-of-charge	85-90%	20-100%	42V PowerNet: 70-90%, HEV: 60-70%[a]
Maximum normal discharge[b]	10C[a]	4C[a]	15C[a]
Maximum normal charge[b]	0.5C[a]	0.5C[a]	8C[a]
Failure modes	Corrosion, shedding	PCL 1, PCL 2[c]	Under-charge and sulphating of negative plates

As mentioned earlier, secondary reactions within the cell are negligible under normal charge regimes. However, at high rates it becomes more kinetically favourable for these secondary reactions to occur. As a result, a high degree of accumulation of sulphate develops on the negative plate. This therefore indicates that in a HRPSoC mode of operation the standard recharge reactions are no longer functioning effectively. In addition, this accumulation will act as a barrier layer and result in an increase in the electrical resistance in the affected part of the battery(22).

The battery in a HEV is required to operate in a partial-state-of-charge in order to accept charge from regenerative braking; it is this that exposes the battery to the many short charge and discharge events at very high rates. These high rate events cause the discharge reaction to take place preferentially at the plate surface, due to diffusion limitations, and near the top, because of a non-uniform potential distribution across the grid(21). Moseley et al.(9) stated that the charge reaction actually proceeds in two stages, the dissolution of $PbSO_4$, followed by deposition of metallic lead in the following manner:

Stage 1

$$PbSO_4 \rightarrow Pb^{2+} + SO_4^{2-} \qquad \textbf{2-16}$$

Stage 2

$$Pb^{2+} + SO_4^{2-} + H^+ + 2e^- \rightarrow Pb + HSO_4^- \qquad \textbf{2-17}$$

This is significant since the solubility of $PbSO_4$ decreases as the concentration of acid increases[33]. A high rate of production of H_2SO_4, arising from high rates of recharge, can exceed the rate at which HSO_4^- ions diffuse away from the reaction sites. This means that the rate of the recharge reaction becomes self-limiting.

The accumulation of sulphate on the surface of the negative plate, derived from the fact that the battery must always operate at an intermediate state-of-charge resulting in the presence of the incomplete discharge product, acts as a barrier to diffusion between the electrolyte and the negative plate; the problem is compounded by the diffusion limitations outlined earlier.

Clearly, research needs to be done to eliminate these constraints to allow more effective and efficient mass transfer at progressively higher rates and to limit the proportion of the current accepted by the cell being taken up by secondary reactions. Despite these issues there are encouraging signs that LABs are making good progress.

A recent road test using modified LABs in a Honda Insight HEV, in place of a nickel-metal hydride battery, demonstrated performance near parity with its more expensive counterpart[34].

2.7 Options for Improving the Lead-Acid Battery

Battery operation for future automotive use requires very high rates to proceed without a regular full charge and also be resilient against life-limiting mechanisms inherent in such operations. In order to do this, new research must focus on ways to limit secondary reactions within the cell while at the same time promote and enhance primary reactions, by minimising diffusion constraints. A number of areas can be investigated in order to bring about this aim.

2.7.1 The Expander

One such area where investigation is warranted is in the effect of composition in the expander material in the negative active material. An expander is a combination of materials, usually lignosulfonate and $BaSO_4$, which serves as a nucleating agent for $PbSO_4$, and carbon black, mixed with the active material in the cell to maintain a high surface area and structural cohesion, among other effects. Without an expander, the surface area would decrease with battery cycling resulting in a decline in capacity. The content of carbon black in the expander material has traditionally been around 0.1-0.2 wt. %.

However, research by Moseley et al[9] has shown that by increasing the proportion of carbon black to 2 wt. % in the expander can increase the conductivity by around five orders of magnitude. The study also indicated that the type and quality of carbon is also important and that different types give rise to many different results when added incrementally to the negative active mass, ranging from excellent protection against sulphate accumulation to none at all. This is by no means surprising given the vast range of different types of carbon available[35].

Separate research has also indicated that elevated amounts of certain types of carbon into the negative plates can overcome the mechanism that is responsible for the accumulation of $PbSO_4$[21], although the type of carbon used is not disclosed. It could simply be the case that increasing the carbon content confers a corresponding increase in the surface area of the active material in the negative plate, and this large surface area constrains the size of the $PbSO_4$ crystals by impeding their growth.

A study conducted by Calábek et al.[36] suggests that this might be the case when they demonstrated that the addition of titanium dioxide (TiO_2) particles instead of carbon ones, provided similar improvement in partial-state-of-charge cycling. The TiO_2 particles seem to prove equally effective due to their ability to impede $PbSO_4$ crystal growth in the same manner as carbon. This also appears to be the case for the positive plate as no accumulation of $PbSO_4$ crystals occurs there, due to the surface area being far greater than that on the negative.

Another theory brought forward by Shiomi et al.[37] attributed the improvement conferred by the extra carbon to enhanced conductivity of the partially discharged negative active material afforded by a conductive network of carbon particles distributed between the crystals of $PbSO_4$. There are in fact a number of distinct functions proposed for the additional carbon that can influence the performance of the negative plate[21].

The work of trying to determine these functions and their relationship to enhanced performance in the negative plate is highly significant as it will ascertain the form or forms of carbon that will allow for the ideal additive(s) in the expander material of the negative active mass and perhaps also determine the optimum volume fraction(s) to be used.

2.7.2 The Electrodes

The power performance of LAB can be improved in two ways: (i) the reduction of the electrical resistance of the current-collector parts, for example the grids and (ii) optimisation of grid material/design[22]. The majority of improvements in the power capability to date have been achieved by the reduction of the internal electrical resistance. For VRLA designs with antimony free grid alloys, the open circuit voltage has been raised to a slightly higher level over the years by an increase in H_2SO_4 concentration from 5 to 5.5 M (relative density of 1.26 or 1.28 to about 1.30 g cm^{-3} or more).

The situation is, however, not so simple. Though these improvements are good, there is room for further reduction in resistance. The internal resistance of a battery is quite complex. There is the ohmic resistance from all the current-collector parts, which include the grids, top bars, inter-cell connections and the terminals, and the electrolyte, but there are also polarisation effects to consider. These polarisation effects include diffusion, charge-transfer reactions and crystallisation. All of these are non-ohmic and depend significantly on the current and the time of current flow, as well as the state-of-charge and whether the battery is on charge or discharge[22].

In the beginning of a high-power discharge, the voltage drop mainly arises from all the ohmic resistances and the charge-transfer reaction. Other effects, such as diffusion and change of active-mass surface, exert an influence and result in a higher voltage loss, which reduces the power capability of the battery. Thus, if very short high-power discharge pulses are required, then the polarisation is less important in comparison with a longer period of high power discharge.

It has been shown that small additions of other elements in both the negative and positive plates can give rise to changes in the overpotentials, and thus change the rates at which the secondary reactions proceed[9].

A study by Australia's Commonwealth Scientific and Industrial Research Organisation, CSIRO, noted by Moseley et al.[9], has found that using zinc as an additive can suppress hydrogen evolution at the negative plate, and that a combination of antimony and iron can suppress oxygen formation at the positive plate.

To add to the complexity, a number of other researchers[38-41] have reported that an inclusion of tin, of sufficiently high content of about 1 wt. % or more, is needed to prevent a poor cycle life caused by the formation of a barrier layer of $PbSO_4$ between the positive grid and the active mass. Table 2-6 shows the concentration of each element that must not be exceeded if the hydrogen evolution current and oxygen evolution current are to be maintained at, or below, their respective critical levels to achieve an acceptable battery life.

***Table 2-6**: Maximum allowable levels of trace elements for maintaining hydrogen and oxygen currents below critical levels[9]*

Elements	Level (ppm)			Maximum allowable level (ppm)
	I_{Float}	$I_{Hydrogen}$	I_{Oxygen}	
Ni	4	16	4	4
Sb	6	5	6	5
Co	4	7	4	4
Cr	7	16	7	7
Fe	-	-	-	10
Mn	5	5	5	5
Cu	33	13	34	13
Ag	76	142	66	66
Se	2	1	2	1
Te	1.5	0.5	1.4	0.3
Tl	25	25	25	25
As	5	-	5	5
Sn	41	-	40	40
Bi	543	-	522	500
Ge	673	250	658	10
Zn	915	-	905	500
Cd	756	-	722	500

It has also been suggested[22] that the use of copper as the negative grid material could be a way of improving the high-power performance for LABs with high capacities and tall plates. The reasoning is that, the taller the lead plates, the greater the ratio of the grid electrical resistance to the total internal resistance of the cell. This gives rise to a lower depth of charge in the bottom regions of the cell, especially for plates taller than 50 cm. This not only causes a significant drop in voltage along the grid and reduces the energy available, but also increases the heat generation in the cell.

A new cell type was developed to attempt to address this problem with a Copper-Stretch-Metal (CSM) grid design[22]. This design, where an expanded copper grid is covered with a thin layer of lead is used on the negative side and standard tubular plates for the positive, proved quite successful when compared to the standard design. The CSM cell had a 17% lower internal resistance than the standard cell. The result of the lower resistance of the negative plate means a more equalised current distribution between the top and the bottom of the cell.

This indicates that there are lower current density differences in the plate and a more equal mass utilisation between the top and the bottom of the cell and therefore, in terms of both charge and discharge modes, this design provides a greater improvement in charge acceptance as well as higher energy efficiency.

Plate thickness is also important to the lifetime of a battery. It has been shown that thick plates in cycling applications are at least as important as those related to additive content such as antimony[42]. For SLI applications however, thinner plates, in some cases of just 1 mm, are required as this reduces the diffusion problem outlined earlier where the lack of electrolyte inside the plates causes the electrode reaction to stop even when there is still sufficient active mass available.

The use of even thinner electrodes have been reported, where they are termed the thin metal foil, or TMF concept[43, 44]. The grids were rolled to a thickness of around 0.6 mm and had an active mass layer of the same dimensions. These were used in spiral round batteries with absorptive glass mat separators and demonstrated extremely high power and excellent chargeability.

This type of battery was developed for use in power tools, SLI and other applications where high power and rapid recharge capability are needed. Although this demonstrates the extremely high-power performance that the lead-acid system can achieve, an acceptable level of reliability and a sufficiently long life is still lacking and more research needs to be conducted to address this deficiency.

There have been attempts to reduce the electrical resistance by improved grid designs for high power applications[45, 46]. However, any changes in the structure of the grid must be performed carefully and with due consideration to any potential casting and pasting problems[38]. A novel grid production method, proposed by Barkleit et al.[47], was designed to avoid any restrictions from grid casting that involves electro-deposition which aims to minimise grid weight and to optimise grid structure for low electrical resistance.

In addition to improving the current technology by alloying, a different approach has been investigated by Soria et al.[48]: the use of polymer-structured electrodes was explored whereby the grids are composed of a polymer that is coated with thin layers of copper and lead. This gives rise to lower weight in comparison to standard lead grids. These polymeric network structure, or PNS, grids had much smaller mesh sizes than the standard grids. The dimensions varied between 1 mm x 1 mm and 3 mm x 3 mm in mesh size. It was demonstrated that this small mesh size produced much better discharge performance, due to the shorter current paths within the active mass.

The results from this study not only showed that this different approach is viable, but also provided promising results. However, the cost of using such an approach may be financially prohibitive, as it will require costly materials as well as modifications to current manufacturing practices.

2.7.3 Cell Design

In addition to the traditional design with flat plates, such as those in VRLA with AGM separators, LABs can adopt a cylindrical configuration with spiral electrodes and AGM separators; an early cylindrical design is shown in Figure 2-5. The cylindrical cells with this spiral design have tightly wound layers of lead-tin grids which allow the separator to be kept under very high compression. This would prevent the expansion of the positive active mass and afford both an excellent cycle-life and a very high-power performance.

The thin electrode design required in this type of battery provides an active mass surface that is significantly larger than in conventional flat-plate batteries which, as demonstrated by Trinidad et al.[49, 50], reduces the internal electrical resistance and provides exceptional high power.

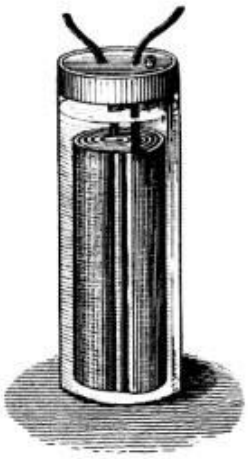

Figure 2-5*: An early example of a cylindrical lead-acid battery*[51]

2.7.4 The Active Mass

Both active materials, the PbO_2 and Pb, act as electrical conductors from the points of the electrode process to the nearest grid members. One must consider, however, that the structure of the active material is porous and that PbO_2 has low conductivity. Add this to the formation of insulating $PbSO_4$ layers from subsequent discharges, the impact on the overall electrical resistance inside the active mass is significant.

In addition, the crystalline structure of the active mass, i.e. the porosity and crystal size, has a strong influence during long discharge periods with high power as this reduces the surface area of the active mass within the paste mixture and the electrolyte.

Due consideration must be given to the content of the paste and the corresponding quantity and density of its constituent parts. Due to the complexity of pasting, curing/drying, soaking and formation, the task of formulating the optimum process becomes significant. Many researchers have, over the years, come up with a number of different methods with varying success[52-55].

The particle size of the active material plays a significant role. By decreasing the particle size of the active material, one can also increase the efficiency of the cell as this increases the true surface area. Polarisation is very much influenced by the surface area of the active mass. During discharge, some of the active mass is consumed and the $PbSO_4$ covers part of the surface. Therefore, with more and more discharge, the available surface area is reduced considerably, which in turn incrementally increases polarisation.

This problem could be somewhat mitigated by decreasing the particle size of the active material. However, it has been reported that increasing the surface area would significantly reduce the life time of the battery, especially in cycling applications[22] and due consideration must be taken.

There has been a considerable amount of focus and research being conducted recently on the possible use of lead nanopowders in LABs. It has been speculated that PbO, obtained by the direct electrochemical oxidation of lead, producing nanopowders, can exhibit superior electrochemical characteristics[56].

Currently the primary and most developed methods of PbO synthesis are via sol-gel and pyrochemical routes. However, powders produced from these methods are amorphous and of a spherical form, which means that they have no definite crystal structure. Lead precursors needed to manufacture nano-oxides are expensive. In addition, the established routes of manufacture are still far from viable for large-scale industrial production, adding another major restraint on the fabrication of nanopowder. Therefore, a technique is required to produce lead nano-oxide that is both effective for use in LABs and also financially feasible.

It has been observed that another disadvantage of using chemical methods is that the resulting nanopowders possess inferior electrochemical characteristics in H_2SO_4 solutions when compared with powders obtained by electrochemical methods[56]. Regardless of this, the overall advantages in the reduction of size of the PbO particles in increasing the true surface area of electrodes which will enhance the performance and efficiency of the electrochemical system is highly attractive.

There have been a number of reported studies on the manufacture of nanostructured lead oxide. Wang et al.[57] for example used a two-step chemical process and formed the electroactive material in a VRLA battery.

Cruz et al.[58] demonstrated that α-PbO thin films from aqueous solutions of $Pb(CH_3COO)_2 \cdot 3H_2O$ can be prepared by spray pyrolysis and be deposited onto a lead substrate. Their research showed that the electrochemical cell could maintain a discharge capacity of 100 mAh g^{-1}, which is 40 wt. % of the theoretical value, upon extensive cycling. Further, Karami et al.[59, 60] showed that uniform nanostructured PbO can be manufactured by a sonochemical method.

Results from their investigation proved that a large discharge capacity and excellent cycle characteristics of the nanostructured powder can be obtained. Another method for generating nanostructured PbO was verified by Salavati-Niasari et al.[61] They showed that PbO powder with an average particle size of 35 nm could be synthesized by decomposing lead oxalate at 500 °C.

A study conducted by Sun et al.[62] showed that ultrafine lead oxide can also be generated from lead acetate trihydrate precursors in either nitrogen or air. Additionally, Sadeghzadeh et al.[63] were able to produce nanostructured PbO by first synthesizing one-dimensional Pb(II) chelate by using 2-pyridinecarboxylic acid, lead acetate and sodium nitrite and then by roasting at 110 to 500 °C.

2.8 Lead-Acid Battery Recovery and Recycling

In order to wholly realise the full potential of the LAB, the major drawback of the current costly method of recycling LABs needs to be addressed. The recycling of lead from used LABs not only contributes to the sustainable development and continued progress of the LAB industry, but also the reduction of lead contaminates exposed to the environment. This is the most important underlying issue in the LAB industry as lead is classified as hazardous to human health.

Depleted LABs consist of four parts. Table 2-7 below shows each part with their approximate corresponding percentage by mass in a spent battery[64]. The mass of each component depends on the function of the battery, for example an industrial high capacity LAB would be designed to have thicker electrodes containing more electroactive paste material.

Table 2-7: *Depleted LAB components and their corresponding percentage by mass*

Battery Components	% by Mass
Lead components (e.g. electrodes)	24 – 30
Depleted electroactive paste material	30 – 40
Organic binders and container material	22 – 30
Electrolyte	11 – 30

The most complex element within the LAB in terms of recycling is the depleted lead paste material[65]. Table 2-8 illustrates the typical composition of an exhausted lead paste in a positive electrode.

Table 2-8: *Components of depleted lead paste and their corresponding percentage by mass in a positive electrode*

Depleted lead paste components	% by Mass
$PbSO_4$	60
PbO_2	28
PbO	9
Pb	3

The current method used to extract lead from battery pastes is by a smelting process known as pyrometallurgical extraction. The temperature required in this process is very high. This is due to the significant amounts of $PbSO_4$ in the spent battery[66] as illustrated in Table 2-7. In order to decompose the $PbSO_4$ the extraction method typically needs to be at 1100 °C or above[67]. This highly energy intensive method not only has significant associated financial costs, there is also an economical issue; this process incurs a one percent loss of lead per cycle[68].

The environmental drawbacks are also significant, as the high temperature carbothermic reduction using coal, coke or natural gas as the source of energy and reductant, generates lead fumes as well as dilute sulphur dioxide (SO_2) gas[69, 70]. The resulting metallic lead is then reoxidized to PbO to be reused in the electroactive paste material in new LABs[71].

The pyrometallurgical process employed around the world currently is either through a single batch rotary furnace or a continuous smelting furnace of the reverberatory, blast or Isasmelt/Aussmelt type[4].

The process in a rotary furnace has four stages of operation and is outlined below:

1. Separation of the plastic container, electrolyte and lead plates by grinding the battery
2. The reduction of lead in a rotary furnace
3. Separating the metallic lead from the slag
4. Refinement of the recycled lead

The effective recycling of lead is of crucial importance in many countries, especially where economic reserves of lead ore are low, such as in the UK, Germany or Brazil[5]. Despite its negative effects at the environmental level the need for LABs as a power source in SLI for automotive, marine and aviation applications are significant. Indeed, its application has been steadily increasing as it expands into its non-traditional areas such as electric bicycles and electric vehicles.

This is especially apparent in China where it has become the international centre of the lead market as it has become the largest consumer and producer of primary and secondary refined lead. Indeed, the global consumption of secondary lead in 2010 was 4.2 million tonnes with 80% of this used in the manufacture of LABs in China [72, 73] . Coupled this with the increased use of high-capacity LABs in industrial applications the need to have a cleaner, efficient and cost-effective recycling process to meet the growing global demand for LABs, overcome lead supply issues and mitigate environmental damage is vitally important.

At present, the lead compounds used to manufacture nanostructured PbO are typically derived from either lead ores or recycled LABs. Both sources are subjected to energy intensive, complex and highly polluting pyrometallurgical processes in order to extract the lead. This process is illustrated in Figure 2-4.

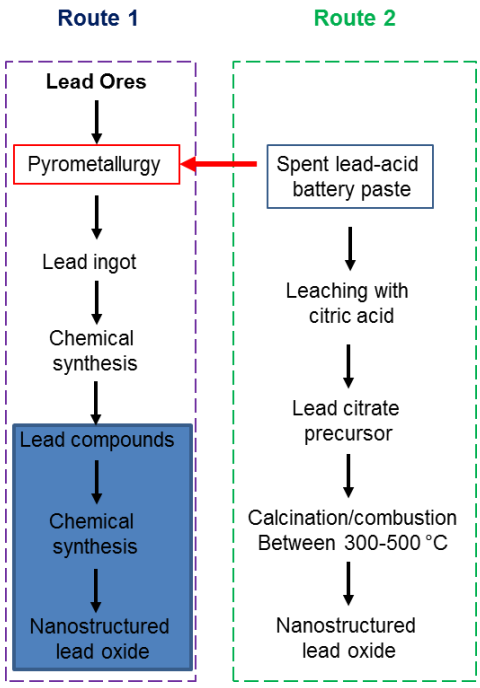

Figure 2-4: *Routes to manufacturing nanostructured PbO*

As route 1 of Figure 2-4 shows, the pyrometallurgical process is followed by further chemical synthesis. Typically, lead compounds such as lead acetate ($Pb(CH_3COO)_2$) and lead nitrate ($Pb(NO_3)_2$ are used to generate nanostructured PbO after extraction and further processing[74].

As the method of pyrometallurgical recycling of spent LABs is associated with emission of pollutants such as SO_2 and lead particulates into the ecosystem[5], more and more attention have been given to efficient and cost effective alternative processes based on chemical, hydrometallurgical and electrochemical methods[1, 65, 67, 75-77]. Hydrometallurgical processes of recovery have especially been a popular area of research for LAB recycling due to its low cost and low polluting procedure of operation. A conventional hydrometallurgical process typically follows these steps:

1. Pre-treatment process to separate the spent lead paste from the battery housing and metallic electrodes.
2. Depleted paste material is desulphurized using sodium carbonate (Na_2CO_3), sodium Hydroxide (NaOH) or ammonium carbonate ($(NH_4)_2CO_3$) solutions, with the PbO_2 being reduced to Pb(II) to facilitate subsequent leaching by using hydrogen peroxide (H_2O_2), iron sulphate ($FeSO_4$) or sodium thiosulphate ($Na_2S_2O_3$)

3. The desulphurized paste is then dissolved in powerful leaching agents such as fluoroboric acid (HBF_4) or hexafluorosilicic acid (H_2SiF_6)[70].
4. Electrowinning is then used to generate metallic lead from the aqueous solution containing lead ions.

The use of Na_2CO_3 in the desulphurisation route is of particular interest as the lead carbonate ($PbCO_3$) by-product has been reported to generate Pb_3O_4 at 450 °C[78], which as detailed earlier is typically formed at around 540 °C from PbO and used to facilitate plate formation. In this process, Na_2CO_3 is used as the leaching agent with the paste in solution according to the following reaction:

$$PbSO_{4(s)} + Na_2CO_{3(aq)} \rightarrow PbCO_{3(s)} + Na_2SO_{4(aq)} \quad \textbf{2-18}$$

The Na_2SO_4 by-product from this reaction is then dried, centrifuged and precipitated to form a crystalline material[79, 80]. However, the use of Na_2CO_3 has proven difficult as intermediate compounds such as $NaPb_2(CO_3)_2OH$ and $Pb_4(SO_4)(CO_3)_2(OH)_2$ and others are known to form depending on pH, concentration of Na_2SO_4 and many other factors giving rise to processing problems[81].

The use of NaOH in desulphurisation has also been explored in some depth and success with the degree of desulphurisation to be around 95%. During this process the $PbSO_4$ in the lead paste is converted to $Pb(OH)_2$ and $NaSO_4$ as shown in equation **2-19** below[82].

$$PbSO_{4(s)} + 2NaOH_{(aq)} \rightarrow Pb(OH)_{2(aq)} + Na_2SO_{4(aq)} \quad \textbf{2-19}$$

The lead may also go into solution as sodium plumbite Na_2PbO_2[70]. The advantages of desulphurization of the spent active paste material are many. The most significant is that it eliminates the need for high temperatures during the pyrometallurgical process. Others include the reduced need of chemical reagents in the refining cycle, SO_2 gas production and increase in the overall lead extraction.

Even though the issue of SO_2 emission is eliminated through the use of such processes, the problem of evolution of hazardous fluorine gases arise in the electrowinning stage. The electrowinning step may also prove a limiting factor as these processes often involve high financial cost. The use of electrochemical methods also has a significant drawback through their low net energy efficiency as most methods draw their electricity source from their respective national grid which generally function at 30-40% efficiency[71].

An alternative process is shown in route 2 of Figure 2-4. The process begins with the leaching of spent paste from used LABs using citric acid ($C_6H_8O_7$) as the main active component[76, 77]. The resulting lead citrate formed from this process is used as the precursor material to synthesize nanostructured PbO through low temperature combustion-calcination.

In addition to generating nanostructured PbO, the main advantages of this recycling process are that it can operate at ambient conditions with toxic pollutants contained and controlled and where all excess reagents can be regenerated and reused, thus minimising waste and enhance financial viability. Indeed, the underlying principles of this process have already been exploited with high degrees of success in other studies[64, 71, 74, 83].

The current study aims to explore this process further with the intention to improve and refine the procedure in order to gain the optimum utility with the primary emphasis on generating salient by-products to maximise LAB operation. In this study, the three major components in a spent lead paste, PbO, PbO_2, and $PbSO_4$ were individually leached to generate a pure lead citrate precursor of either $Pb_3(C_6H_5O_7)_2 \cdot 3H_2O$ or $Pb(C_6H_6O_7) \cdot H_2O$. Conditions were optimized for individual lead compounds which were then used as the basis for leaching real spent paste from industry. Lead citrate is readily crystallized from the aqueous solution due to its low solubility and can be combusted to directly produce nanostructured PbO as a precursor for making new battery pastes.

Citrate is unique among other ions that could have been used to form a complex with lead. It was found by Kety[84] that citrate is about 1000 times as effective as ascorbate, lactate or acetate in its ability to bind to lead. This, together with the commercial availability of $C_6H_8O_7$, makes lead citrate an attractive choice in terms of the innovative direction for lead recycling.

2.9 Summary

In this chapter, a background to the LAB has been outlined including the state of the art and the many improvements that have been made to the electrochemical system since its inception, including the many drawbacks and possible remedies to them. One of those is the fact that LABs cannot sustain a stable high energy output comparable to the combustion engine. Electric vehicles are far slower and unable to carry as much weight as normal cars. The LAB is the main focus of the current study because in addition to the advantages mentioned earlier, out of all the materials used for batteries, lead is the cheapest and the most abundant, the only one abundant enough to have several kilograms of it in every single car in the world.

As mentioned previously, one of the advantages of the lead-acid system is its wide usage which has led to a well-established recycling infrastructure. The current widely used method of pyrometallurgical recycling has some major drawbacks however. The recycling of lead, $PbSO_4$, PbO_2 and PbO from LABs involves the combustion of the paste at high temperatures, which consumes high amounts of energy and is highly polluting. An ideal process would be a way to the recycle spent electroactive paste at low cost, without the emission of harmful gases and with low loss of lead that would also result in a new active material that is more efficient than those currently in use.

Citric acid is well known for its ability to chelate metal ions in water. In the presence of $C_6H_8O_7$, PbO and $PbSO_4$ form an ionic compound initially soluble in water. To leach the PbO_2 the compound must first be reduced to PbO before further treatment. The lead citrate crystallizes out of the solution and thus can easily be extracted for further use. The combustion of the lead citrate can result in the formation of PbO containing some Pb which is the primary component used to form the active material of LABs.

Sonmez and Kumar[76] have stated that their hydrometallurgical recycling process may also be used to alter the microstructure of the recycled PbO and produce nanoparticles of various morphologies. The purpose of the initial stage of the current study, therefore, is to assess the potential application of this new hydrometallurgical recycling process in generating nanostructured PbO that can be reused as the active material with a high surface area in LABs. The ability to control the polymorphic ratio of PbO is also an important factor in helping to understand, control and optimize LAB formation and utility.

An initial study of the citrate leaching process will be conducted. The structural and morphological studies of generated by-products and their relationship with potential reaction characteristics in a battery will form the core part of this project. The aim is to enable a process whereby the recycled battery paste can be reused in a more efficient electrochemical cell which can in turn be eventually recycled and reused again using one cheap, environmentally friendly and convenient closed process, directly linking the recycling to a more efficient reuse stage.

3 Experimental Procedures

3.1 Introduction

A general description of the experimental procedure for synthesising lead citrate, from which further investigations were based, is outlined together with the experimental techniques used in this study. The utilisation of various analysis techniques in literature is reviewed along with an introduction to their theoretical basis.

3.2 Synthesis of Lead Citrate

Lead citrate is an organic compound with a lead core connected ligand group. It is possible to form lead citrate, then combust it at low temperatures to form PbO. In the recycling process proposed, the main problem is the formation of lead citrate from the number of different compounds present in the spent battery paste. Two of the lead compounds are PbO and $PbSO_4$ which are reacted without a catalyst and during the preliminary reaction are stirred in an aqueous $C_6H_8O_7$ solution. As the reaction progresses the lead citrate precipitates out as crystals and can be extracted through simple filtering. Two other compounds present are metallic lead and PbO_2 which do not react with $C_6H_8O_7$ or react too slowly to be of any interest on the industrial level. PbO_2 can be treated separately or in situ with concentrated H_2O_2, which can reduce PbO_2 to PbO and can then react with $C_6H_8O_7$. There are essentially two different reactions that are considered important in the industrial application stage, $C_6H_8O_7$ with PbO and $C_6H_8O_7$ with $PbSO_4$ in an aqueous phase.

Analytically pure and commercially sourced chemicals from Sigma Aldrich were initially used to simulate the components in the depleted electroactive paste materials from LAB grids in order to investigate the characteristics of each constituent. Leaching experiments were conducted individually with PbO, PbO_2 and $PbSO_4$ as precursor waste simulants. All the initial mixtures consisted of stoichiometric amounts of $C_6H_8O_7.H_2O$ relative to their corresponding lead compound, together with the optimised primary reactant solid to liquid ratio (S:L) which is defined as the initial mass of the reacting compound to the initial mass of the solvent, as detailed in Sonmez et al's works[76, 77].

The samples were filtered through a Büchner funnel and dried in a vacuum oven overnight at 80 ˚C after each reaction and analysed for phase purity. This would form the basis of further experimental investigations which will be outlined separately.

3.3 X-Ray Diffraction

X-ray diffraction (XRD) is a non-destructive analytical technique generally used to obtain information on the phase assemblage of materials and crystallographic structure by means of X-ray scattering.

When the crystalline material is irradiated by the monochromatic X-ray beam with wavelength *lambda* (λ) at an angle *theta* (θ), diffraction occurs, if the wavelength of radiation λ is of the same order as the distance (*d*) between neighbouring atoms in crystalline solids[85]. The diffracted X-rays interfere constructively and an X-ray intensity maximum is observed producing a diffraction pattern, if the difference of their lengths is equal to complete number *n* of wavelengths. A schematic of this is shown in Figure 3-1 below:

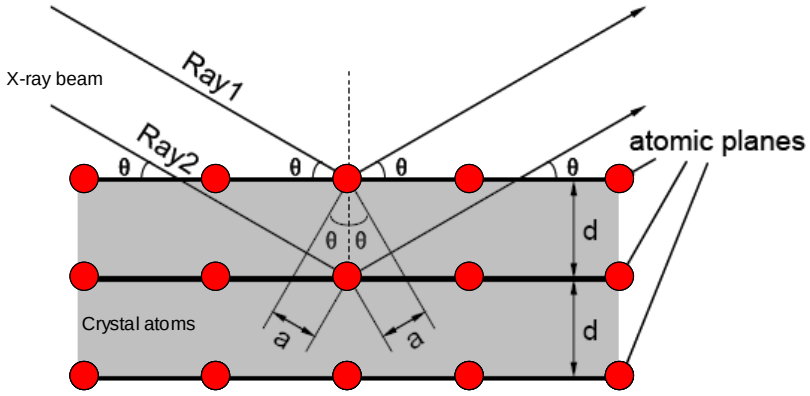

***Figure 3-1**: Schematic diagram of X-ray diffraction on crystal atomic planes*

The scattering angle, 2θ, is related to the spacing between the responsible atomic planes, d_{hkl}, and the wavelength of the incident X-ray, λ, and the reflected waves will be present in phase on their diffractions from the crystal with constructive interference, which can be expressed by Braggs' law[85, 86]:

$$n\lambda = 2d_{hkl} \sin\theta \qquad \textbf{3-1}$$

This technique was used to analyse purity and phase content of samples generated from the current study. Powder samples were placed on an aluminium holder with a glass slide used to create a flat surface. A Philips PW1830 X-ray diffractometer operating at 40 kV and 40 mA was generally used to obtain diffractograms. Scans were generally conducted with Cu-Kα radiation in the range 10-90°, with a step size of 0.05° and a scan rate of $2°\cdot min^{-1}$. The obtained patterns were analysed using X'Pert Highscore Plus software where they were compared with International Center Diffraction Data (ICDD). The ICDD enabled a comparison of measured d-spacings to those similar compounds in the data files.

3.3.1 Crystallite Size Analysis

Crystallite size measurements can be made by the evaluation of peak broadening from X-ray diffraction patterns, as the diffracted beam is broadened when the particle size is small. This procedure however, is made complicated by effects from lattice distortion and crystallite size distribution and by the absence of strong higher orders. Therefore, these measurements are typically made from first order reflections, from which an estimate of apparent crystallite size is made[87].

The crystallite size or lattice strain can be derived by comparing the profile width of a standard profile with a sample profile according to the Scherrer formula. The Scherrer formula relates the width of a powder diffraction peak to the average dimensions of crystallites in a polycrystalline powder. It uses a shape factor in X-ray diffraction and crystallography to correlate the size of sub-micrometre particles, or crystallites, in a solid to the broadening of a peak in a diffraction pattern[88]. The Scherrer equation is shown below:

$$\tau = \frac{K\lambda}{\beta \cos\theta} \qquad \textbf{3-2}$$

Where K is the shape factor, λ is the X-ray wavelength, β is the line broadening or full width at half the maximum (FWHM) intensity in radians, θ is the Bragg angle and τ is the mean size of the ordered crystalline domain. It should be noted that there are a number of factors that affect K and crystallite size analysis which include: how the peak width is defined, how crystallite size is defined, the shape of the crystal and the size distribution[86, 89].

The value of K is slightly different depending upon whether the FWHM or the integral width is chosen to characterize the peak breath[90]. This evaluation using the Scherrer formula is implemented in the X'Pert Highscore Plus software and was used to estimate the crystallite size of each sample.

3.4 Density Measurements

The apparent density of each powdered sample was measured using a Micromeritics AccuPyc 1330 pycnometer. Each sample was weighed and then placed in a cylindrical chamber of known volume. The technique involves measuring the amount of displaced gas in the chamber. The pressure observed upon filling the sample chamber and then the subsequent discharge into a second empty chamber allows the sample solid phase volume to be calculated, thus allowing the density, defined as weight per unit volume, to be determined.

3.5 Scanning Electron Microscopy

3.5.1 Secondary Electron Imaging

Scanning Electron Microscopy (SEM) images were taken using a JEOL JSM 6340FEG and a FEI Nova NanoSEM FEG scanning electron microscopes, with an accelerating voltage of 5-10 kV. This technique was used to analyse the surface topography, morphology and particulate size/structural distribution of all samples. Prior to analysis, each sample was mounted on aluminium stubs which were thoroughly cleaned with acetone.

The samples were secured using double-sided carbon conductive tape (G3939, Agar Scientific). These were then mounted onto stub holders in an Emitech K575 sputter coater for platinum coating so as to reduce charge accumulation on the sample surface during exposure to the electron beam, thus limiting the reduction of image quality from territorial over-contrast or signal drift.

3.5.2 Energy Dispersive X-ray Spectroscopy (EDS)

Energy dispersive X-ray analysis[91] was conducted using a Jeol JSM 5800LV scanning electron microscope with an accelerating voltage of 20 kV. This was used to map the elemental spatial distribution of some samples. Each sample underwent preparation similar to that required for SEM imaging as mentioned previously.

The electron microprobe produces two-dimensional images of elemental distributions by displaying X-ray photon-caused pulses on a cathode ray tube as the electron beam progressively scans the sample over an area of interest[92]. The resultant element map is essentially a pixel by pixel image based on chemical elements present in the sample. This technique enables the determination of different elements and their relative positions over the same area of interest thus allowing the degree of homogeneity within each mixture of sample to be assessed.

3.6 Surface Area and Porosity Measurements

The surface area and porosity of some powdered samples were investigated using physical nitrogen gas adsorption and capillary condensation principles. The Brunauer-Emmett-Teller (BET) model[93] was used to determine the specific surface area of each sample, and the Barrett-Joyner-Halenda (BJH) method[94] was used to calculate the pore size distributions.

The apparatus used was a TriStar 3000 BET surface area analyzer from Micromeritics Instruments. Prior to surface area measurements, the samples were each weighed and degassed at 60 ˚C overnight under vacuum to remove physically adsorbed gases and water vapour. The total surface area, total pore volume and pore size distribution of each sample were calculated through the construction of adsorption-desorption isotherms relating the amount of nitrogen gas adsorbed and the thickness of the adsorbed layer. It is a physical method for studying sample surface properties by a condensation or adsorption process of gas molecules with known sizes, generally N_2, Ar or CO_2, on the unknown material surface.

Each sample was contained in an evacuated sample tube and then cooled to cryogenic temperatures, -196.15 °C (77 K). They were then exposed to the analysis gas at a series of precisely controlled pressures. As the pressure is increased incrementally so does the number of gas molecules adsorbed on the sample surface.

3.6.1 Brunauer, Emmett and Teller Theory

The evaluation of BET theory is based on the capacity of the monolayer formed on a given surface, i.e. the number of adsorbed molecules in the monolayer, by fitting the experimental adsorption data into the BET equation below:

$$\frac{P}{V(P_0 - P)} = \frac{1}{V_m C} + \frac{C-1}{V_m C}\left(\frac{P}{P_0}\right) \qquad \textbf{3-3}$$

Where V is the volume of gas adsorbed by the sample, V_m the monolayer capacity, P is the actual gas pressure, P_0 is the saturation pressure of the gas at the temperature analysed and C the constant related to the enthalpy of adsorption of the first adsorbed layer. This theory of multilayer gas adsorption is an extension of Langmuir monolayer adsorption theory[95]. The equilibrium pressure (P) is compared to the saturation pressure (P_0) and their relative pressure ratio (P/P_0) is recorded along with the quantity of gas adsorbed by the sample at each equilibrium pressure. As adsorption proceeds, the thickness of the adsorbed film increases. The open pores on the surface are filled first, with the free surface becoming completely covered, and the larger pores being filled last by capillary condensation. This process may proceed to the point of bulk condensation of the analysis gas.

The next stage is the desorption process, in which the pressure is systematically reduced, resulting in the liberation of the adsorbed molecules. As with the adsorption process, the changing quantity of gas on the solid surface at each decreasing equilibrium pressure is measured. These two sets of data describe the adsorption and desorption isotherms. The specific surface area can therefore be determined by multiplying the monolayer capacity and the cross-sectional area of the individual molecule adsorbed.

The plot of BET isotherm is a curve of quantity of adsorbed gas (ml/g) versus relative pressure (P/P_0)[95]. The gas adsorption isotherms at temperatures not far from their condensation points show two regions for most adsorbents[93]. The isotherm is concave in the range of low pressures while at higher pressures the isotherm is convex. Two stages must be involved in the evaluation of the surface area by BET method from the isotherm. The first, the linear plot of $1/[Q(P/P_0 - 1)]$ versus P/P_0, needs to be constructed over approximate range of relative pressures P/P_0 = 0.05-0.35 to obtain the monolayer capacity Q_m[96]. The second stage is to calculate the specific surface area S_{BET}. This requires knowledge of the average area, δ, occupied by each molecule of adsorptive gas.

The derivation of the above equation is based on the following assumptions: the surface area is flat; the adsorption energy on all adsorption sites is identical; there are no lateral interactions present between adsorbed molecules; the molecular adsorption energy is equal to the liquefaction energy except for the molecules in the first layer; and an infinite number of layers can be formed[97]. However, in reality, for adsorption on a porous solid, these assumptions will not usually apply. Hence, this method could only offer a rough approach to evaluate the material surface properties. The second equation used in calculating the specific surface area, S_{BET}, is:

$$S_{BET} = \frac{Vm}{M} N_0 \delta * 10^{-20} \qquad \textbf{3-4}$$

Where N_0 is Avogadro's constant, 6.023×10^{23}, δ is the diameter of one molecule of adsorptive gas[95].

Analysis of the shape of the BET gas adsorption-desorption isotherms provides information about the surface and internal pore characteristics of the samples. The gas adsorption isotherms may be grouped into six categories (left) as illustrated in Figure 3-2:

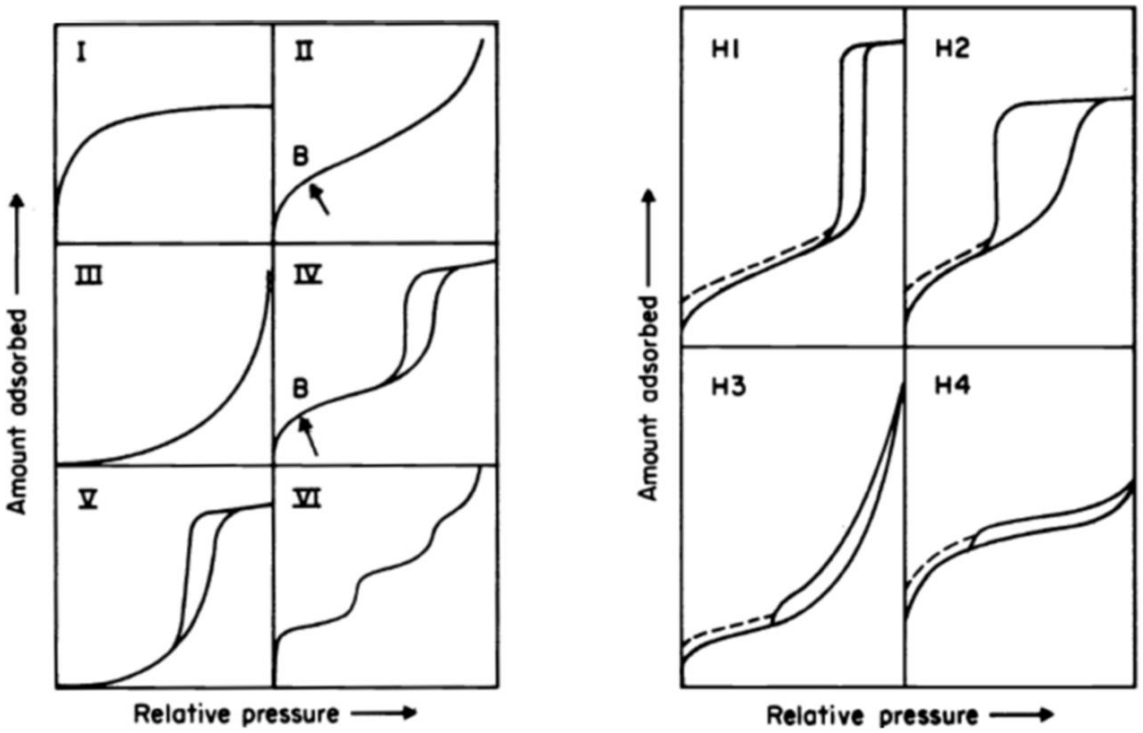

***Figure 3-2**: Type of gas sorption isotherms (left) and classification of adsorption-desorption hysteresis loops (right)*[97, 98]

Type I isotherm usually gives an indication of adsorption in micropores, pore diameters <2 nm[96], or monolayer adsorption; Type II typically demonstrates unrestricted monolayer-multilayer adsorption, which is due to the presence of non-porous or macroporous, pore diameters >50 nm[96], adsorbent; Type III is not common, but can be observed when lateral interactions between adsorbed molecules play an important role in the system; Type IV is a normal indication of adsorption involving capillary condensation in mesopores, pore diameters: 2-50 nm[96]; Type V again is an unusual case responding to adsorbate-adsorbate interactions; Type VI illustrates a step-like shape related to the system and environmental temperature, corresponding to the stepwise adsorption on a uniform non-porous surface[97, 98].

In the gas sorption in mesoporous structures, the capillary condensation and capillary evaporation normally do not occur at the same pressure, which causes the emergence of hysteresis loops. The shape of such hysteresis loops may vary widely depending on the sorption meta-stabilities and/or pore connectivity of the specimen. According to the IUPAC index[98] the hysteresis loops can typically be classified into four groups, as seen in Figure 3-2, (Right).

The Type H1 loop is typical of materials with relatively high pore size homogeneity and simple pore network, which consist of assemblages of rigidly joined particles, or approximately uniform spheres formed in a fairly regular means and highly uniform cylindrical pore geometry[97]. The Type H2 loops are often observed for many porous materials with a wide range of pore size distributions and an increase of irregular shapes. The network effects (pore geometries), such as ink-bottle pores or channel/cage-like pores, are the main causes of this behaviour.

Isotherms with a Type H3 hysteresis loop are found in materials with loose assemblages of plate-like particles leading to slit-like pores. Finally, the feature of Type H4 loops may be attributed to the presence of narrow slit-shaped pores, or a mesopores array embedded with pores with relatively larger sizes.

Furthermore, some systems may cause low-pressure hysteresis arising from the adsorbent swelling or coexistence of irreversible chemical interactions during the adsorption process. It should be noted, however, that in practical measurements, many specimens tend to have ambiguous features.

The shape of the isotherm is highly dependent on the nature of the gas-solid system[95]. The amount of N_2 gas adsorbed per gram of sample depends on the surface area and porosity of the material as well as the temperature and the relative pressure of gas P/P_0[96].

3.6.2 Barret, Joyner and Halenda

In the Barret, Joyner and Halenda method[94] assumptions made include: the pores having well defined shapes, their distribution is confined to the mesopore range and that the meniscus curvature is controlled by pore size and shape[96]. The assumed shape of pores in these estimations is cylindrical[99]. The BJH method is based upon the Wheeler theory of combined physical adsorption and capillary condensation. This theory can be summarised by the following equation:

$$V_s - V = \pi \int_R^{\infty} (r-t)^2 L(r) dr \qquad \textbf{3-5}$$

Where V_s is the volume of the gas adsorbed at saturation pressure, V is the volume of the gas adsorbed at pressure p, L(r)dr is the total length of pores whose radii fall between r and r+dr. R is the critical radius (or Kelvin radius) i.e. the radius of the largest pore still completely filled with liquid adsorbate at any given pressure and t is the multilayer thickness which is normally built up at pressure p[94]. This equation states that the volume of gas V_s – V not yet absorbed at a pressure p is equal to the total volume of pores which have not been filled.

The left hand side of the equation is known from experimental data and is used to determine the pore size distribution function L(r) which when integrated will show agreement with the experimental data[100]. The BJH method is based on the removal of condensed gas in the step by step lowering of the relative pressure P/P_0 during the desorption phase of the process at about -195 ˚C in a porous solid. In desorption, when the pressure is decreased from the saturation pressure to a relative pressure, P/P_0, pores with a radii larger than R desorb to leave an adsorbed layer of thickness *t* on the pore walls. The quantity R – *t*, the Kelvin radius, is related to P/P_0 by the Kelvin equation[101], and the thickness *t* as a function of P/P_0 has been established empirically for adsorption on nonporous materials. When the pressure is further decreased, smaller pores desorb and the thickness of the adsorbed layer decreases[99].

The pore distribution is then calculated from curves generated relating pore volume and pore dimensions in the form of cumulative plot of pore volume v (ml/g) versus size D (nm), relating a differential amount desorbed to the differential volume of pores emptied.

3.7 Thermal Analysis

3.7.1 Differential Thermal Analysis (DTA)

Differential thermal analysis was used to investigate the temperatures, thermodynamics and kinetics of reactions of the synthesised citrate samples. Small quantities of sample were placed in an alumina crucible that was symmetrically positioned alongside another that contained a reference inert material.

A schematic diagram of this set up is shown in Figure 3-3. The temperature difference between the sample and the reference material is monitored over the heating profile applied. Endothermic reactions would result in the sample having a lower temperature than the reference while exothermic reactions would result in an elevation[102]. This set up can be used to create a “heat-flux” and used in differential scanning calorimetry (DSC) analysis with the temperature difference being converted to energy per unit time.

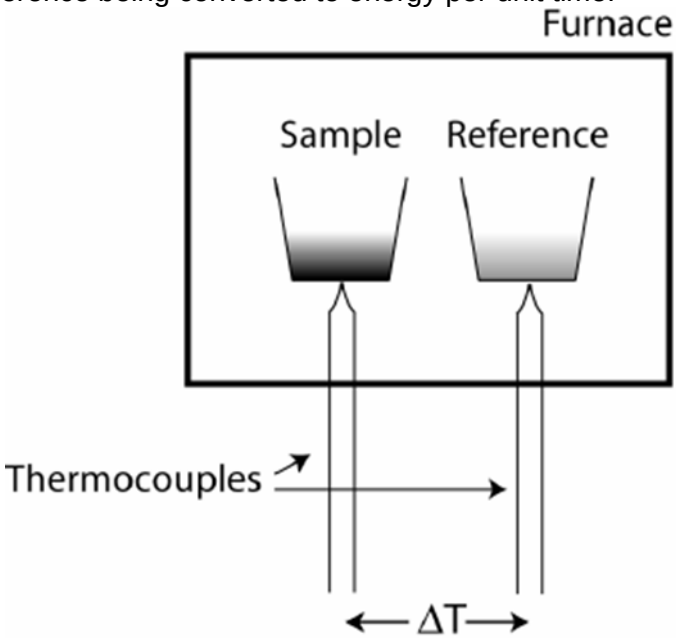

***Figure 3-3**: A schematic diagram of a DTA/DSC experimental setup*

3.7.2 Thermogravimetric Analysis (TGA)

Thermogravimetric analysis was used to monitor the changes in the physical and chemical properties of the citrate materials by measuring the weight change as a function of temperature[103]. The capabilities of the DTA/DSC can be combined with TGA to obtain simultaneous data sets. Thus, TGA plots can be used to incorporate DTA information associated with the mass change.

3.8 Voltammetric Measurements

Voltammetry is the measurement of current which flows at an electrode as a function of the potential applied to the electrode[104]. Current-potential curves, voltammogramms, are generated as a result of these measurements from which qualitative, quantitative, thermodynamic and kinetic information about the redox active species can be determined[6, 105].

Most voltammetric measurements use a potentiostat, which is capable of applying a controlled potential to a working electrode and measuring the current that passes as a result of electron transfer to solution species of interest. The working electrode, along with a reference electrode and an auxiliary electrode, counter electrode, were placed in an electrochemical cell containing H_2SO_4 with a concentration of 4.5 M (specific gravity of 1.26 g/cm^3).

A Solartron SI1287 was used to characterise cured samples containing synthesised PbO from the current study that formed the working electrode. The reference electrode used was a mercury/mercurous sulphate (Hg/Hg_2SO_4) electrode, which is widely used in LAB research due to its stability in the system[106] and the counter electrode was platinum.

A standard one-compartment three-electrode system was used, in which the potential is controlled at the working electrode against the reference electrode, and the current response is measured between the working electrode and the counter electrode. An example of the cathodic potential changing in a waveform is shown in Figure 3-4:

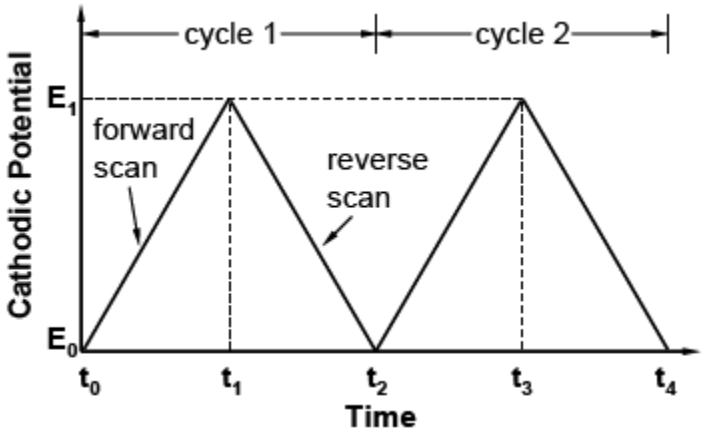

***Figure 3-4**: Typical potential waveform of voltammetric cycles[107]*

3.9 Acid Absorption and Reactivity

Acid absorption and reactivity analysis on synthesised samples of interest were conducted using titration. The degree of acid absorption for a given sample of PbO is an important factor in paste mixing when forming an electroactive paste material for a LAB. It is a measure of the wetted surface of the oxide and gives an indication of the reactivity of the material with H_2SO_4[108].

5 grams of a given sample was mixed with 10 mL of 1.75 M H_2SO_4. The mixture was vigorously stirred using a magnetic impeller at approximately 1000 rpm for 10 minutes before being allowed to settle for 5 minutes. The liquid and its contents were filtered under vacuum. To determine the reactivity, the contents were thoroughly washed with deionised water several times until the solution emanating from the samples was pH neutral. The filtrate was then titrated with 1 M solution of NaOH. A blank of the original acid solution was also titrated with the NaOH solution to determine the difference in concentration and thus indicate the degree of acid reactivity.

The difference in the acid concentrations was then used to determine the mass (mg) of H_2SO_4 per gram of oxide (mg/g). Absorption measurements were determined by titration without thorough washing of the samples. This is an important property in the active paste materials as any electrolyte absorbed in the material will be readily assessable during battery operation.

4 Investigation and Synthesis of Lead Citrate

4.1 Leaching PbO

4.1.1 Introduction

In the following study into treating the PbO component of spent paste materials from LABs, the leaching and crystallisation behaviour was evaluated in order to determine the need and possible routes for optimisation. The basis from which this study evolved derived from the recycling procedure devised by Sonmez et al[76].

4.1.2 Experimental

All initial mixtures were consistent with the 1:1 molar ratio for PbO to $C_6H_8O_7.H_2O$ and a 1:3 S:L ratio at room temperature in Sonmez's study[76]. The $C_6H_8O_7.H_2O$ was first mixed in distilled water in a glass beaker and magnetically stirred at a constant rate of ~250 rpm until fully dissolved.

The PbO powder was subsequently added and the mixture stirred to maintain suspension and reaction until crystallisation of lead citrate from the solution. The pH was monitored and moderated using NaOH to ensure that it remained ~4 to optimise the concentration of $C_6H_7O_7^-$, which is the reactive component.

Synthesis conditions were then altered by varying the molar ratios of the PbO with the other reactants, the duration of reaction and the initial pH to optimize the reaction conditions to generate lead citrate.

4.1.3 Results and Discussion

In the initial experiments, it was observed that the reaction easily began but did not proceed and complete until several hours later. In order to improve this, the concentration of the $C_6H_8O_7.H_2O$ and the volume of water were doubled to increase the rate of reaction. This resulted in a significant decrease in the processing time to under an hour. Although this has the disadvantage of having excess $C_6H_8O_7.H_2O$ remaining in the mixture, this can be reprocessed and recovered in the filtration stage. A schematic diagram of critic acid is shown in figure 4-1.

The processing time was then further reduced to less than 1 hour by increasing the molar ratio of PbO to $C_6H_8O_7.H_2O$ to 1:3 with the S:L ratio altered to 1:5 . The alterations in the processing, yielding an increase in the rate of reaction, are due to the mechanisms of the reactions taking place. Over the course of the formation process, $C_6H_8O_7.H_2O$ is first dissolved in water. The PbO is added and reacts with the $C_6H_8O_7.H_2O$. As the reaction progresses, lead citrate is formed and precipitates out forming a creamy white colloidal solution.

The reason the initial experiments took so long to come to completion could be that the lead citrate, which represents half of the volume of the species at the end of the reaction, may have been hindering the movement of the reactants within the solution. An additional reason might be that if there were too much lead citrate in the solution this could have coated the PbO and thus prevented any contact between PbO and the solution inhibiting further reactions.

Therefore, by doubling the volume of the solvent, the degree of dispersion of the lead citrate particles was increased, thus reducing its concentration. The reaction proceeded in the following manner:

$$PbO_{(s)} + C_6H_8O_{7(aq)} \rightarrow Pb(C_6H_6O_7)\cdot H_2O_{(s)} \qquad \textbf{4-1}$$

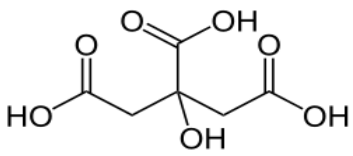

***Figure 4-1**: Molecular formula for citric acid*

The reaction initially proceeds with the apparition of a white precipitate of lead citrate within the solution and comes to completion when all the PbO powder, that is yellow-red in colour, has fully dissipated, appearing pink when completely mixed with the white lead citrate. The progression of the reaction can be observed by monitoring the pH of the solution.

As $C_6H_8O_7.H_2O$ is consumed the solution increases in pH. In one example experiment, after filtering, the lead citrate was dried at 80 ˚C and weighed giving 53.98 g of powdered by-product. At that point, the exact formula of lead citrate could be determined because 3 forms are known to exist: 1 lead for 1 citrate giving $PbC_6H_6O_7$, 1 lead for 2 citrates giving $Pb(C_6H_7O_7)_2$ or 3 leads for 2 citrates resulting in $Pb_3(C_6H_5O_7)_2$.

Using molecular masses, it was determined that the first form of lead citrate was the one obtained since its molecular mass is 397.34 g/mol and 0.134 moles of that gave a theoretical value of 53.24 g. The extra measured mass above the theoretical maximum was assumed to be retained water in the sample. The powder was then analysed for phase purity by XRD. This was compared with a pattern for $Pb(C_6H_6O_7)\cdot H_2O$ created from single crystal XRD analysis by Kourgiantakis et al[109] and is used here as the reference pattern. This was to further corroborate the finding and is shown in Figure 4-2.

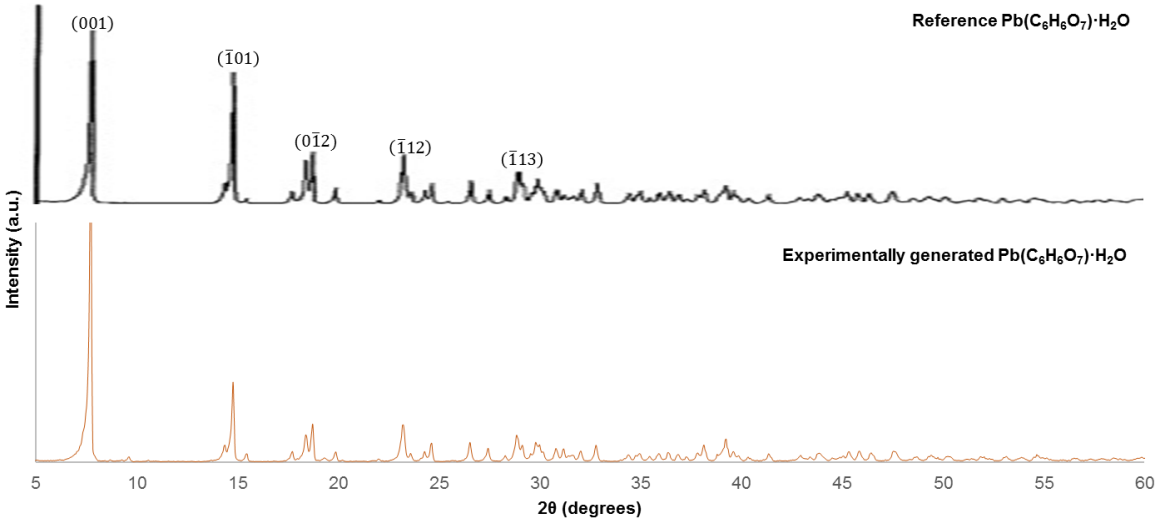

***Figure 4-2**: Comparison of X-ray diffraction analysis of $Pb(C_6H_6O_7)\cdot H_2O$ created by Kourgiantakis et al[109] (top) compared with experimentally generated $Pb(C_6H_6O_7)\cdot H_2O$ (bottom)*

The diffraction pattern of the experimentally generated $Pb(C_6H_6O_7)\cdot H_2O$ shows good agreement with that of the reference pattern with all the major peaks being matched. The reaction can be represented in equation **4-2**.

$$PbO_{(s)} + C_6H_8O_7.H_2O_{(aq)} \rightarrow Pb(C_6H_6O_7)\cdot H_2O_{(s)} + H_2O_{(l)} \qquad \textbf{4-2}$$

The pH of reaction is significant due to the number of reactive forms of $C_6H_8O_7.H_2O$ and their respective pH dependence. $C_6H_8O_7.H_2O$ has 3 carboxylic functional groups, shown in Figure 4-1 with equations **4-2** to **4-4** illustrating the dissociation expressions for $C_6H_8O_7.H_2O$. It is a weak tri-acid and as per any weak acid when mixed in water forms dissociation equilibria. The following are typical equations for the behaviour of the multi-carboxylic acid in aqueous solution, for $C_6H_8O_7.H_2O$ they are as follows:

$C_6H_8O_7 + H_2O \leftrightarrow C_6H_7O_7^- + H_3O^+$	pKa=3.13	**4-3**
$C_6H_7O_7^- + H_2O \leftrightarrow C_6H_6O_7^{2-} + H_3O^+$	pKa=4.76	**4-4**
$C_6H_6O_7^{2-} + H_2O \leftrightarrow C_6H_5O_7^{3-} + H_3O^+$	pKa=6.4	**4-5**

When $C_6H_8O_7.H_2O$ is dissolved in water the 4 compounds, above, form an equilibrium between each other and the concentration of each species is governed by the pH in solution.

Through calculations using the pKa of each successive equilibrium it was determined that the concentration of form $C_6H_8O_7$ is maximum when the pH is below 3, form $C_6H_7O_7^-$ is at maximum concentration when the pH is around 3.94, form $C_6H_6O_7^{2-}$ is at maximum concentration when the pH is around 5.58 and the last form $C_6H_5O_7^{3-}$ is at maximum concentration when the pH is above 9.

This is important as out of the 4 forms in equilibrium in solution it was reported that only one of them reacts with PbO to give lead citrate in a 1:1 ratio.

This reinforces the significance of the form of $C_6H_8O_7.H_2O$ within the solution during the reaction. Various tests implied that only the form $C_6H_7O_7^-$ reacts toward PbO to generate $Pb(C_6H_6O_7)\cdot H_2O$ when the pH was moderated from the initial reaction media between PbO and $C_6H_8O_7.H_2O$. Therefore, the pH of around 4 had to be maintained to maximise the concentration of $C_6H_7O_7^-$ for a given quantity of $C_6H_8O_7.H_2O$ dissolved in solution in order to synthesize $Pb(C_6H_6O_7)\cdot H_2O$.

However, it was discovered that if the initial reaction media with PbO was above pH 9 using NaOH, before the introduction of $C_6H_8O_7.H_2O$, the resulting reaction would generate the $Pb_3(C_6H_5O_7)_2$ form. This implies that the initial pH as oppose to the moderation of the pH determines which citrate ion is largely dominate in the reaction and thus directly influences which corresponding lead citrate type is subsequently formed. Table 4-1 details 2 reactions with the same molar ratios of PbO to $C_6H_8O_7.H_2O$ and NaOH with a S:L of 1:5, but with different starting pH.

***Table 4-1**: XRD results from leaching PbO using the same molar ratios of NaOH and $C_6H_8O_7 \cdot H_2O$ with different starting pH*

Sample	Molar ratio of PbO to NaOH	Molar ratio of PbO to $C_6H_8O_7 \cdot H_2O$	Starting pH	XRD analysis of by-product
(a)	1/2	1/3	~3.5	$Pb(C_6H_6O_7) \cdot H_2O$
(b)	1/2	1/3	~12.6	$Pb_3(C_6H_5O_7)_2 \cdot 3H_2O$

The starting pH was altered by changing the sequence of mixing. Sample (a) was mixed in the same sequence as outlined in the experimental method with $C_6H_8O_7.H_2O$ initially dissolved giving a pH of ~3.5 before adding PbO and in sample (b) NaOH was initially dissolved giving an initial pH of ~12.6 before adding PbO and then $C_6H_8O_7.H_2O$. The XRD patterns for these experiments are displayed in Figure 4-3 with an analytically pure sample of $Pb_3(C_6H_5O_7)_2 \cdot 3H_2O$ obtained from Sigma Aldrich used as a reference. The hkl values for this reference pattern were obtained from single crystal XRD analysis conducted by Zhang et al[110].

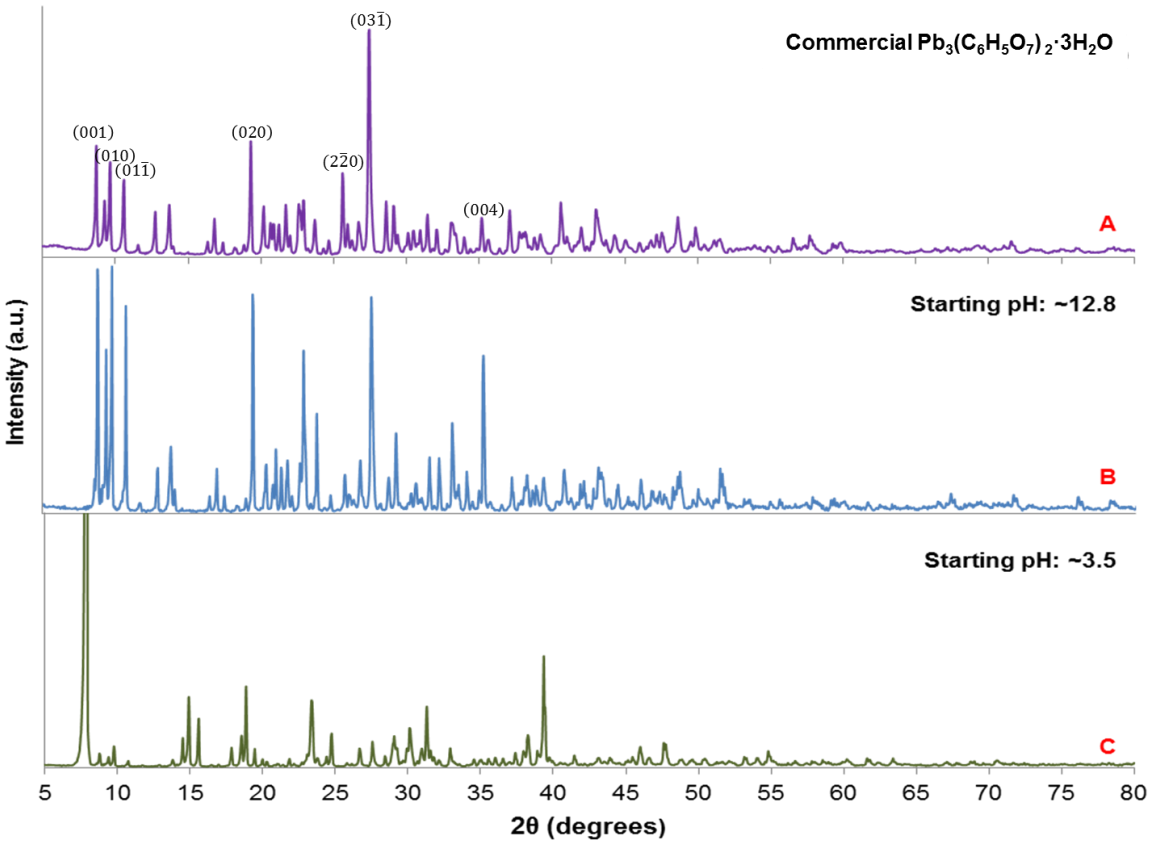

***Figure 4-3**: X-ray diffraction patterns of an analytically pure sample of $Pb_3(C_6H_5O_7)_2 \cdot 3H_2O$ from Sigma Aldrich (A) compared with samples synthesised with a starting pH of ~12.8 (B) and ~3.5 (C)*

The XRD patterns shown in Figure 4-3 and mass change calculations demonstrates that the differing starting pH had resulted in different end products. For sample B, the initial pH of ~12.8 resulted in $C_6H_5O_7^{3-}$ being the dominant species in the reaction leading to the formation of $Pb_3(C_6H_5O_7)_2 \cdot 3H_2O$, the XRD pattern matched well with the analytically pure sample procured from Sigma with all peak positions showing good agreement with some intensity mismatch. The reaction can be represented by the following:

$$3NaOH_{(aq)} + C_6H_8O_{7(aq)} \rightarrow 3Na^+_{(aq)} + C_6H_5O_7^{3-}{}_{(aq)} + 3H_2O_{(l)} \quad \textbf{4-6}$$

$$3PbO_{(s)} + 2C_6H_5O_7^{3-}{}_{(aq)} + 3H_2O_{(l)} \rightarrow Pb_3(C_6H_5O_7)_{2(s)} + 6OH^-{}_{(aq)} \quad \textbf{4-7}$$

This demonstrates the importance of the initial reaction environment in determining the dominant reactive species available to generate the final product. The final product of either form of lead citrate benefited from a S:L ratio of 1:5 with a molar ratio of 1:3 and 1:2 for PbO to $C_6H_8O_7.H_2O$ and NaOH respectively in terms of maintaining a processing time of <1 hour and generating the lead citrate compound.

4.2 Leaching PbO_2

4.2.1 Introduction

In their work on lead citrate synthesis from PbO and PbO_2, Sonmez et al[76] demonstrated that $Pb(C_6H_6O_7)\cdot H_2O$ can be generated by reacting PbO_2 with a mixture of $C_6H_8O_7\cdot H_2O$ and H_2O_2. They found that in order to effectively leach PbO_2 the compound needed to be reduced and for this they used H_2O_2. A H_2O_2 to PbO_2 molar ratio of >2 was found to be required to produce uncontaminated $Pb(C_6H_6O_7)\cdot H_2O$ along with a minimum of 4 moles of $C_6H_8O_7\cdot H_2O$ per mole of PbO_2.

It was further established that the optimal parameters for leaching pure PbO_2 with H_2O_2 and $C_6H_8O_7\cdot H_2O$ was a reaction time of 60 minutes at 20 °C with 1/5 as the starting PbO_2/liquid ratio.

In the current study, NaOH has been used, as in the previous investigation, to supplement the PbO_2 reaction with H_2O_2 and $C_6H_8O_7\cdot H_2O$ as a means to regulate the pH to gauge the effects of this added parameter. In the first set of experiments the author sought to replicate the work of Sonmez et al[76] in order to make a clear comparison with the current study. All experiments were conducted at ambient conditions with a 1/5 starting PbO_2/liquid ratio and reacted for 60 minutes unless otherwise stated.

4.2.2 Experimental

Analytically pure and commercially available materials were used and obtained from Sigma Aldrich for all the following experiments. In the initial investigation, leaching experiments were carried out using PbO_2 and $C_6H_8O_7\cdot H_2O$ as starting reagents. The leaching and crystallisation of PbO_2 first required the reduction of the dioxide before the compound could be recovered as citrate. 30 wt. % solution of H_2O_2 of varying amounts were used to reduce the dioxide. 1, 2 and 3 moles of H_2O_2 for 1 mole of PbO_2 were used in three separate respective experiments in the presence of 4 moles of $C_6H_8O_7\cdot H_2O$ for 1 mole of PbO_2 in each reaction.

Investigations were carried out by magnetically stirring each mixture at a constant rate in a borosilicate glass beaker for 1 hour. Each sample was filtered using a Büchner funnel and flask before being allowed to dry overnight at 80 °C. The dried end products were analysed using X-ray powder diffraction for phase identification.

4.2.3 Results and Discussion

Figure 4-4 below illustrates X-ray diffraction patterns of (a) $Pb(C_6H_6O_7)\cdot H_2O$ generated from work conducted by Kourgiantakis et al[109] and used here as the reference pattern, (b) 1 to 3 molar ratio of PbO_2 to H_2O_2, (c) 1 to 2 molar ratio of PbO_2 to H_2O_2 and (d) 1 to 1 molar ratio of PbO_2 to H_2O_2.

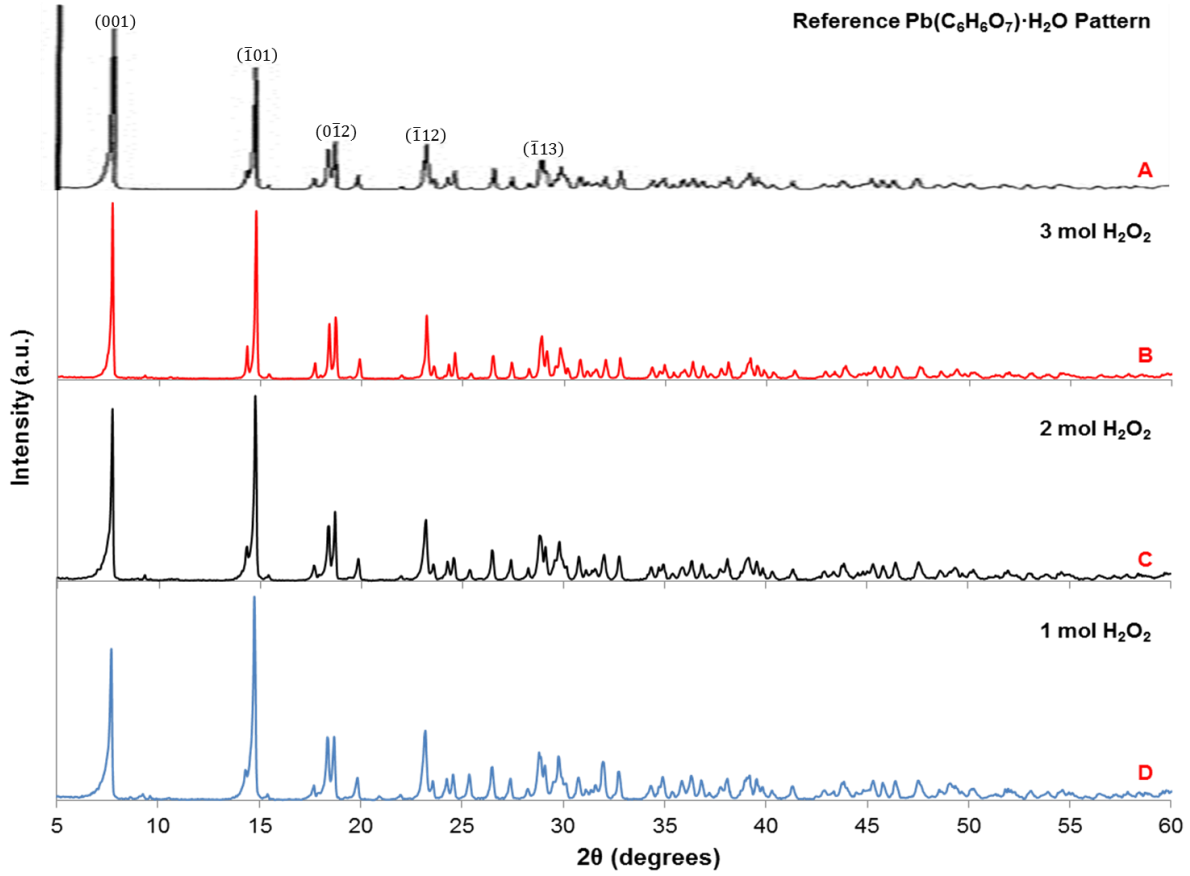

***Figure 4-4**: Comparison of X-ray diffraction analysis of $Pb(C_6H_6O_7)\cdot H_2O$ (a) created by Kourgiantakis et al with PbO_2 leached using (b) 1/3 molar ratio with H_2O_2, (c) 1/2 molar ratio with H_2O_2 and (d) 1/1 molar ratio with H_2O_2*

As the XRD analysis demonstrates, all the samples that were investigated using different amounts of H_2O_2 showed a good pattern match for $Pb(C_6H_6O_7)\cdot H_2O$. These reactions can be described by the following expression:

$$PbO_{2(s)} + C_6H_8O_7\cdot H_2O_{(aq)} + H_2O_{2(aq)} \rightarrow Pb(C_6H_6O_7)\cdot H_2O_{(s)} + O_{2(g)} + 2H_2O_{(l)} \quad \textbf{4-8}$$

Table 4-2 gives more detailed information on each reaction with molar ratios of starting materials and their corresponding XRD result of the product.

***Table 4-2**: XRD results from leaching PbO_2 using different molar ratios of H_2O_2 in the presence of $C_6H_8O_7 \cdot H_2O$*

Sample	Molar ratio of PbO_2 to H_2O_2	Molar ratio of PbO_2 to $C_6H_8O_7 \cdot H_2O$	XRD analysis of by-product
(b)	1/3	1/4	$Pb(C_6H_6O_7) \cdot H_2O$
(c)	1/2	1/4	$Pb(C_6H_6O_7) \cdot H_2O$
(d)	1/1	1/4	$Pb(C_6H_6O_7) \cdot H_2O$

Although XRD analysis established the presence of $Pb(C_6H_6O_7) \cdot H_2O$ in the end product of each experiment, its relative abundance in each sample is less clear. From observation of the changes in the physical characteristics of the samples, a trend can be deduced. This trend pointed to a decrease in the relative abundance of $Pb(C_6H_6O_7) \cdot H_2O$ with decreasing PbO_2/H_2O_2 molar ratio.

This is consistent with results gathered from Somez et al[76] on reactions using less than 2 moles of H_2O_2 and the physical changes observed in each of the experiments over the reaction period, which are documented in Table 4-3.

***Table 4-3**: Reaction characteristics of leaching PbO_2 using different molar ratios of H_2O_2 in the presence of $C_6H_8O_7 \cdot H_2O$*

Sample	pH & Temperature pre-PbO_2	pH, Temperature and appearance 10 mins post-PbO_2	pH, Temperature and appearance 50 mins post-PbO_2
(b)	<1, 14 °C	~1, 24 °C - Grey	~1.1, 20 °C – Light Pink
(c)	<1, 14 °C	~1, 24 °C – Dark Grey	~1.1, 20 °C – Dark Pink
(d)	~1, 15 °C	~1, 23 °C - Black	~1, 23 °C – Light Brown

Table 4-3 shows the observed changes in the leaching experiments conducted for PbO_2 as a function of H_2O_2 molar concentration. As seen in the table, a direct trend is apparent. As the PbO_2/H_2O_2 molar ratio decreases, from (b) to (d), the final product differs from the characteristic white crystalline powder that typifies lead citrate. Even with 3 moles of H_2O_2, the pink hue observed in the end product indicates an incomplete conversion to the citrate.

There is also a strong correlation between peak intensity and H_2O_2 concentration, with both decreasing with respect to each other. This relationship was also observed through the changing visual properties of the final products as samples (a) to (d) went from pink to light brown. It has been observed by the author that lead citrate forms more readily in higher pH regions than the peroxide-citrate system can provide.

Therefore, in the following investigation NaOH was used as a means to regulate and raise the pH of reaction. The parameters of the previous investigation was maintained with the molar ratio between PbO_2 to H_2O_2 increasing from 1 to 1 up to 1 to 3 with $C_6H_8O_7 \cdot H_2O$ kept at 4 as before for every reaction.

The molar ratio of PbO_2 to NaOH in this first set of experiments was maintained at 1 to 3. This was to gauge the effect of NaOH on the reaction characteristics of the leaching process as a function of H_2O_2 molar concentration.

As before, investigations were carried out by magnetically stirring each mixture at a constant rate in a borosilicate glass beaker for an hour. Each sample was filtered using a Büchner funnel and flask before being allowed to dry overnight at 80 °C.

The dried end products were analysed using X-ray powder diffraction for phase identification. Figure 4-5 below illustrates X-ray diffraction patterns of (a) $Pb(C_6H_6O_7) \cdot H_2O$ generated from work conducted by Kourgiantakis et al[109] and used here as the reference pattern, (b) 1 to 3 molar ratio of PbO_2 to H_2O_2, (c) 1 to 2 molar ratio of PbO_2 to H_2O_2 and (d) 1 to 1 molar ratio of PbO_2 to H_2O_2, with 3 and 4 moles of NaOH and $C_6H_8O_7 \cdot H_2O$ respectively in each reaction.

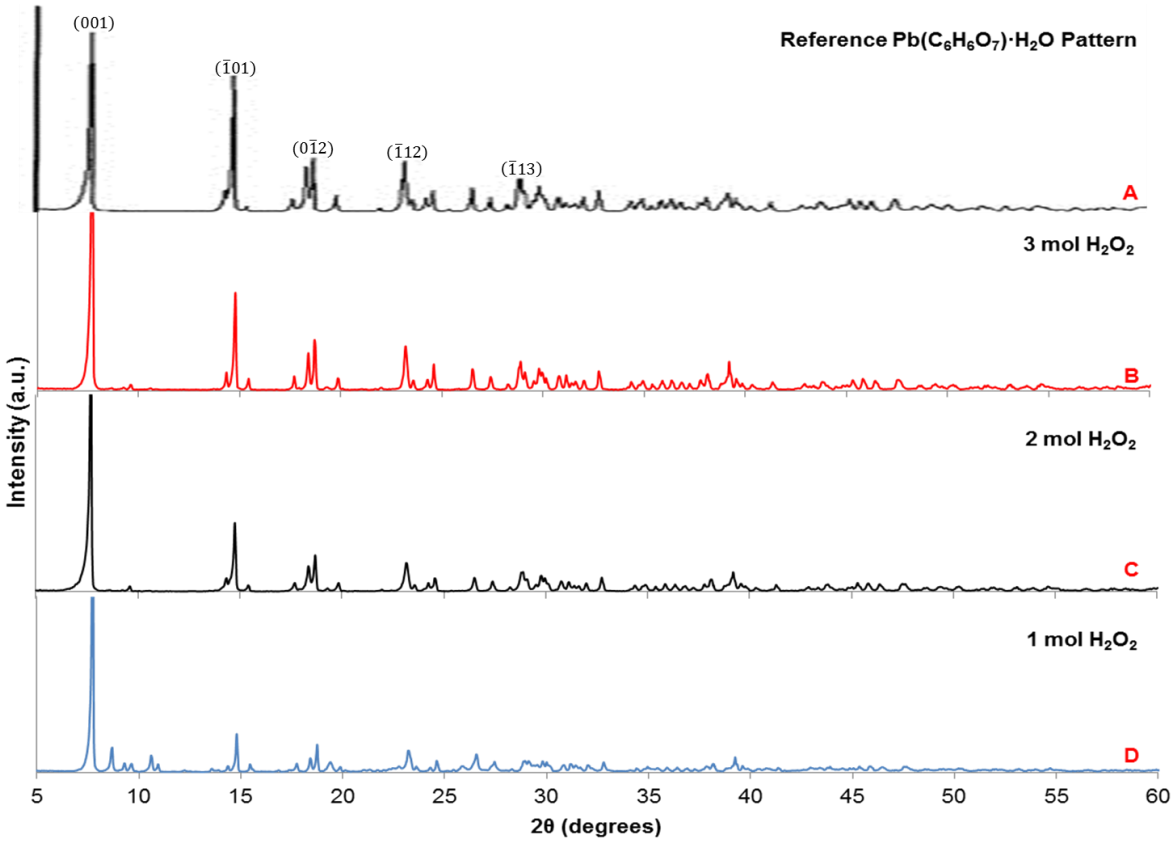

***Figure 4-5**: Comparison of X-ray diffraction analysis of $Pb(C_6H_6O_7)\cdot H_2O$ (a) created by Kourgiantakis et al with PbO_2 leached using 1/3 molar ratio with NaOH and (b) 1/3 molar ratio with H_2O_2, (c) 1/2 molar ratio with H_2O_2 and (d) 1/1 molar ratio with H_2O_2*

As with previous results, XRD analysis from Figure 4-5 illustrates that all the samples investigated using different amounts of H_2O_2 with NaOH showed good agreement with that of $Pb(C_6H_6O_7)\cdot H_2O$. The best match out of the 3 samples investigated was that of (a). As with the study carried out earlier, without NaOH, the peak intensities began to decrease along with the PbO_2/H_2O_2 molar ratio.

Table 4-4 gives more detailed information on each reaction, including the molar ratios of the starting materials and the corresponding XRD results of their end products.

***Table 4-4**: XRD results from leaching PbO_2 using different molar ratios of H_2O_2 in the presence of $C_6H_8O_7 \cdot H_2O$ and NaOH*

Sample	Molar ratio of PbO_2 to H_2O_2	Molar ratio of PbO_2 to $C_6H_8O_7 \cdot H_2O$	Molar ratio of PbO_2 to NaOH	XRD analysis of by-product
(b)	1/3	1/4	1/3	$Pb(C_6H_6O_7) \cdot H_2O$
(c)	1/2	1/4	1/3	$Pb(C_6H_6O_7) \cdot H_2O$
(d)	1/1	1/4	1/3	$Pb(C_6H_6O_7) \cdot H_2O$

As Table 4-5 demonstrates, the addition of NaOH has brought about a change in the visual properties of the final product that are more closely aligned to what is expected for $Pb(C_6H_6O_7) \cdot H_2O$ than those seen earlier. The presence of NaOH not only served to increase the pH of reaction, but also the temperature. The exothermic reaction induced by NaOH increased the reaction temperature to ~38 °C from ambient conditions.

***Table 4-5**: Reaction characteristics of leaching PbO_2 using different molar ratios of H_2O_2 in the presence of $C_6H_8O_7 \cdot H_2O$ and NaOH*

Sample	pH & Temperature pre-PbO_2	pH, Temperature and appearance 10 mins post-PbO_2	pH, Temperature and appearance 50 mins post-PbO_2
(b)	~2.7, 38 °C	~3.1, 33 °C - Pink	~3.2, 20 °C – Creamy Pink
(c)	~2.8, 38 °C	~3, 32 °C – Light Grey	~3.1, 20 °C – Light Pink
(d)	~2.7, 41 °C	~3, 29 °C - Black	~3, 20 °C – Grey (Increased viscosity)

The presence of 3 moles of NaOH appeared to have skewed the reaction more favourably towards synthesising lead citrate at lower PbO_2/H_2O_2 ratios. Therefore, further investigations were conducted using 4 moles of NaOH. As before, the molar ratio of PbO_2 to H_2O_2 was increased from 1 to 1 up to 1 to 3 while the $C_6H_8O_7 \cdot H_2O$ and NaOH molar ratio of 1 to 4 with respect to PbO_2 was maintained in the following set of experiments.

The same experimental procedures were applied as before with the final products analysed using XRD. Figure 4-6 below illustrates X-ray diffraction patterns of (a) $Pb_3(C_6H_5O_7)_2 \cdot 3H_2O$ generated from an analytically pure sample from Sigma Aldrich and used here as the reference pattern, (b) 1 to 3 molar ratio of PbO_2 to H_2O_2, (c) 1 to 2 molar ratio of PbO_2 to H_2O_2 and (d) 1 to 1 molar ratio of PbO_2 to H_2O_2, with 4 moles of NaOH and $C_6H_8O_7 \cdot H_2O$ in each reaction.

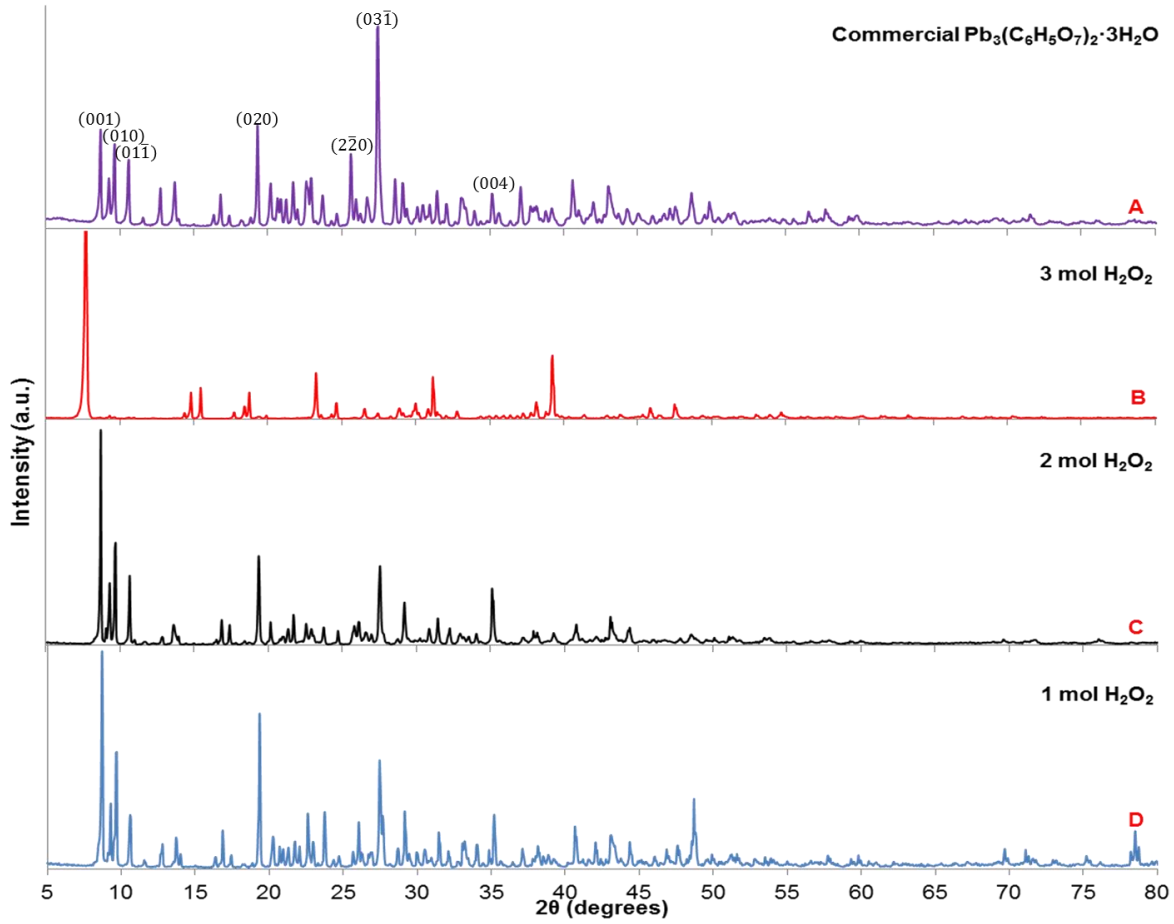

***Figure 4-6**: Comparison of X-ray diffraction analysis of (a) commercially sourced $Pb_3(C_6H_5O_7)_2 \cdot 3H_2O$ with PbO_2 leached using 1/4 molar ratio with NaOH and (b) 1/3 molar ratio with H_2O_2, (c) 1/2 molar ratio with H_2O_2 and (d) 1/1 molar ratio with H_2O_2*

As with previous experiments the reaction with 1 to 3 molar ratio of PbO_2/H_2O_2 yielded $Pb(C_6H_6O_7) \cdot H_2O$ as shown in (b) in Figure 4-6. However, reactions using 1 to 2 and 1 to 1 ratios of PbO_2/H_2O_2 in the presence of 4 moles of $C_6H_8O_7 \cdot H_2O$ and NaOH appear to have resulted in the synthesis of the tribasic form of lead citrate, $Pb_3(C_6H_5O_7)_2 \cdot 3H_2O$. As Figure 4-6 illustrates, samples (c) and (d) show good agreement with the diffraction pattern of $Pb_3(C_6H_5O_7)_2 \cdot 3H_2O$ from an analytically pure sample from Sigma Aldrich.

Table 4-6 illustrates more detailed information on each reaction with molar ratios of starting materials and their corresponding XRD result of the end products.

***Table 4-6**: XRD results from leaching PbO_2 using different molar ratios of H_2O_2 in the presence of $C_6H_8O_7 \cdot H_2O$ and NaOH*

Sample	Molar ratio of PbO_2 to H_2O_2	Molar ratio of PbO_2 to $C_6H_8O_7 \cdot H_2O$	Molar ratio of PbO_2 to NaOH	XRD analysis of by-product
(b)	1/3	1/4	1/4	$Pb(C_6H_6O_7) \cdot H_2O$
(c)	1/2	1/4	1/4	$Pb_3(C_6H_5O_7)_2 \cdot 3H_2O$
(d)	1/1	1/4	1/4	$Pb_3(C_6H_5O_7)_2 \cdot 3H_2O$

As Table 4-7 shows, the pH and temperature difference between each corresponding stage of reaction within each of the experiments was negligible. It was observed for the reaction for sample (a) that the conversion from the dioxide to citrate was immediate upon contact. The end product in sample (a) showed the characteristic creamy white solution of lead citrate and white crystalline powder after drying. Experiments with samples (c) and (d) resulted in white powders with a light pink colour.

Since the variance in temperature and pH between each experiment is negligible, the difference in the end products may be due to the rate of reaction. The higher rate of reaction observed in sample (b) might indicate a transition from one form of citrate to the other within the same reaction period.

***Table 4-7**: Reaction characteristics of leaching PbO_2 using different molar ratios of H_2O_2 in the presence of $C_6H_8O_7 \cdot H_2O$ and NaOH*

Sample	pH & Temperature pre-PbO_2	pH, Temperature and appearance 10 mins post-PbO_2	pH, Temperature and appearance 50 mins post-PbO_2
(b)	~3, 46 °C	~3.3, 36 °C – White	~3.4, 23 °C – Creamy White
(c)	~3, 48 °C	~3.3, 35 °C – Light Grey	~3.3, 21 °C – Creamy Light Pink
(d)	~3.2, 53 °C	~3.5, 38 °C - Grey	~3.4, 22 °C – Pink

The formation of $Pb_3(C_6H_5O_7)_2 \cdot 3H_2O$ has been observed in other studies where it was synthesised from the leaching of PbO_2 with acetic acid[71], but this is the first instance where NaOH has been noted to do the same with PbO_2. This can be expressed by the following:

$$3NaOH_{(aq)} + C_6H_8O_{7(aq)} \rightarrow 3Na^+_{(aq)} + C_6H_5O_7^{3-}{}_{(aq)} + 3H_2O_{(l)} \quad \textbf{4-9}$$

$$PbO_{2(s)} + H_2O_{2(aq)} \rightarrow PbO_{(s)} + H_2O + O_{2(g)} \quad \textbf{4-10}$$

$$3PbO_{(s)} + 2C_6H_5O_7^{3-}{}_{(aq)} + 3H_2O_{(l)} \rightarrow Pb_3(C_6H_5O_7)_{2(s)} + 6OH^-{}_{(aq)} \quad \textbf{4-11}$$

Since a 1 to 1 PbO_2/H_2O_2 molar ratio was sufficient to generate lead citrate in the presence of 4 moles of NaOH, further investigations were conducted to determine the minimum quantity of reagents required to synthesise the compound. The molar ratio between PbO_2 to H_2O_2 was maintained at 1 to 1 while the molar ratio between PbO_2 and $C_6H_8O_7{\cdot}H_2O$ was investigated from 1 to 1 through to 1 to 3. The NaOH molar ratio of 1 to 4 with respect to PbO_2 was maintained as before in the following set of experiments. The same experimental procedures were applied as before with the final products analysed using XRD.

Figure 4-7 below illustrates X-ray diffraction patterns of (a) lead citrate tribasic trihydrate ($Pb_3(C_6H_5O_7)_2{\cdot}3H_2O$) generated from an analytically pure sample from Sigma Aldrich and used here as the reference pattern, (b) 1 to 3 molar ratio of PbO_2 to $C_6H_8O_7{\cdot}H_2O$, (c) 1 to 2 molar ratio of PbO_2 to $C_6H_8O_7{\cdot}H_2O$ and (d) 1 to 1 molar ratio of PbO_2 to $C_6H_8O_7{\cdot}H_2O$, with 4 moles of NaOH and 1 mole of H_2O_2 in each reaction.

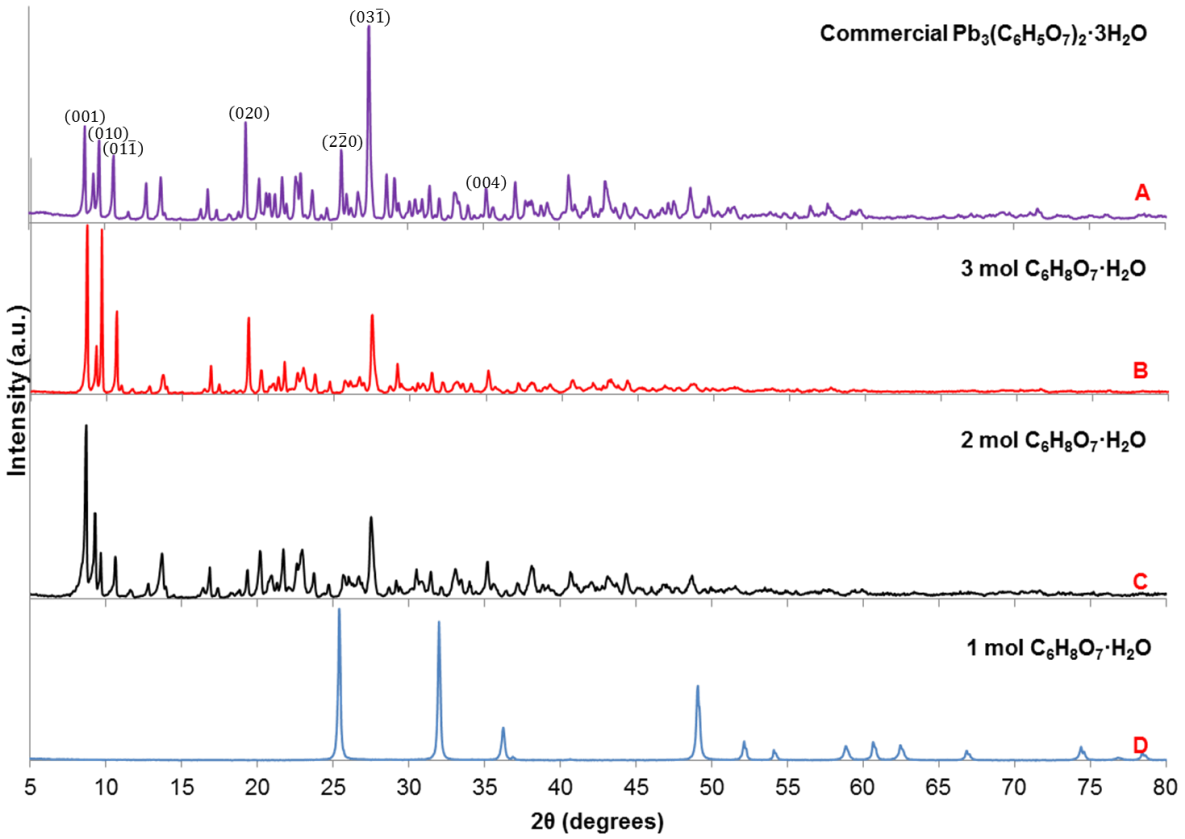

***Figure 4-7**: Comparison of X-ray diffraction analysis of (a) commercially sourced $Pb_3(C_6H_5O_7)_2{\cdot}3H_2O$ with PbO_2 leached using 1/4 molar ratio with NaOH and (b) 1/3 molar ratio with $C_6H_8O_7{\cdot}H_2O$, (c) 1/2 molar ratio with $C_6H_8O_7{\cdot}H_2O$ and (d) 1/1 molar ratio with $C_6H_8O_7{\cdot}H_2O$*

As observed previously, the 1 to 1 PbO_2/H_2O_2 molar ratio with 4 moles of NaOH had yielded $Pb_3(C_6H_5O_7)_2 \cdot 3H_2O$. The results, as illustrated in Figure 4-7, show that this trend continued with smaller amounts of $C_6H_8O_7 \cdot H_2O$.

The use of this set of reaction parameters allowed for the synthesis of $Pb_3(C_6H_5O_7)_2 \cdot 3H_2O$ using half the amount that was previously reported as being the minimum required when using H_2O_2 and $C_6H_8O_7 \cdot H_2O$ only.

The minimum required amount of $C_6H_8O_7 \cdot H_2O$ in this case appears to be a 1 to 2 molar ratio with PbO_2. As seen in Figure 4-7, when $C_6H_8O_7 \cdot H_2O$ was reduced to 1 mole, negligible conversion was observed in the XRD pattern, indicating pure PbO_2 for sample (d). The specific details of the molar ratios of starting reagents and their corresponding by-products are illustrated in Table 4-8.

***Table 4-8**: XRD results from leaching PbO_2 using different molar ratios of $C_6H_8O_7 \cdot H_2O$ in the presence H_2O_2 and NaOH*

Sample	Molar ratio of PbO_2 to H_2O_2	Molar ratio of PbO_2 to $C_6H_8O_7 \cdot H_2O$	Molar ratio of PbO_2 to NaOH	XRD analysis of by-product
(b)	1/1	1/3	1/4	$Pb_3(C_6H_5O_7)_2 \cdot 3H_2O$
(c)	1/1	1/2	1/4	$Pb_3(C_6H_5O_7)_2 \cdot 3H_2O$
(d)	1/1	1/1	1/4	PbO_2

As Table 4-9 shows, the by-products for samples (b) and (c) did not produce the characteristic creamy white solution typically associated with the formation of lead citrate. However, after drying, sample (b) turned into a white crystalline powder with a pink hue. The diffraction intensity was also observed to be low compared to the reference. The peak intensity for sample (c) was lower still compared to sample (b).

***Table 4-9**: Reaction characteristics of leaching PbO_2 using different molar ratios of $C_6H_8O_7 \cdot H_2O$ in the presence H_2O_2 and NaOH*

Sample	pH & Temperature pre-PbO_2	pH, Temperature and appearance 10 mins post-PbO_2	pH, Temperature and appearance 50 mins post-PbO_2
(b)	~3.7, 52 °C	~4.2, 33 °C - Grey	~4.2, 20 °C – Purple
(c)	~4.4, 55 °C	~5.4, 31 °C – Purple	~5.6, 21 °C – Pink
(d)	~10.7, 57 °C	~12.1, 35 °C - Black	~12.4, 23 °C – Black

In order to determine whether smaller amounts of reagents can be used to generate lead citrate, a further investigation was conducted using 1 to 1 PbO_2/H_2O_2 molar ratio with 3 moles of $Pb(C_6H_6O_7)\cdot H_2O$ and 3 moles of NaOH. As Figure 4-8 illustrates this was insufficient in leaching PbO_2 and sample (b) matches well when compared to the X-ray pattern of a commercially acquired sample of PbO_2.

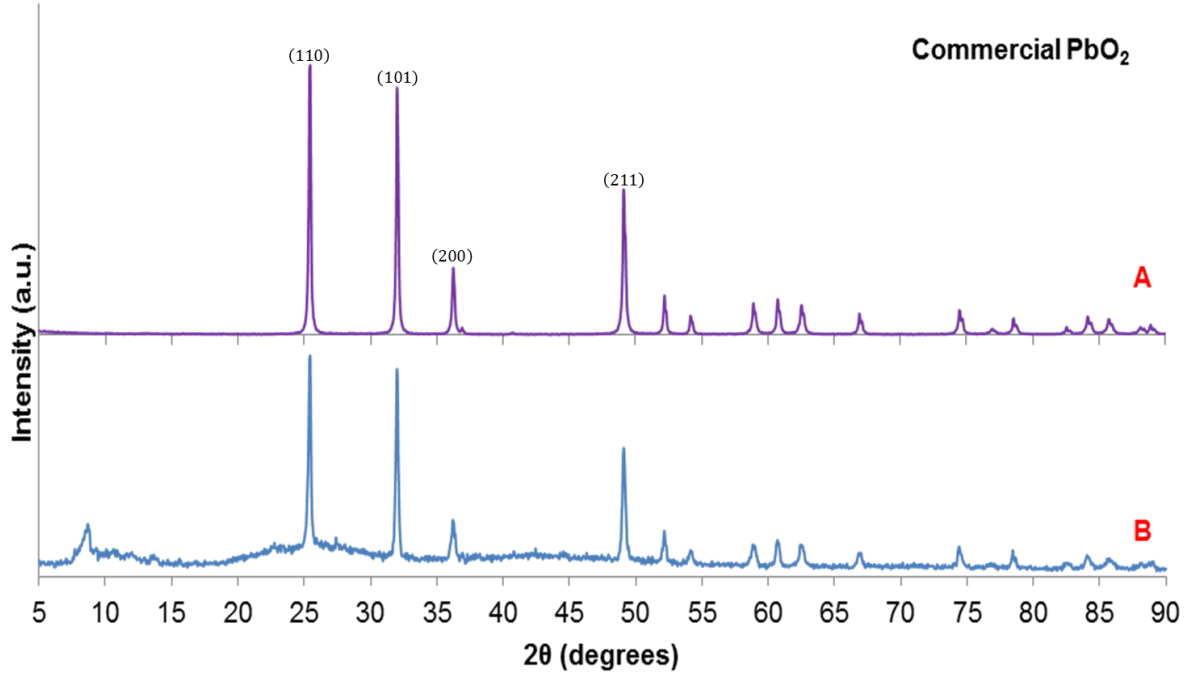

***Figure 4-8**: Comparison of X-ray diffraction analysis of (a) commercially sourced PbO_2 with 1 to 1 PbO_2/H_2O_2 molar ratio reacted with 1/3 molar $C_6H_8O_7\cdot H_2O$ and 1/3 molar NaOH*

It was observed that in the presence of 4 moles of NaOH, with a 1 to 3 PbO_2/H_2O_2 ratio and 4 moles of $C_6H_8O_7\cdot H_2O$ the leaching reaction was immediate. It was further observed that the form of lead citrate generated may depend on the rate and period of reaction, as evidenced by the XRD results gathered from experiments using different PbO_2/H_2O_2 molar ratios.

To further investigate this phenomenon experiments using the same procedure and reagent parameters as before were instigated with individual reactions stopped at 20, 40 and 60 minutes to analyse the by-product via XRD. Figure 4-9 illustrates the X-ray diffraction patterns from those experiments compared to $Pb_3(C_6H_5O_7)_2\cdot 3H_2O$ generated from an analytically pure sample sourced from Sigma Aldrich.

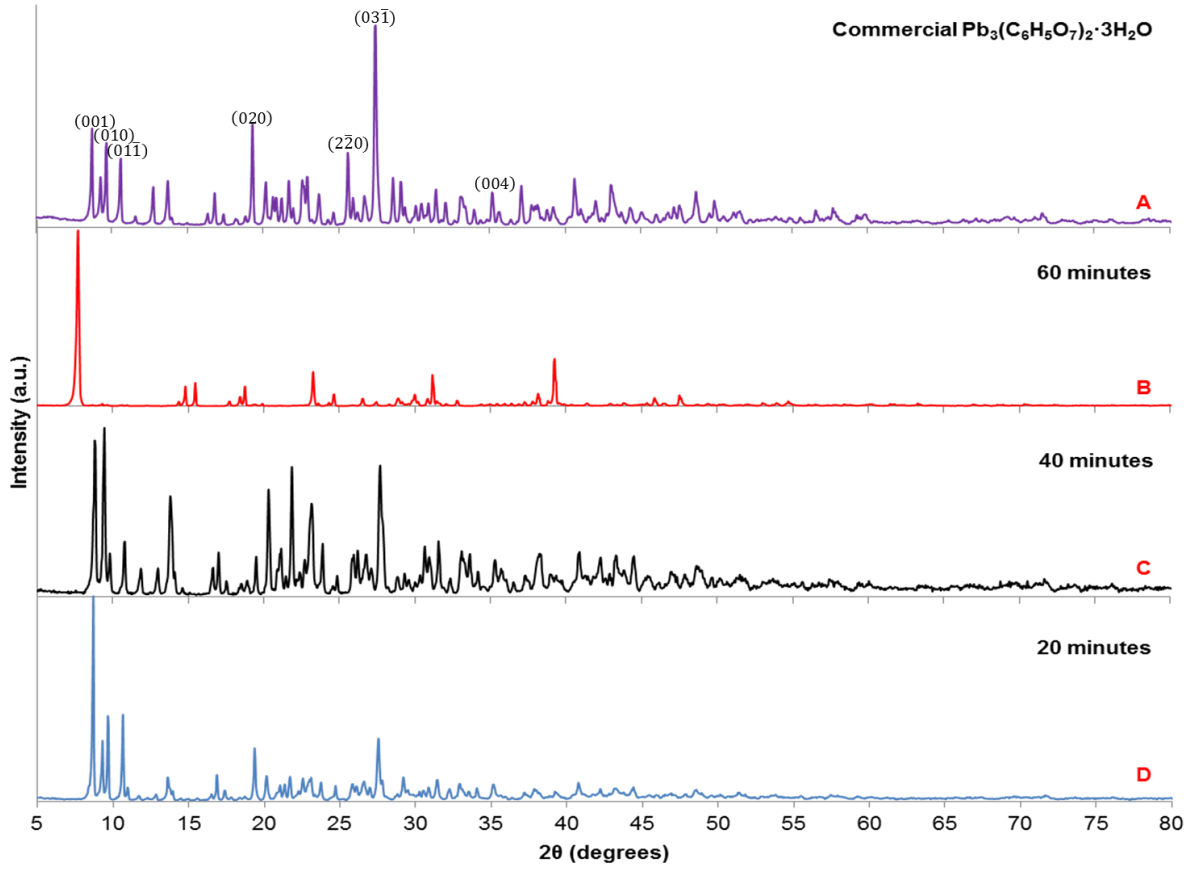

***Figure 4-9**: Comparison of X-ray diffraction analysis of (a) commercially sourced $Pb_3(C_6H_5O_7)_2 \cdot 3H_2O$ with PbO_2 leached using 1/4 molar ratio $C_6H_8O_7 \cdot H_2O$, 1/4 molar ratio with NaOH and 1/3 molar ratio H_2O_2 reacted for (b) 60 minutes, (c) 40 minutes and (d) 20 minutes*

The XRD patterns from Figure 4-9 indicate what appears to be a transition from the trihydrate form of lead citrate, $Pb_3(C_6H_5O_7)_2 \cdot 3H_2O$, to the monohydrate form, $Pb(C_6H_6O_7) \cdot H_2O$, from 20 minutes into the reaction up until 60 minutes. This may indicate that those reactions with lower PbO_2/H_2O_2 molar ratios than 1/3, as seen in Figure 3, may generate the monohydrate form if allowed to react for a longer period. These results are interesting as these distinct forms of lead citrate were previously known to only form in different pH environments.

Table 4-10 gives a clearer outline of the molar ratios used and their corresponding by-products as a function of reaction time.

***Table 4-10**: XRD results from leaching PbO_2 using $C_6H_8O_7 \cdot H_2O$, H_2O_2 and NaOH as a function of reaction time*

Sample	Molar ratio of PbO_2 to H_2O_2	Molar ratio of PbO_2 to $C_6H_8O_7 \cdot H_2O$	Molar ratio of PbO_2 to NaOH	Reaction Time (Mins)	XRD analysis of by-product
(b)	1/3	1/4	1/4	60	$Pb(C_6H_6O_7) \cdot H_2O$
(c)	1/3	1/4	1/4	40	$Pb_3(C_6H_5O_7)_2 \cdot 3H_2O$
(d)	1/3	1/4	1/4	20	$Pb_3(C_6H_5O_7)_2 \cdot 3H_2O$

As Table 4-11 illustrates, the final pH, temperature, and visual properties before sample processing were very similar for all three experiments. The major observable differences in the experiments were that samples (c) and (d) became highly viscous which made filtering very difficult. This may be due to an intermediate reaction phase where the compound binds cohesively together before forming the final product.

***Table 4-11**: Reaction characteristics of leaching PbO_2 using $C_6H_8O_7 \cdot H_2O$, H_2O_2 and NaOH as a function of reaction time*

Sample	pH & Temperature pre-PbO_2	pH, Temperature and appearance 10 mins post-PbO_2	pH, Temperature and appearance at end of reaction
(b)	~3, 46 °C	~3.3, 36 °C – Creamy White	~3.4, 23 °C – Creamy White
(c)	~3, 46 °C	~3.3, 35 °C – Creamy White	~3.1, 20 °C – Creamy White (Highly viscous emulsion)
(d)	~3, 43 °C	~3.4, 29 °C – Creamy White	~3.4, 25 °C – Creamy White (Highly viscous emulsion)

The leaching of pure PbO_2 with 3 and 2 moles of H_2O_2 solution together with 4 moles of $C_6H_8O_7 \cdot H_2O$ and 3 moles of NaOH per mole of PbO_2 for 60 minutes with 1/5 starting PbO_2/H_2O ratio appeared to have been more favourable in generating $Pb(C_6H_6O_7) \cdot H_2O$ compared with experiments conducted without NaOH. Increasing the NaOH molar content to 4 resulted in what was observed to be an enhanced rate of reaction when in combination with 3 moles of H_2O_2 per mole of PbO_2.

The use of 4 moles of NaOH and $C_6H_8O_7 \cdot H_2O$ also resulted in the synthesis of $Pb_3(C_6H_5O_7)_2 \cdot 3H_2O$ when combined with 2 and 1 moles of H_2O_2 solution per mole of PbO_2. This led to the discovery that over the 60 minute reaction period $Pb_3(C_6H_5O_7)_2 \cdot 3H_2O$ transitions into $Pb(C_6H_6O_7) \cdot H_2O$ when every mole of PbO_2 is exposed to 4 moles of NaOH and $C_6H_8O_7 \cdot H_2O$, together with 3 moles of H_2O_2 solution.

The use of NaOH appears to facilitate the chelation of the metal ion complex and aided in lowering the amount of $C_6H_8O_7 \cdot H_2O$ required while increasing the rate of lead citrate formation.

Experimental results also yielded the minimum moles of H_2O_2 solution required for leaching pure PbO_2 to generate $Pb_3(C_6H_5O_7)_2 \cdot 3H_2O$ to be 1 when reacted with 2 and 4 moles of $C_6H_8O_7 \cdot H_2O$ and NaOH respectively, per mole of PbO_2. Both forms of citrate can be converted to PbO through a combustion-calcination process to be reused in LABs as outlined in chapter 5.

By increasing the pH value using NaOH, the leaching reaction was greatly enhanced in the PbO and PbO_2 experiments. The increase in the rate of reaction and greater utilisation of the $C_6H_8O_7 \cdot H_2O$ under alkaline conditions is consistent with findings in works conducted by Zhang et al[111]. In their work, they found that at higher pH values, the result of an increase in OH^- favoured the formation of chelate complexes between $C_6H_8O_7 \cdot H_2O$ and metal cations. Furthermore, $C_6H_5O_7^{3-}$ is reported to be a stronger complexing agent than $C_6H_6O_7^{2-}$, which can speed up the complex-crystallization reaction[71] and has been observed throughout this study thus far.

4.3 Leaching $PbSO_4$

4.3.1 Introduction

The main chemical component of spent LABs is $PbSO_4$ and is the rate limiting step in the leaching of the waste material. As mentioned in 4.1, $C_6H_8O_7$ is a triprotic acid and can therefore exist in three different forms in solution, the ionic distribution of $C_6H_7O_7^-$, $C_6H_6O_7^{2-}$ and $C_6H_5O_7^{3-}$ varies in a system containing $C_6H_8O_7{\cdot}H_2O$ and NaOH[112, 113]. Its three carboxyl groups can therefore theoretically provide 3 moles of protons, H^+.

In the leaching process, lead from the spent paste can form three types of coordination complexes by chelation with the citrate: $PbC_6H_7O_7$, $Pb(C_6H_6O_7)_2$ and $Pb_3(C_6H_5O_7)_2$. Stoichiometric amounts of precursor materials of $PbSO_4$, $C_6H_8O_7{\cdot}H_2O$, acetic acid (CH_3COOH) and NaOH were used as the starting point to investigate the potential viability of leaching $PbSO_4$ using these compounds in solution.

The reaction was monitored and the by-products evaluated. The pH of the solution was also monitored as the dissociation of $C_6H_8O_7$ is dependent on this. In addition, duration of reaction and temperature were also monitored and varied to gauge their effects on the reaction kinetics to help identify the optimum leaching parameters.

In the current study NaOH has been used to leach $PbSO_4$ in the presence of $C_6H_8O_7{\cdot}H_2O$ However, the leaching conditions can be a limiting factor to the viability of the whole process. The next step was to evaluate different leaching conditions as well as the use of CH_3COOH and NaOH in the process to expand on the work done by Sonmez and Kumar[77].

4.3.2 Experimental

All initial experiments were conducted in ambient conditions with a 1/5 starting $PbSO_4$/liquid ratio and reacted for 60 minutes. NaOH and $C_6H_8O_7{\cdot}H_2O$ were used to prepare the leaching media. The use of NaOH effectively replaces the $Na_3C_6H_5O_7$ used in Sonmez's study[77] in order to simplify the leaching procedure as both the PbO and PbO_2 had been treated in a similar manner.

CH_3COOH was also used in the leaching of $PbSO_4$ to gauge its potential effectiveness in facilitating the hydrometrical process as this has been reported to enhance the leaching/crystallization efficiency[71].

4 and 5 moles of NaOH for 1 mole of $PbSO_4$ were used in the following experiments in the presence of 4 moles of $C_6H_8O_7{\cdot}H_2O$ for 1 mole of $PbSO_4$ in each reaction. Investigations were carried out by magnetically stirring each mixture at a constant rate in a borosilicate glass beaker for an hour.

Additional experiments were carried out with 1 to 2 molar ratios of $PbSO_4$ to CH_3COOH added to the mixture. Each sample was filtered using a Büchner funnel and flask before being allowed to dry overnight at 80 °C as before.

4.3.3 Results and Discussion

The dried end products were analysed using X-ray powder diffraction for phase identification. Figure 4-10 below illustrates X-ray diffraction patterns of (a) $Pb(C_6H_6O_7)\cdot H_2O$ generated from work conducted by Kourgiantakis et al[109] and (b) 1 to 4 molar ratio of $PbSO_4$ to NaOH.

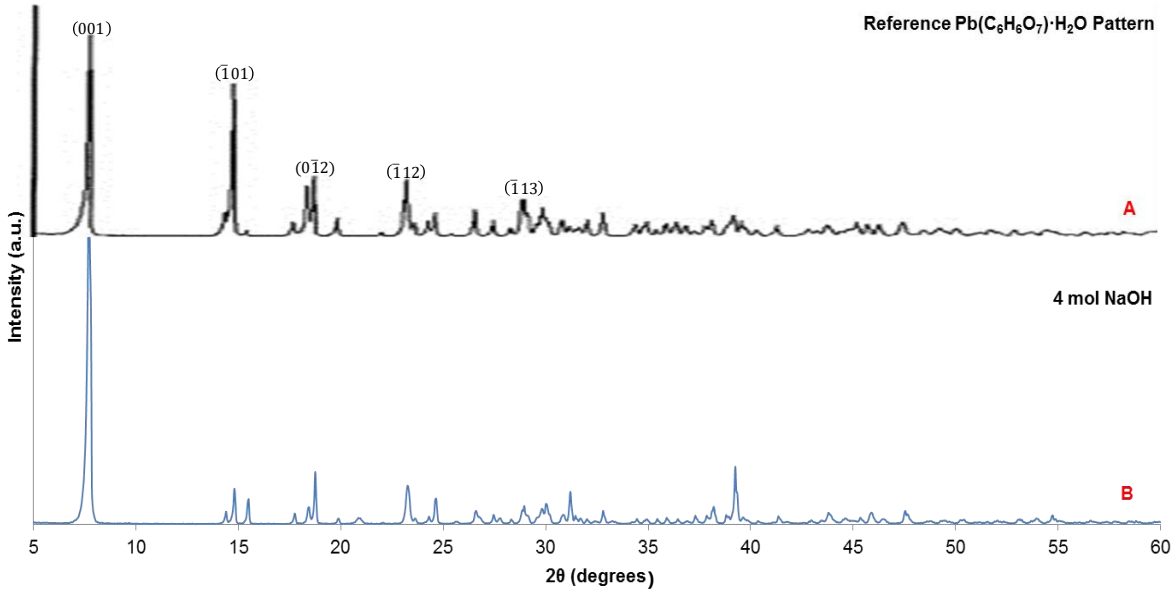

***Figure 4-10**: Comparison of X-ray diffraction analysis of $Pb(C_6H_6O_7)\cdot H_2O$ (a) created by Kourgiantakis et al with $PbSO_4$ leached using (b) 1/4 molar ratio with NaOH and $C_6H_8O_7\cdot H_2O$*

As the XRD comparison demonstrates, the sample shows a good pattern match for $Pb(C_6H_6O_7)\cdot H_2O$. However, the peak intensities are observed to be quite low, which may indicate low relative abundance. In this reaction, $PbSO_4$ was allowed to react with NaOH in solution for approximately 2 minutes.

The starting pH was recorded as 11.8. Upon addition of $PbSO_4$, the pH was observed to show a slight increase with a corresponding small decrease in temperature being noted (from 37 to 35 °C). The solution formed a white mixture with a yellow hue, which continued after the addition of $C_6H_8O_7\cdot H_2O$ and eventually turned to pale green and then to pure white after 20 minutes. On the addition of $C_6H_8O_7\cdot H_2O$ the pH was recorded to be 2.8 with a temperature of 37.5 °C.

The final product was a creamy white emulsion which is a noted visual characteristic of lead citrate. The reaction can be expressed by the following:

$$PbSO_{4(s)} + C_6H_8O_7\cdot H_2O_{(aq)} + 2NaOH_{(aq)} \rightarrow Pb(C_6H_6O_7)\cdot H_2O_{(s)} + Na_2SO_{4(aq)} + 2H_2O_{(l)} \quad \textbf{4-12}$$

In the next investigation, the molar concentration of NaOH was increased relative to $PbSO_4$ to a ratio of 5 to 1. The same reaction and processing procedure was applied as before with the final product analysed using XRD. Figure 4-11 below illustrates X-ray diffraction patterns of (a) lead citrate tribasic trihydrate ($Pb_3(C_6H_5O_7)_2 \cdot 3H_2O$) from Sigma Aldrich used as the reference pattern, (b) 1 to 5 molar ratio of $PbSO_4$ to NaOH with 4 moles of $C_6H_8O_7 \cdot H_2O$.

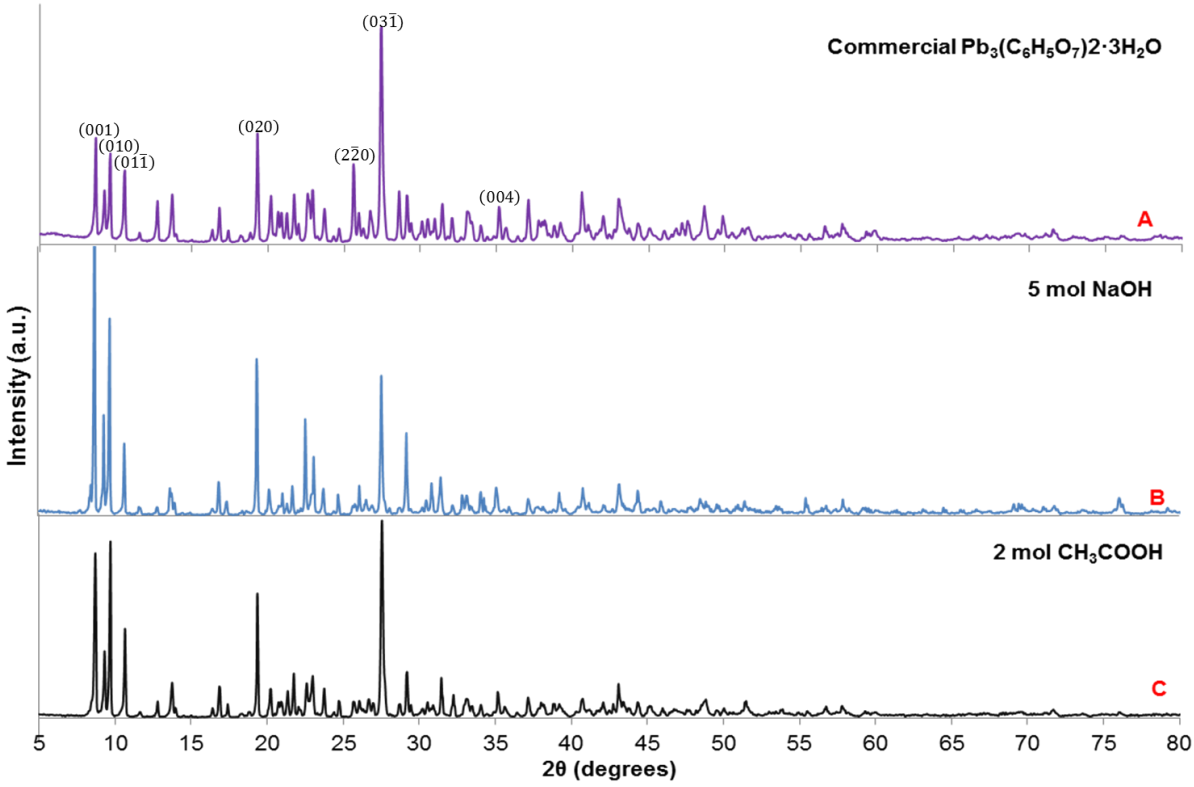

***Figure 4-11**: Comparison of X-ray diffraction analysis of (a) commercially sourced $Pb_3(C_6H_5O_7)_2 \cdot 3H_2O$ with $PbSO_4$ leached using 1/5 molar ratio with NaOH*

From Figure 4-11, the increase in the molar concentration of NaOH by 1 appear to have generated an end product that closely matches $Pb_3(C_6H_5O_7)_2 \cdot 3H_2O$, the third possible coordination complex that could be formed from chelation with $C_6H_8O_7$, with good agreement on the majority of peak positions.

Figure 4-11C illustrates the XRD pattern from the by-product from leaching with 1/2 ratio of $PbSO_4$ to CH_3COOH together with 1/2 $C_6H_8O_7 \cdot H_2O$ and 1/6 ratio with NaOH. The pattern matches well with $Pb_3(C_6H_5O_7)_2 \cdot 3H_2O$.

Table 4-12 details the comparison of the results illustrated from Figures 4-10 and 4-11 for clarity. Visual observations of the reaction characteristics match closely with that of the previous experiment with a pale green compound being formed upon the addition of $PbSO_4$ into the NaOH solution.

The starting pH was again noted to be 11.8. As with the previous reaction the pH was noted to increase slightly upon mixing with a corresponding decrease in temperature (40 to 37 °C). The solution forms a white emulsion after 15 minutes beyond the addition of $C_6H_8O_7 \cdot H_2O$. The pH was noted to be higher at 3.3 compared to the previous reaction just before termination.

The end product was again indicative of lead citrate in its physical characteristics. Furthermore, the end compound was noted to be more viscous than the previous sample. The expression for this reaction can be noted by the following:

$$3PbSO_{4(s)} + 2C_6H_8O_7 \cdot 2H_2O_{(aq)} + 6NaOH_{(aq)} \rightarrow Pb_3(C_6H_5O_7)_2 \cdot 3H_2O_{(s)} + 3Na_2SO_{4(aq)} + 5H_2O$$

4-13

***Table 4-12**: XRD comparison results from leaching $PbSO_4$ using $C_6H_8O_7 \cdot H_2O$, CH_3COOH and NaOH with varying molar ratios*

Molar ratio of $PbSO_4$ to CH_3COOH	Molar ratio of $PbSO_4$ to $C_6H_8O_7 \cdot H_2O$	Molar ratio of $PbSO_4$ to NaOH	XRD analysis of by-product
-	1/4	1/4	$Pb(C_6H_6O_7) \cdot H_2O$
-	1/4	1/5	$Pb_3(C_6H_5O_7)_2 \cdot 3H_2O$
1/2	1/2	1/6	$Pb_3(C_6H_5O_7)_2 \cdot 3H_2O$

As Table 4-12 shows, the use of CH_3COOH appear to facilitate the leaching of $PbSO_4$ with less $C_6H_8O_7 \cdot H_2O$ needed, but more NaOH was required to obtain a pure by-product. It is assessed that the $C_6H_8O_7 \cdot H_2O$ and NaOH in the reaction would form sodium citrate, which would in turn provide citrate ions to form lead citrate. The likely mechanism for the formation of lead citrate from $PbSO_4$ would first involve the dissolution and dissociation of $PbSO_4$, followed by the chelation and precipitation of lead citrate.

The rate of reaction would therefore depend on both the concentration of lead and citrate ions near the surface of the crystals. Therefore, while keeping the concentration of the lead ion constant, the increased amount of $C_6H_8O_7 \cdot H_2O$ and NaOH in the precursor mix provided the extra citrate ions. As a result, the increased concentration of sodium citrate facilitated the rate at which $Pb_3(C_6H_5O_7)_2 \cdot 3H_2O$ was formed in-situ.

In addition, for the reactions involving CH_3COOH, the acetate ion, which has a lower association constant than that of the citrate ion would have had an effect on the coordination complex when lead chelates with the citrate. Lead acetate ($Pb(C_2H_3O_2)_2$) is likely to have formed from $PbSO_4$ following from its interactions with CH_3COOH.

Having a higher solubility than lead citrate, $Pb(C_2H_3O_2)_2$ cannot precipitate out easily, which would affect the diffusion of lead ion and the dissolution of $PbSO_4$.

The sequence of reagent mixing/reaction was explored to determine their significance in the reaction characteristics as in 4-1. An experiment was conducted using the same parameters as the previous investigation with 5 moles of NaOH per mole of $PbSO_4$ in the presence of 4 moles of $C_6H_8O_7 \cdot H_2O$. In this experiment $PbSO_4$ was added to a mixture of NaOH and $C_6H_8O_7 \cdot H_2O$ in solution.

The starting pH for this reaction was recorded to be 3.7. Upon addition of the $PbSO_4$ the pH was noted to remain unchanged with the temperature decreasing from 53 to 43 °C. The pH remained the same throughout the reaction period with no visual changes observed. Figure 4-12 illustrates the X-ray diffraction pattern of the dried end product from this experiment.

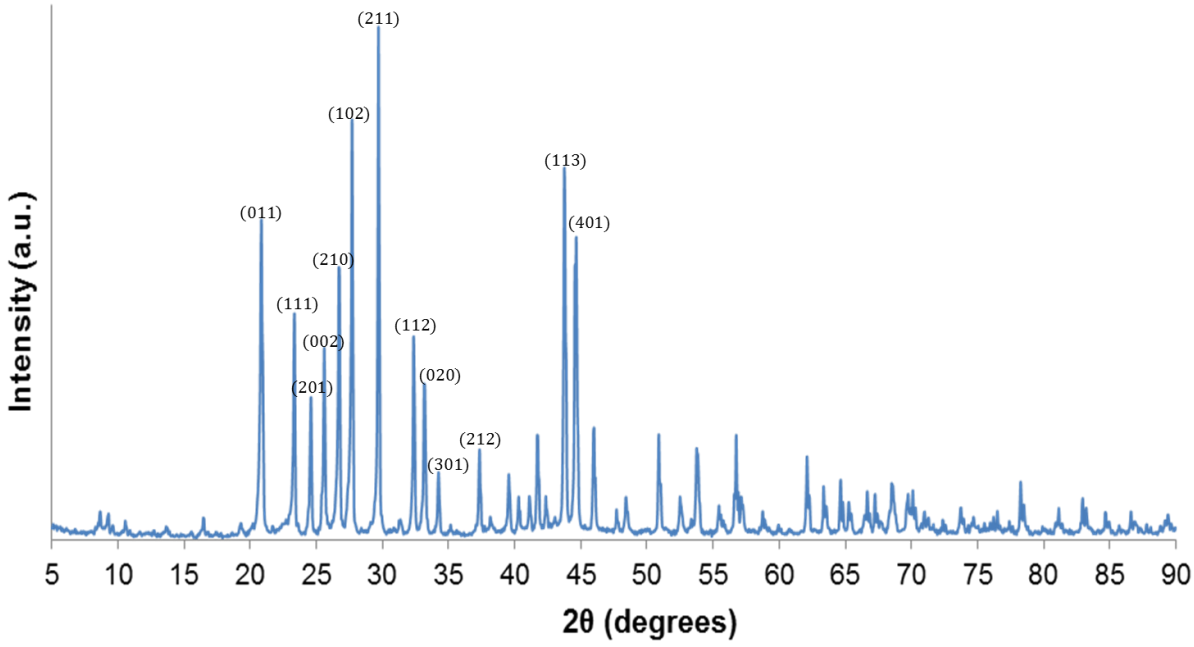

***Figure 4-12**: $PbSO_4$ leached using 1/5 molar ratio with NaOH*

The result of this investigation clearly demonstrates the importance of the sequence of mixing in the reaction process. The by-product was analysed using XRD with the resulting pattern being a perfect match for $PbSO_4$ (reference code: 01-083-1720) indicating no reaction had occurred.

From various investigations under different pH and temperatures, the optimum molar ratio of reactants are those shown in Table 4-12 to produce lead citrate from $PbSO_4$ with a S:L ratio of 1:5 at ambient conditions in <1 hour. Although experiments conducted with lower ratios of $PbSO_4$ to the other precursor materials proved successful, the reaction and purity of by-products were commercially prohibitive and were not pursued further.

The current investigation shows for the first time that $PbSO_4$ can be successfully leached using NaOH and $C_6H_8O_7 \cdot H_2O$ to generate different forms of lead citrate as a function of NaOH molar concentration.

Previous studies into leaching $PbSO_4$[71] required CH_3COOH to facilitate the reaction. The current study has demonstrated that the use of NaOH has the potential to leach $PbSO_4$ in a timely manner in a simpler reaction procedure. Further, it was observed in the current study that lead citrate is readily crystallized from aqueous solution and can directly generate PbO through combustion-calcination for LABs, which will be discussed in greater detail in chapter 5.

4.4 Leaching Spent Battery Paste from Industry

4.4.1 Introduction

Depleted paste materials from both the positive and negative grids of discarded LABs as well as the by-products derived from the gradual loss of these components through normal operation, known as shedding, were obtained from industry for leaching and recycling experiments. The results obtained from experiments conducted with laboratory grade materials from 4.1, 4.2 and 4.3 were used to develop a leaching procedure for the battery pastes.

4.4.2 Experimental

All as-received waste materials were first analysed using XRD to determine the phase composition of each plate material before leaching experiments were conducted. Each constituent waste material was extracted from their respective grids, ground and leached separately to gauge the reaction characteristics. The purity of the by-products generated as a function of leaching conditions derived from precursor formulations tailored for each waste composition as determined by XRD.

Following a series of satisfactory trials, the waste materials from both the positive and negative grids were combined and leached together. Each waste material was mixed in equal amounts with leaching precursor materials adjusted accordingly. The same protocol was then followed for the mixing and leaching of a combined waste compound containing materials from both the positive and negative grids as well as the shedding.

Each leaching experiment was conducted for one hour under constant magnetic stirring at approximately 250-300 rpm. The high initial pH leaching procedure was used as this was favourable in generating the $C_6H_5O_7^{3-}$ species in order to speed up the complex-crystallisation reaction and increase utilisation of $C_6H_8O_7{\cdot}H_2O$. Experiments were also conducted using a municipal water source as well as deionised water as the main solvent. This was conducted as a proof of concept in order to demonstrate the feasibility of using a more readily available and cost-effective source of solvent for potential wider industrial application.

4.4.2 Results and Discussion

The grid materials were first separated from the bulk by sectioning the main components to facilitate handling and extraction. An example of a section of a severed grid is shown in Figure 4-13. As shown in the figure, the waste materials were extracted from the grid leaving the metallic structure intact.

***Figure 4-13**: A severed section of a positive grid to facilitate extraction and analysis*

The waste materials from the grids were ground using mortar and pestle until a powder-like consistency was obtained before being dried overnight at 80 °C. The dried powders were analysed using XRD to determine phase composition. Figures 4-14 to 4-16 illustrate the XRD patterns from the processed as-received positive, negative and shedding materials respectively.

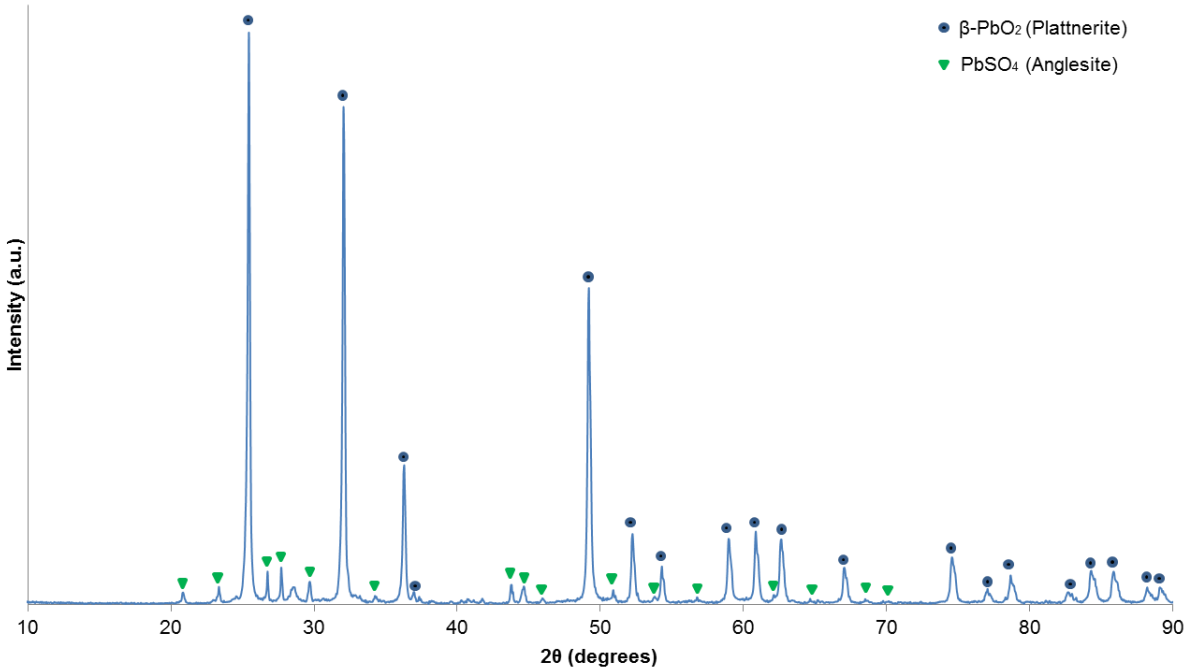

***Figure 4-14**: XRD pattern of as received dried paste from a used LAB positive grid*

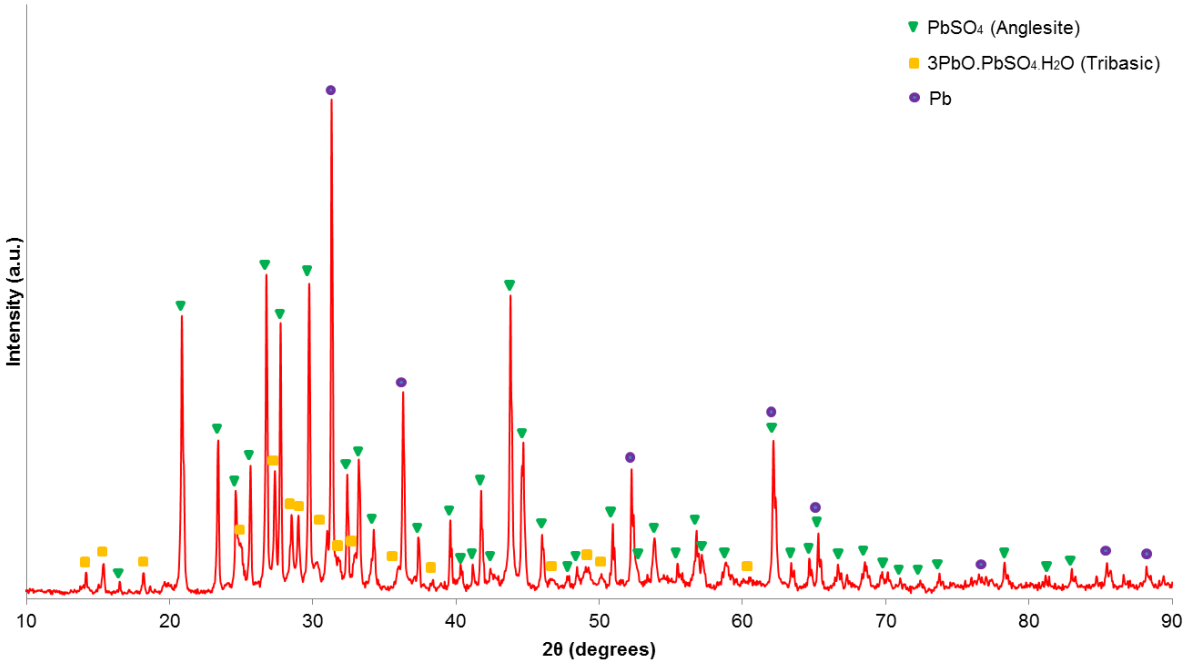

***Figure 4-15**: XRD pattern of as received dried paste from a used LAB negative grid*

-

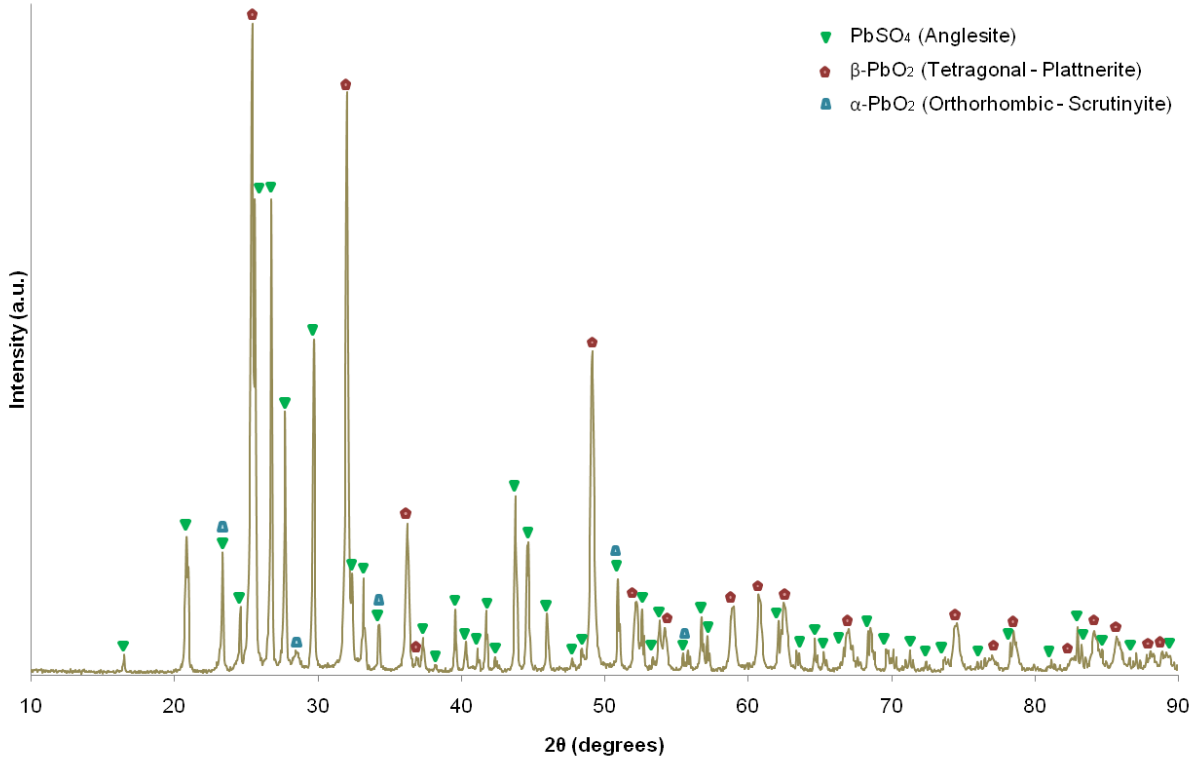

***Figure 4-16**: XRD pattern of as received shedding material from a used LAB*

As illustrated in Figures 4-14 and 4-15, these diffraction patterns indicate the presence of the typical by-products associated with a discharged LAB from the positive and negative grids respectively. The low peak intensities in Figure 4-14 attributed to $PbSO_4$ together with high peak intensities assigned to PbO_2 indicate that the battery from which the material was derived still had significant utility.

The diffraction pattern for this material does not typify that of a depleted electroactive material, whereas the as-received shed material shown in Figure 4-16 illustrates well what is usually observed from spent electroactive positive grids. The presence of both the orthorhombic and tetragonal form of PbO_2, known as α-PbO_2 and β-PbO_2 respectively, as well as significant $PbSO_4$ formation exemplifies a LAB at or towards the end of its utility.

The same is true for the negative grid material illustrated by the XRD pattern in Figure 4-15. The presence of tribasic lead sulphate ($3PbO\cdot PbSO_4\cdot H_2O$) together with a significant $PbSO_4$ content in the waste product is indicative of an electroactive material that is towards the end of its efficacy. However, the high metallic lead (Pb) content, indicated by its high relative peak intensities, demonstrates that the material is still potentially electrochemically viable. Each constituent waste material from the positive, negative and shedding was leached separately according to their respective phase composition.

The positive waste material was treated as if leaching pure PbO_2 from 4.2, the negative was leached according to the optimum conditions found in 4.3 for $PbSO_4$ and the shedding was leached by a mixture of the two procedures. Having obtained results observed in their respective simulant counterparts, the three waste materials were combined and leached together.

The initial investigation used the highest effective molar concentrations, with a slight excess, used in the individual leaching experiments outlined in 4-1 to 4-3 with a S:L ratio of 1:5. As outlined in Table 4-13, leaching experiments were carried out both with and without CH_3COOH to compare the by-products generated. Figure 4-17 illustrates an image of a filtered sample after leaching for 1 hour without CH_3COOH as outlined in Table 4-13C.

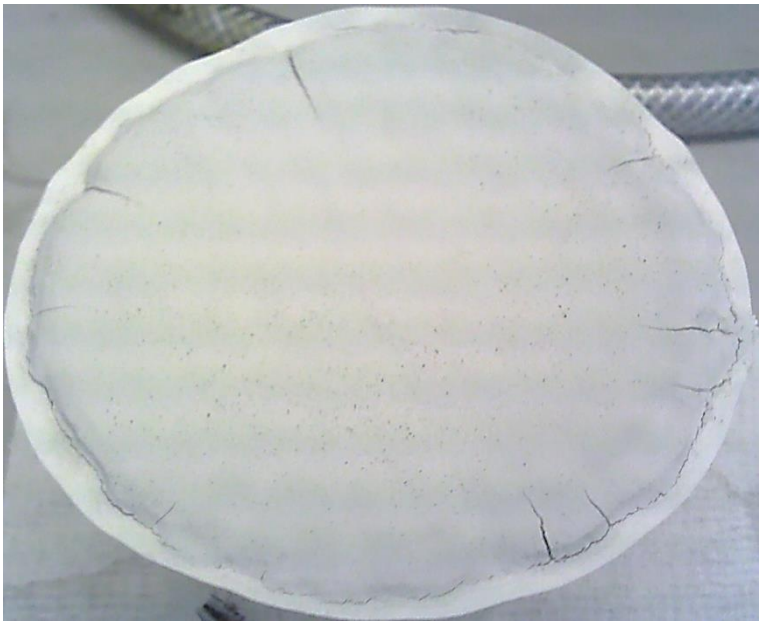

***Figure 4-17**: Image of leached mixed waste material after filtration*

Following leaching/crystallisation and filtration, each sample was dried at approximately 80 ˚C overnight. Once dried, each sample was processed into a powder and analysed using XRD to determine phase purity and composition.

All individual and combined samples indicated strong correlation with $Pb_3(C_6H_5O_7)_2 \cdot 3H_2O$. Figure 4-18 illustrates a comparison of XRD patterns obtained for a sample of analytically pure $Pb_3(C_6H_5O_7)_2 \cdot 3H_2O$ (a) with a sample synthesized from mixed waste materials using municipal water as the solvent with CH_3COOH (b) and without CH_3COOH (c). As both synthesis routes provided a similar degree of purity in by-product, future investigations were simplified and conducted without the use of CH_3COOH.

As with experiments conducted with simulants, the reaction with the industrial paste generates an emulsion indicating the formation of lead citrate. The emulsion formed is very pale grey to light white in colour.

The grey hue points to the presence of unreacted carbon and metallic lead. Despite the presence of impurities and the mixture of the different compounds from the grids and shedding, the total mass of the combined waste materials was taken as equivalent to the individual constituent simulants investigated earlier in this study.

Therefore, the optimised sum of the reagents from those studies was used in experiments conducted with the combined industrial waste per given mass. This can be further optimised from quantitative analysis by XRD of the mixed waste material to determine the corresponding reagents required for effective leaching. Although this may lead to an excess of reagents used, these can be recycled when scaled up to industrial applications through evaporation and filtration.

***Table 4-13**: XRD comparison results from leaching mixed waste materials using $C_6H_8O_7 \cdot H_2O$, CH_3COOH, H_2O_2 and NaOH with varying molar concentrations*

Sample	Molarity of CH_3COOH (M)	Molarity of H_2O_2 (M)	Molarity of $C_6H_8O_7 \cdot H_2O$ (M)	Molarity of NaOH (M)	XRD analysis of by-product
B	1.3	2.5	2	4	$Pb_3(C_6H_5O_7)_2 \cdot 3H_2O$
C	-	2.5	3.2	3.5	$Pb_3(C_6H_5O_7)_2 \cdot 3H_2O$

As detailed in Table 4-13, the by-products from leaching with and without CH_3COOH resulted in $Pb_3(C_6H_5O_7)_2 \cdot 3H_2O$ in the same time period. The leaching procedure using CH_3COOH meant less $C_6H_8O_7 \cdot H_2O$ being required and therefore may provide an option for industrial scale-up should the commercial price of $C_6H_8O_7 \cdot H_2O$ fluctuate positively.

Additionally, the option exists where plate materials can be treated like for like, according to their specific chemistries, to avoid the excess use of reagents that will be required for combined leaching of the negative and positive paste materials.

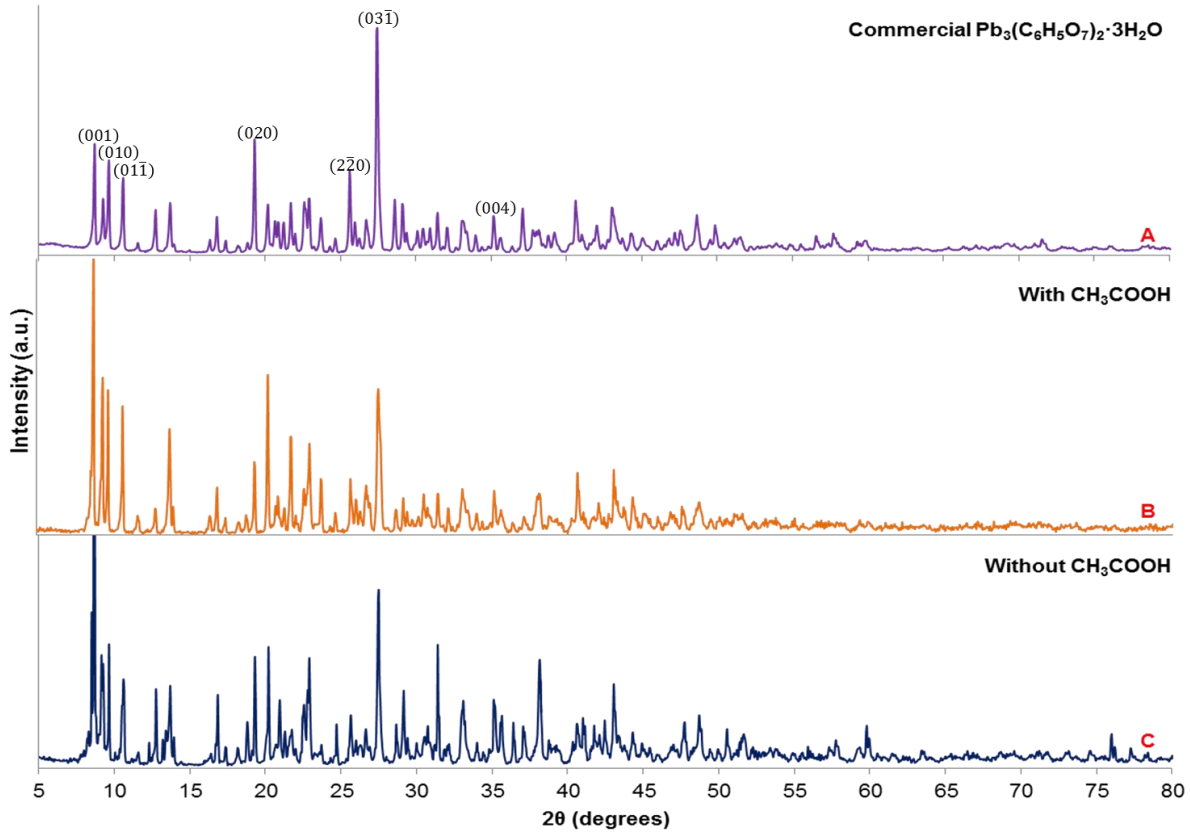

***Figure 4-18**: XRD patterns of commercial $Pb_3(C_6H_5O_7)_2 \cdot 3H_2O$ from Sigma Aldrich (a) compared with by-products leached with CH_3COOH (b) and without CH_3COOH (c)*

Figure 4-18 typifies the results obtained for all successfully leached samples. The purity of the solvent used does not appear to have any observable impact on the quality of the by-products generated. The next stage of investigation will be to generate PbO from these recycled materials and determine their potential reuse in LABs.

4.5 Summary

Initial leaching experiments conducted with waste simulants using analytically pure compounds for PbO demonstrated the importance of the initial reaction environment in determining the dominant reactive species available to generate the final product. The final product of either form of lead citrate benefited from a S:L ratio of 1:5 with a molar ratio of 1:3 and 1:2 for PbO to $C_6H_8O_7.H_2O$ and NaOH respectively in terms of maintaining a processing time <1 hour and generating an analytically pure compound.

It was found that the pH of reaction played a vital role in reaction kinetics. Increasing the pH, using NaOH, resulted in an increase in the rate of reaction and greater utilisation of the $C_6H_8O_7{\cdot}H_2O$. This was due to an increase in OH^- favouring the formation of chelate complexes between $C_6H_8O_7{\cdot}H_2O$ and the metal cations. Furthermore, $C_6H_5O_7^{3-}$ was found to be the stronger complexing agent compared to the other two citrate species, which can speed up the complex-crystallization reaction. As a result, the minimum moles of H_2O_2 solution required for leaching pure PbO_2 to generate $Pb_3(C_6H_5O_7)_2{\cdot}3H_2O$ was found to be 1 when reacted with 2 and 4 moles of $C_6H_8O_7{\cdot}H_2O$ and NaOH respectively per mole of PbO_2.

It was demonstrated that $PbSO_4$ can be successfully leached using NaOH and $C_6H_8O_7{\cdot}H_2O$ to generate different forms of lead citrate as a function of NaOH molar content. As a result of these investigations the molar concentrations, with a S:L ratio of 1:5, of 2.5 M H_2O_2, 3.2 M $C_6H_8O_7{\cdot}H_2O$, and 3.5 M NaOH were used to leach depleted LAB paste and shedding material from industry and were successful in synthesising $Pb_3(C_6H_5O_7)_2{\cdot}3H_2O$ after less than an hour of reaction time.

The individual leaching procedures for the positive and negative paste materials could also be used as the option exists where plate materials can be treated like for like, according to their specific chemistries, to avoid the excess use of reagents that will be required for combined leaching of the negative and positive paste materials.

5 Study and Application of Lead Citrate

5.1 Introduction

The recycling process under consideration can be broken down into 3 stages:

- Stage 1. Leaching/crystallisation of the spent active paste from the battery.
- Stage 2. Filtration, drying and processing of the leachate
- Stage 3. Combustion-calcination of the leachate to convert the materials back into useable PbO for the manufacture of LABs.

As stated previously, the morphology, particulate size and shape can be potentially controlled by the combustion-calcination conditions used in regenerating PbO from lead citrate. Stage 3 will now be explored in greater detail using the lead citrate synthesised as outlined in chapter 4.

5.2 Combustion-calcination of Lead Citrate

5.2.1 Introduction

To further optimise the recycling method outlined earlier, the following line of investigation seeks to gain a fuller understanding of some of the underlying processing conditions. In so doing, the aim is to determine the best approach for commercialisation of this technique. At this stage, the optimisation of the processing conditions to produce PbO from $Pb_3(C_6H_5O_7)_2 \cdot 3H_2O$ is investigated. The next step in the recycling process is the combustion-calcination of the manufactured $Pb_3(C_6H_5O_7)_2 \cdot 3H_2O$ precursor.

5.2.2 Experimental

The synthesised $Pb_3(C_6H_5O_7)_2 \cdot 3H_2O$ from earlier experiments was first characterised by TG-DSC analysis to determine its combustion-calcination behaviour in order to formulate further thermal experimental procedures.

Samples of $Pb_3(C_6H_5O_7)_2 \cdot 3H_2O$ were then subjected to a variety of thermal treatments to determine the degree to which the microstructure of PbO can be altered. BET, BJH, apparent density, XRD, SEM/EDS and acid reactivity measurements were then made to characterise the PbO resulting from the combustion-calcination processes used.

5.2.3 Results and Discussion

TG–DSG analysis of the decomposition of the processed $Pb_3(C_6H_5O_7)_2 \cdot 3H_2O$ precursor was conducted in air from room temperature to 600 °C and held there for 1 hour at a heating rate of 5 °C/min, before being allowed to naturally cool.

This was to ascertain the processes that occur during the combustion-calcination of samples of lead citrate, in order to aid in directing heat treatments to optimise product manufacture. Figure 5-1 shows the decomposition process of a sample of $Pb_3(C_6H_5O_7)_2 \cdot 3H_2O$.

The graph illustrates a complex decomposition reaction that involves a number of stages. The initial stage displays a gradual mass loss of ~2.52% between 80-180 °C, which had no corresponding DSC peaks. This initial stage, given the temperature range, can be attributed to dehydration, or the liberation of loosely bound molecular water. The successive three stages occurring between 240-295, 295-315 and 315-335 °C with percentage mass losses of 9.97, 5.12 and 10.51% respectively corresponded with exothermic peaks from the DSC at 269, 299 and with the major peak at 328 °C.

Further mass loss of ~3.8% was observed between 335-460 °C, which corresponded to a DSC peak at 420 °C, seen in Figure 5-2. This could indicate the combustion of the remaining $Pb_3(C_6H_5O_7)_2 \cdot 3H_2O$ in the system. These exothermic peaks show the combustion of intermediate compounds within the sample, with the major peak illustrating the combustion of $Pb_3(C_6H_5O_7)_2 \cdot 3H_2O$ which is assessed to be a combined decomposition process.

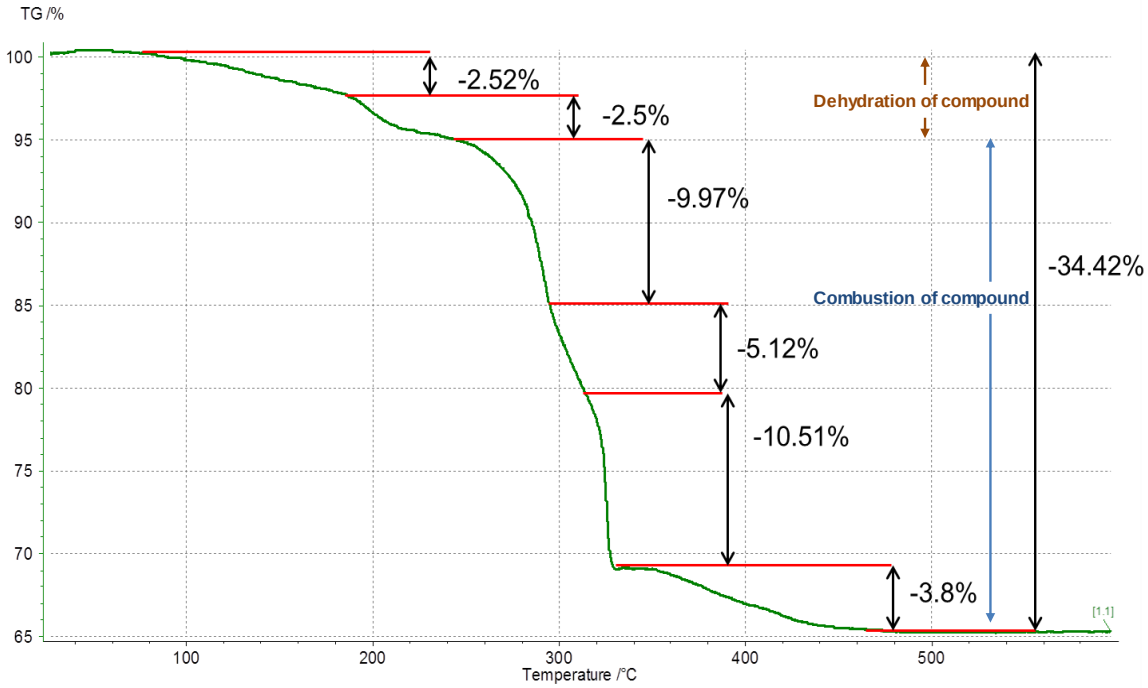

***Figure 5-1**: TG graph of $Pb_3(C_6H_5O_7)_2 \cdot 3H_2O$ heated in air from room temperature to 600 °C at 5 °C/min*

A tabulation of these results is shown in Table 5-1. The final product at the end of the analysis showed a powder that was light yellow with shades of orange in colour. This mixture points to the presence of both α and β-PbO.

***Table 5-1**: TG-DSC analysis of $Pb_3(C_6H_5O_7)_2 \cdot 3H_2O$ heated from room temperature to 600 °C in air at 5 °C/min*

Temperature (°C)	80-180	180-240	240-295	295-315	315-335	335-460
Mass loss (%)	2.52	2.5	9.97	5.12	10.51	3.8
DSC peak (°C)	-	-	269	299	328	420

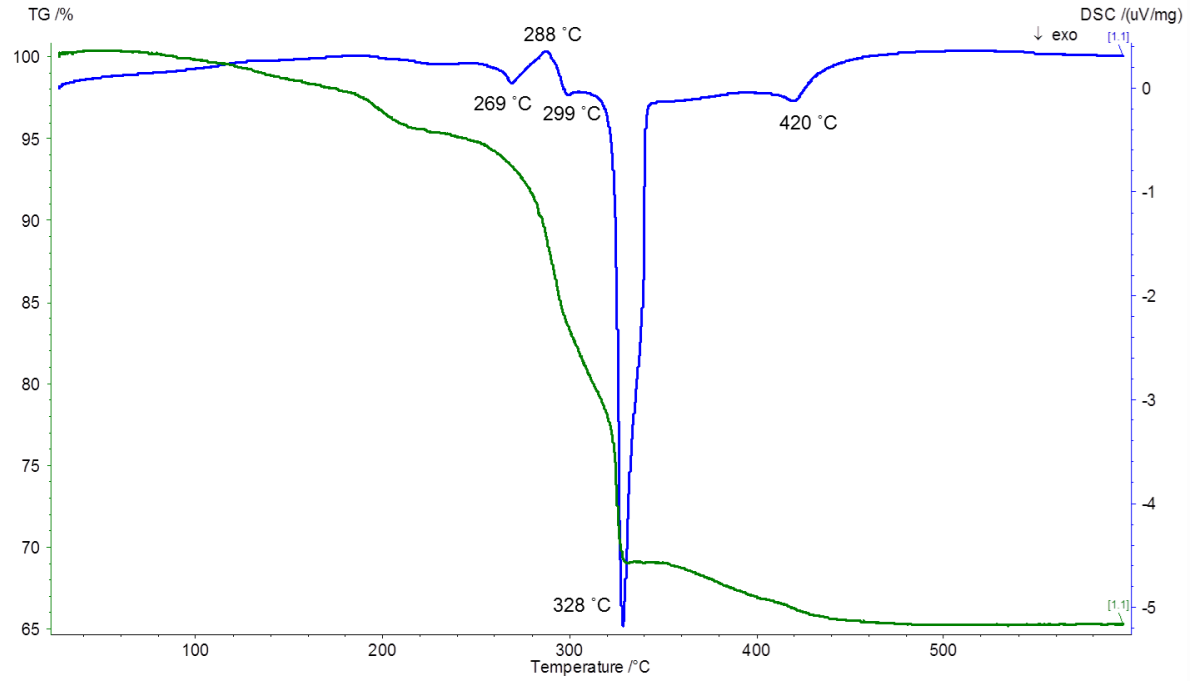

***Figure 5-2**: TG-DSC comparison graph of $Pb_3(C_6H_5O_7)_2 \cdot 3H_2O$ heated from room temperature to 600 °C in air at 5 °C/min*

Analysis conducted with different heating rates yielded a diverse number of final products. This was illustrated by the varying colours, indicating differing polymorph ratio imparted on the samples as a function of heating rate. The percentage mass loss also varied according to the rate of heating.

However, the formation of by-products such as PbO_2 and/or other intermediates cannot be discounted. The analysis of the final product of the 5 °C/min sample showed only PbO was present and was the optimum heating rate when compared to other samples with different heating rates.

This, therefore, was the rate chosen for more specific experiments. In addition, the back calculated molecular weight, using stoichiometric amounts from this analysis indicated that the formed precursor lead citrate was $Pb_3(C_6H_5O_7)_2 \cdot 3H_2O$, further corroborating the XRD analysis conducted earlier.

Following successful leaching, filtering, drying and analysis, a sample of synthesized $Pb_3(C_6H_5O_7)_2 \cdot 3H_2O$ was heated to 350 °C for one hour at a rate of 5 °C/min. Figure 5-3 illustrates a typical sample of processed $Pb_3(C_6H_5O_7)_2 \cdot 3H_2O$ before and after combustion-calcination.

***Figure 5-3**: Images of leached, filtered and dried waste paste material from a used LAB (Top) and its by-product after combustion-calcination at 350 °C at 5 °C/min for 1 hour (Bottom)*

The by-product from the combustion-calcination of $Pb_3(C_6H_5O_7)_2 \cdot 3H_2O$ generated a highly textured, porous and multi-coloured compound and was such that a fine powder was easily made after processing. XRD analysis was conducted to determine the phase composition of the sample illustrated in Figure 5-3 and is shown in Figure 5-4.

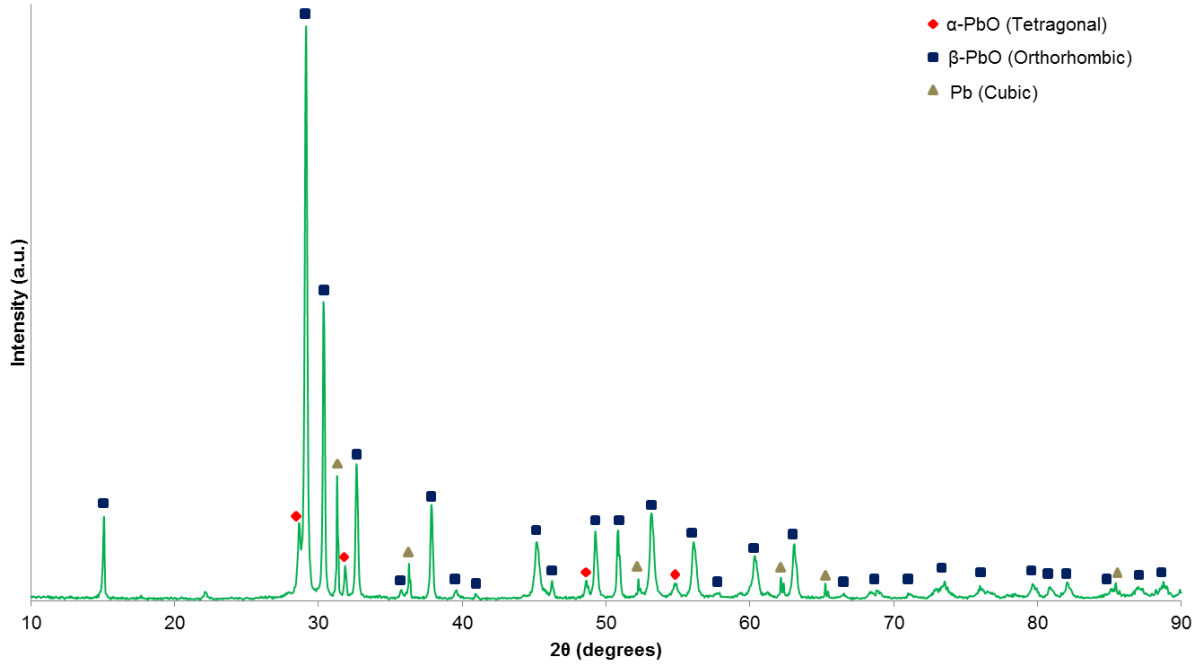

***Figure 5-4**: XRD pattern of leached material after combustion-calcination at 350 °C at 5 °C/min for 1 hour*

As illustrated in Figure 5-4, the XRD pattern indicates the presence of both polymorphs of PbO, tetragonal and orthorhombic, as well as metallic Pb. This is consistent with the type of PbO found in commercial production by the Barton Pot process[114] and points to the potential reuse of the leached waste materials from this recycling process in a new LAB.

SEM was used to examine the physical changes to the microstructure compared with the starting material, including the intermediate stage of processing. Images were taken at different magnifications to characterise the material at macroscopic and microscopic levels, permitting examination of the morphology, shape, size, and general topography of each sample. Measurements were also taken of individual particles as well clusters to gain an appreciation of the degree of change in particle size.

Figure 5-5 illustrates SEM images of a mixture of all three of the as-received waste materials shown in A with that of the synthesised $Pb_3(C_6H_5O_7)_2 \cdot 3H_2O$ after leaching, filtration and drying shown in B together with PbO after combustion-calcination at 350 °C at 5 °C/min for 1 hour, shown in C and D.

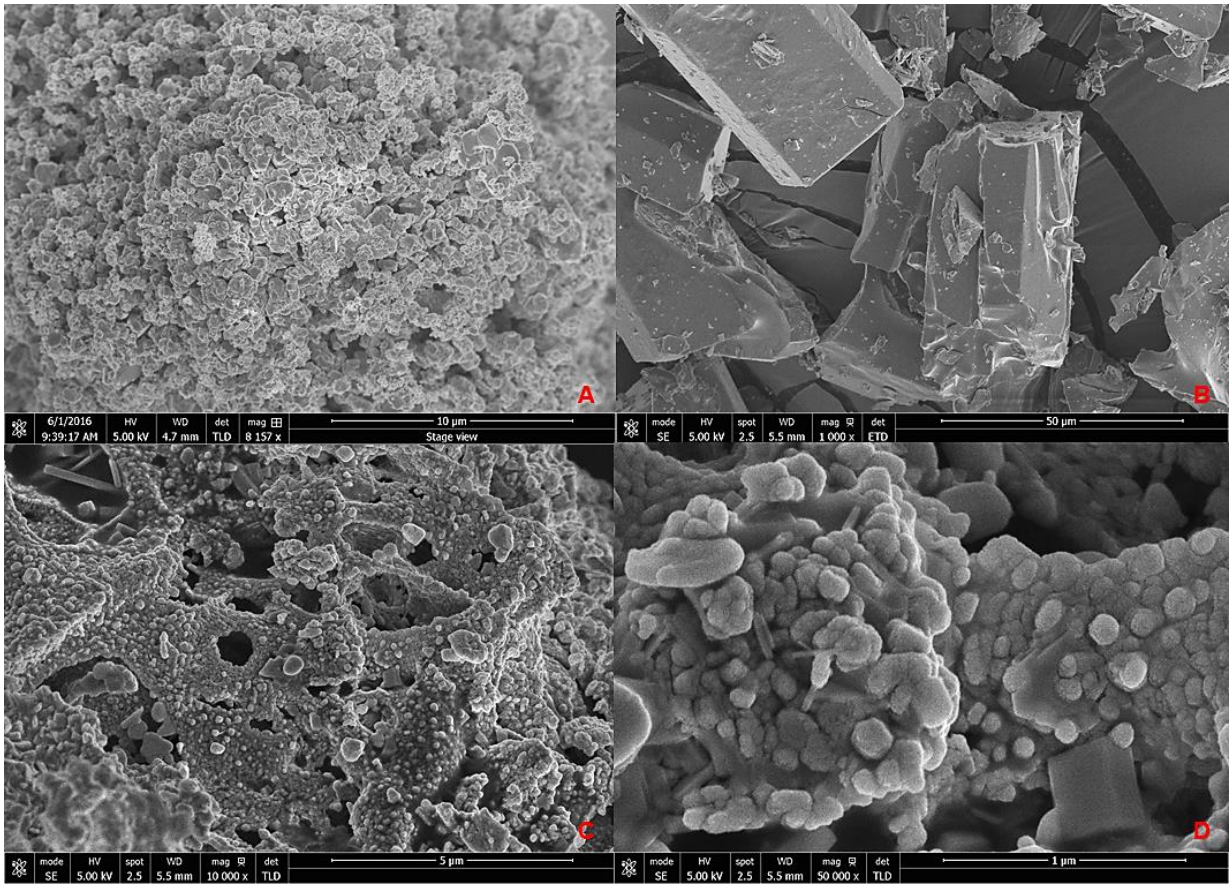

***Figure 5-5**: SEM images of mixed waste material (A) before being leached and the synthesis of $Pb_3(C_6H_5O_7)_2 \cdot 3H_2O$ (B) after leaching compared with its by-product after combustion-calcination at 350 °C (C and D)*

Figure 5-5 displays the SEM images that pictorially illustrates the process of the recycling of LAB wastes (A) through to its reprocessing to reusable PbO (C and D) via $Pb_3(C_6H_5O_7)_2 \cdot 3H_2O$ (B) after leaching. As depicted in Figure 5-5B, the dried compound that resulted from the hydrometallurgical leaching of the LAB by-products shows clear signs of the complexing-crystallisation reaction that took place.

The large distinct blocks of columnar shaped particles seen in 5-5B, formed of the smaller, rounded particles of the waste materials shown in 5-5A are indicative of the incorporation of one into the other found in a number of similar studies[64, 74, 115, 116].

The process by which the waste material is converted to lead citrate, from A to B, is thought to initially begin with the solvation of the material by $C_6H_8O_7 \cdot H_2O$ in solution. At this stage, the bonds in the waste materials are broken for each of the ions to be solvated in the solution.

The particles become highly dispersed in a large volume. Having low solubility, lead citrate particles precipitate out immediately. These particles would then precipitate preferentially onto other lead citrate crystals, forming larger crystals over time. In the case of this experiment, columnar shapes are formed from this coalescence of particles.

Figures 5-5C and D illustrates imagery of the microstructure of the PbO generated from $Pb_3(C_6H_5O_7)_2 \cdot 3H_2O$ after combustion-calcination at x10,000 and 50,000 magnifications respectively. As seen in C, the general morphology consists of a highly textured surface containing rounded and spherical particles ranging from tens to hundreds of nanometres in size.

A close-up image in D shows a high degree of agglomeration consisting mainly of spherical particles between 100-200 nm in diameter. This nanostructure appears relatively porous with some areas of high density from sintering during the calcination process. The nanostructure formed after combustion-calcination is attributed to the structure of the lead citrate precursor.

The organic component of the lead citrate is arranged such that the relative positions of the lead atoms are dispersed from one another within the crystalline structure. This can be better illustrated in Figure 5-6.

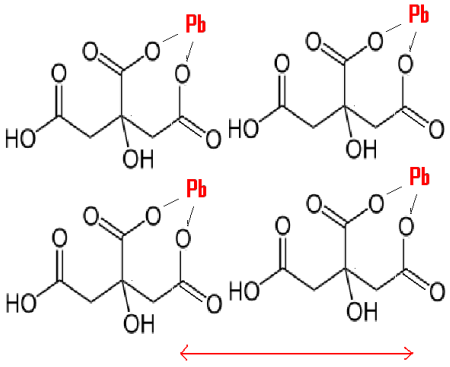

***Figure 5-6**: Position of lead atoms in lead citrate*

During combustion, the citrate bonds are broken and volatile species are formed. This result in the removal of the citrate and the volume they once occupied that had separated the lead particles that were bonded to the citrate.

The remaining lead particles at this stage form into PbO via combustion. The citrate therefore acts as a fugitive agent in generating a porous nanostructure in addition to its primary complexing role. Table 5-2 details the surface area, pore volume and diameter, apparent density as well as the acid reactivity of the sample illustrated in Figure 5-3.

***Table 5-2**: BET surface area, BJH pore volume and size, apparent density and acid reactivity of sample reacted at 350 °C*

Sample	**350 °C**
BET Surface area (m^2 g^{-1})	1.3
BJH Cumulative pore volume between 1.7 nm and 300 nm (ml/g)	0.02
BJH average pore diameter (nm)	45.1
C constant	67
Apparent density (g/ml)	8.2
Acid reactivity (mg/g)	128

Having successfully converted $Pb_3(C_6H_5O_7)_2 \cdot 3H_2O$ to PbO, a number of other samples were reacted at different temperatures with varying heating regimes to determine the degree of alteration to the composition as well as the microstructure these may have. Three examples of these experiments were analysed in depth. Their heating parameters are displayed in Table 5-3.

***Table 5-3**: Sample combustion-calcination experiments with varying temperatures and heating rates*

Sample	**Temperature (˚C)**	**Heating Rate (˚C/min)**
1	400	50
2	410	30
3	430	30

All samples were held for one hour at their target temperatures before cooling and processing for analysis. XRD results for samples investigated under the parameters listed in Table 5-3 demonstrated similar diffraction patterns to those shown in Figure 5-4. The different heating regimes did, however, appear to alter the microstructure of the PbO in the sample and are shown in Figure 5-7.

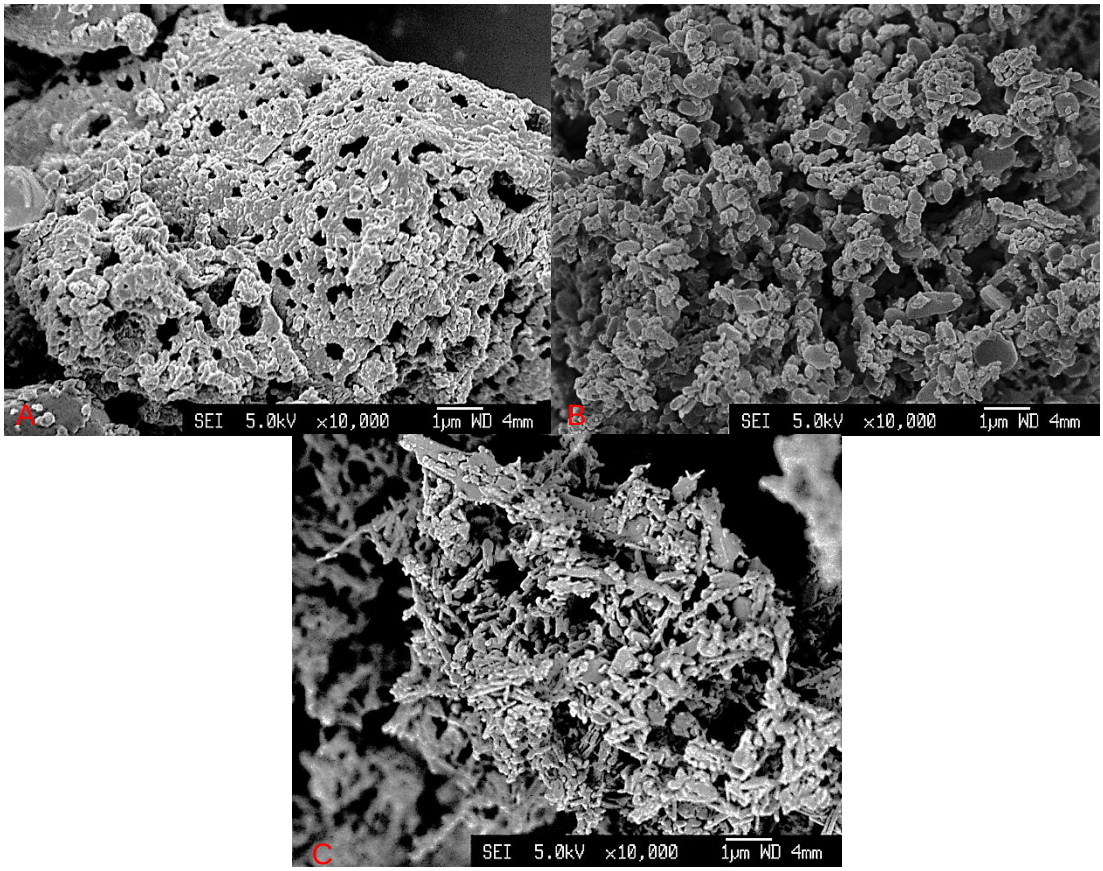

Figure 5-7: *SEM micrographs of samples 1 (A), 2 (B) and 3 (C)*

The SEM images shown in A to C in Figure 5-7 illustrate samples 1 to 3 respectively. Sample 1 displays a porous, sponge like structure with a degree of agglomeration. Sample 2, displays a more open structure with a distribution of spherical particles and coarse agglomerates with varied particulate sizes and well-defined particles.

Sample 3 produced a distribution of slightly elongated and spherical particles forming an open structure with a reduced particulate size distribution of smaller and more defined particles compared to samples 1 and 2. The small incremental changes in the heating temperature and their corresponding heating rates appear to have a notable effect on the microstructure.

This may be attributed to the rate of citrate removal as a result of the heating rate, thereby giving rise to a potential relationship between the rate of citrate removal at a given temperature of reaction and the type of microstructure produced that is preferential for the given conditions.

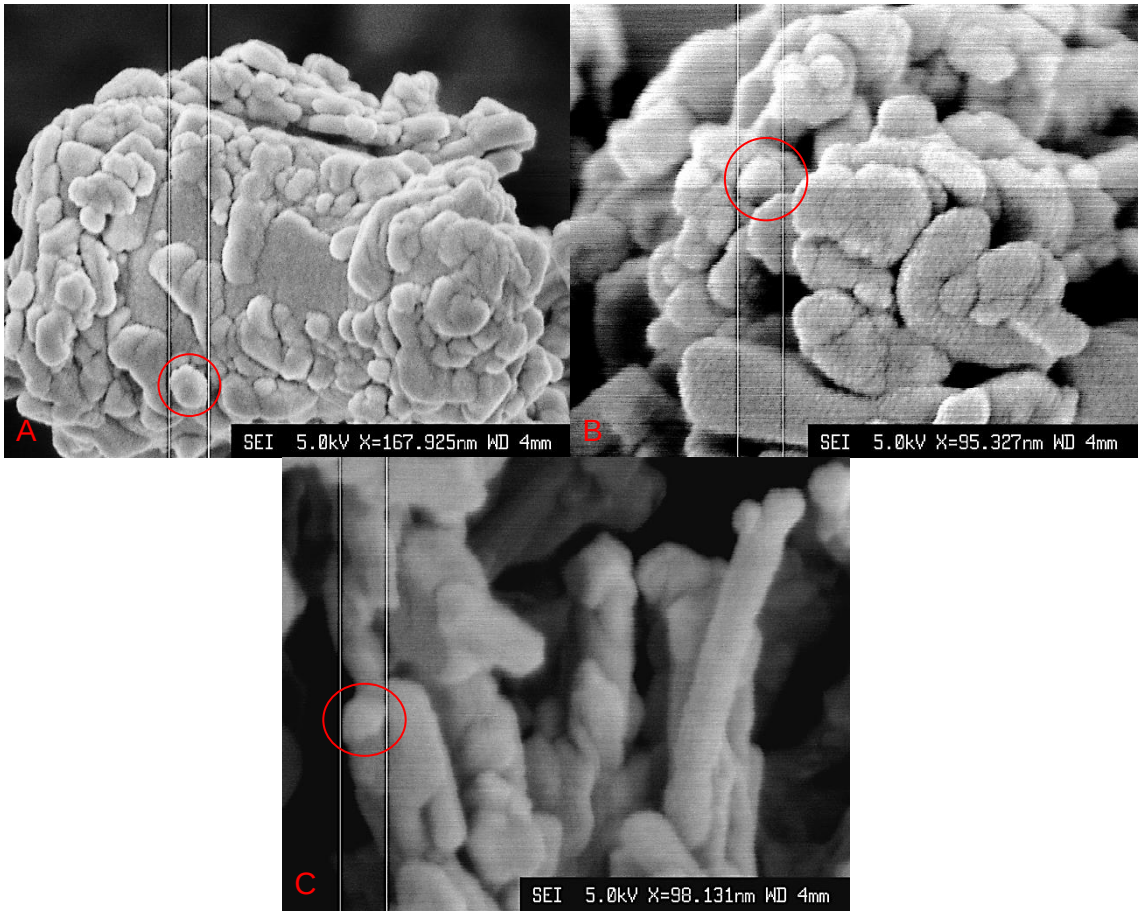

***Figure 5-8**: SEM micrographs of samples 1 (A), 2 (B) and 3 (C)*

Images A to C in Figure 5-8 illustrate the diameter of a primary particle from each of sample 1 to 3 measured using SEM. As described earlier, the structures became more open from sample 1 to 3 leading to an exposed and porous structure with elongated particles in sample 3. This is corroborated by the measurements made on each sample.

The diameter of primary particles showed a variety of sizes, for example, images in Figure 5-8 illustrate micrographs of sample 1, 2 and 3 having particle sizes of ~900, ~320 and ~130 nm respectively. However, there is a high degree of primary particles in each sample with a measured particle size distribution of 60-80 nm, an example of which can be seen in Figure 5-9 below.

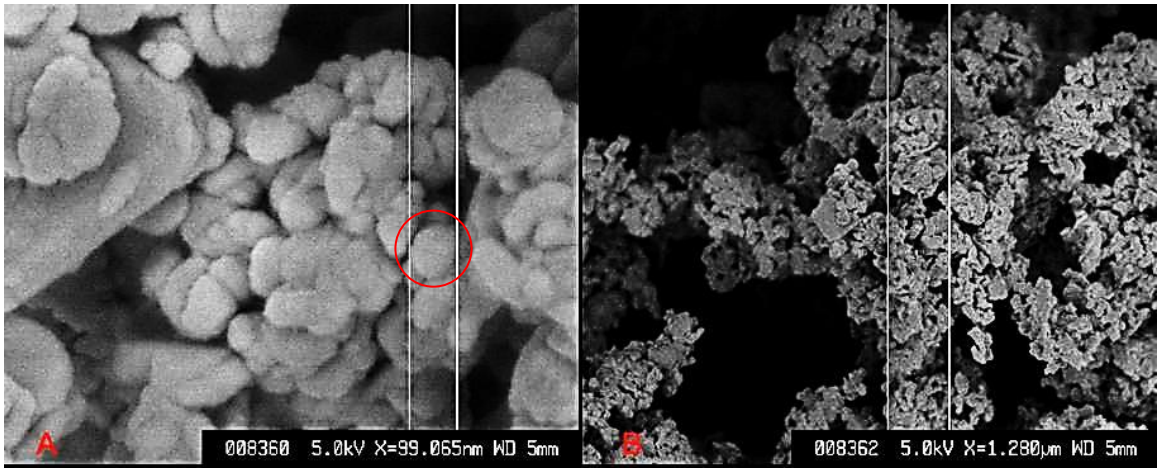

***Figure 5-9**: SEM micrograph of PbO powder heated to 430 °C at 5 °C/min*

The measured particle size in Figure 5-9A is 65 nm taken from a sample that was heated to 430 ˚C at 5 ˚C/min. It can be observed from SEM micrographs that there is a wide distribution of particle size and shapes in all samples manufactured by the hydrometallurgical method.

The elongation of particles displayed in sample 3 could be the result of inter-particulate coalescence at its early stages. At this higher temperature, the small particles start to form together, eliminating particulate boundaries thus reducing the overall surface area to volume ratio as they agglomerate. As agglomeration proceeds with increasing temperature the surface energy of the system will tend to decrease and preferentially form these rods.

The three samples listed in Table 5-3 of PbO powders were further characterised by XRD with their resulting diffraction patterns used to calculate their crystallite size using the X'Pert Highscore Plus software. Though the shape of crystallites is usually irregular, it is often possible to calculate a mean value.

The SEM images shown above indicate a number of irregular shapes, but on average the observed particles are noted to be spherical. Indeed, most applications of Scherrer analysis assume spherical crystallite shapes[117]. The value selected for the Scherrer constant K was therefore 0.89, the shape factor for spheres.

It is important to note that crystallite size is different to particle size as a particle may consist of several different crystallites. However, in many cases crystallite size matches grain size[117].

Diffraction peaks between 30 and 50 degrees 2θ were used, as peak asymmetry below 30 degrees 2θ compromises profile analysis[117]. Calculated crystallite size for each sample are shown in Table 5-4.

***Table 5-4**: Calculated crystallite size of samples 1 to 3*

Sample	**1 (400 ˚C)**	**2 (410 ˚C)**	**3 (430 ˚C)**
Crystallite size (nm)	41.4	41.2	41.2
	55	41.6	55.1
	32.8	42.2	55.3
	41.8	34.6	35
	34.6	29.8	36
Average size (nm)	41.1	37.9	44.5

The calculated average crystallite size for each sample is consistent with the size of primary particles observed in the SEM micrographs for all three samples, indicating that crystallite size and particle size are indeed largely the same in the present case. The particle size found is significantly smaller than those generated by either the Barton Pot or the ball mill processes, 3-4 mm and 2-3 mm[13] respectively.

It must be noted that any such formula as the one used in the determination of the above results for crystallite size can only give approximate estimates of particle size, and in fact little significance can be attached to the precise value of the constant K, since it is not expected that the particles will be all the same size and that such a method is within 20-30% accuracy[118]. Overall, the results do fit well with what has been observed of the primary particle size of samples along with a wide distribution of particulate size within the nanometre scale.

The apparent density is defined as the weight per unit volume of the PbO and includes not only the solid particles, but also the volume of the pores between them[13]. The apparent density of PbO is an important parameter used to monitor and control the operating conditions in the PbO manufacturing process, as the value is affected both by the ratio between fine and coarse grains, and by the amount of non-oxidised lead in the PbO powder. Table 5-5 shows the measured densities of samples 1 to 3.

***Table 5-5**: Measured densities for each PbO powder sample*

Sample	**1 (400 ˚C)**	**2 (410 ˚C)**	**3 (430 ˚C)**
Density (g/ml)	5.3	6.9	6.5

These apparent density values for each sample are notably higher than those of commercially manufactured PbO where they can range from 1.1 to 2.3 g/ml[13]. This difference in density values may be the result of the wide range of particle size distributions coupled with the significantly smaller average particulate size.

The result may also suggest a high ratio between fine and coarse grains which would have facilitated a more closely bound packing arrangement, thereby decreasing the volume occupied by a given mass of powder. This arrangement has been observed by micrograph images constructed by SEM, and these results indicate this arrangement is replicated throughout each sample.

The specific surface area of lead oxide is determined by both the particle size and shape. Both the surface area and pore size distribution are important factors in understanding the chemical and electrochemical processes that occur at the electrode and its interaction with the electrolyte in the lead-acid cell. The microscopic interfacial area has a dependence on the porosity and pore distribution within the active material of the electrode. Any changes to the electrode/electrolyte interface will have an overall effect on the performance of the lead-acid battery.

Figure 5-10 below shows BET isotherms reflecting the formation of the multilayer of gas adsorbed onto the surface of sample 1, building up due to the increase of P/P_0 and subsequently due to $V^{(95)}$. The linear isotherm plot illustrates a convex curve to the pressure axis over the range of relative pressures P/P_0 >0.2.

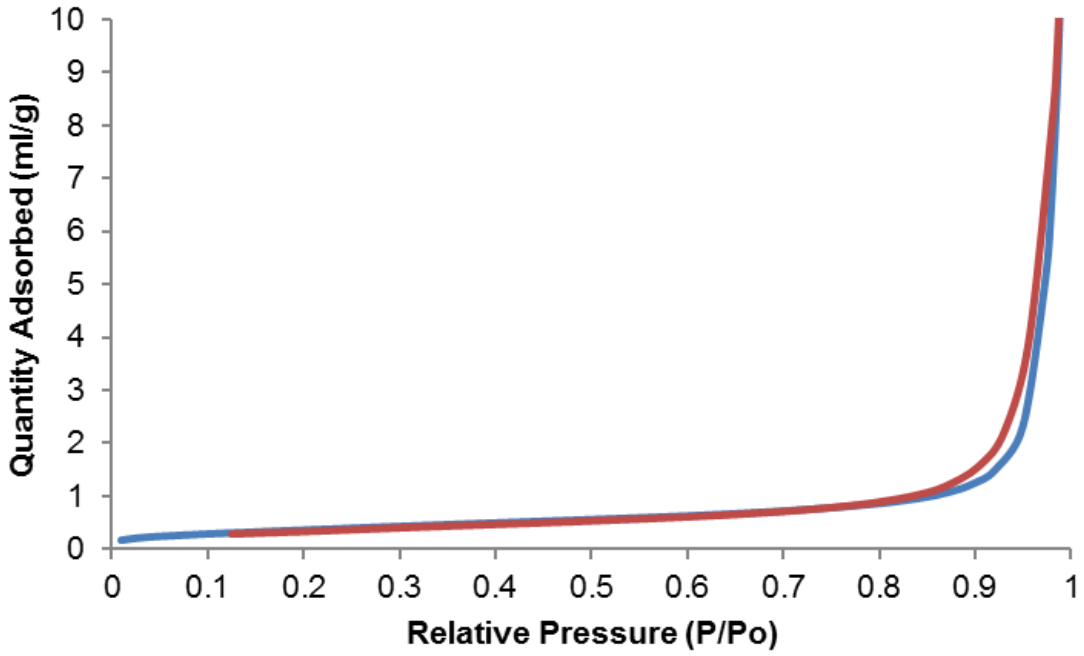

***Figure 5-10**: BET isotherm linear plot for sample 1, PbO powder heated to 400 ˚C*

It can be observed from the BET plot that there is no significant hysteresis loop in the N_2 absorption and desorption isotherm, therefore indicating that the majority of the pore sizes are smaller than mesopores. The increase in N_2 absorption at high relative pressures, typifies type II isotherms, indicates the presence of macropores in the sample.

Additional data collected can identify the specific gas-sample interactions by determining the value of C, which is related exponentially to the heat of adsorption in the first layer[96]. Figure 5-11 illustrates a linear BET surface area plot for sample 1.

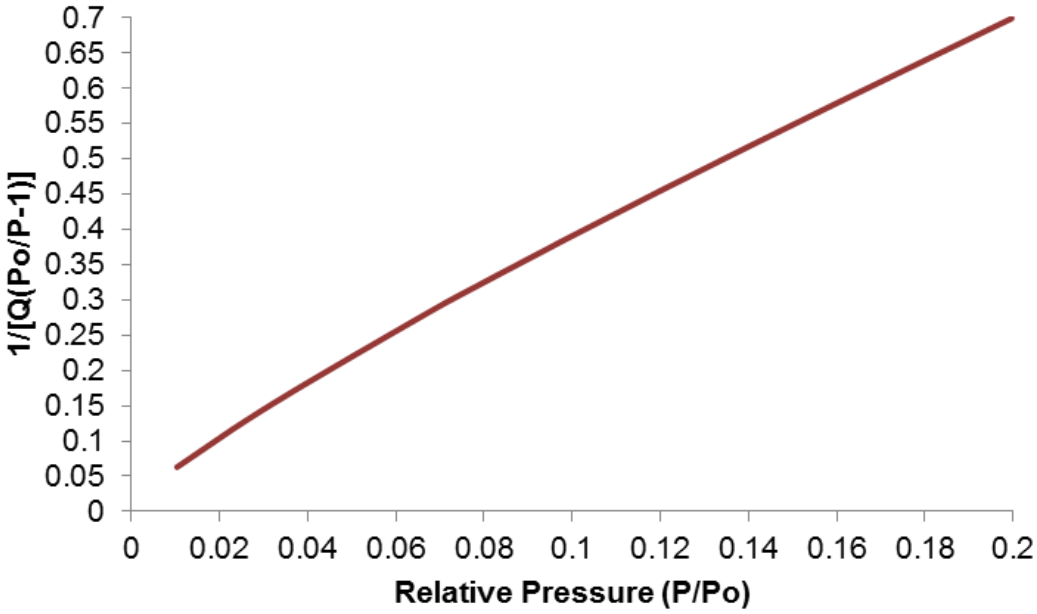

***Figure 5-11**: BET surface area plot*

The value of C as given in equation 5-1 can be determined from the experimental results by the following equation:

$$C = 1 + \frac{S}{Y} \qquad \textbf{5-1}$$

where Y is the intercept of the straight line and S is the slope of the straight line. If the value of C is high, i.e. >350, this indicates a strong gas-sample interaction and usually occurs at low relative pressures[96].

However, if the C value is low, i.e. <20, this indicates a weak gas-sample interaction that usually occurs at high relative pressures. The value for the C constant for sample 1 was calculated to be 199.3, which demonstrates good gas-sample interactions with adequate N_2 gas adsorption at the surface of the sample and further indicates an even monolayer along the sample surface.

BJH analysis was also conducted on each sample and this enabled the determination of the cumulative volume of pores as well as the average pore diameter within each sample, with the pore size distribution expressed by dv/dD against D. This analysis was based on the gradual removal of the condensed gas phase by the decremented lowering of the relative pressure during the desorption process. Figure 5-12 displays the BJH desorption dv/dD pore volume plot.

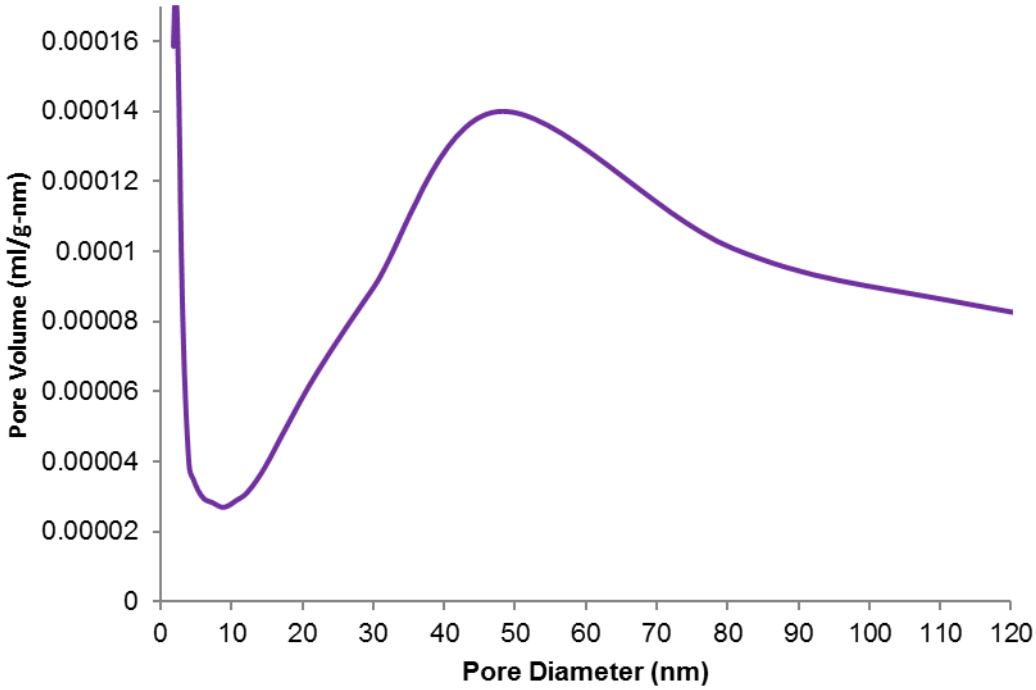

***Figure 5-12**: BJH desorption dv/dD pore volume*

Figure 5-12 illustrates the presence of a wide pore size distribution within the powder sample and clearly shows that the majority of the pore size is concentrated in the 40-50 nm range. The remaining samples displayed similar graphical characteristics to those of sample 1 shown above when analysed. The calculated BET surface area, porosity measurements and acid reactivity of samples 1 to 3 are shown in Table 5-6.

***Table 5-6**: BET surface area, BJH pore volume and size and acid reactivity of processed samples*

Sample	**1 (400 °C)**	**2 (410 °C)**	**3 (430 °C)**
BET Surface area (m^2 g^{-1})	1.6	2.7	3.4
BJH Cumulative pore volume between 1.7 nm and 300 nm (ml/g)	0.013	0.014	0.015
BJH average pore diameter (nm)	33.8	23.2	19.2
C constant	199.3	237.7	176.5
Acid reactivity (mg/g)	43.2	78.5	38.3

In the battery industry, in order to achieve a high specific surface, additional processes are introduced to generate finer grains, as spherical and flake-like particles are generally manufactured by the Barton pot and ball mill processes respectively. Since flat particles are preferred due to the higher surface area afforded by this geometry, PbO manufacturers subject the Barton lead oxide to additional grinding in hammer mills.

These energy intensive processes generate PbO with average specific surface, as measured by BET, of 0.7-1.4 m^2 g^{-1} for the Barton type and 2.4-2.8 m^2 g^{-1} for the ball mill type respectively[13]. The hydrometallurgical process employed in this study is highly efficient compared to the energy intensive mechanical processes currently in use in manufacturing PbO for LABs and has been demonstrated to produce PbO with comparable or, in the case of sample 3, higher surface area.

However, despite this, the acid reactivity from titration of these samples demonstrate very low values compared to samples heated to 350 °C at 5 °C/min of 128 mg/g. This may indicate, as was suggested by Boden[14], that an increase in surface area alone may not bring the benefits of enhanced electroactive reactions and indeed a combination of pore volume and median diameter may also have a significant contribution.

It must be noted however, that though the average particle size has been significantly reduced, which has been reflected in the density results, the absence in any significant change being translated into the specific surface area in this study further demonstrates the complex balance between, not only the size and shape of particles, but also their relative proportions and their respective degree of uniformity of packing in a given area.

However, the smaller mean particle size may prove more significant as the PbO will be homogeneously mixed with other precursor materials to form the active mass of a paste. This will create a more disperse arrangement of PbO and thus may potentially generate a greater number of accessible electroactive sites for electrolytic interface.

A more comprehensive combustion study was undertaken where six samples were heated to different target temperatures at the same rate of 5 °C/min and for 1 hour before cooling. A summary of the results obtained will now be outlined to demonstrate the degree of change that can be obtained as a function of reaction temperature.

Each sample was weighed before and after heat treatment to determine the percentage of mass loss as a function of temperature to compare with the TG-DSC analysis outlined earlier. Table 5-7 below shows the combustion-calcination temperatures of each sample with their corresponding mass loss after the reaction process.

***Table 5-7**: Combustion-calcination temperature with corresponding percentage mass loss*

Combustion-calcination Temperature (°C)	**Percentage of mass loss (%)**
335	35.5
370	35.8
410	37.4
430	36.3
450	36.1
550	35.2

As Table 5-7 illustrates, the percentage mass loss of each sample agrees well with the TG-DSC analysis. Therefore, it would be reasonable to assume that the reaction profile for these experiments followed that of those observed outlined in the TG-DSC analysis. All samples listed also showed XRD patterns showing good agreement with peaks corresponding to both polymorphs of PbO as well as metallic Pb as before.

SEM was used to image each sample to study their microstructure in order to examine any differences that may have resulted as a function of reaction temperature in air. In each figure lead citrate is shown as the reference precursor material (A) before combustion-calcination.

This is followed by the product produced after combustion-calcination imaged at x5000 magnification (B), the same as the $Pb_3(C_6H_5O_7)_2 \cdot 3H_2O$, to compare the transition from citrate to oxide. A closer examination of the microstructure was conducted under increased magnification at x10,000 (C) and x25,000 (D). Figure 5-13 illustrates the transition of lead citrate (A) after the combustion-calcination reaction to PbO (B, C and D) at 335 °C.

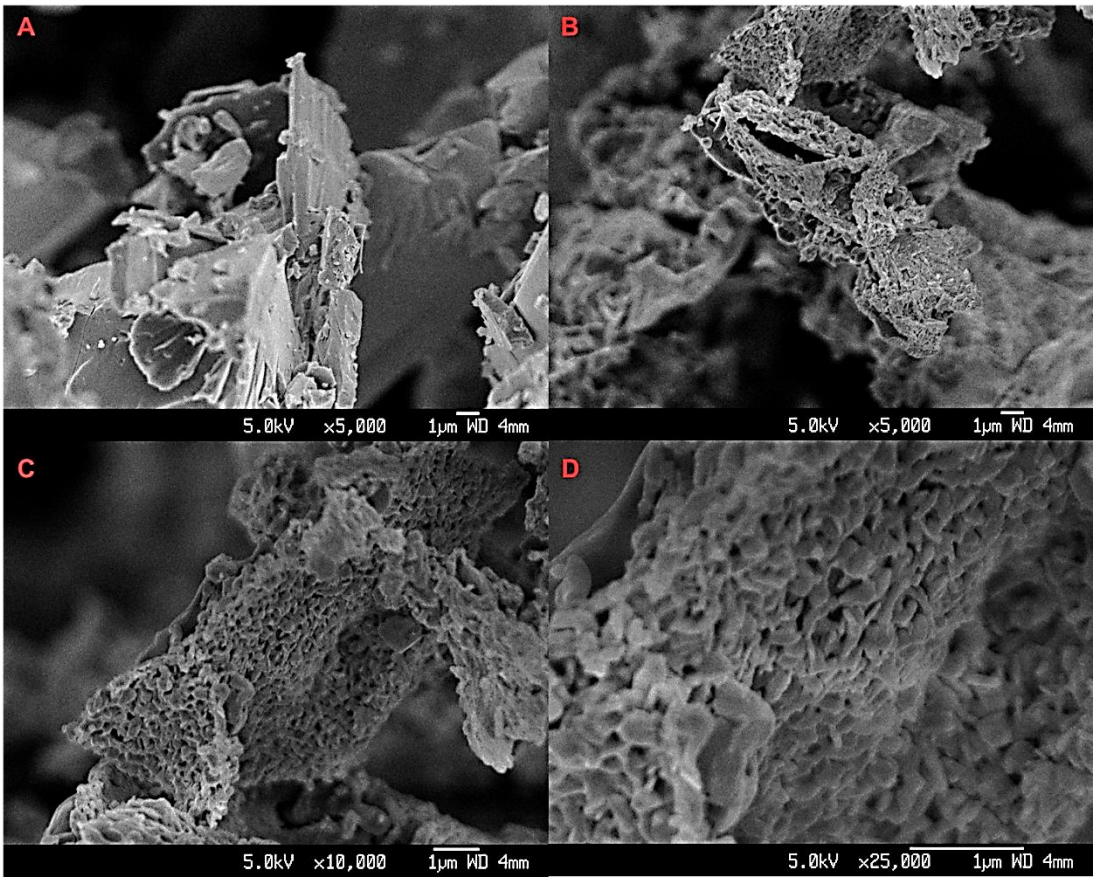

***Figure 5-13**: SEM images of $Pb_3(C_6H_5O_7)_2 \cdot 3H_2O$ (A) and PbO (B, C and D) after combustion-calcination at 335 °C*

The images presented in Figure 5-13 indicate a rather dense, branched, skeleton type structure.

The particles appear to be interwoven forming into distinct sheets which are themselves interlocked with other sheets with no distinct orientation. The surface layer of particles appears to be smooth and covered with distinct patches of pores left from the combustion of the citrate. The particle size distribution appears to be quite broad with primary particle size ranging in the tens of nanometres to fused particles in the hundreds of nanometres.

Figure 5-14 illustrates the transition of $Pb_3(C_6H_5O_7)_2 \cdot 3H_2O$ (A) after the combustion-calcination reaction to PbO (B, C and D) at 370 °C.

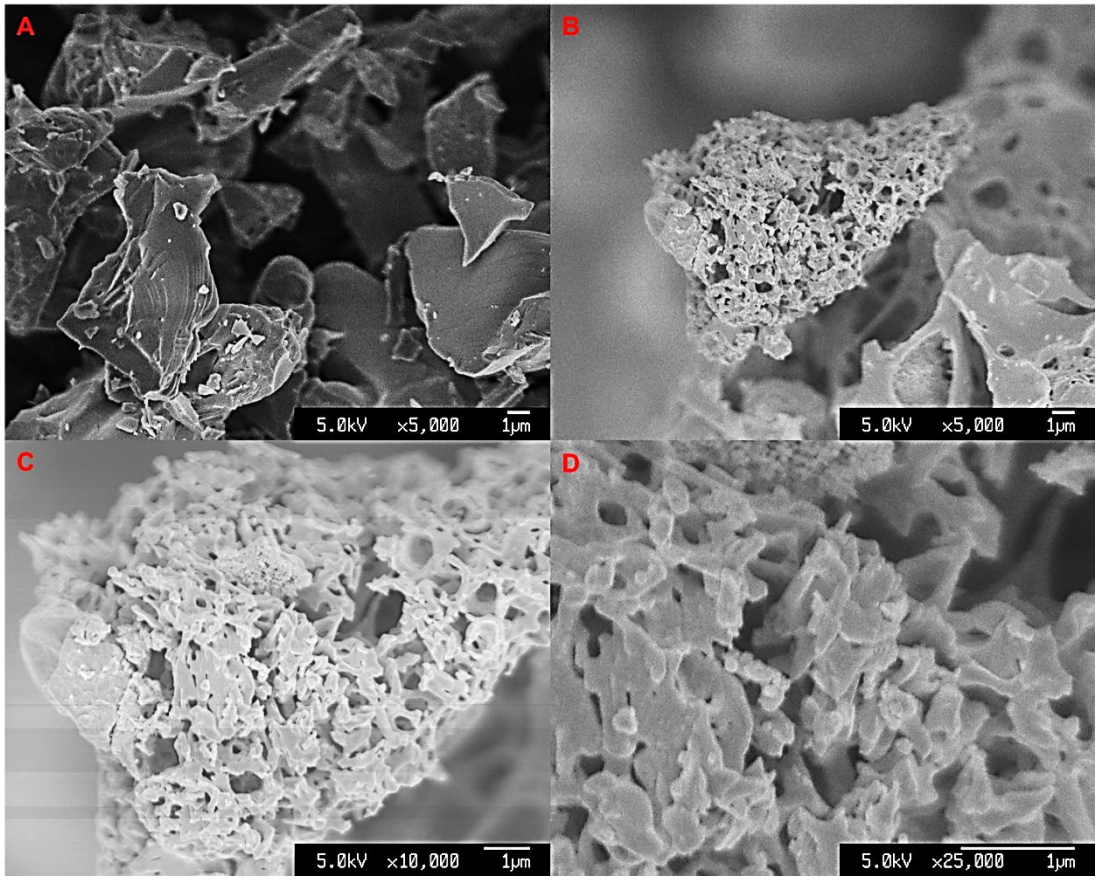

***Figure 5-14**: SEM images of $Pb_3(C_6H_5O_7)_2 \cdot 3H_2O$ (A) and PbO (B, C and D) after combustion-calcination at 370 °C*

The images in Figure 5-14 shows a slightly different morphology to that observed in Figure 5-13. The 370 sample shows a discontinuous microstructure with distinct overlapping plate-like structures.

A mixture of geometries with some branch-like structures including spherical and elongated arrangements can be seen. As with the 335 sample, measurements conducted using the SEM indicated a broad particle size distribution. This ranged from tens of nanometres with spherical particles, to hundreds of nanometres with elongated structures.

Figure 5-15 illustrates the transition of $Pb_3(C_6H_5O_7)_2 \cdot 3H_2O$ (A), after the combustion-calcination reaction, to PbO (B, C and D) at 410 °C.

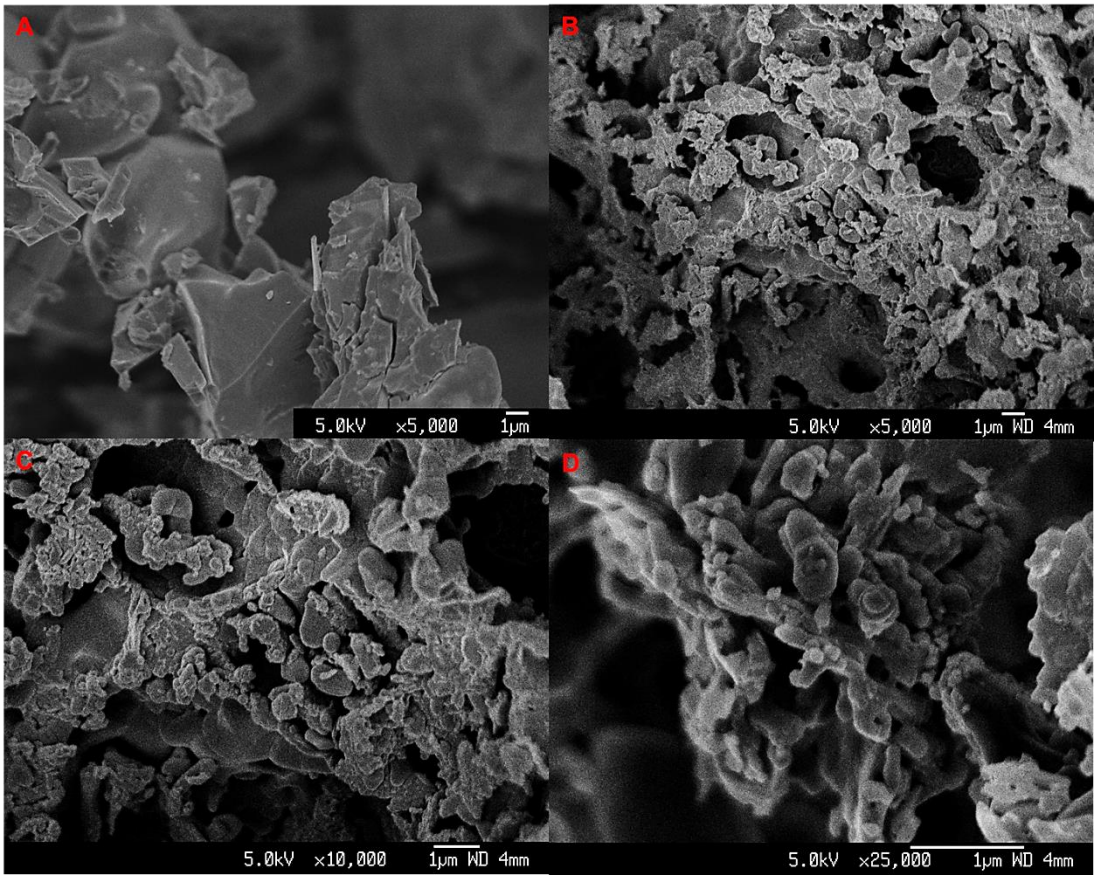

***Figure 5-15**: SEM images of $Pb_3(C_6H_5O_7)_2 \cdot 3H_2O$ (A) and PbO (B, C and D) after combustion-calcination at 410 °C*

The images illustrated in Figure 5-15 shows a slightly different morphology to that observed in Figures 5-13 and 5-14. The 410 sample shows a discontinuous microstructure with distinct interspersed clusters of agglomerates of various sizes. The trend in the size distribution continues with particulate sizes ranging from the tens of nanometres in the case of a large proportion of individual particles to large agglomerates and particles that are in the hundreds of nanometres.

There also appears to be a higher number of rounded, sub-rounded and angular particles of low sphericity compared to the previous 2 samples. A number of large distinct voids can also be observed from the combustion of the organic material.

Figure 5-16 illustrates the transition of $Pb_3(C_6H_5O_7)_2 \cdot 3H_2O$ (A) after the combustion-calcination reaction to PbO (B, C and D) at 430 °C.

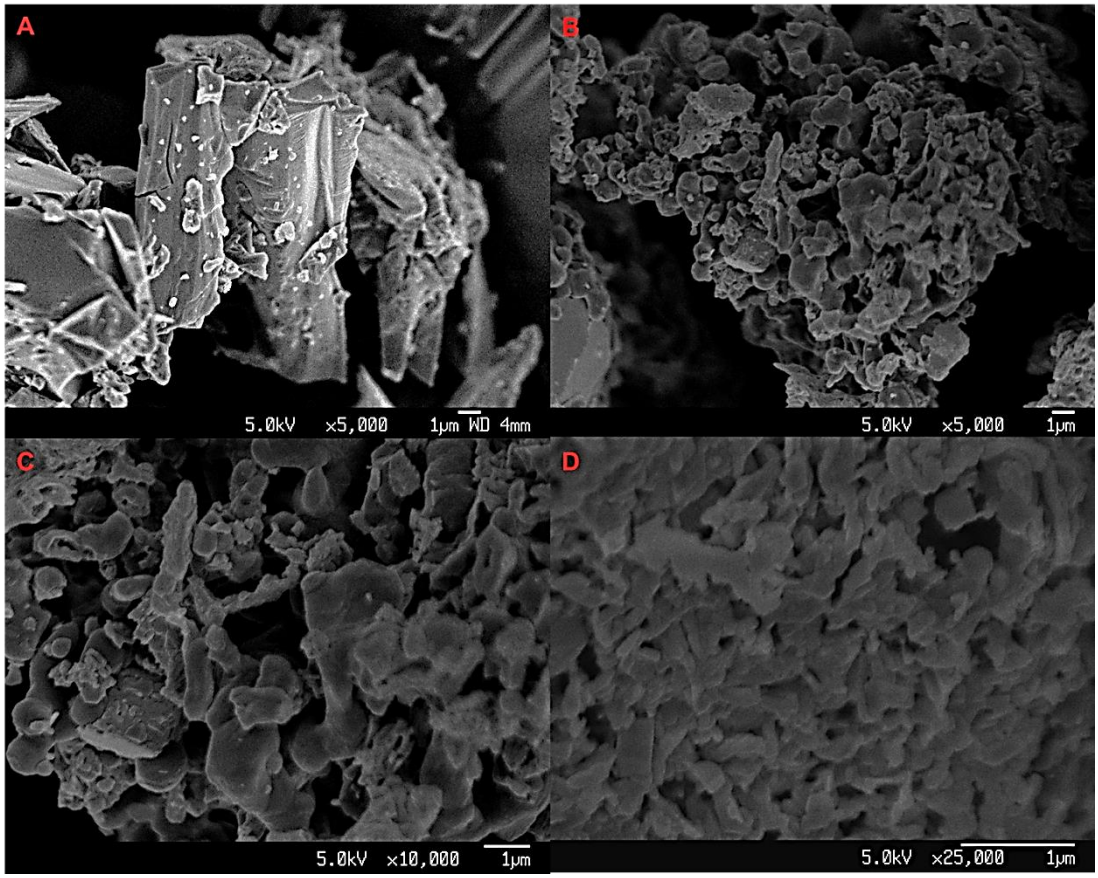

***Figure 5-16**: SEM images of $Pb_3(C_6H_5O_7)_2 \cdot 3H_2O$ (A) and PbO (B, C and D) after combustion-calcination at 430 °C*

A widely spread erratic distribution of shapes and sizes of particles are observed in the 430 sample, with some areas of continuity where particles have formed in close proximity to each other into woven-like sheets.

Irregular rod-like particles are also observed along with ellipsoidal, rounded and flake-like geometries closely situated with each other. These, again, range from tens to hundreds of nanometres in size.

Figure 5-17 illustrates the transition of $Pb_3(C_6H_5O_7)_2 \cdot 3H_2O$ (A) after the combustion-calcination reaction to PbO (B, C and D) at 450 °C.

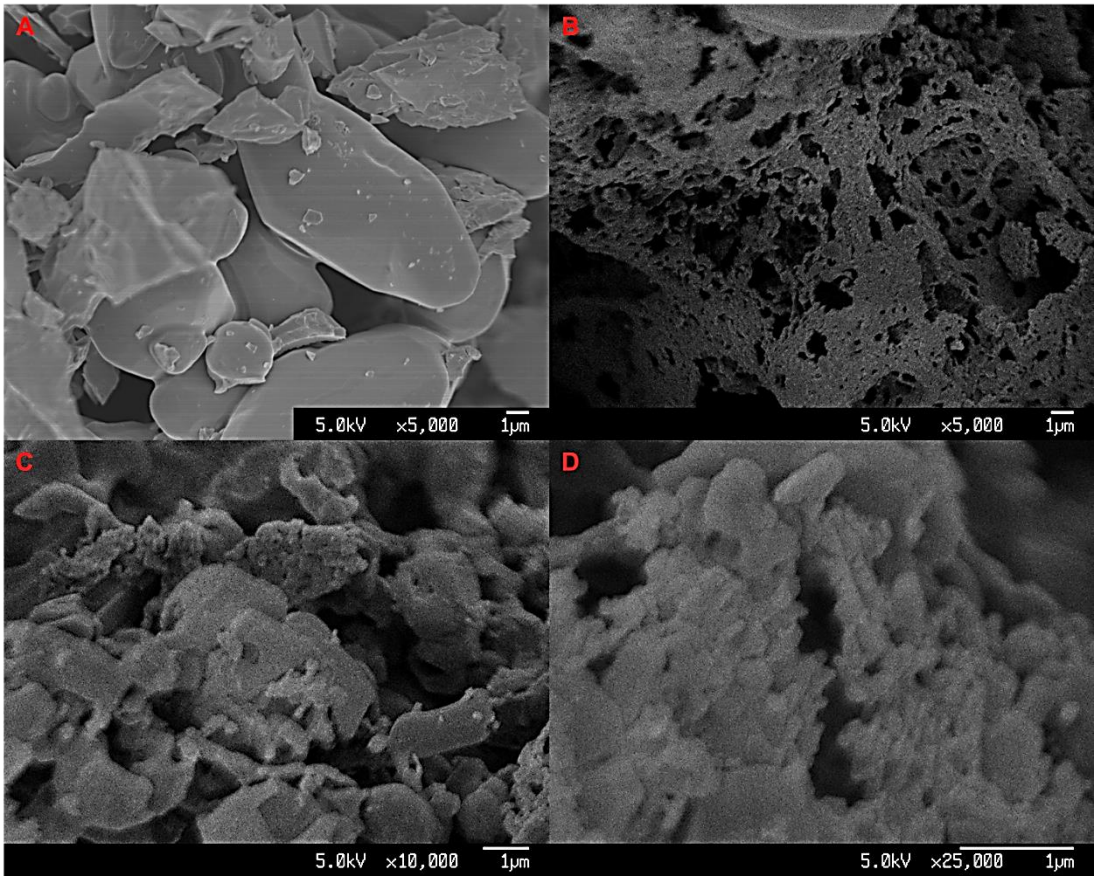

***Figure 5-17**: SEM images of $Pb_3(C_6H_5O_7)_2 \cdot 3H_2O$ (A) and PbO (B, C and D) after combustion-calcination at 450 °C*

The 450 sample is similar to that of the 430 sample with a wide distribution of shapes and sizes. However, as the low magnification micrograph in B shows, a thin spongy skeleton type structure has begun to form.

A wider distribution of pores and voids are also evident, with a higher degree of observable sintering as a result of the elevated processing temperature can be seen in micrographs C and D.

A wide range of shapes are again apparent as in the earlier samples, with many rounded, angular and irregular cylindrical particles fused together to form clusters of different sizes. This has given rise to large agglomerates hundreds of nanometres in size.

Figure 5-18 illustrates the transition of $Pb_3(C_6H_5O_7)_2 \cdot 3H_2O$ (A) after the combustion-calcination reaction to PbO (B, C and D) at 550 °C.

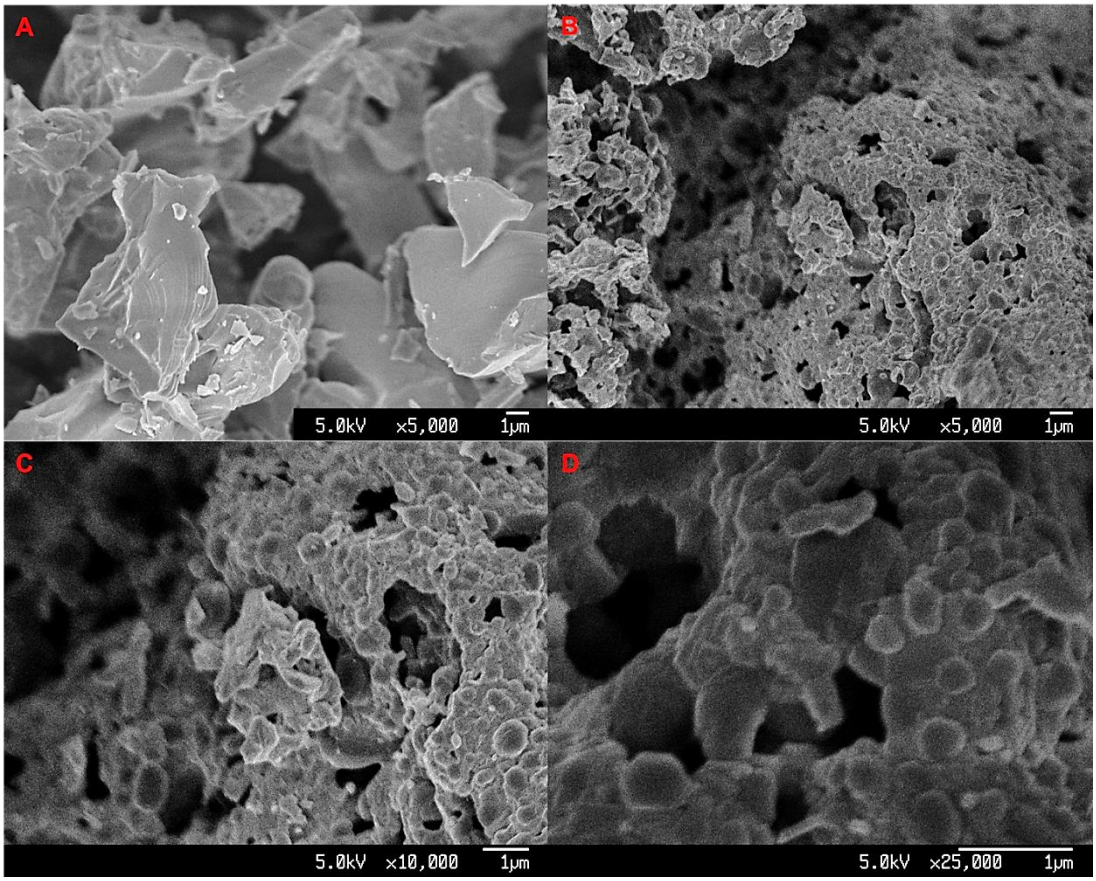

***Figure 5-18**: SEM images of $Pb_3(C_6H_5O_7)_2 \cdot 3H_2O$ (A) and PbO (B, C and D) after combustion-calcination at 550 °C*

A much higher degree of sintering is observed in the 550 sample as a result of the elevated processing temperature. The result of this is the formation of a continuous microstructure with a smooth textured surface. Clusters of protruding particles remain, but are fewer in number compared to previous samples. The distribution of primary particle shapes is dominated by spherical, sub-rounded, rounded and well-rounded geometries with a high degree of sphericity.

The general void size appears to be smaller and less numerous, with a lower degree of structural porosity as a result of sintering. While it is observed that primary particle size still remains in the tens of nanometres the continuous nature of the microstructure results in a macrostructure that is tens of micrometres in size. The calculated results of all samples from BET and BJH analysis are shown in Table 5-8.

***Table 5-8**: BET surface area, BJH pore volume and size of processed samples*

Sample (°C)	**335**	**370**	**410**	**430**	**450**	**550**
BET Surface area (m^2 g^{-1})	1.0	2.1	1.3	0.8	0.7	0.4
BJH Cumulative pore volume between 1.7 and 300 nm (ml/g)	0.005	0.0104	0.008	0.002	0.002	0.001
BJH average pore diameter (nm)	23.3	18.7	24.2	9.3	10.2	12.8
C constant	113.3	117.9	119.5	138.4	125.6	443.6

BET and BJH analysis points to a developing trend starting from the 370 sample. This indicates a lowering of surface area as a function of temperature with a corresponding decrease in pore size distribution. This may show that the combustion-calcination characteristics of this form of lead citrate maybe different to that examined earlier by the author.

The results may suggest that this form of lead citrate is more prone to sintering and may benefit from a lower dwell time, i.e. less time of exposure at temperature. Figure 5-19 displays the sintering process that would have occurred during combustion-calcination that would have led to the decrease in surface area and pore size distribution in some of the samples.

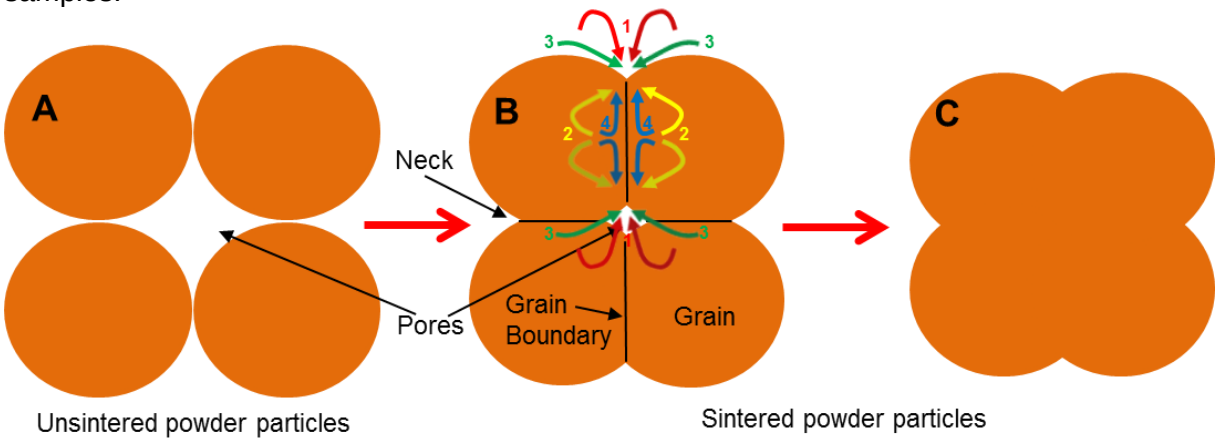

***Figure 5-19**: Stages of Sintering*

Diagram A in Figure 5-19 illustrates initial unsintered powder particles, experimental examples of which can be seen in SEM images previously shown. In B, the diagram details the diffusion mechanisms that occur during the sintering process:

(1) Vaporisation and solidification
(2) Volume diffusion
(3) Surface diffusion
(4) Grain boundary diffusion

As the powder particles begin to adhere to each other, they begin to form necks, grain boundaries and open pores at and in-between the inter-particulate interfaces. As seen in the SEM images earlier, specifically in the 335 and 370 samples where interwoven and interlocking sheets were detected, the initial stages of sintering are observed. The images show the formation of networks of open pores of various shapes and sizes. As sintering progresses, necks and grain boundaries evolve further and the number of open pores begins to diminish both in physical size and frequency, as observed with samples at higher processing temperatures.

As sintering proceeds further, the elimination of some pores begins, as illustrated in diagram C. It follows that with more sintering, the amount and physical size of pores in a given system will decrease and so therefore the surface area and the volume fraction of electroactive sites. Data gathered from SEM images, BJH and BET analysis for the combustion-calcination of this form of lead citrate, $Pb_3(C_6H_5O_7)_2 \cdot 3H_2O$, suggests that the proportion of particles of the type described in diagram C follows a linear increase via A and B as a function of temperature with a corresponding decrease in proportions of particles of the kind illustrated in A and B.

5.3 Self-sustained Combustion

5.3.1 Introduction

An investigation into possible environmental conditions that would allow a self-sustaining combustion of $Pb_3(C_6H_5O_7)_2 \cdot 3H_2O$ to generate PbO to take place was conducted after the intense exothermic peak observed in Figure 5-2 demonstrated the possibility of a self-sustaining reaction at around 328 °C. The aim was to find a more energy efficient and novel method of generating PbO.

5.3.2 Experimental

Samples of $Pb_3(C_6H_5O_7)_2 \cdot 3H_2O$ were placed evenly along the length of an alumina crucible boat and systematically heated from 200 °C at 10 °C increments at 5 minute intervals before one end of the powder was exposed to an ignition heat source. The minimum temperature and time was determined when the entire sample was assessed to have been thermally reacted to generate PbO.

5.3.3 Result and Discussion

The minimum temperature required, in static air, in order to initiate self-sustained combustion was found to be around 270 °C after ~15 minutes of dwell time. The form of combustion observed was that of smouldering, where a self-sustaining combustion front was observed to propagate across the powder. This is due to the exothermic oxidation of a condensed phase occurring on the fuel surface[119].

The process is self-sustaining because the energy released during smouldering is efficiently trapped and recirculated, thus further preheating the combusted powder ahead of the reaction front. As with typical smouldering combustion, the rate of reaction observed was slow as the heat response was limited by the rate of oxygen-transport to the surface of the $Pb_3(C_6H_5O_7)_2 \cdot 3H_2O$. Smouldering ignition requires the supply of heat flux to the solid fuel.

The subsequent temperature increase of the solid first sets off the thermal degradation reactions, mainly endothermic pyrolysis, and then oxidation, until the net heat released by oxidation is high enough to balance the heat required for propagation.

This net heat released by the reactions is partially transferred by conduction, convection and radiation ahead of the reaction and partially lost to the environment. The oxidizer is transported to the reaction zone by diffusion and convection, in turn feeding the oxidation reactions[120]. Once ignition occurs, the smoulder reaction advances gradually through the material.

Figure 5-20 shows the product of self-sustained combustion of $Pb_3(C_6H_5O_7)_2 \cdot 3H_2O$. The time to completion was observed to be ~35 minutes, giving the total processing time of ~55 minutes.

***Figure 5-20**: Self-sustained combustion of $Pb_3(C_6H_5O_7)_2 \cdot 3H_2O$ at 270 °C after ~35 minutes*

Although smouldering is characterised as a surface phenomenon, upon further investigation, due to the porous nature of the samples the smouldering was found to propagate into the interior of the citrate where they were permeable to flow.

As found in other studies on smouldering combustion[121, 122], the rate of propagation of the combustion front and net heat generated are affected by the velocity of air flow, pore diameter of the medium, and the fraction of porosity occupied by fuel, air and nonreacting materials. As illustrated in Figure 5-20 above, some carbon-based residue is left after combustion. This is due to the porous nature of the samples as the char minimises heat losses and enables the reaction to propagate.

The combustion characteristics may be improved in order to minimise the formation of carbon-based residue by the addition of an inert porous media that can provide the required insulation in the absence of fuel.

This would have to be a material that can be easily extracted after complete combustion or can be incorporated into the final PbO for electrochemical use. As observed in a study conducted by Ohlemiller[121] the initiation of the combustion process is dominated by kinetics of oxidation of the solid whereas the propagation is controlled, to a large degree, by the rate of oxygen transport to the reaction zone.

The control via transport rate occurs because the heat evolved during smouldering initiation raises the local temperature and thus the local reaction rate, until all of the neighbouring oxygen is consumed.

The reaction continues to consume oxygen as fast as it reaches the reaction zone, which lowers the local oxygen level, which limits the reaction rate. Given sufficient oxygen in the box furnace in the current study, this is in-line with what was observed with the rate of reaction increasing as a function of preheated temperature. For example, at 300 °C with an exposure time of 15 minutes, the combustion reaction was completed after 5 minutes.

In general, the smouldering combustion propagates in a creeping manner, and at its slowest was at a rate of 0.1 mm/s. Upon visual inspection, the overall green and yellow colour of the by-product would suggest a material dominated by the β polymorph when compared to the by-product generated from controlled combustion-calcination shown in Figure 5-3.

In order to confirm this, XRD analysis was conducted on the sample, together with another sample heated to the same temperature of 270 °C at 5 °C/min and held for 1 hour without the application of an external ignition source and are shown in Figure 5-21A and B respectively.

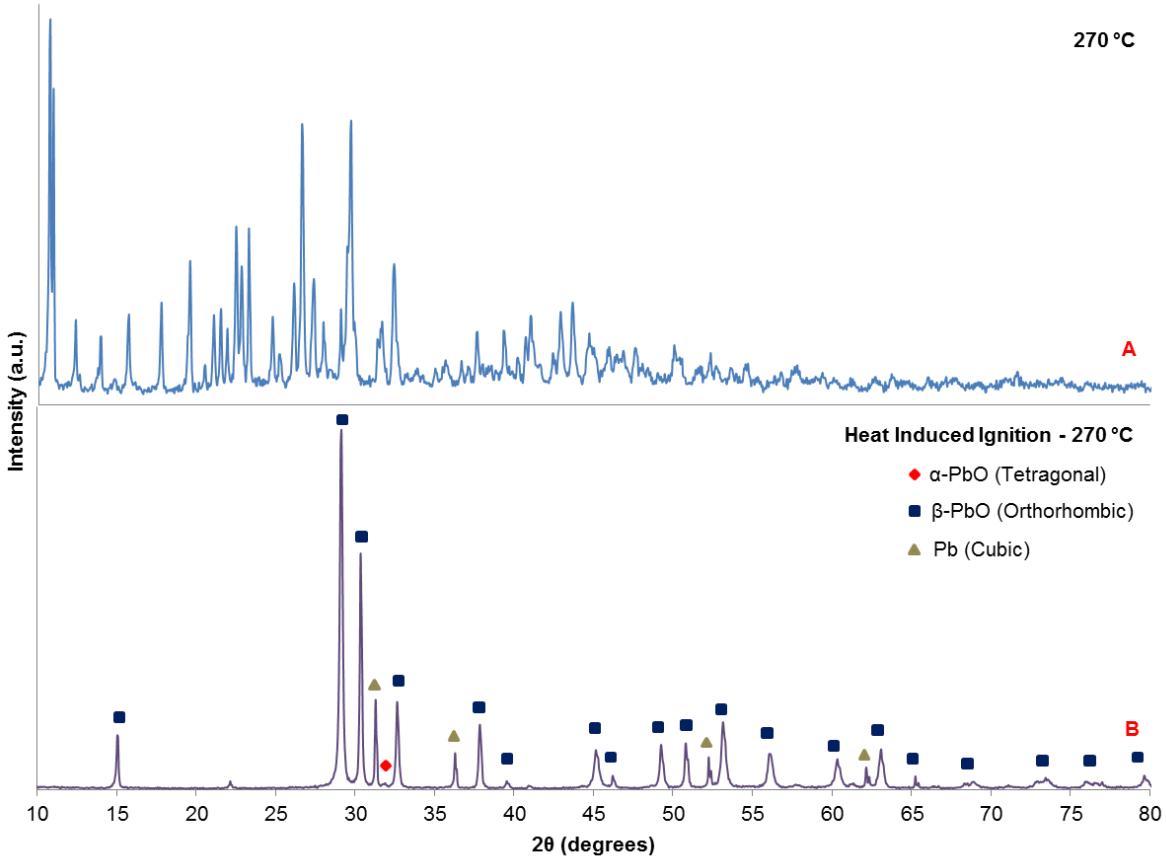

***Figure 5-21**: XRD patterns of $Pb_3(C_6H_5O_7)_2{\cdot}3H_2O$ heated to 270 °C (A) compared to another with an external heat source applied (B)*

As shown in Figure 5-21, $Pb_3(C_6H_5O_7)_2{\cdot}3H_2O$ is capable of fuelling its own combustion from 270 °C through to completion once an external source of heat is applied.

The self-sustained reaction was successful in generating PbO that is dominated by the orthorhombic phase with metallic Pb.

This is evident in Figure 5-21, where a sample is heated to the same temperature with a longer dwell time failed to react without an external heat source, shown in A, compared to B.

This may be beneficial as an active material in LABs as pure β-PbO has been reported to improve reproducibility in paste mixing and simplifies the curing process[14].

Figure 5-22 illustrates SEM images of $Pb_3(C_6H_5O_7)_2 \cdot 3H_2O$ (A) before and after self-combustion at 270 °C (B), (C) and (D).

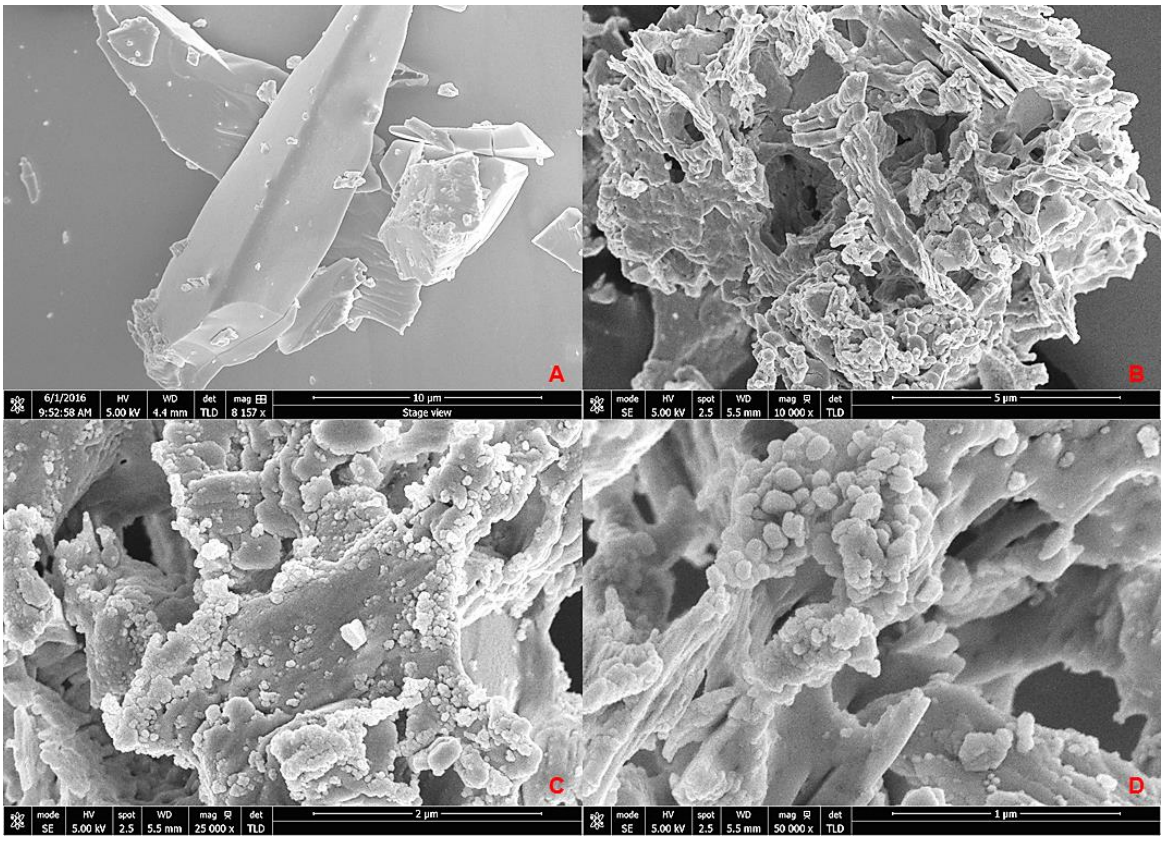

***Figure 5-22**: SEM comparison of $Pb_3(C_6H_5O_7)_2 \cdot 3H_2O$ (A) self-combustion at 270 °C forming PbO at x10,000 (B), 25,000 (C) and 50,000 (D) in SEI*

The microstructure illustrated in Figure 5-22 share similarities with that observed in Figure 5-5 for the controlled combustion-calcination at 350 °C at 5 °C/min for 1 hour. As seen in C, both samples have a general morphology consisting of a highly textured surface containing rounded and spherical particles ranging from tens to hundreds of nanometres in size. In addition, the surfaces of this sample appear to be smoother and generally denser.

However, as depicted in B, significant particulate elongation is apparent with a great variety of particle shapes, size and texture. On closer inspection, image D serves to highlight the complexity of the microstructure formed with large, smooth sintered surfaces collocated with round and spherical particles between 100-200 nm in diameter.

The microstructure is characterised by a collection of irregular, discontinuous and distorted nanostructures mixed with areas of high density and porosity with distinct interspersed clusters of agglomerates of various size. Table 5-9 details the surface area, pore volume and diameter, apparent density as well as the acid reactivity of the sample.

***Table 5-9**: BET surface area, BJH pore volume and size, apparent density and acid reactivity of PbO sample from self-sustained combustion at 270 °C*

Sample	**270 °C**
BET Surface area (m^2 g^{-1})	0.74
BJH Cumulative pore volume between 1.7 nm and 300 nm (ml/g)	0.054
BJH average pore diameter (nm)	159.1
C constant	62
Acid reactivity (mg/g)	111.3
Apparent density (g/ml)	9.6

The low measured surface area together with a good recorded acid reactivity adds to the suggestion of the important role of the pore volume and median diameter has on the acid absorption and therefore potential electroactive performance of manufactured PbO. The apparent density for the sample closely matches that of β-PbO, 9.72 g/ml[14], which further corroborates both visual and XRD analysis of the by-product.

This self-combustion process adds a new avenue of approach to the third stage of the recycling process. This not only provides a more energy efficient option for synthesis, but also a potential continuous process for industrial production.

5.4 Electrochemical Testing of Generated PbO

5.4.1 Introduction

The paste manufacturing process is very important as battery performance and life are determined by the properties of the paste. The main objective in paste preparation for both the anode and cathode is to generate and control particles of defined shape and composition.

These particles form the foundation of the paste which will eventually be electrochemically converted into the active material during the formation process which will yield the electrodes of the lead-acid cell. The formation process is preceded by a curing process, during which the particles are interlocked into a porous mass with the electrode to which it has been applied.

The way the paste is applied to the electrode/current collector is also important to reduce the variability in both the weight of paste in the electrode and the thickness of the pasted electrode. The wet, pre-cured, and cured pastes produced from the three PbO powders processed under different conditions were analysed to compare and contrast their effect on the formation of the porous electrochemically active mass.

5.4.2 Experimental

The physical differences in the PbO powders resulting from the variation in the processing meant that the formulation and time of mixing had to be altered to account for the unique physical characteristics that each sample possessed. PbO powders generated from $Pb_3(C_6H_5O_7)_2 \cdot 3H_2O$ outlined in Table 5-3 were used to generate 3 anode paste mixtures for electrochemical testing.

This was to determine their potential viability for use in a new electrochemical cell. The content and relative mass fraction of each compound used in each mixture was based on conventional formulations of anode paste materials from industry and literature[54, 59, 123]. Table 5-10 outlines the compounds with their corresponding percentage by mass in the pastes made.

Table 5-10. *Content and percentage by mass in anode paste mixtures*

Component	% Mass
Lead oxide (PbO)	68.7
Carbon black	0.2
Lignosulfonate (lignin)	0.2
Sodium Sulphate (Na_2SO_4)	0.1
Graphite	0.1
Hydroxy propyl cellulose (HPC)	0.2
Barium sulphate ($BaSO_4$)	0.5
Water (H_2O)	20
Sulphuric acid (H_2SO_4)	10

The weighed components were subjected to dry and wet mixing using water and H_2SO_4. The mixture was blended for 2 and 6 minutes respectively in a mortar and pestle followed by more water and acid additions until a paste was created. A portion of each sample was cured in a RCOM Suro incubator at 40 ˚C with a humidity of 90-100% for 72 hours consistent with battery paste curing procedure outlined by Pavlov and Kapkov[124].

A portion of each cured paste material was characterised with another portion of the wet pastes applied to graphite tubes and cured in the incubator forming the working electrode for electrochemical analysis. Pre-cured, cured and electrochemically investigated paste materials were analysed at each stage to monitor any physical changes to each sample.

5.4.3 Results and Discussion

In general, the following was observed and postulated during the mixing process: when water is added to PbO, it first infiltrates the porous structure of the particles and then begins to coat them. The oxide continues to absorb water, the rate and degree of absorption was noted to depend on the physical characteristic of the PbO powder and thus time of mixing became dependent on this factor.

The absorption of water continues until all the particles are coated and water has displaced the air that was among the particles. At the sites of contact between the particles a wedge of liquid is formed, this wedge forms water rings on the surface of partially wetted particles in the contact regions, these rings exert a cohesive force which hold the separate particles together in a loose system.

Water is essentially used as a pore melting agent during paste preparation[13]. Particles held together by the wedge liquid form capillary spaces.

The forces acting in these spaces flood the capillaries with liquid. A plastic state is reached characterized by a definite density and consistency, which allows the paste not only to be applied uniformly onto electrodes but also to be retained there. Figure 5-23 illustrates the liquid-particle system in the paste.

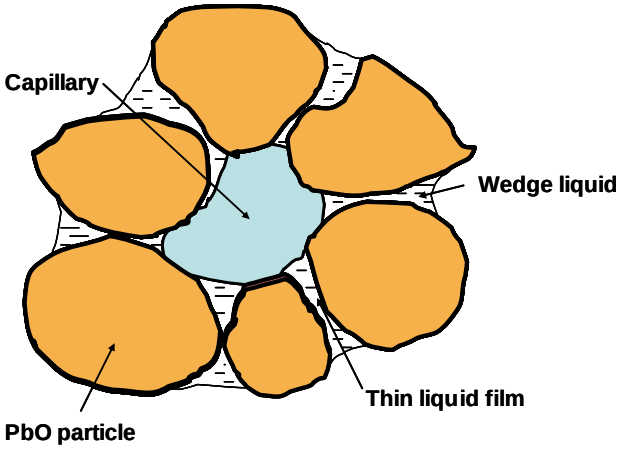

***Figure 5-23**: Liquid-particle system in the PbO paste*

At this stage, the paste is a firm mass which will not flow unless force is applied to it. The addition of more water forces the oxide particles apart, causing bulking of the paste and an improvement of flow characteristics.

Eventually, water fills all open spaces among the particles and the paste reaches its maximum plasticity. If water is added beyond this point, the paste becomes loose and increases the solid/liquid surface energy resulting in heat evolution.

There appears to be a critical limit in which the amount of water added exceeds the liquid film between particles holding them together, which grows in thickness. The bonding between particles is then weakened and the entire system thus transforms into a suspension.

The pH of the paste at this stage is between 9 and 10, indicating that a reaction is taking place between oxide and water. This could be due to the formation of lead hydroxide ($Pb(OH)_2$), releasing OH^- ions to the solution.

Once acid is added to the mixture, heat is evolved and the paste notably stiffens. Additional application of acid changes the plasticity and texture of the paste with a corresponding increase in temperature. This is assessed to be the result of thermal effects of the chemical reactions, the heat of dilution of the H_2SO_4 and the mechanical work of mixing the paste creating friction between particles. When the acid initially interacts with the wet PbO, it is likely that it reacts to form $PbSO_4$.

The amount of water added to each mixture had to be modified slightly from that of the stated formulation as the powder characteristics varied from sample to sample. For instance, sample 2 appeared to have a physical structure that was able to absorb a greater amount of water. This may have the effect of decreasing its wet density and increase its plastic flow characteristics as the paste becomes less viscous as a result.

Such variability as a direct result of method of manufacture, particle size and shape among many other factors has been well documented by Prout[54]. It is this variability that has allowed the LAB to compete in a wide spectrum of applications, as this yields a wide range of allowable optimizations for different applications from deep cycle batteries used as power storage on wind and solar farms to SLI batteries in combustion engines.

The chemical composition and element distribution of a given area were analysed to determine the degree of homogeneity after mixing the precursor materials together with each PbO powder.

The even distribution of all precursor materials is important as it not only allows the quality of mixing to be gauged, but also gives an indication of the degree of homogeneous formation of the porous mass after curing. This is essential as a uniform distribution of precursor particles throughout the paste ensures an even level of porosity, active surface and hardness of the active mass and of its connection to the electrode. Figure 5-24 illustrates a number of EDS micrographs of the principal elements present in sample 2 and their distribution after mixing.

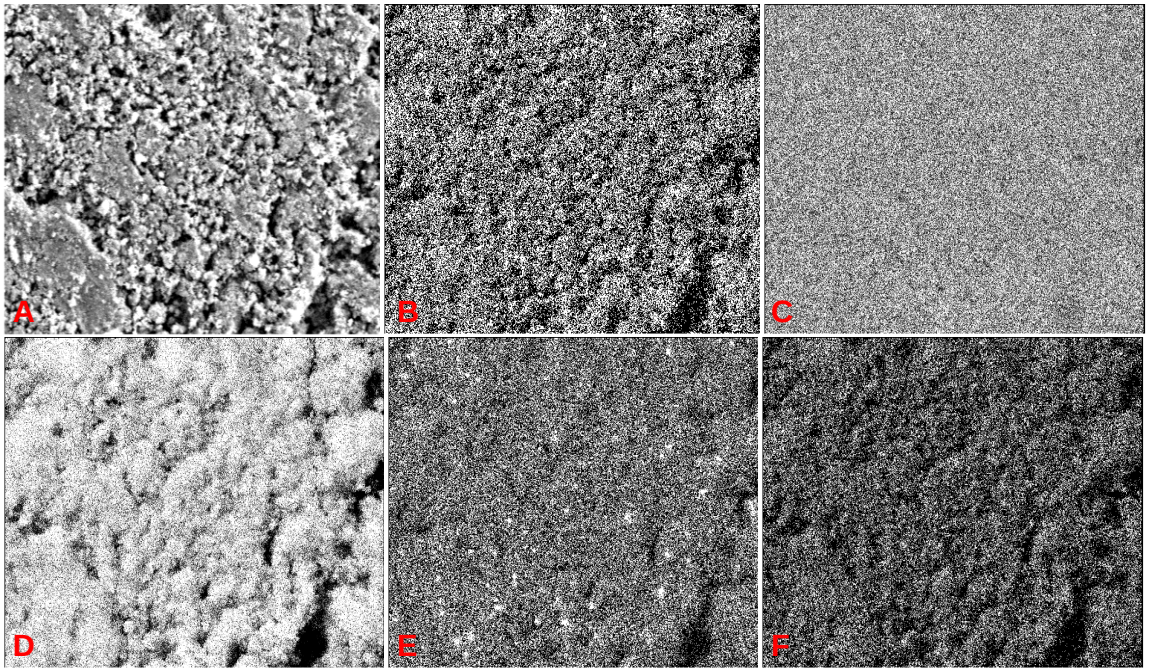

***Figure 5-24**: SEM images and EDS micrographs of element distribution in sample 2 after wet mixing. Micrograph A is a SEI of a selected area with distribution of carbon shown in (B), lead in (C), sulphur in (D), barium in (E) and sodium in (F)*

Micrographs in Figure 5-24 labelled A to F are of a selected area of the surface of a pre-cured paste mixture containing PbO powder that was heated to 410 ˚C at a heating rate of 30 ˚C/min (sample 2).

Micrograph A is a secondary electron image of the selected area with B to F illustrating a pixel by pixel image based on chemical elements selected to be analysed which were carbon (B), lead (C), sulphur (D), barium (E) and sodium (F) respectively.

The micrographs show that each of the principal elements in the paste mixture to be well distributed and uniformly mixed with the slight exception of barium which has a few clusters concentrated in some areas. To illustrate the degree of intimate inter-particulate mixing further Figure 5-25 shows the element maps of lead, sulphur and carbon overlaid onto one map.

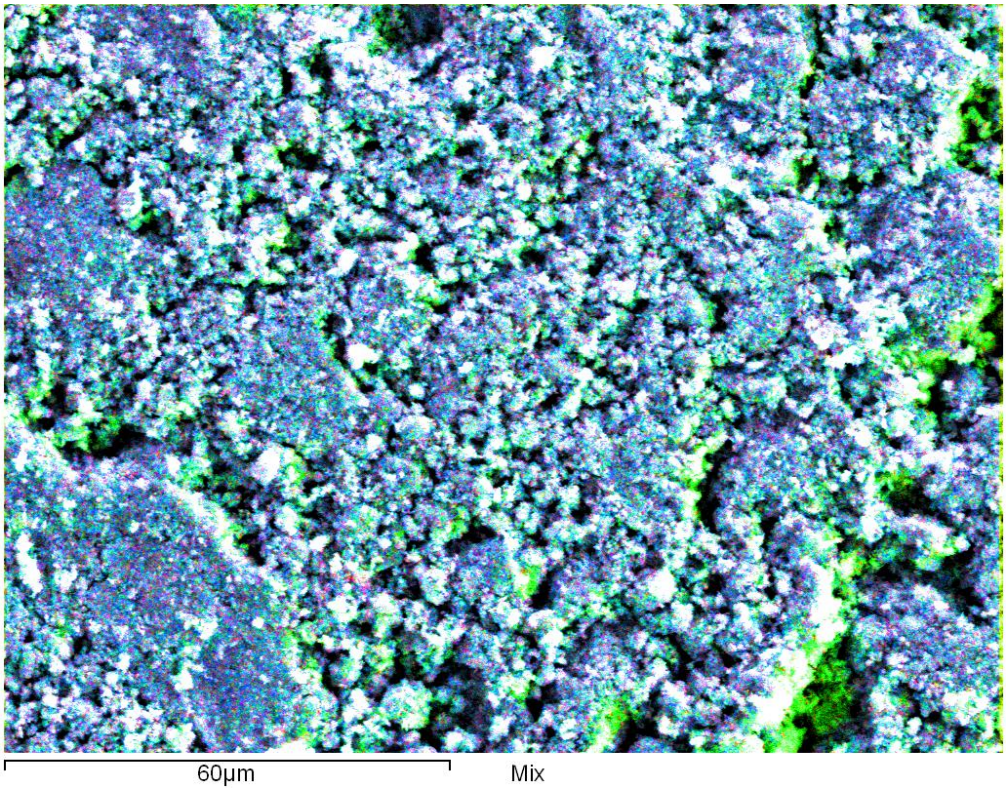

***Figure 5-25**: Element map overlay of carbon, lead and sulphur of pre-cured, sample 2, paste mixture*

Figure 5-25 illustrates the element maps of lead (blue), sulphur (red) and carbon (green) and demonstrates a well-mixed porous mass with some carbon accumulation at the particulate boundaries.

Sample 1 and 3 displayed similar results as that above, demonstrating good homogeneous mixing and enabled the next stage of curing to proceed.

The chemical composition and element distribution of a given area were again analysed to determine any changes to the degree of homogeneity of precursor particles throughout the paste material after curing. Figure 5-26 illustrates a number of EDS micrographs of the principal elements present and their distribution in sample 1 after curing.

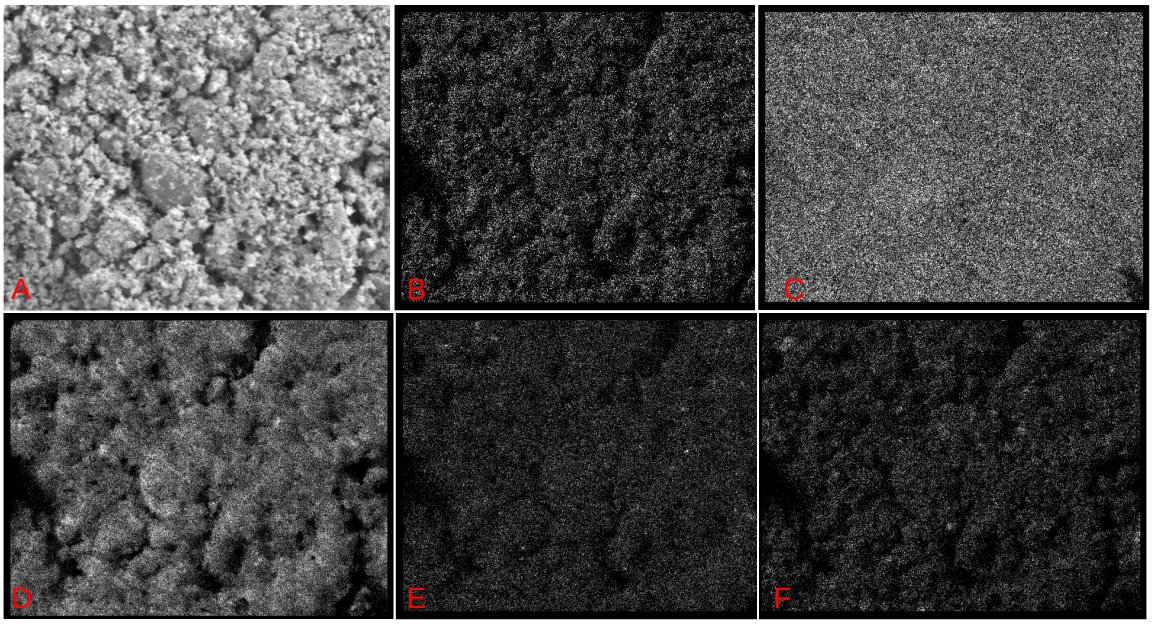

***Figure 5-26**: SEM image and EDS micrographs of element distribution in sample 1 after curing. Micrograph A is a SEI of a selected area with distribution of carbon shown in (B), lead in (C), sulphur in (D), barium in (E) and sodium in (F)*

Micrographs in Figure 5-26 labelled A to F are of a selected area of the surface of a cured paste mixture containing PbO powder that was heated to 400 ˚C at a heating rate of 50 ˚C/min, (sample 1). Micrograph A is a secondary electron image of the selected area with B to F illustrating a pixel by pixel image based on chemical elements selected to be analysed which were carbon (B), lead (C), sulphur (D), barium (E) and sodium (F) respectively.

The micrographs show that each of the principal elements in the cured paste mixture to be well distributed and has maintained its uniformity with the exception of sulphur which has a few clusters concentrated in some areas. To illustrate the degree of intimate inter-particulate mixing further, Figure 5-26 shows the element maps of lead, sulphur and carbon overlaid onto one map.

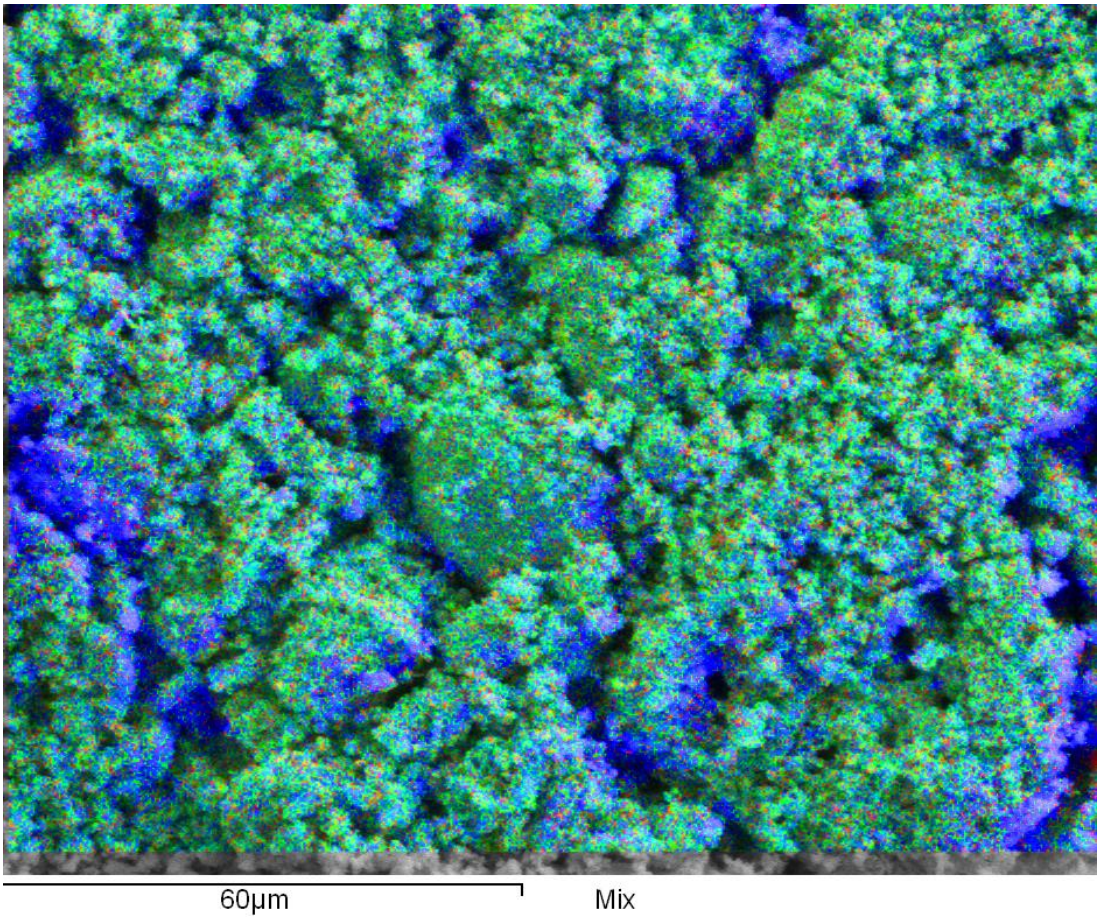

***Figure 5-26**: Element map overlay of carbon, lead and sulphur of cured, sample 1, paste mixture*

Figure 5-26 illustrates the element maps of lead (blue), sulphur (red) and carbon (green) and demonstrates a well-mixed interlocked porous mass with some lead enrichment at the particulate boundaries, which could be the result of segregation during curing.

In general, each mixture, samples 2 and 3, displayed similar results as that above, demonstrating good homogeneous distribution of interlocked particles in a porous mass with some preferential accumulation of PbO particles at the grain boundaries.

Secondary electron images (SEI) were captured of selected areas of both the pre-cured and cured paste mixtures to form a visual comparison of any physical changes that may have occurred on the surface of each mixture. Figures 5-27 to 5-29 illustrate both the micrographs of each sample in the pre-cured and cured states side by side, from sample 1 to 3 respectively.

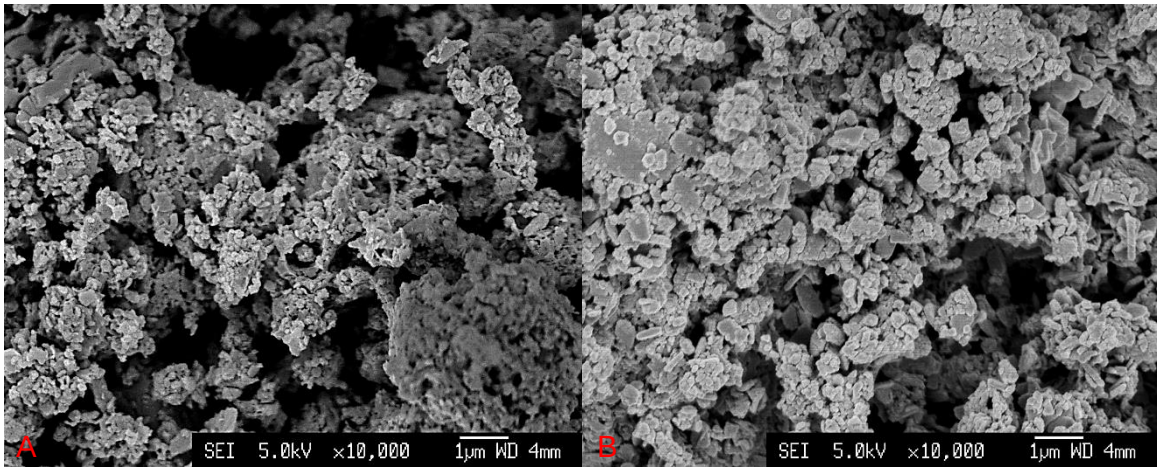

***Figure 5-27**: SEI of pre-cured (A) and cured (B) paste mixture of sample 1*

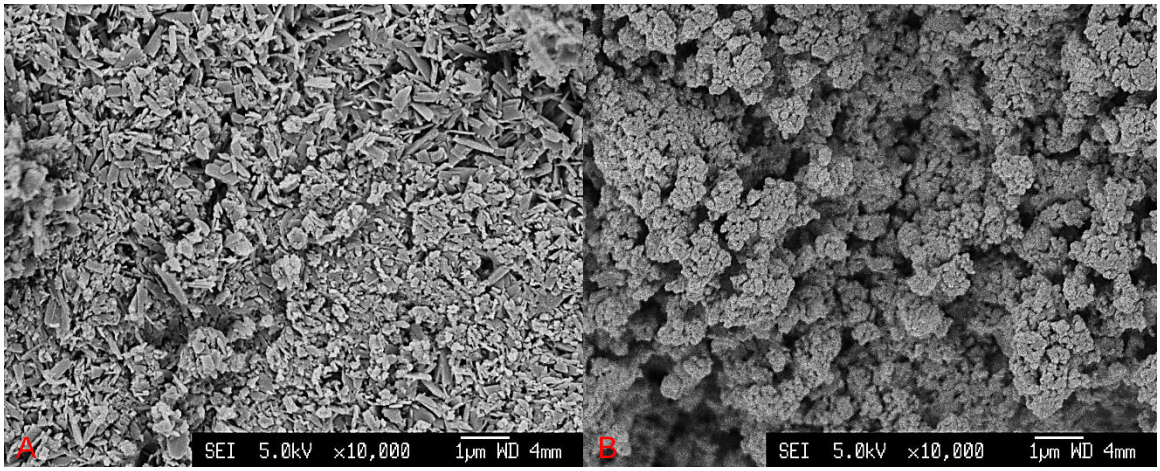

***Figure 5-28**: SEI of pre-cured (A) and cured (B) paste mixture of sample 2*

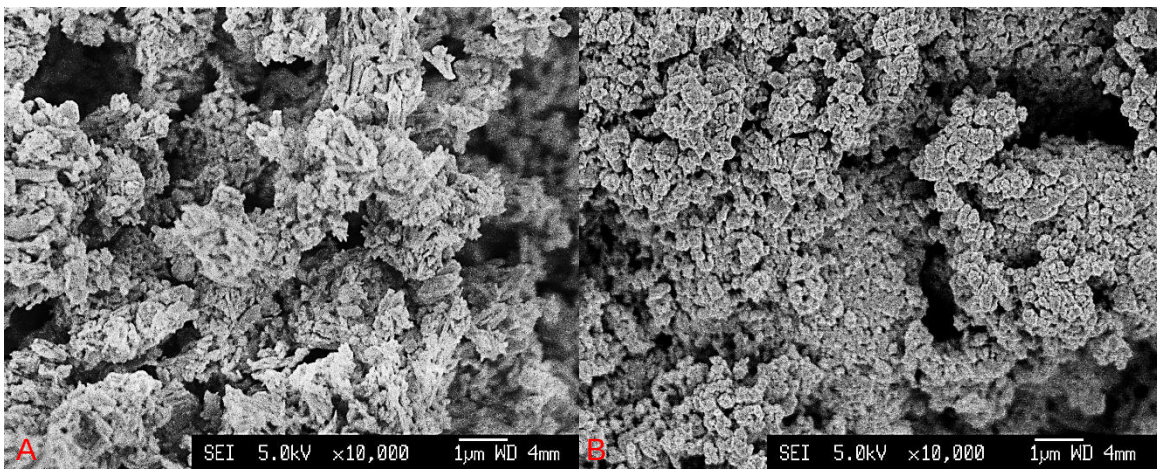

***Figure 5-29**: SEI of pre-cured (A) and cured (B) paste mixture of sample 3*

All three images display pre-cured micrographs, labelled A, and cured micrographs, labelled B, showing clearly that all cured samples had formed into clusters of uninterrupted interlocked particles in a porous mass.

Where there was individual needle like structures in the pre-cured mixture they have formed into smaller spherical, sometimes plate like particles coalesced together during the curing process. This is significant as it is the size of the paste particles that determines the porosity of the active materials.

Appropriate porosity ensures high specific active surface, adequate hardness of the porous mass and optimum pore distribution allowing easy access of ions from the electrolyte and water molecules to every part of the electrode volume.

The paste density is responsible for the porosity of the formed active masses, which in turn ensures large active surface and impacts on the capacity of the battery. Density of the paste determines the bonding between particles under static conditions. Wet paste densities used in industry for the “positive” electrode (the cathode in the fully charged state of the battery) are between 3.90 and 4.40 g/ml[54] and between 4.10 and 4.50 g/ml for the “negative” electrode (the anode in the fully charged state of the battery).

The changes in paste density have a slight effect on phase composition of the cured paste and of the formed active mass as well as on capacity performance; they do however exert a strong influence on battery cycle life. The cycle life is reported to be extended with increase of paste density[13].

Paste density is an important parameter to monitor as below a critical value the structure of the formed active mass will disintegrate, and above a critical value the pore system will not be capable of ion transport. The cured, solid phase density is between 6.5 and 8 g/ml.

***Table 5-11**: Pre-cured and cured paste densities*

Sample	**1 (400 ˚C)**	**2 (410 ˚C)**	**3 (430 ˚C)**
Pre-cured density (g/ml)	3.2	4	3.4
Cured density (g/ml)	5.75	5.91	5.9

The densities measured for both the pre-cured and cured pastes, shown in Table 5-11, are lower than that of those reported by industry. There are a number of factors that could affect the density of both phases of pastes. The parameters for curing used in the current study are one of many that are in current operation in the battery industry and other laboratories.

Different curing environments resulting from varying parameters, such as heat and humidity, result in differing mechanisms of reaction and formation that can occur in the paste mixture during curing. The mixture, composition and packing of the paste particles also play a role in the densification process.

The low experimental densities could also be the result of excess water in the initial mixture and will therefore need to be adjusted to gauge the effect on density and consistency. The difference in measurement procedure should also be taken into consideration.

During the curing process, a system of pores is created in the cured paste which determines the pore system of the active masses during the subsequent electrode formation phase. This pore system is one of the factors that determines the capacity and power performance of the battery.

Both the pre-cured and cured paste mixtures were characterized using BET and BJH analysis to compare and observe the effect of curing on the samples surface areas and porosities. As was observed in the SEM micrographs and reflected in the density measurements the paste particles in each sample interconnect into a skeleton of a hard-porous mass hence the increase in density.

It is expected therefore that the surface area will decrease from the pre-cured phase to the cured phase of transition as the pastes densify. It should be noted that the pre-cured paste had to be degassed and dried to enable the measurements to take place and therefore will not be a true surface area representation of wet paste mixtures.

All BET plots for the pre-cured samples were consistent with the standard type II isotherms, an example of which is shown in Figure 5-30. All BJH plots for the nanostructured lead oxide also displayed consistent characteristics, the results of which are illustrated in Table 5-12.

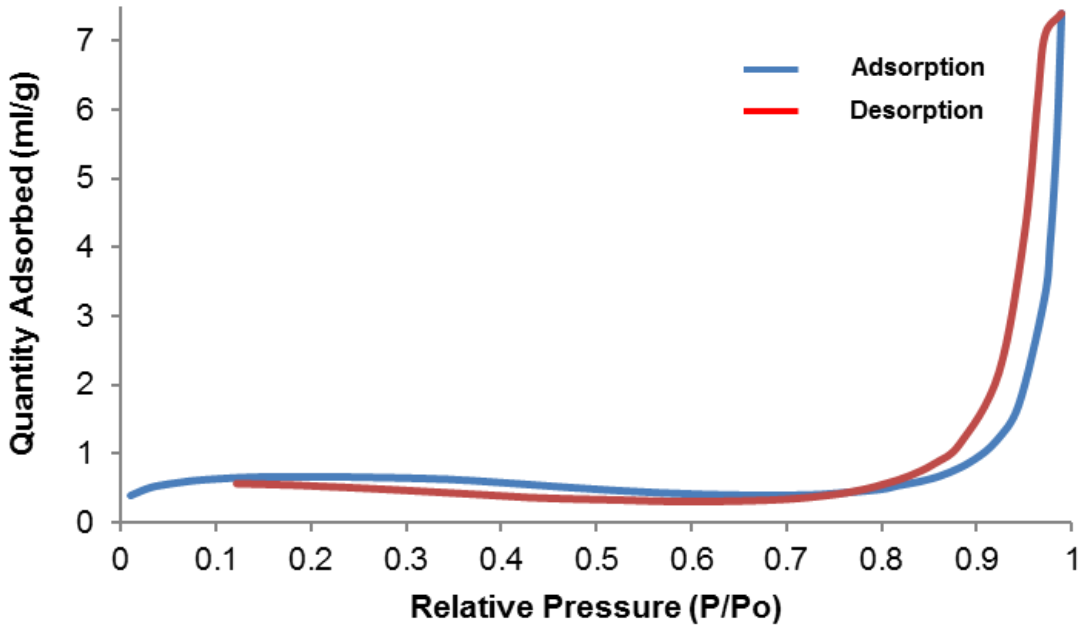

***Figure 5-30**: BET isotherm linear plot for pre-cured paste, sample 3*

Figure 5-30 and 5-31 shows BET isotherms indicating the formation of multilayers of gas adsorbed onto the surface of the pre-cured and cured paste mixture of sample 3, building up due to the increase of P/P_0. The linear isotherm plot illustrates a convex curve to the pressure axis over the range of relative pressures P/P_0 >0.1.

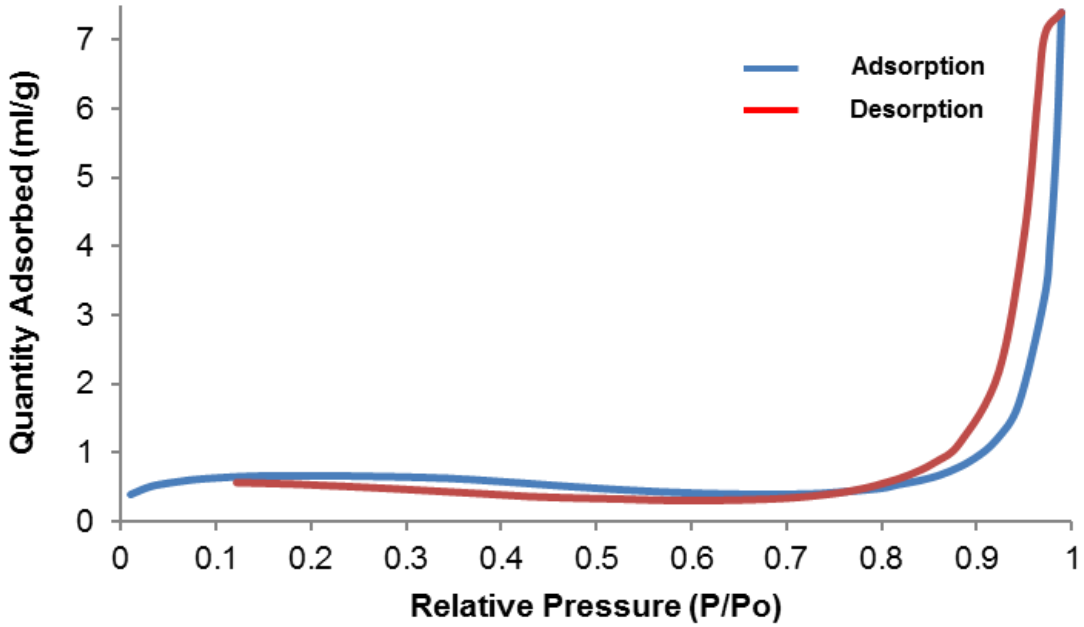

***Figure 5-31**: BET isotherm linear plot for cured paste, sample 3*

As previously mentioned, the shape of the isotherm is highly dependent on the nature of the gas-solid system. The amount of N_2 gas adsorbed per gram of sample depends on the surface area and porosity of the material as well as the temperature and the relative pressure of gas P/P_0.

It can be observed from the BET plot that there is no apparent hysteresis loop in the N_2 absorption and desorption isotherm, therefore indicating that the majority of the pore sizes are smaller than mesopores. The increase in N_2 absorption at high relative pressures, typifies type II isotherms, indicates the presence of macropores in the sample.

There is, however, a notable dip between 0.6 and 0.9 relative pressure in Figure 5-31 for the cured sample, which is replicated in all cured samples, and indicates that the quantity of absorption had decreased markedly and may indicate a smaller number of macropores from that of the pre-cured phase and also a decrease in surface area and porosity as was expected from the curing process.

The value for the C constant for sample 3 was calculated to be 2582, which demonstrates very strong gas-sample interactions with adequate N_2 gas adsorption at the surface of the sample and further indicates a significant monolayer gas distribution along the sample surface.

This contrasts with the same pre-cured sample which had a C constant of 79.4 which further illustrates the structural changes to each sample as a result of curing. The same trend was also noted for both sample 1 and 2, with less significant differences and displaying good to strong gas-sample interaction, shown in Table 5-12.

Figure 5-32 and 5-33 illustrate BJH desorption dv/dD pore volume plots on the pre-cured and cured sample 3 mixtures respectively.

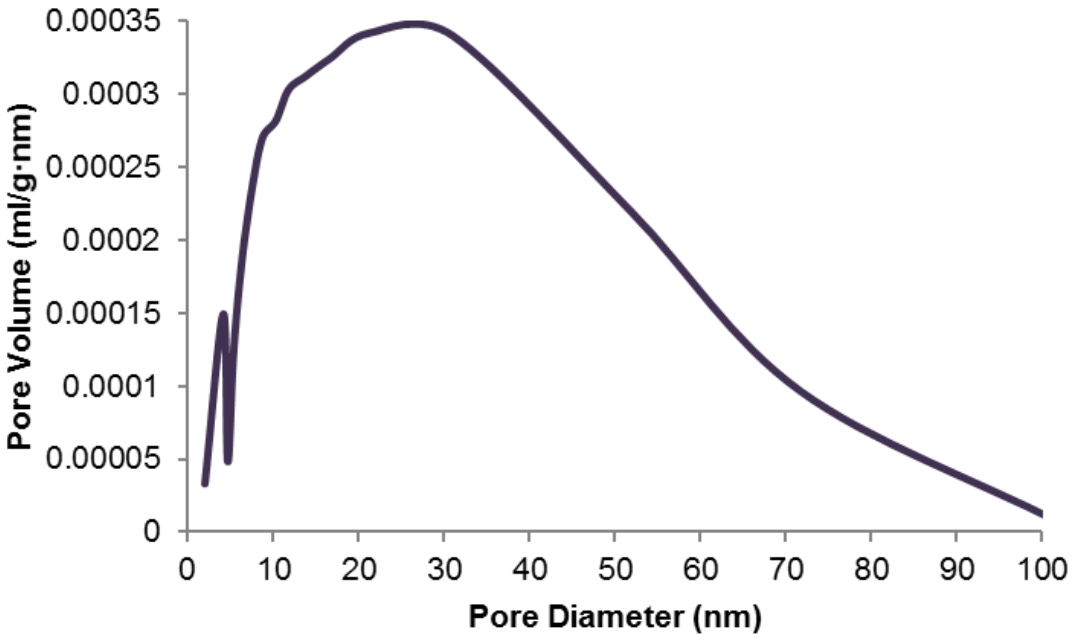

***Figure 5-32**: BJH desorption dv/dD pore volume of pre-cured sample 3 mixture*

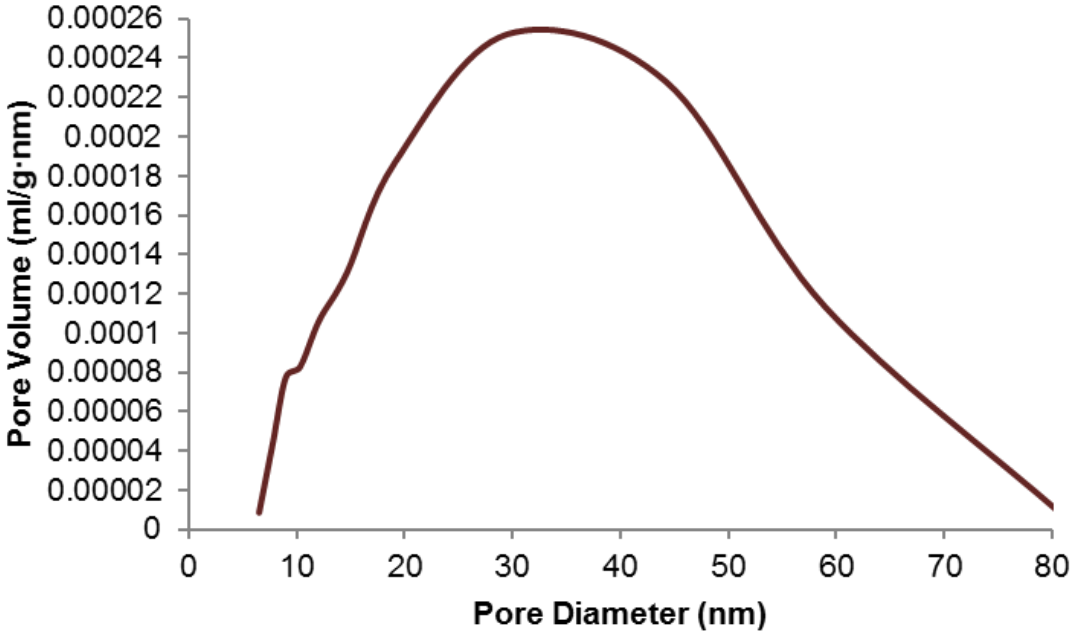

***Figure 5-33**: BJH desorption dv/dD pore volume of cured sample 3 mixture*

Both Figures 5-32 and 5-33 illustrate the presence of a wide pore size distribution within their respective samples. However, it can be observed that after curing the pore size range had narrowed, decreasing the upper size limit from 100 to 80 nm, and so too had the pore volume.

This again can be explained by particulate interlock, contracting the porous mass and decreasing the pore volume as the paste mixture densified during curing. Both sample 1 and 2 also displayed this behaviour and all results are shown in Table 5-12.

***Table 5-12**: BET surface area, BJH pore volume and size of pre-cured and cured paste samples*

Pre-cured sample	**1 (400 ˚C)**	**2 (410 ˚C)**	**3 (430 ˚C)**
BET surface area (m^2 g^{-1})	2.982	5.991	4.865
BJH cumulative pore volume between 1.7 nm and 300 nm (ml/g)	0.0121	0.0350	0.0203
BJH average pore diameter (nm)	21.6	28.4	23.7
C constant	131.7	125.6	79.4
Cured sample	**1**	**2**	**3**
BET Surface Area (m^2 g^{-1})	1.632	1.710	2.412
BJH cumulative pore volume between 1.7 nm and 300 nm (ml/g)	0.0069	0.0090	0.0114
BJH average pore diameter (nm)	26.67	31.07	29.34
C constant	365.1	325.4	2582.2

BET surface area of cured pastes used in commercial LABs can range from 0.3 to 1.6 m^2 g^{-1}[13, 125]. Surface area values around and above the upper limit of typical materials produced by industry have been achieved here with sample 3 demonstrating a superior BET surface area of 2.412 m^2 g^{-1}.

Although the density value of the cured paste mixtures may suggest a short cycle life, the surface area may point to better battery performance by providing high discharge current densities and increasing the specific capacity due to more accessible electro-active sites and the increase in the volume-fraction of active materials available.

Paste mixtures containing manufactured nanostructured PbO were examined with electrochemical techniques. The first technique used was a potentiodynamic sweep, which applies a potential between two specified points and measures the current as a function of the applied potential to the electrode.

The second was cyclic voltammetry, which measures the current as a function of applied potential and scan rate, swept in two directions.

In the current research, the electrochemical technique was employed to determine the property of nanostructure PbO produced from the citrate precursor.

A potentiodynamic sweep was used to determine the potential at which the PbO in the paste mixture reduces to Pb. This identified the formation potential required to reduce PbO to Pb to form the anodic electrode. Figure 5-34 illustrate a voltammogram for sample three, which typifies those seen in samples one and two also.

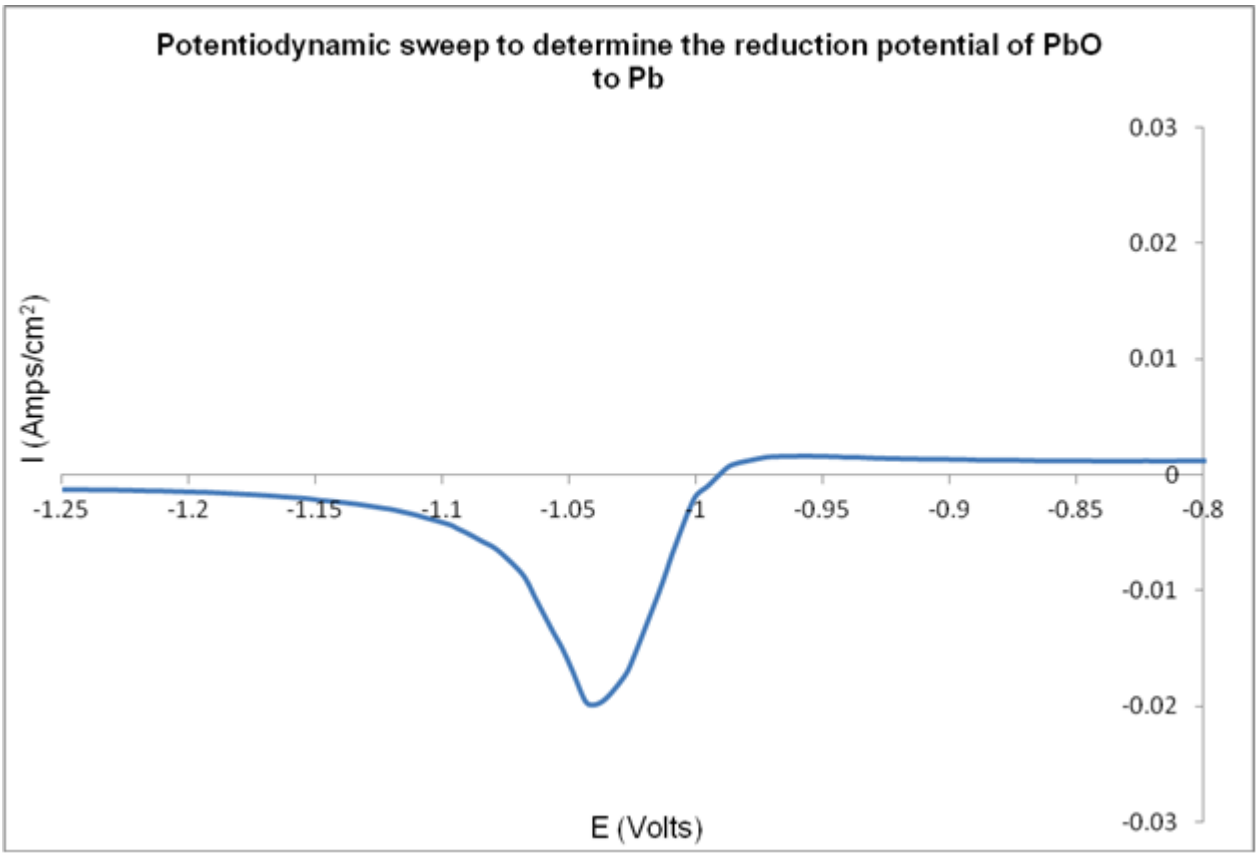

***Figure 5-34**: Voltammogram of electrode containing sample 3 to determine the reduction potential of PbO to Pb. Using Hg/Hg_2SO_4 as a reference electrode*

Figure 5-34 shows the current being measured beginning to change in the current-potential curve at ~-0.99 V and peaks at ~-1.04 V and tails off at ~-1.2 V. Taking into account the difference between the standard hydrogen electrode (SHE) and the mercury electrode, Hg/Hg_2SO_4 being 0.6524 V, the standard reduction potential for $PbO + 2H^+ + 2e^- \rightarrow Pb + H_2O$ which is -0.58 V against the standard hydrogen electrode (SHE) and -1.2324 V against the Hg/Hg_2SO_4 electrode, these observations are consistent with known reduction potential values and reaffirm the active material present in the analyte.

Having identified the reduction potential, a potentiostatic sweep was employed, which applied a constant potential and monitors the current as a function of time.

The potential used was -1.3 V and was applied until a change in current was observed which indicates the full reduction of PbO to Pb, thus forming the anode.

Once formed the working electrode was analysed by cyclic voltammetry. In this method, the potential scan is reversed at a specified point beyond the peak and scanned back in the direction of the initial potential.

Figure 5-35 illustrate a cyclic voltammogram of an electro-active paste made using PbO from sample 3. The voltammogram shown is typical of current-potential curves observed for both samples 1 and 2.

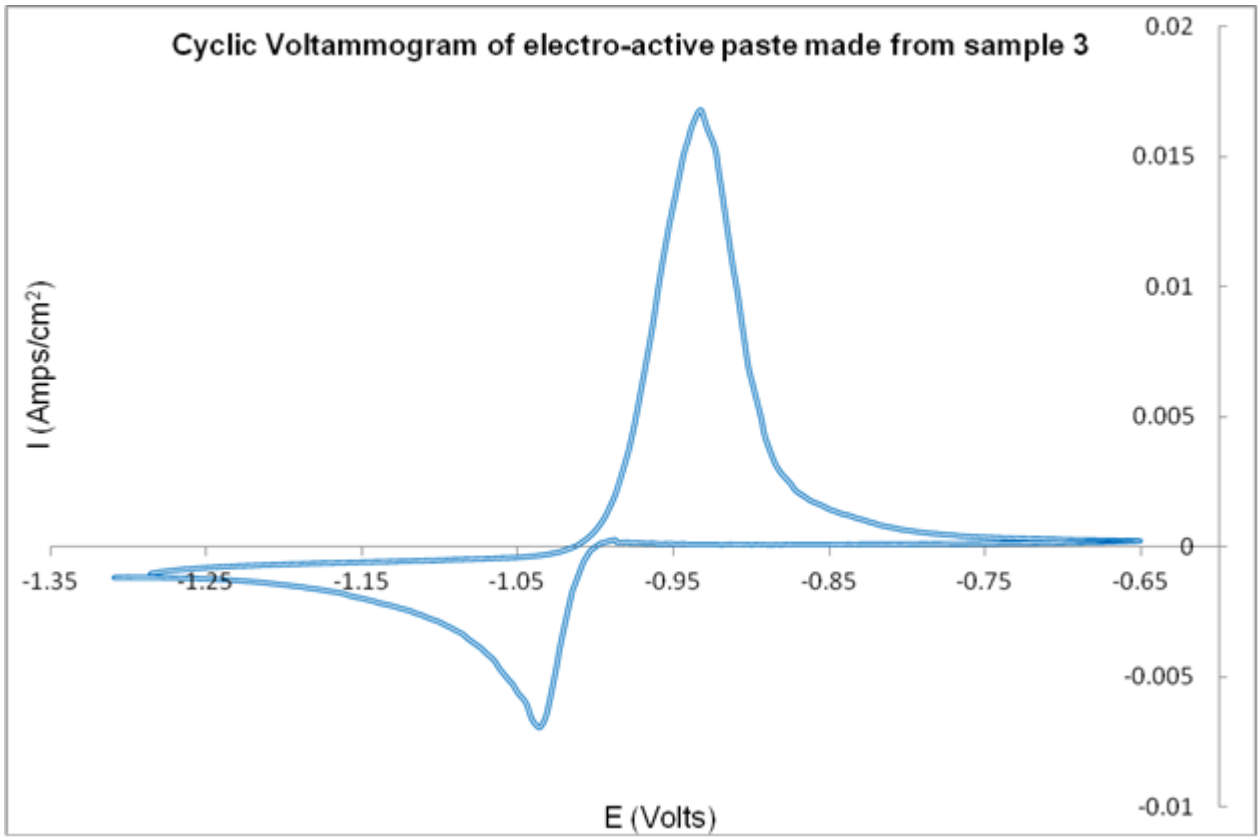

Figure 5-35: *Cyclic voltammogram of electrode containing sample 3. Using a Pt counter electrode, Hg/Hg_2SO_4 reference electrode at a scan rate of 20 mV/s.*

During the cathodic sweep from -0.65 V to -1.3 V, at a scan rate of 20 mV/s, a peak begins to form at ~-1 V which reaches its apex at ~-1.04 V and gradually tails off at ~-1.3 V, as shown in Figure 5-35. On the reverse sweep the beginnings of an anodic peak is observed at ~-1 V, peaking at ~-0.93 V, tapering off at ~-0.7 V. This is consistent with the standard reduction potential for $Pb + HSO_4^- \rightarrow H^+ + 2e^- + PbSO_4$ which is -0.36 V against the SHE and -1.01 V against the Hg/Hg_2SO_4 electrode used in this experiment. These results were observed at sweep rates of 1, 5, 10, 20, 30 and 50 mV/s and were recorded to be stable throughout each experiment.

The reversibility was still apparent over a hundred cyclic sweeps within the set potential range and under different sweep rates. These initial results suggest that the conversion of $Pb_3(C_6H_5O_7)_2 \cdot 3H_2O$ to PbO to be reused in new LABs have shown good efficacy and indicates a clear commercial viability for further development.

5.5 Summary

The combustion-calcination of $Pb_3(C_6H_5O_7)_2 \cdot 3H_2O$ was successful in generating PbO containing both forms of the polymorph α and β together with metallic Pb. The manner in which the heating regime was implemented had a direct effect on the microstructure generated, which demonstrates the degree to which the final PbO product can be potentially manipulated to preferentially produce a desirable by-product to cater for specific end use in a variety if LAB application.

A novel method to generate PbO from lead citrate was found through a self-sustaining combustion route where the leached waste materials from LABs were preheated to 270 °C for ~15 minutes and was found to self-sustain a smouldering reaction to produce PbO with a predominately β phase containing metallic Pb when an external heat source was introduced. The method points to a potential application where a continuous and energy efficient method could be introduced to the manufacturing of PbO from recycled waste materials from LABs. Furthermore, results obtained from acid reactivity measurements showed no direct relationship between the surface area of materials and the degree of reactivity of a given sample. The results point to a more complex combination of factors including pore volume and size to be the main contributing features to the reactivity of PbO.

Electrochemical analysis of PbO from $Pb_3(C_6H_5O_7)_2 \cdot 3H_2O$ demonstrated the viability in the by-product to be used in an electroactive paste to be used in new LABs. The variability in the microstructure of PbO, and therefore performance, as a function of heat treatment of $Pb_3(C_6H_5O_7)_2 \cdot 3H_2O$ demonstrates the potential ability to cater for the various criteria demanded from industry of active materials for a variety of battery needs.

6 Chemical and Thermal Study of Lead Compounds

6.1 Introduction

Further to the observation of the enhanced chelation effect induced by NaOH in the previous hydrometallurgical leaching experiments, a series of in-depth investigations was carried out to study the effect of different concentrations of NaOH on all compounds of interest to the current study.

In the current chapter, pure α-PbO and β-PbO were obtained from lead citrate at room temperature without the need for a purification process, the use of ammonia, leached silicon and/or at elevated temperatures as reported in other works[126, 127]. Further, the use of glycerol was introduced to determine its applicability as a reducing agent in generating metallic Pb in PbO in calcination experiments.

6.2 Synthesis of α and β-PbO from Lead Citrate under NaOH

6.2.1 Introduction

A series of experiments was conducted at room temperature using the two forms of lead citrate, $Pb(C_6H_6O_7)\cdot H_2O$ and $Pb_3(C_6H_5O_7)_2\cdot 3H_2O$ synthesised in the current study as the starting reagent with NaOH. This was to investigate the effect on lead citrate by the use of NaOH reagent as a function of molar concentration.

6.2.2 Experimental

While maintaining a S:L ratio of 1 to 20, the molar ratio of NaOH was increased from 1 to 10 with respect to lead citrate. Each experiment was conducted using borosilicate beakers under constant magnetic stirring using an impeller at a constant rate of ~300 rpm. Each experiment used a combined pH and temperature probe to monitor the respective reactions as different reagents are applied.

6.2.3 Results and Discussion

Figure 6-1 illustrates the physical changes observed in a solution containing $Pb_3(C_6H_5O_7)_2\cdot 3H_2O$ over a period of 20 minutes from the point of NaOH addition from (A) to (E). The molar ratio in the illustrated experiment was 1 to 10. The solution was stirred at a constant rate using a magnetic impeller as were all experiments discussed throughout this chapter.

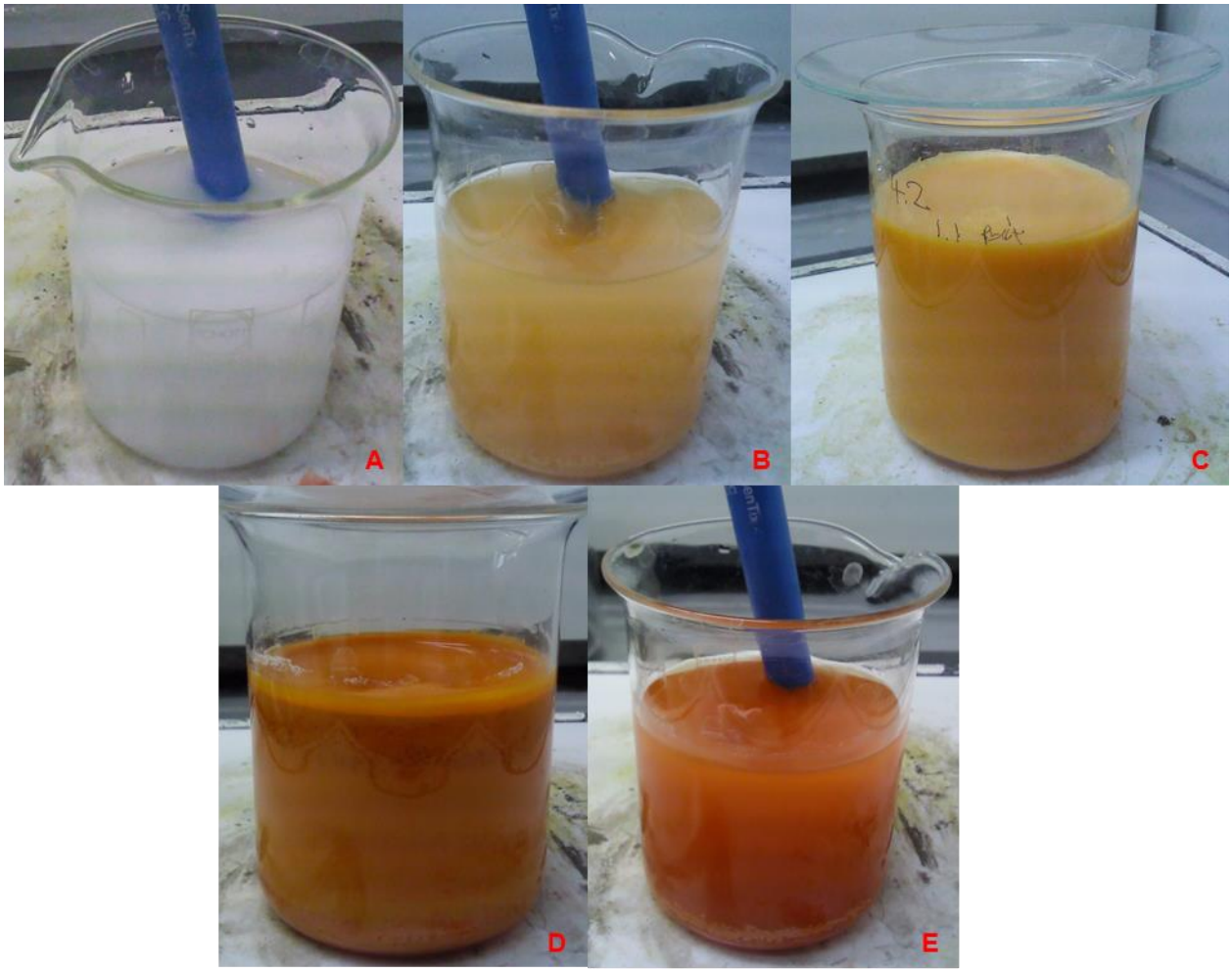

***Figure 6-1**: Progression of chemical conversion of $Pb_3(C_6H_5O_7)_2 \cdot 3H_2O$ to α-PbO under NaOH*

Within seconds of exposure to NaOH the pH of the solution rose from 4.8 to 12.6 with a recorded temperature increase of 6 °C from 24 to 30 °C. As seen in Figure 6-1A and B, the colour of the solution began to change from white to light orange with the observed turbidity slightly decreasing before significantly increasing as observed in (C). The decrease in turbidity is assessed to be the dissolution of the citrate into solution.

The transition to the light and then darker orange, seen in (B) to (C), is the characteristic colour of PbO. The turbidity of the solution appears to reach its maximum after ~15 minutes as observed in (D) with the colour of the solution becoming dark orange. The turbidity began to drop and dark red particulates, characteristic of pure α-PbO, becomes visible by the 20th minute as observed in (E).

After filtration and drying, the sample was analysed for phase identification under XRD. Figure 6-2A and B illustrates the diffraction patterns of $Pb_3(C_6H_5O_7)_2 \cdot 3H_2O$ and the dried reacted by-product respectively. The XRD pattern for the by-product matched perfectly with α-PbO (ref. code: 03-065-0398).

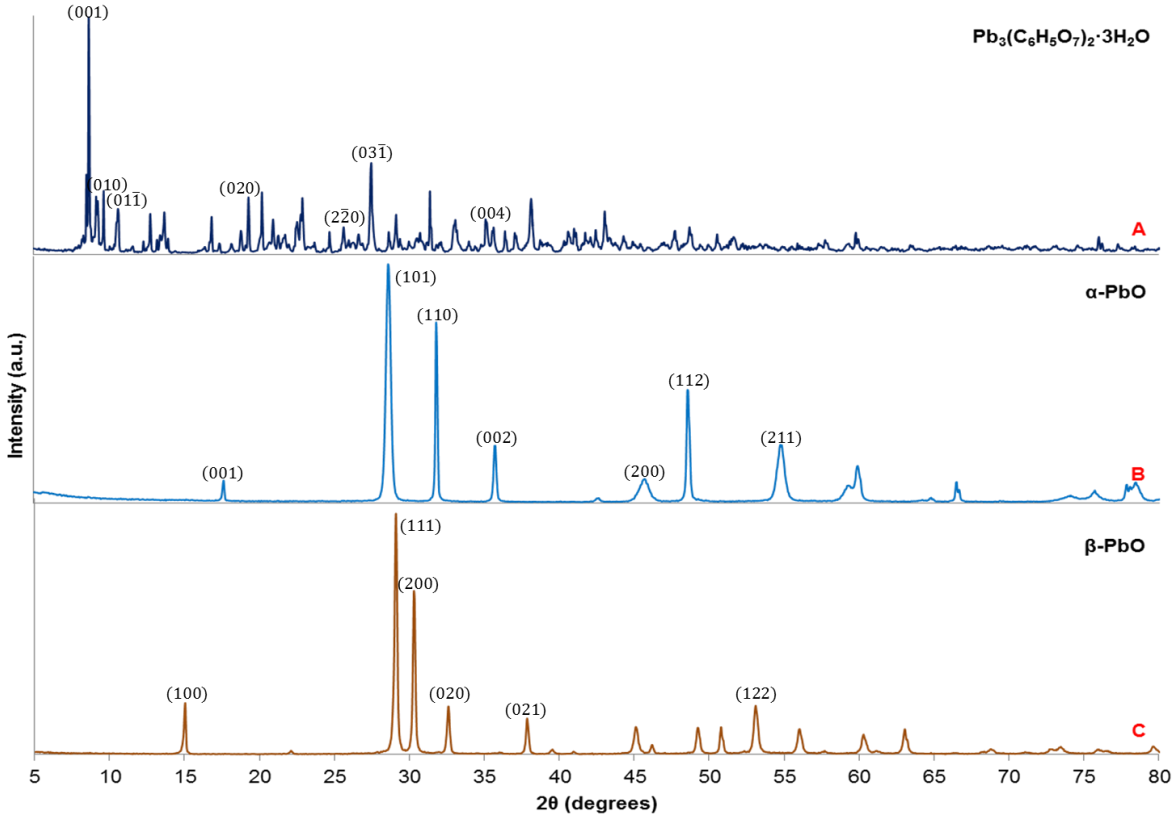

***Figure 6-2**: XRD patterns showing the sequence of samples obtained through chemical conversion from $Pb_3(C_6H_5O_7)_2{\cdot}3H_2O$ (A) to α-PbO (B) and β-PbO (C) using NaOH*

Results obtained from experiments conducted with 1:3 through to 1:10 ratios of NaOH demonstrated good agreement with that shown in Figure 6-2B. Although experiments conducted with 1:1 and 1:2 ratios of NaOH showed signs of disassociation, they were not to the same degree as those outlined above to yield pure α-PbO.

It was observed that the rate of reaction and temperature increased as a function of molar concentration for both forms of lead citrate. Figure 6-4 illustrates the dried by-product from the 1:10 molar ratio of $Pb_3(C_6H_5O_7)_2{\cdot}3H_2O$ to NaOH reaction.

Reactions involving lead salts with NaOH are typically used in precipitation reactions such as the following in equation **6-1**:

$$Pb^{2+}_{(aq)} + 2OH^{-}_{(aq)} \rightarrow Pb(OH)_{2(s)} \qquad \textbf{6-1}$$

This reaction may well have occurred, however as the alkaline conditions progressively increased the cation would quickly hydrolyse, forming $Pb(OH)^{+}$, $Pb(OH)_2$, $Pb(OH)_3^{-}$ and other species which may include a number of polynuclear species such as $Pb_4(OH)_4^{4+}$, $Pb_3(OH)_4^{2+}$ and $Pb_6O(OH)_6^{4+(128)}$.

Therefore, the precipitation of the pure α phase of PbO was unexpected given the products that might typify such a chemical reaction. Figure 6-3 illustrates a flow diagram of the reaction process for forming α-PbO from $Pb(C_6H_6O_7)\cdot H_2O$.

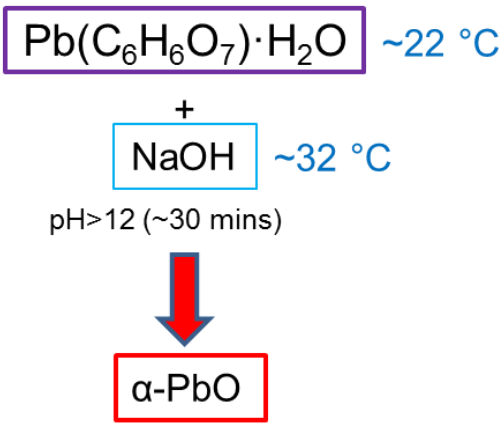

***Figure 6-3**: Flow diagram showing the sequence of forming α-PbO from $Pb(C_6H_6O_7)\cdot H_2O$ using NaOH*

***Figure 6-4**: Image of chemically converted α-PbO from $Pb_3(C_6H_5O_7)_2\cdot 3H_2O$ using 1:10 molar ratio of NaOH*

During the 20 minute reaction period, NaOH had fully disassociated $Pb_3(C_6H_5O_7)_2\cdot 3H_2O$ to precipitate pure α-PbO. As illustrated in Figure 6-4, the appearance of the by-product is that of a fine powder with the characteristic dark red colour of pure α-PbO, further confirming the XRD analysis.

Upon completion, the filtrate can be reused in the leaching solution in future hydrometallurgical remediation of spent LAB pastes. Alternatively, there is potential for the filtrate to be recovered as either monosodium ($NaC_6H_7O_7$) or trisodium citrate ($Na_3C_6H_5O_7$) as both are commercially valuable. Table 6-1 depicts an example reaction process of $Pb(C_6H_6O_7)\cdot H_2O$ with NaOH with their corresponding mass when mixed and the measured changes observed.

***Table 6-1**: An example reaction using $Pb(C_6H_6O_7)\cdot H_2O$ with NaOH in 100 ml solution with a 1:10 molar ratio*

Reagent	Reagent Mass (g)	Measured pH and Temp (°C)	Physical Characteristic	Product Mass (g)
$Pb(C_6H_6O_7)\cdot H_2O$	5	4/22 °C	White	
NaOH	4.8	12.4/33 °C	Light Red	
				1.2

Further to this finding, an extended study found that from a molar ratio of 1:16 lead citrate would fully dissolve into solution. The compound reprecipitated when H_2SO_4 was slowly poured into the mixture until lime coloured particulates were observed to form.

The amount required for reprecipitation was observed to be variable, but can be as high as 1:33 molar ratio of $Pb(C_6H_6O_7)\cdot H_2O$ to H_2SO_4. XRD analysis of a dried sample taken after filtration demonstrates a perfect phase match for β-PbO (ref. code: 00-005-0570) and is shown in Figure 6-2C for comparison.

A flow diagram is shown in Figure 6-5 to illustrate the reaction process with $Pb(C_6H_6O_7)\cdot H_2O$ as the starting reagent.

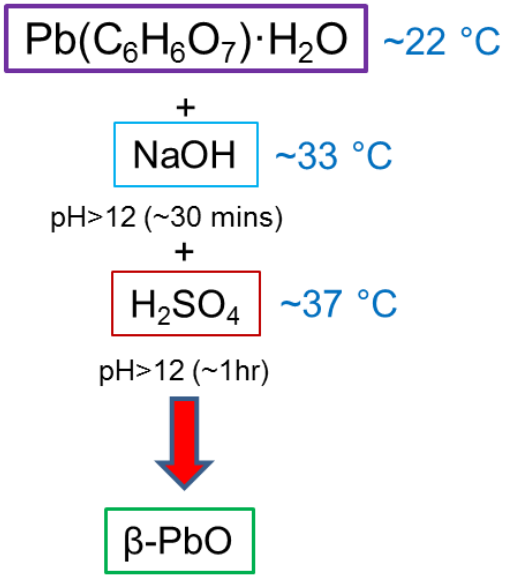

***Figure 6-5**: Flow diagram showing the sequence of forming β-PbO from $Pb(C_6H_6O_7)\cdot H_2O$ using NaOH and H_2SO_4*

SEM was used to analyse the morphology of the α-PbO generated from $Pb_3(C_6H_5O_7)_2 \cdot 3H_2O$ and is illustrated in Figures 6-6B, C and D at x1200, x5000 and x10000 magnification respectively.

Figure 6-6A illustrates a micrograph of a sample of $Pb_3(C_6H_5O_7)_2 \cdot 3H_2O$ captured at x1200 magnification to demonstrate, for comparison, the microstructural changes brought about by its dissociation, and precipitation of α-PbO.

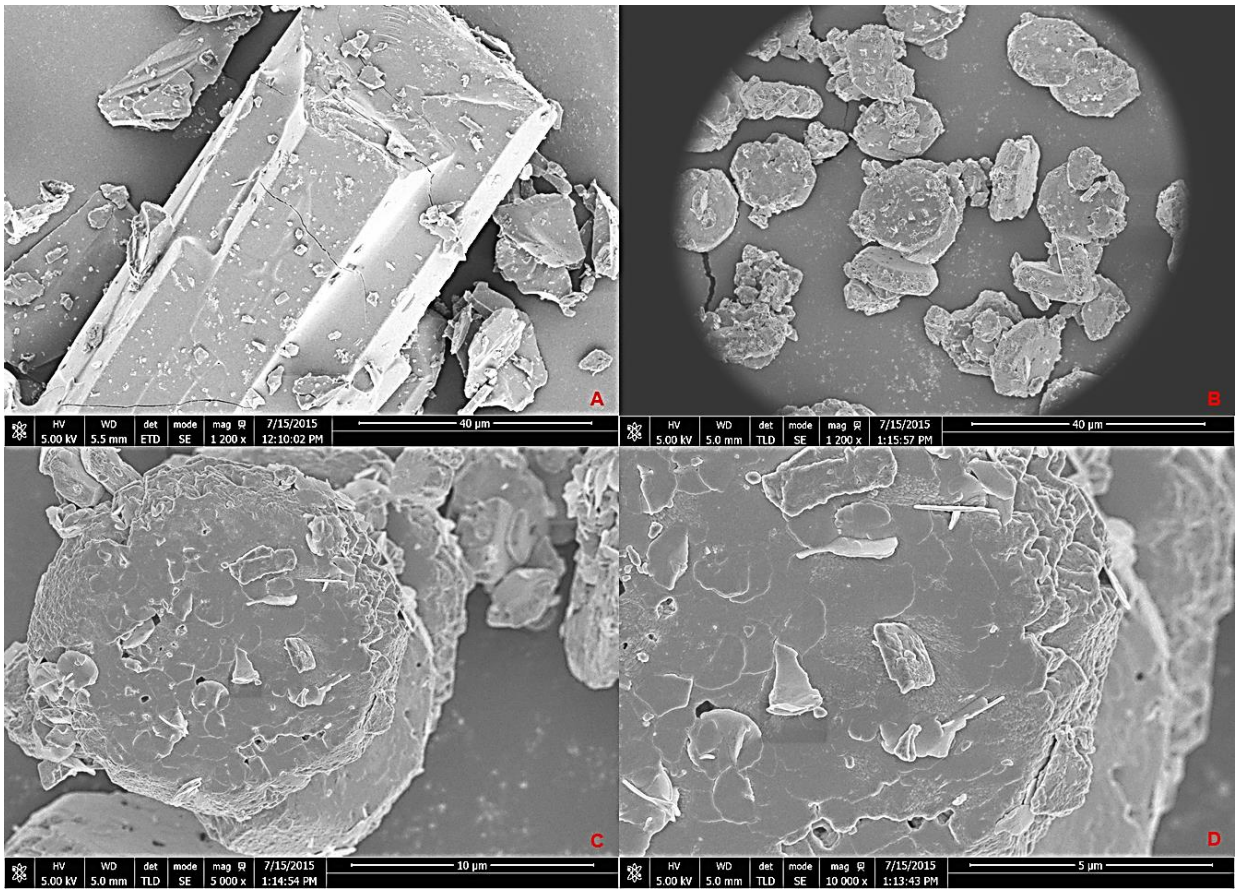

***Figure 6-6**: SEM imagery of $Pb_3(C_6H_5O_7)_2 \cdot 3H_2O$ at x1200 (A) compared to α-PbO at x1200 (B) and at x5000 (C) and x10000 magnifications (D) after chemical conversion using NaOH*

The image captured using SEM of α-PbO converted from $Pb_3(C_6H_5O_7)_2 \cdot 3H_2O$ shows a microstructure much reduced with large textured and rounded agglomerated particles of various sizes. The agglomerated particles appear to be composed of layers of sheets stacked against each other forming irregular tiled structures. Some of these sheets appear as outcrops and are randomly distributed as seen in Figure 6-6C.

At higher magnification, the particulate layering becomes more evident as illustrated in Figure 6-6D with sheets appearing to be peeling off the surface. These peelings appear in a range of sizes from a few to several hundred nanometres in diameter. The topography of the α-PbO demonstrates a microstructure with a significantly smaller surface area and lower porosity than those seen in PbO generated from the combustion-calcination of lead citrate.

Despite generating the same results as $Pb_3(C_6H_5O_7)_2 \cdot 3H_2O$ with respect to those seen in the XRD patterns shown in Figure 6-7B and C in high alkali conditions, the microstructure produced from the chemical conversion from $Pb(C_6H_6O_7) \cdot H_2O$ to α-PbO demonstrates a significant contrast as seen in Figure 6-7.

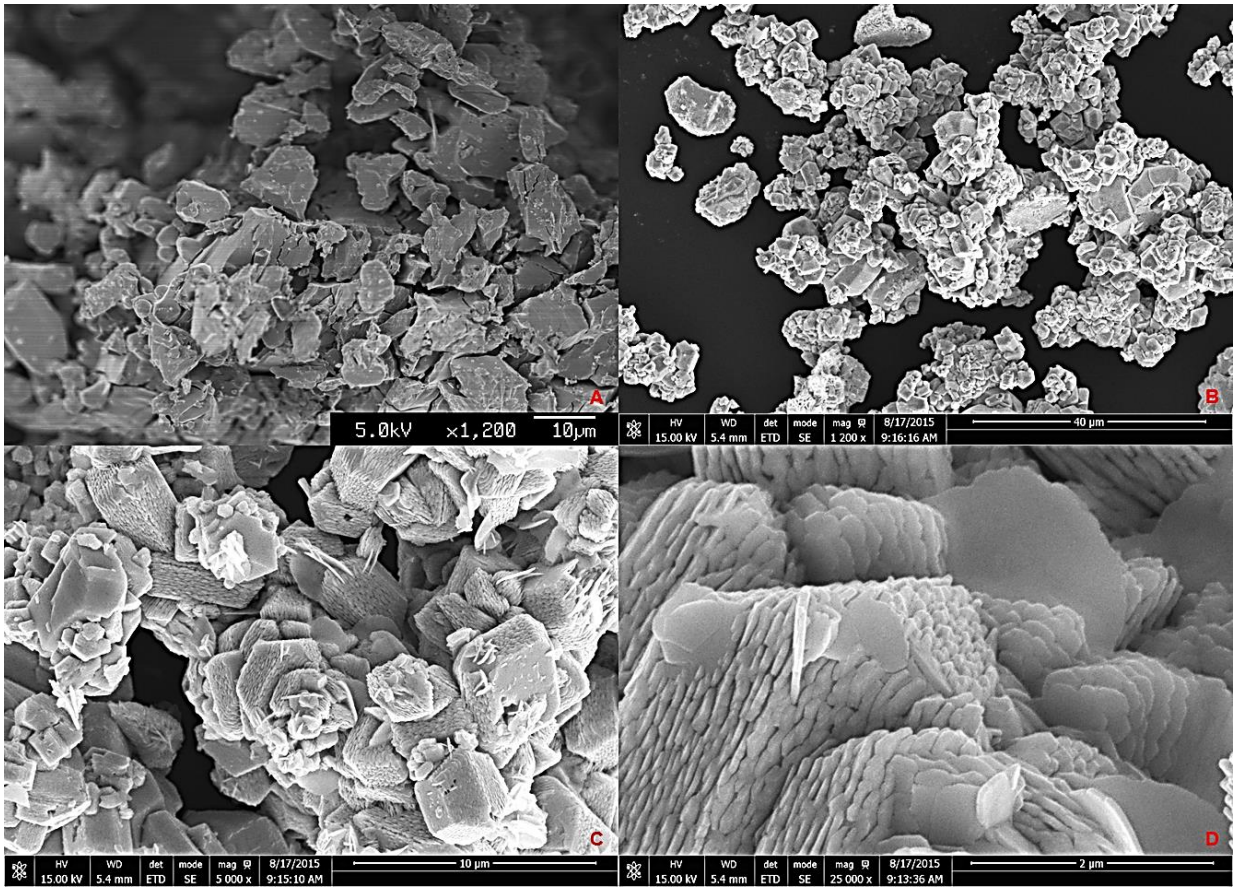

***Figure 6-7**: SEM imagery of $Pb(C_6H_6O_7) \cdot H_2O$ at x1200 (A) compared to α-PbO at x1200 (B) and at x5000 (C) and x10000 magnifications (D) after chemical conversion using NaOH*

The SEM imagery established for α-PbO converted from $Pb(C_6H_6O_7) \cdot H_2O$ shows a microstructure dominated by highly textured blocks of particles of various sizes. The blocks appear to be composed of layers of sheets stacked against each other forming a series of tiled structures. These structures appear to be more defined compared to those formed from $Pb_3(C_6H_5O_7)_2 \cdot 3H_2O$.

Some of these sheets appear as outcrops and are randomly distributed as seen in Figure 6-7C. On closer inspection, the particulate layering becomes more evident as illustrated in Figure 6-7D with protruding sheets ranging from a few to several hundred nanometres in diameter distributed randomly at different angles.

Much like the topography of the α-PbO generated from $Pb_3(C_6H_5O_7)_2 \cdot 3H_2O$, the microstructure observed here is significantly smaller in surface area with lower porosity than those seen in PbO generated from the combustion-calcination of lead citrate of both forms.

SEM was used to investigate the morphology of the β-PbO derived from $Pb(C_6H_6O_7)\cdot H_2O$ and is illustrated in figures 6-8B, C and D at x1200, x5000 and x25000 magnification respectively. Figure 6-8A illustrates a micrograph of a sample of $Pb(C_6H_6O_7)\cdot H_2O$ imaged at x1200 magnification to demonstrate the microstructural changes induced by its disassociation, and precipitation of β-PbO.

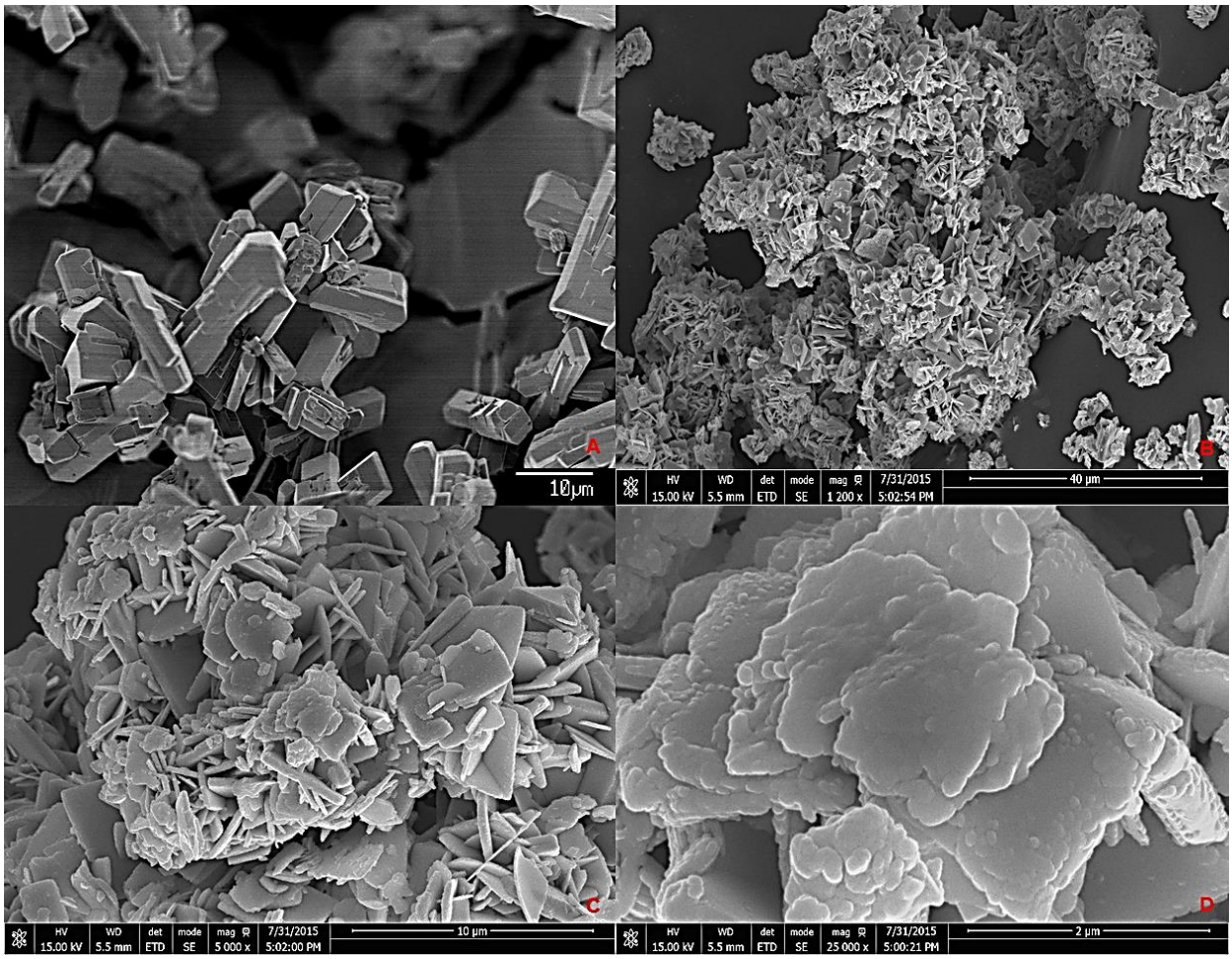

***Figure 6-8**: SEM imagery of $Pb(C_6H_6O_7)\cdot H_2O$ at x1200 (A) compared to β-PbO at x1200 (B) and at x5000 (C) and x25000 magnifications (D) after disassociation and reprecipitation using NaOH and H_2SO_4*

The imagery obtained from SEM for β-PbO converted from $Pb(C_6H_6O_7)\cdot H_2O$ shows a microstructure with a wide range of shapes and size. As illustrated in Figure 6-8A, the angled blocks that characterise the $Pb(C_6H_6O_7)\cdot H_2O$ microstructure has been replaced by a random distribution of flake-like, rod shaped and spherical particles intermixed together following the disassociation and reprecipitation reaction, shown in Figure 6-8B.

These structures appear to be more varied than those seen for α-PbO and indeed the β-PbO generated from $PbSO_4$ discussed in the next section. The various shapes and sizes of the particles that characterise this microstructure are also randomly orientated forming distinct clusters as seen in Figure 6-8C.

At higher magnification, as illustrated in Figure 6-8D, some of the flake-like particles appear to be layered with a textured surface comprising of agglomerated particles. The highly complex mixed structure may appear to lend itself to a relatively high degree of porosity.

6.3 Synthesis of α-PbO from PbO

6.3.1 Introduction

The study on the effects of high alkali environments on lead bearing compounds of interest was extended to laboratory grade PbO from Sigma Aldrich that contained a mixture of the two polymorphic forms α and β. A smaller study was conducted with NaOH compared to previous investigations on this occasion.

6.3.2 Experimental

In this study, a series of experiments from 1:1 to 1:5 molar ratios of PbO to NaOH was undertaken while maintaining a S:L ratio of 1 to 20. Magnetic stirring was maintained throughout at ~300 rpm at room temperature in glass beakers with each reaction monitored using a combined pH and temperature probe as before.

6.3.3 Results and Discussion

Table 6-2 illustrates an example reaction using laboratory grade PbO with NaOH mixed in 100 ml solution with a 1:3 molar ratio with corresponding measured and observed changes before and after mixing.

***Table 6-2**: An example reaction using PbO with NaOH in 100 ml solution with a 1:3 molar ratio*

Reagent	Reagent Mass (g)	Measured pH and Temp (°C)	Physical Characteristic	Product Mass (g)
PbO	5	pH 10/22 °C	Orange	
NaOH	2.69	pH 12.5/27 °C	Light Red	
				4.07

The filtered and dried by-products were analysed using XRD to determine the phase purity of each product. Figure 6-9 illustrates the diffraction patterns of a sample of PbO before and after exposure to a high alkali environment emanating from a solution containing a 1:3 PbO to NaOH molar ratio, with details tabulated in Table 6-2.

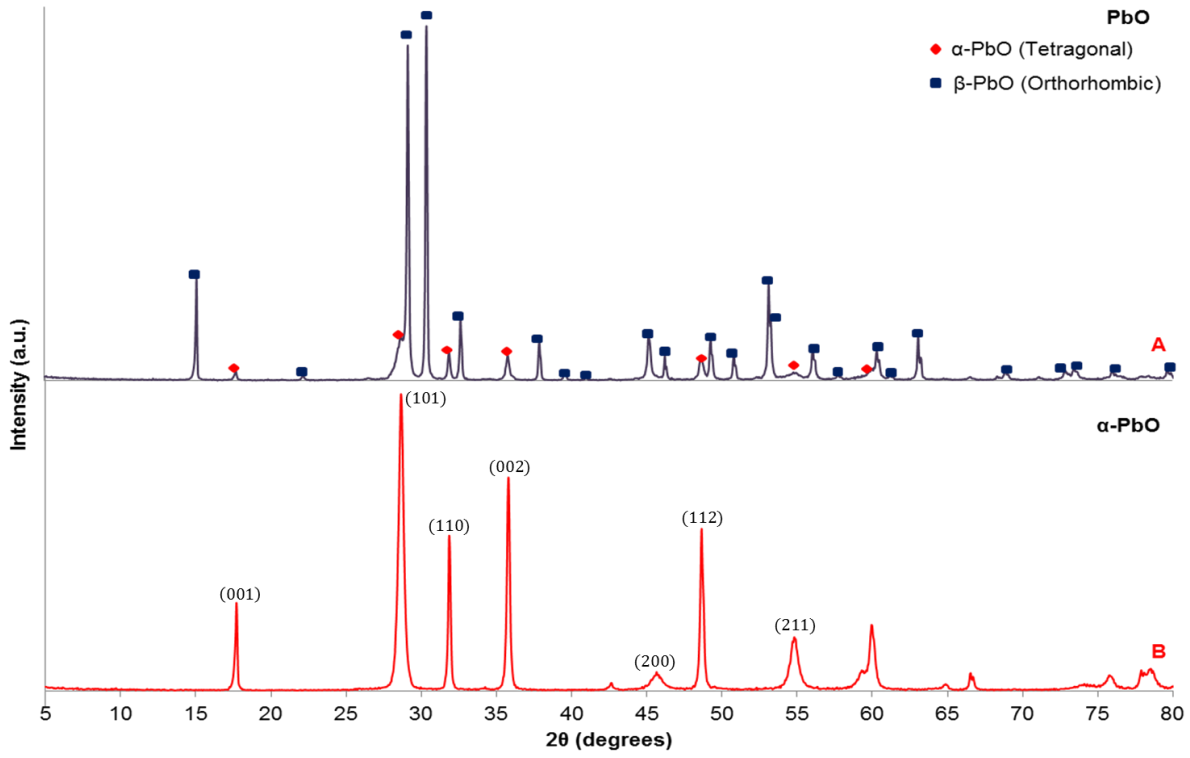

***Figure 6-9**: XRD patterns showing the chemical conversion of commercial PbO from Sigma Aldrich in (A) to pure α-PbO (B) using NaOH*

As with the results found for $Pb(C_6H_6O_7)\cdot H_2O$ and $Pb_3(C_6H_5O_7)_2\cdot 3H_2O$, the high alkali environment generated a pure α-PbO sample, shown in Figure 6-9B, from PbO that contained both forms of the polymorphs, as seen in Figure 6-9A. It is unclear as to how these conversions have occurred. Figure 6-10 illustrates a flow diagram to demonstrate the reaction process in generating α-PbO from PbO.

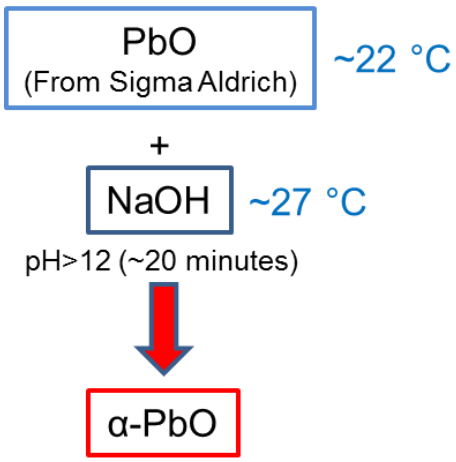

***Figure 6-10**: Flow diagram showing the sequence of forming α-PbO from commercially sourced PbO powder*

Polymorphic phase transitions (PPT) is well known in solid-state physics and chemistry[129, 130], where such transitions are either mechanically or, more commonly, thermally induced at elevated temperatures. Indeed α-PbO has been documented to transition to β-PbO at 490 °C[131] and transformations from β to α have been observed mechanically through shock compression in the range of 9.5-35 GPa[132].

Chemically induced PPTs of this kind, i.e. from orthorhombic to tetragonal, is not considered physically possible. In order for any chemically induced change to occur, the bulk material must be penetrated by the acting reagent, unless a surface transition could somehow propagate into the material, this mechanism is unlikely to have taken effect.

Experiments in high alkali environments were conducted with PbO powder of different starting sizes from Sigma Aldrich. The results showing the successful production of pure α-PbO in Figure 6-9 were from PbO powder <10 μm in size. However, investigations carried out using much larger PbO powder yielded negligible change in the α to β ratio. This would suggest that the reaction is dependent on a high surface area of the precursor material, but does not necessary point to any form of chemically induced surface PPT.

Further, it has been determined in other studies[133] that the high solubility of PbO is caused by the formation of strong Pb(II) hydroxo complexes when treated in alkaline solutions. It is generally known that in alkaline solutions Pb^{2+} ions form strong complexes primarily consisting of $Pb(OH)_3^-$. As with their finding, PbO solubility was found to increase with NaOH concentration, however no formation of α-PbO were reported and the study did not go as far as to investigate the effects of alternating the pH environment in the same system.

In their work with β-PbO-NaOH-H_2O-alcohol systems Yurkinskii et al[133] found that β-PbO solubility in their systems depends on the Pb(II) complexation and that an optimal concentration of NaOH of about 1 M in their alcohol containing complexes resulted in the dissolution of β-PbO. Similar results were also indicated in the same study for higher concentrations of NaoH without alcohol.

In a study on the solubility of α-PbO in alkaline media, Ziemniak et al[134] found that the solubilities of α-PbO are controlled by the sequence of three dissolution reaction equilibria as shown in equation 6-2:

$$\alpha\text{-}PbO_{(s)} + (2\text{-}n)H^+ \rightarrow Pb(OH)_n^{2-n} + (1\text{-}n)\ H_2O \qquad \textbf{6-2}$$

where n = 1, 2 and 3.

Therefore, α-PbO solubility is determined by the quantitative presence of three Pb(II) hydrolytic species: $Pb(OH)^+$, $Pb(OH)_2$ and $Pb(OH)_3^-$.

The findings from these two separate studies on the solubilities of α and β-PbO in alkaline solutions together with the observations made from the current study suggests the difference in solubility between α and β as a function of pH resulted in the expression of one over the other in a given reaction environment.

Thus, it was possible to generate the distinct tetragonal and orthorhombic phases of PbO separately from $Pb(C_6H_6O_7)\cdot H_2O$ and $Pb_3(C_6H_5O_7)_2\cdot 3H_2O$ by isolating the α phase through the dissolution of the β phase as a function of pH, which also proved to be successful for <10 μm powders of PbO. The complete dissolution of both phases at much higher alkalinity and subsequent re-precipitation at lower pH led to the preferential expression of the β phase. The latter part of this process was investigated using laboratory grade $PbSO_4$ sourced from Sigma Aldrich and is reported in the next section.

6.4 Synthesis of β-PbO through dissolution of $PbSO_4$ under NaOH

6.4.1 Introduction

Following from the results obtained from the dissolution and reprecipitation experiments using lead citrate in 6.2, an investigation was carried out using $PbSO_4$ to determine the applicability of the process using NaOH on the compound.

6.4.2 Experimental

A series of experiments was conducted using molar ratios of 1:10 through to 1:23 of $PbSO_4$ to NaOH with a S:L ratio of 1:20 maintained for each experiment and were stirred using a magnetic impeller at a constant rate. A typical chemical reaction between $PbSO_4$ and NaOH is expressed in the following:

$$PbSO_{4(s)} + 4NaOH_{(aq)} \rightarrow Na_2PbO_{2(s)} + Na_2SO_{4(aq)} + 2H_2O_{(l)} \quad \textbf{6-3}$$

6.4.3 Results and Discussion

The dissolution of $PbSO_4$ began when the molar ratio reached 1:20 with complete dissolution observed at 1:23. Figure 6-11 illustrates the sequence from when $PbSO_4$, while in solution, shown in 6-11A, began to dissolve to complete dissolution, shown in 6-11B, and then to the precipitation of the β phase, shown in 6-11C.

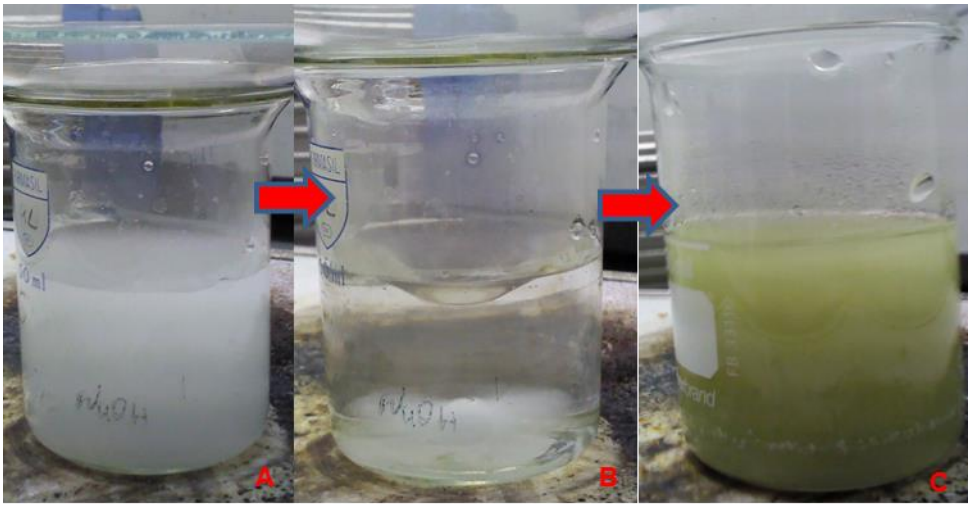

***Figure 6-11**: Sequence of chemical conversion from $PbSO_4$ (A) with NaOH induced dissolution (B) through to precipitation of pure β-PbO (C)*

The orthorhombic phase was the exclusive reprecipitated form of PbO upon lowering the pH by about 0.3. To confirm that the reaction was pH controlled as opposed to a chemical interaction with the reagent, both $NaHCO_3$ and H_2SO_4 were used to lower the alkalinity of the solution.

By lowering the pH using either compound it was observed that the pure orthorhombic phase was instantly reprecipitated each time whereas the precipitation of the β form from lead citrate took up to an hour to complete. The dried compound was imaged and shown in Figure 6-12B and analysed using XRD to confirm phase purity shown in Figure 6-13.

A comparison of β-PbO precipitated from $Pb(C_6H_6O_7)\cdot H_2O$ and $PbSO_4$ are shown in Figure 6-12A and B respectively.

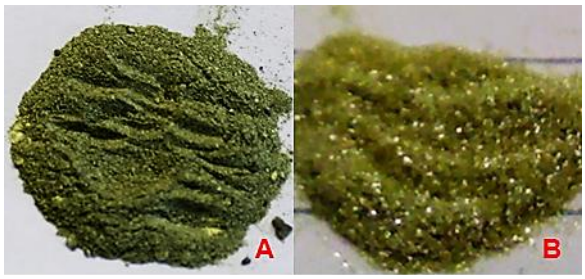

***Figure 6-12**: Chemically formed β-PbO from $Pb(C_6H_6O_7)\cdot H_2O$ (A) and $PbSO_4$ (B) in dissolution/precipitation reaction using NaOH and H_2SO_4*

The β-PbO powders generated from $Pb(C_6H_6O_7)\cdot H_2O$ and $PbSO_4$ demonstrate a variance in physical characteristics as Figures 6-12A and 6-12B illustrates. The β-PbO powder derived from the dissolution of $Pb(C_6H_6O_7)\cdot H_2O$ exhibit a higher bulk density than that of the powder emanating from $PbSO_4$. The appearance of the powder from $PbSO_4$ is that of optically reflective metallic-like flakes.

The bulk behaviour of the powder denotes a material that is very light in weight where it is easily affected by the slightest changes in its local environment. Figure 6-13 shows XRD diffraction patterns of $PbSO_4$ before and after dissolution and reprecipitation of β-PbO in 6-13A and B respectively.

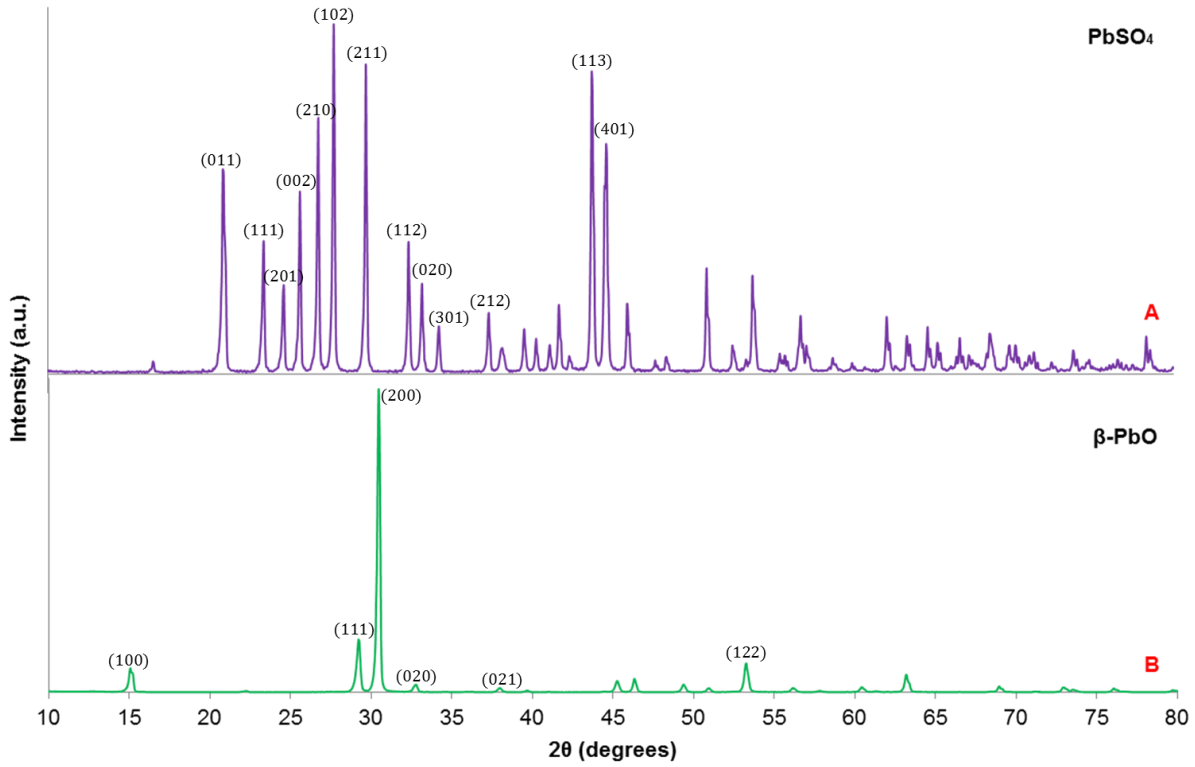

***Figure 6-13**: XRD patterns showing the chemical conversion of $PbSO_4$ from Sigma Aldrich (A) to pure (B) using NaOH and H_2SO_4*

The relative peak intensities for β-PbO generated through this manner, shown in Figure 6-13B, are different to those typically observed, as in Figure 6-2C. Although a perfect match for the orthorhombic phase, the intensity mismatch could be due to preferred orientation. As illustrated in the SEM imagery, in Figure 6-15, of the compound the β-PbO microstructure generated from $PbSO_4$ appear to consist of large textured sheets.

From the image shown in Figure 6-12B, these sheets appear to be smooth enough to be optically reflective giving the appearance of sparkling metallic-like shards. The sample was very difficult to handle as the powder was very light/ fluffy and adhered to all surfaces it was exposed to.

The flake-like particles were very sensitive to sample preparation and loading and tended to lie flat on the surface when secured for analysis. This could have led to intensity enhancements in some Bragg reflections while reducing the intensities of others, as in this case. The larger particle sizes in these samples may also be contributing factors in the intensity mismatch shown in the diffraction pattern.

A flow diagram in Figure 6-14 denotes the sequence with recorded measurements at each stage for the precipitation of β-PbO from the dissolution of $PbSO_4$.

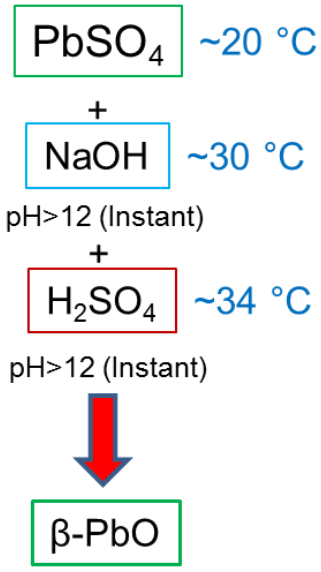

***Figure 6-14**: Flow diagram showing the sequence of forming β-PbO from commercially sourced $PbSO_4$ powder using NaOH and H_2SO_4*

$NaHCO_3$ was also used in separate experiments to lower the alkalinity of the solution to investigate the pH dependence of β-PbO precipitation. Table 6-3 shows an example of the sequence of reagent mixing with their corresponding mass and observed changes over the course of the procedure.

***Table 6-3**: An example reaction using $PbSO_4$ with NaOH solution with a 1:23 molar ratio and $NaHCO_3$ in 100 ml*

Reagent	Reagent Mass (g)	Measured pH and Temp (°C)	Physical Characteristic
$PbSO_4$	5	pH 5/22 °C	White
NaOH	15.18	pH 12.8/31 °C	Colourless
$NaHCO_3$	10	pH 12.4/33 °C	Dark Green

As with the use of precise amounts of H_2SO_4, the addition of $NaHCO_3$ lowered the alkalinity of the solution within the pH region where β-PbO is observed to be stable and was precipitated as a result. The morphology of the powder was analysed using SEM in a range of magnifications and is shown Figure 6-15.

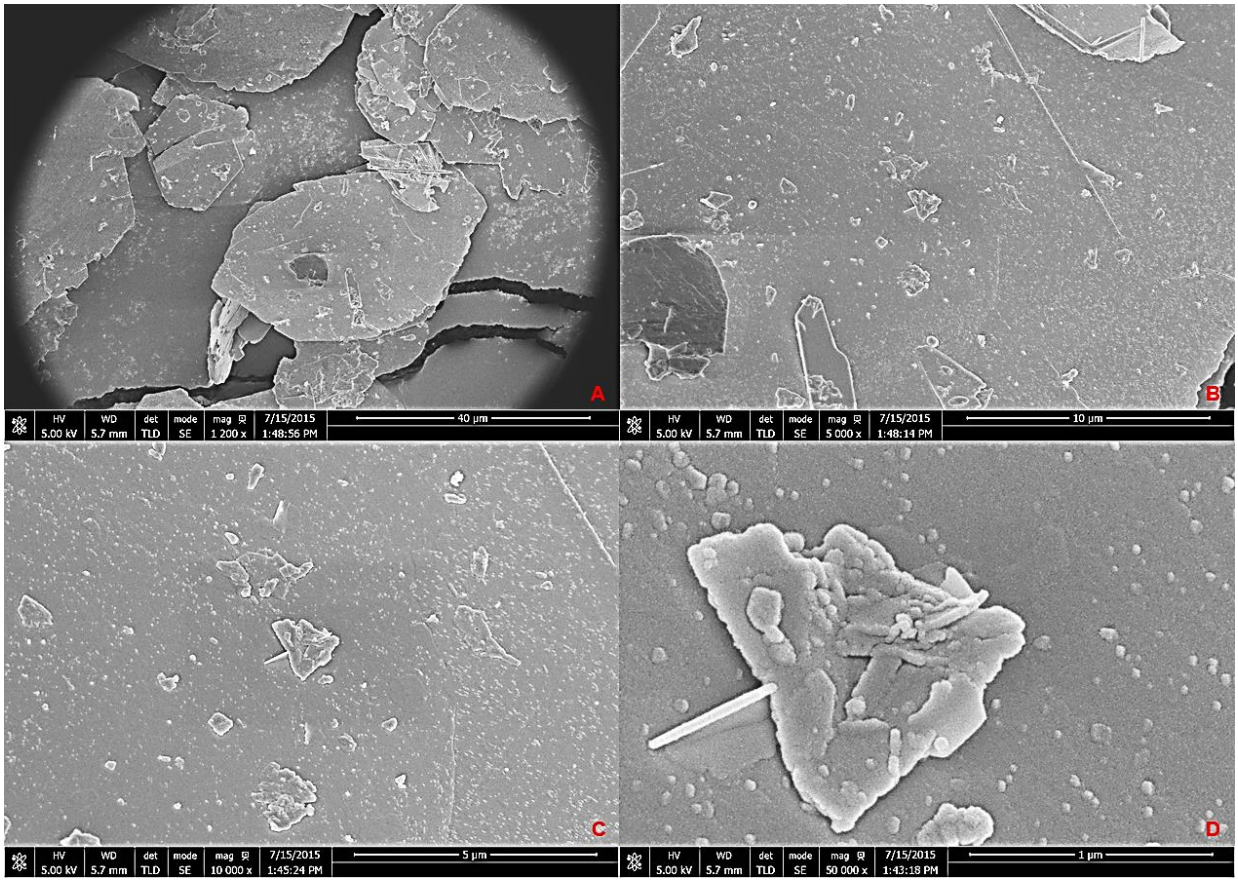

Figure 6-15: SEM imagery of β-PbO at x1200 (A), x5000 (B), x10000, (C) and x50000 magnifications after the dissolution of $PbSO_4$ and precipitation using NaOH and $NaHCO_3$

As alluded to earlier, the microstructure of β-PbO derived from $PbSO_4$ appears to consist of large flat particulate sheets. As seen in Figure 6-15A, the sheets are tens of microns in diameter. With increasing magnification, Figure 6-15B to C illustrates a lightly textured surface with smaller sheets and flakes of various sizes from a few to several microns interspersed on the exterior.

This is significantly different to the microstructure observed for β-PbO precipitated from $Pb(C_6H_6O_7)\cdot H_2O$. A comparison is drawn in Figure 6-16 of SEM images at the same magnification for β-PbO from $PbSO_4$ and $Pb(C_6H_6O_7)\cdot H_2O$ in 15A and B respectively. Although some features are shared between the two microstructures as seen in Figure 6-15D, with spherical and rod-like particles appearing on the surface, the proportion of such artefacts are significantly smaller. The differences in microstructure are considerable and reflect the bulk behaviour and general appearance of the two materials seen in Figure 6-12.

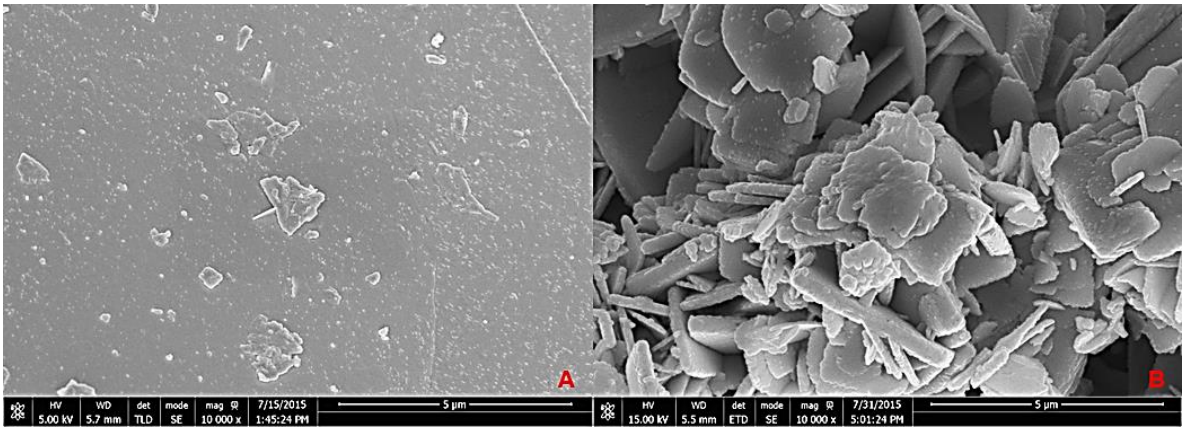

***Figure 6-16**: SEM imagery of chemically converted β-PbO from $PbSO_4$ (A) compared with β-PbO chemically converted from $Pb_3(C_6H_5O_7)_2 \cdot 3H_2O$. Both shown at x10,000 magnification*

The general distribution and shape of the particles in the microstructure observed in 6-16B denotes a porous, yet compact, and territorially rough topography giving rise to a relatively higher bulk density compared to that observed in 6-16A.

The light and fluffy physical characteristics observed for the $PbSO_4$ derived β-PbO is symptomatic of the large, thin and loose particulate sheets seen in the microstructure illustrated in 6-16A. The free-flowing behaviour exhibited by the bulk material is also attributed to the wide separation and distribution of these particulate sheets seen in 6-16A, where they can easily be disturbed by natural turbulence and random motion of air.

The β-PbO precipitated from these two compounds and the evident formations of different microstructures are also observed for α-PbO from the two forms of lead citrate. This may also be true of the microstructure from the α-PbO derived from PbO, however further investigations will need to be pursued in future works.

Although these results and those from literature may infer that the α and β phases of PbO may have distinct solubility products, another possibility is that they may have the same solubility but one phase may be more kinetically soluble than the other at a given pH.

In this situation, the kinetics for the dissolution reaction for β-PbO may be several orders of magnitudes higher than that of α-PbO. The issue between thermodynamic and kinetic solubility is well documented[135-137] and it has been noted that the most commonly encountered type of metastable solubility is observed in studies involving the solubility of polymorphic compounds. This may provide an explanation to the results seen here.

6.5 Leaching $PbSO_4$ with $NaHCO_3$

6.5.1 Introduction

As found earlier in the current study, the negative plate from LABs can be treated as if dealing with pure $PbSO_4$ in terms of leaching through the citrate based hydrometallurgical recycling method used.

However, with $PbSO_4$ being the major constituent waste product in the LAB and pollution derived from widely used pyrometallurgical based recycling methods resulting in highly hazardous SO_2 fumes, a quick, easy, less polluting and financially viable option for desulphurisation may be more appropriate in areas of the world with a less developed infrastructure.

$PbSO_4$ could also easily be converted to $PbCO_3$ using sodium carbonate (Na_2CO_3) as alluded to and found by other studies[79, 81]. However, in the current study $NaHCO_3$ was used instead as this was found to avoid the conversion to hydrocerussite $Pb_3(CO_3)_2(OH)_2$ that was reported by Gong et al[79]. In their work, it was established that any $PbCO_3$ formed locally was rapidly converted to hydrocerussite and remained as the major reaction product.

6.5.2 Experimental

In the current study, it was found that the use of $NaHCO_3$ enabled a rapid reaction to occur within the pH range where $PbCO_3$ is known to be stable. The Pourbaix diagram for lead compounds in water at 24.85 °C (298 K), illustrated in Figure 6-17, demonstrates the stability range of $PbCO_3$ to be from pH 6 to 10 and was used to design a series of experiments to leach $PbSO_4$ with $NaHCO_3$ to form $PbCO_3$.

Figure 6-17 shows the calculated potential stability relationship between lead compounds in solution containing carbonate species as a function of pH. This will also become important in the following section where the manufacture of $PbCO_3$ will be explored further, together with an elaboration on the utility of $PbCO_3$ in LABs.

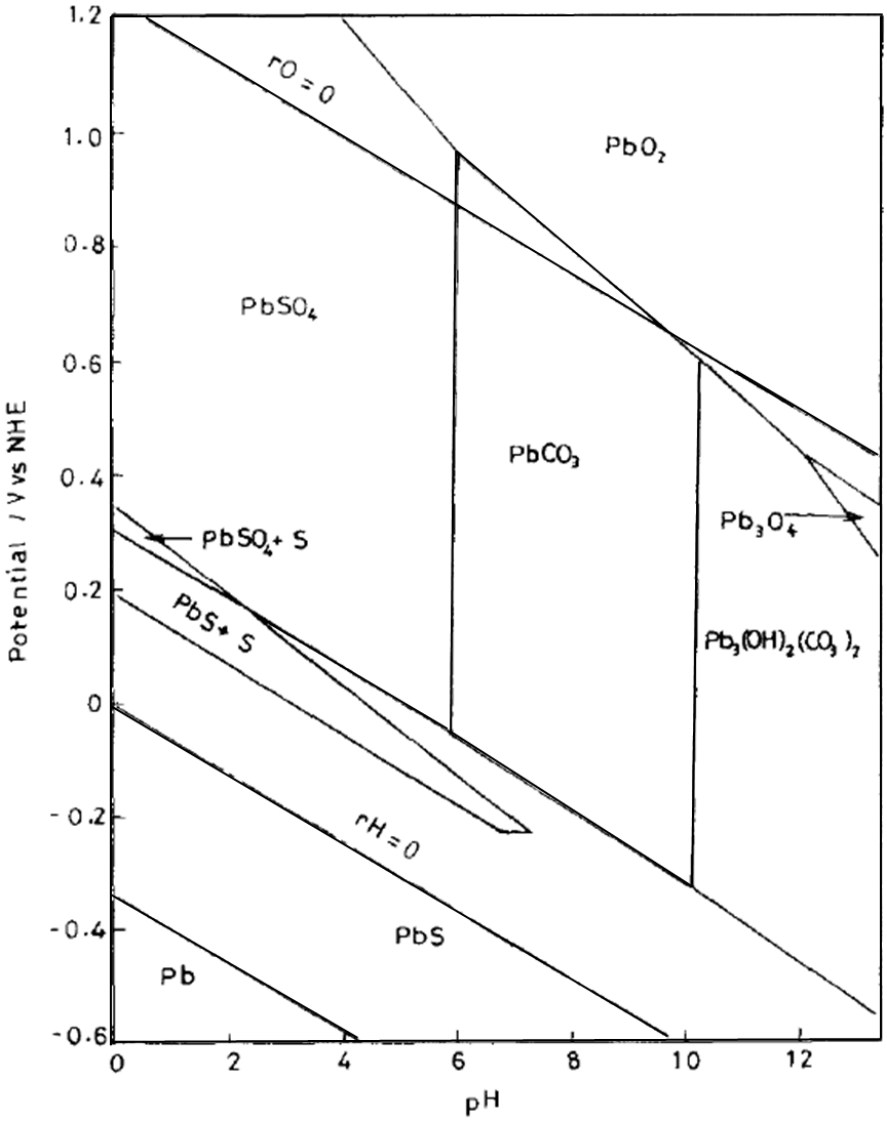

***Figure 6-17**: Pourbaix diagram of lead compounds in water at 24.85 °C (298 K). Total sulphur species a = $10^{-1.5}$, total carbonate species, a = 10^{-1}[81]*

A series of experiments was conducted using molar ratios of 1:5 through to 1:11 of $PbSO_4$ to $NaHCO_3$ with a S:L ratio of 1:30 maintained for each experiment and were stirred using a magnetic impeller at a constant rate. This was also done as a function of time from 10 minutes up to 60 at 10-minute increments to determine the reaction rate. The leaching of $PbSO_4$ can be expressed by the following:

$$PbSO_{4(S)} + HCO_3^-{}_{(aq)} \rightarrow PbCO_{3(S)} + SO_4^{2-}{}_{(aq)} + H^+{}_{(aq)} \quad \textbf{6-4}$$

$$PbSO_{4(S)} + CO_3^{2-}{}_{(aq)} \rightarrow PbCO_{3(S)} + SO_4^{2-}{}_{(aq)} \quad \textbf{6-5}$$

To facilitate the current investigation into the use of $NaHCO_3$, typical conversion rate curves for the leaching of $PbSO_4$ in carbonate solutions at 24.85 °C (298 K) like the one shown in Figure 6-18, and other salient data from other related works[70, 79, 81, 138] will be used.

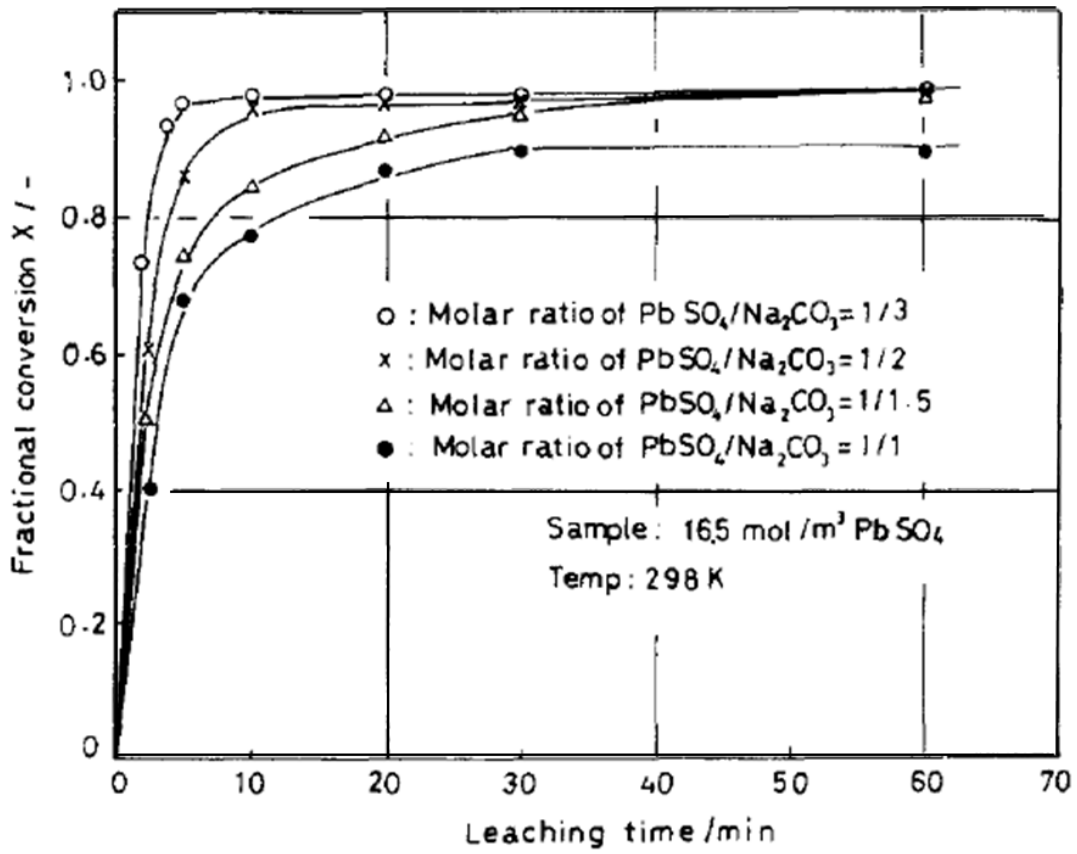

***Figure 6-18**: Typical leaching rate curves of $PbSO_4$ in carbonate solutions*[81]

The molar ratios used in this study far exceed those shown in Figure 6-18, but nonetheless was used as a guide to the expected fractional conversion of $PbSO_4$ as the rate of conversion is considered to be greatly affected by the concentration of carbonate ions in the system.

The main purpose of the current study was to determine whether the bicarbonate was able to induce the conversion of $PbSO_4$ within the stability range of $PbCO_3$ without the need to modulate the solution pH.

6.5.3 Results and Discussion

It was found that all the experiments conducted with $NaHCO_3$ proved successful in converting $PbSO_4$ into $PbCO_3$. As documented by all the studies reviewed, the rate of reaction was dependent on the initial carbonate ion concentration. However, in contrast to other findings the use of the bicarbonate reagent did not adversely affect the rate of conversion, although it is recognised that the amount used in the current study is far in excess of those from said studies.

$NaHCO_3$ was successful in acting both as the source of carbonate ions and in maintaining reaction pH within $PbCO_3$ stability region. Table 6-4, illustrates an example experiment conducted using 1:11 molar ratio of $PbSO_4$ to $NaHCO_3$.

***Table 6-4**: An example reaction using $PbSO_4$ with $NaHCO_3$ with a 1:11 molar ratio in 300 ml solution*

Reagent	Reagent Mass (g)	Measured pH and Temp (°C)	Physical Characteristic	Product Mass (g)	Expected Mass (g)	Conversion (%)
$PbSO_4$	10	5.3/20 °C	White			
$NaHCO_3$	30.05	7.7 – 8.2/18 °C	White			
				8.69	8.81	~99%

As Table 6-4 shows, the total by-product for this typical example experiment yielded 8.69 g of recoverable material. Assuming complete conversion from molar calculations of total Pb^{2+} ions present, the theoretical total $PbCO_3$ that can be obtained is 8.81 g. This gives a conversion percentage of approximately 99%. The reaction induced by $NaHCO_3$ within this stability region was attributed to the amphoteric nature of $NaHCO_3$ and will be expanded upon in the next section.

For clarity, Figure 6-19 illustrates a flow diagram of the example given in Table 6-4. Experiments conducted with 1:11 molar ratio was successful in generating $PbCO_3$ from 20 through to 60 minutes. Upon addition of $NaHCO_3$ the measured pH of reaction was around 7.7 and ended at around 8.2 where it is stabilised and conversion is assessed to be completed.

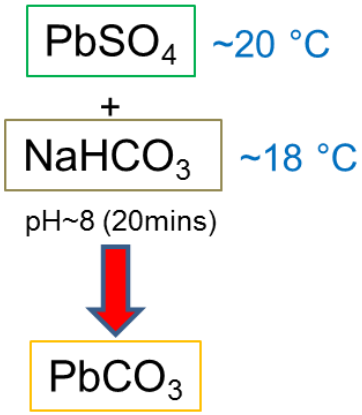

***Figure 6-19**: Flow diagram showing the sequence of forming $PbCO_3$ from commercially sourced $PbSO_4$ powder using $NaHCO_3$*

Once completed the by-products were filtered and dried overnight before XRD analysis for phase purity. Figure 6-20 illustrates an example diffraction pattern of the reaction described in the flow diagram.

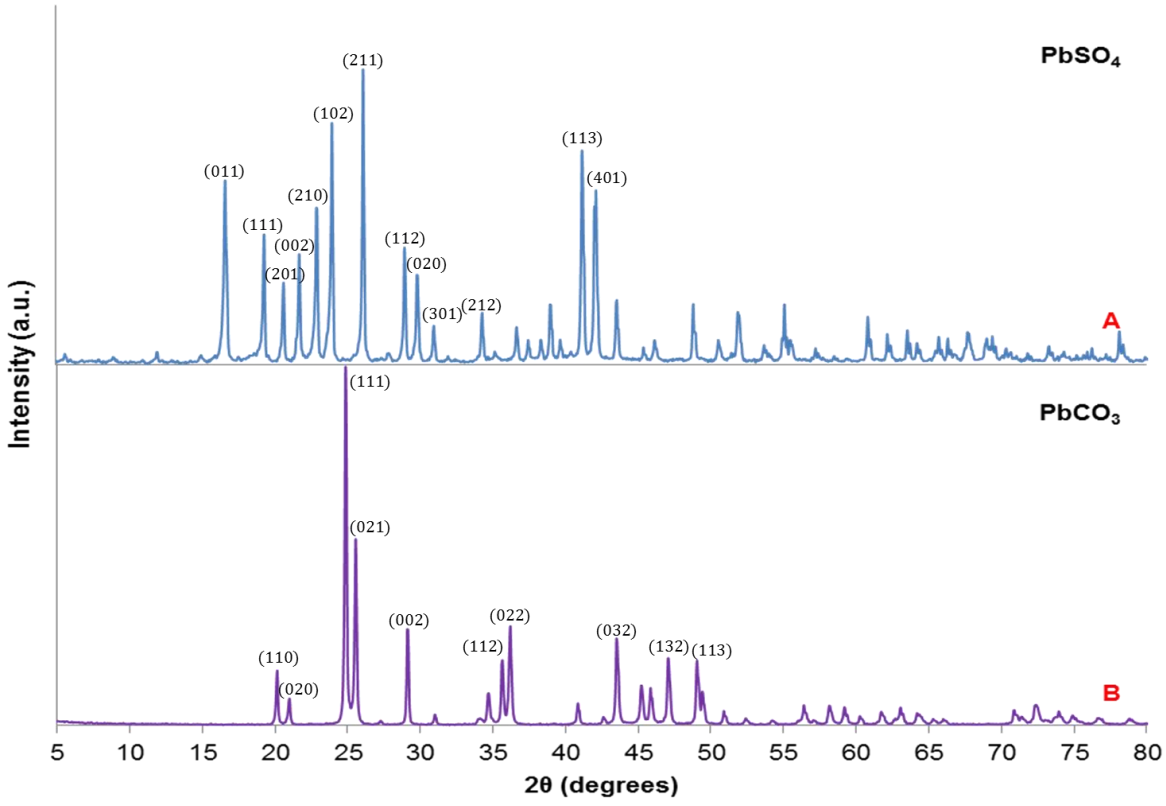

***Figure 6-20**: XRD patterns showing the chemical conversion of $PbSO_4$ from Sigma Aldrich (A) to $PbCO_3$ (B) using $NaHCO_3$ after 20 minutes*

XRD analysis of the dried sample, as seen in Figure 6-20B, demonstrated a perfect match for $PbCO_3$ (Ref code: 01-076-2056).

Additional routes of conversion to $PbCO_3$ were explored in depth where the by-products of the citrate based hydrometallurgical recycling procedure employed in this study could be used. In the following section, the work and observations discussed so far will be used and expanded upon in order to demonstrate additional avenues in exploiting the current innovations under investigation.

6.6 Chemical Synthesis of $PbCO_3$ from Lead Citrate

6.6.1 Introduction

A series of experiments was conducted to determine whether the disassociation of either forms of lead citrate by NaOH can be exploited to generate other commercially useful compounds. It was found that by reacting lead citrate, once dissolved under NaOH, with $NaHCO_3$, $PbCO_3$ can be generated.

6.6.2 Experimental

$NaHCO_3$ is an amphoteric compound. When in aqueous solution carbonic acid and hydroxide ions are formed, as shown in equation **6-6**, and therefore creates a mildly alkaline environment.

$$HCO_3^- + H_2O \rightarrow H_2CO_3 + OH^- \quad \textbf{6-6}$$

Carbonic acid is diprotic and therefore has two dissociation constants. The first constant is for the dissociation into the bicarbonate ion HCO_3^- and is shown in equation **6-7**:

$$H_2CO_3 \rightleftharpoons HCO_3^- + H^+ \quad \textbf{6-7}$$

With $K_{a1} = 2.5x10^{-4}$ and $pK_{a1} = 3.6$ at 25 °C

The second constant is for the dissociation of the bicarbonate ion into the carbonate ion CO_3^{2-} and is shown in equation **6-8**:

$$HCO_3^- \rightleftharpoons CO_3^{2-} + H^+ \quad \textbf{6-8}$$

With $K_{a2} = 4.69x10^{-11}$ and $pK_{a2} = 10.329$ at 25 °C

The diprotic nature of carbonic acid therefore means that the distribution of its dissociation products of HCO_3^- and CO_3^{2-} are themselves a function of pH. Additionally, the presence of NaOH may also generate sodium carbonate (Na_2CO_3) thus:

$$NaHCO_3 + NaOH \rightarrow Na_2CO_3 + H_2O \quad \textbf{6-9}$$

To illuminate the possible species generated from this mixture as a function of pH, Figure 6-21 illustrates the concentrations of dissolved carbonate species as a function of pH and is typically used to show the aqueous carbonate system of natural terrestrial water systems.

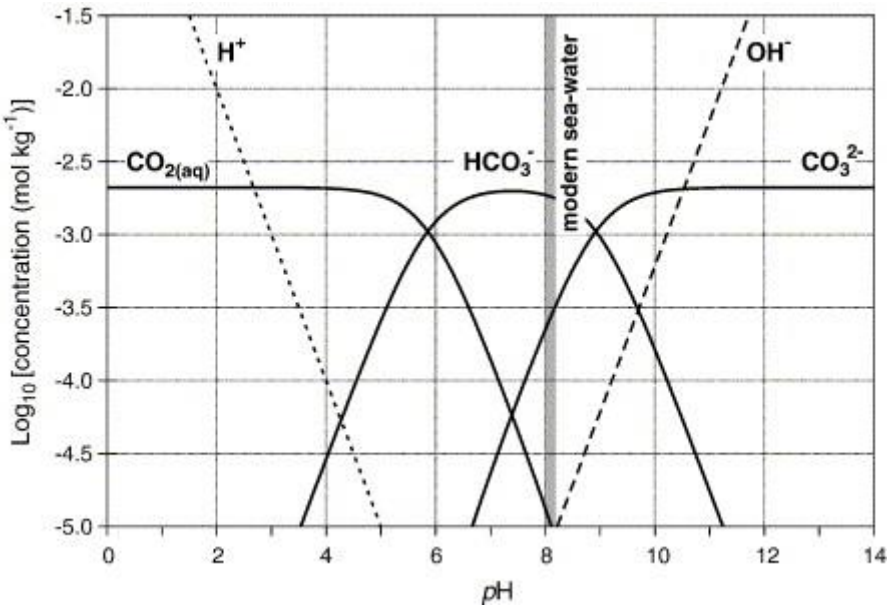

***Figure 6-21**: The concentrations of dissolved carbonate species as a function of pH. Also referred to as the Bjerrum plot*[139]

Carbonates, being weak salts of a weak acid, carbonic acid (H_2CO_3), have solubilities that are pH dependent. H_2CO_3 has an important role in the reaction process as it is essential for the O_2 isotope equilibrium since the exchange between H_2O and carbonate species occurs via H_2CO_3.

As illustrated in Figure 6-21, CO_3^{2-} is the dominate carbonate species in solution at high pH as HCO_3^- is isotopically heavier than CO_3^{2-}, the O_2 isotopic composition of the total dissolved carbonate species decreases as a function of pH[140].

As the corresponding critical pH is a function of the total dissolved inorganic carbon, the critical state of supersaturation depends on the initial concentration of $NaHCO_3$ added into the mixture. Figure 6-21 therefore can be used as a guide to determine the concentrations of the dissolved carbonate species required as a function of pH in the reacting solution.

As illustrated in Figure 6-21, the concentration of carbonate ions increases with pH until all dissolved carbonate is essentially carbonate ion. The sequence of mixing and their respective reaction times are shown in Figure 6-22 below.

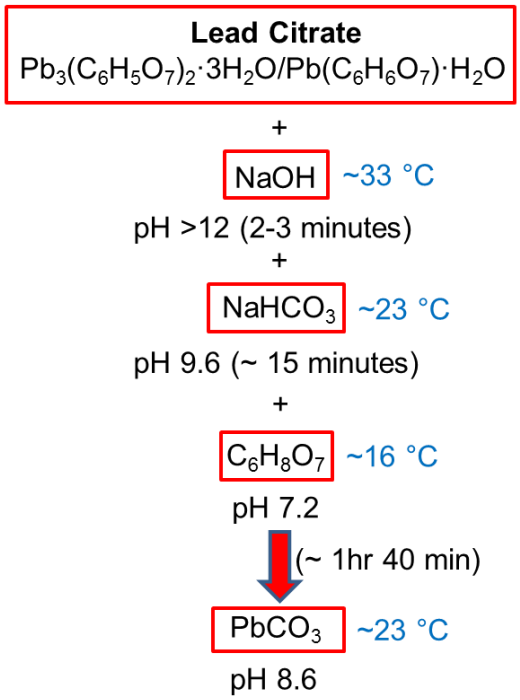

***Figure 6-22**: Sequence of mixing using lead citrate to chemically convert to $PbCO_3$*

As shown in Figure 6-22 the starting reagent was first dissolved using NaOH until a pH >12 was reached. The temperature of the solution rapidly increased to ~33 °C upon addition of NaOH. The reaction was allowed to proceed for approximately 3 minutes, at which point $NaHCO_3$ was added and the temperature decreased to ~23 °C along with the pH to around 10. In such a high alkaline environment both Pb^{2+} and CO_3^{2-} ions are expected to be mobile in the mixture and react to form $PbCO_3$.

However, since $PbCO_3$ is slightly soluble in both strong acidic and alkali conditions, it is not at equilibrium at this stage of the reaction. The pH was therefore brought down to around 7 by $C_6H_8O_7$ after approximately 15 minutes, at which point the temperature was recorded to be ~16 °C, in order to establish a heterogeneous equilibrium in favour of $PbCO_3$. Upon addition of $C_6H_8O_7$ the pH fell from around 9.6 to approximately 7 and was observed to slowly rise to approximately pH 8.6 where it remained unchanged.

The reaction appeared to have come to completion after around 1 hour 40 minutes within the pH range where $PbCO_3$ is known to be stable as seen in Figure 6-23 (and 6-17).

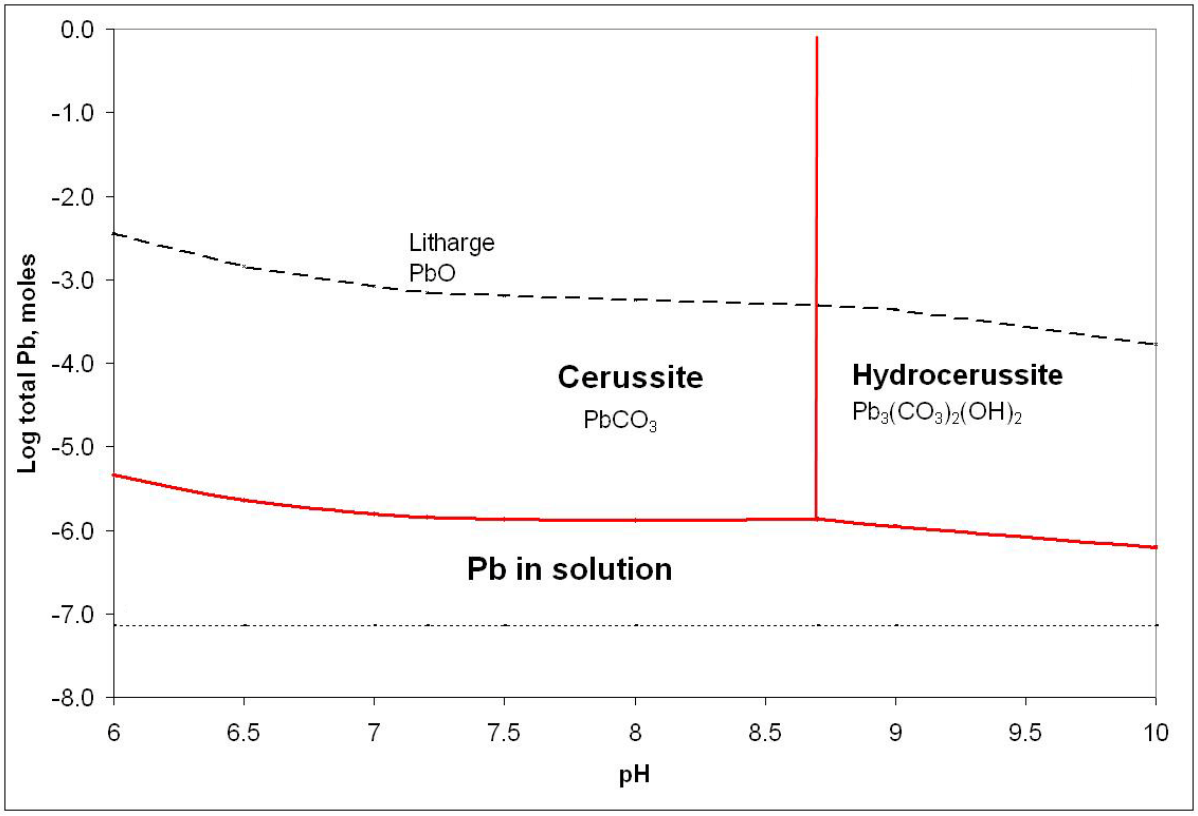

***Figure 6-23**: Lead-carbonate distribution as a function of pH*[141]

Once the reaction appeared to have stabilised the mixture was filtered and dried overnight at 80 °C. XRD was used to analyse the dried sample and was found to match perfectly with $PbCO_3$ (Ref code: 01-076-2056) as illustrated in Figure 6-24B.

6.6.3 Results and Discussion

From the results of this investigation, the procedure for the experiment appears to have established an equilibrium at pH 8.6 as shown in equation **6-10**:

$$PbCO_{3(s)} \rightleftharpoons Pb^{2+}_{(aq)} + CO_3^{2-}{}_{(aq)} \qquad \textbf{6-10}$$

The equilibrium established lies very much to the left and so can be related to the equilibrium constant or the solubility product (K_{sp}) for $PbCO_3$ outlined in expression **6-11**:

$$(K_{sp}) = [Pb^{2+}]\,[CO_3^{2-}] \qquad \textbf{6-11}$$

The K_{sp} for $PbCO_3$ is $7.4x10^{-14(142)}$. The solubility product is a value, which is obtained when the solution is saturated. In order for this equilibrium constant to apply, solid $PbCO_3$ must be present in a saturated solution of $PbCO_3$.

This means that if the Pb^{2+} and CO_3^{2-} ions in the presence of some $PbCO_3$ and the activities of the ions are multiplied the result would be $7.4x10^{-14}$. Therefore, the product of the ionic concentrations of Pb^{2+} and CO_3^{2-} in solution must exceed the solubility product in order for precipitation to occur. Once this occurs, the solid generated will reduce the concentrations of the Pb^{2+} and CO_3^{2-} ions down to a value, which the solubility product allows.

An example of one of the investigations is outlined below to give an indication of the degree of precipitation from the concentrations used in a given experiment.

In a given experiment 0.024 moles of lead citrate was mixed with 0.357 moles of $NaHCO_3$ in 0.1 L, giving concentrations of 0.24 M and 3.57 M respectively at the start of the reaction.

Since $K_{sp} = [Pb^{2+}]_{equil}\,[CO_3^{2}]_{equil}$, then the solubility quotient, or ion product, $Q_c = [Pb^{2+}]_{init}\,[CO_3^{2}]_{init}$. Substituting the initial conditions in the expression for Q_c gives:

$$Qc = (0.24)\,(3.57) = 0.857$$

Given that the value for Q_c is greater than K_{sp} precipitation of $PbCO_3$ is expected to occur under these conditions. The degree to which precipitation was complete, was further assessed by calculating the equilibrium concentration of Pb^{2+} ion remaining in the solution after $PbCO_3$ had precipitated.

Assuming a limiting reagent problem where all the $PbCO_3$ that is possible precipitates. Then using the K_{sp}, the amount that can be re-dissolved can be determined. From the initial ion products, it can be calculated that 3.3 M of CO_3^{2-} ions remain in solution after precipitation. Substituting into the K_{sp} expression for $PbCO_3$ and assuming "*x*" is negligible compared to 3.3.

Solving for "*x*" we get $x = 7.4\text{x}10^{-14} / 3.3 = 2.24\text{x}10^{-14}$ M Pb^{2+} remaining in solution. The number of moles of Pb^{2+} in the solution prior to precipitation was 0.024, therefore the percentage of Pb^{2+} remaining in the solution in this given experiment is:

$2.24\text{x}10^{-15} / 0.024 \text{ x } 100\% = 9.3\text{x}10^{-12}\%$ and would generally be considered a complete precipitation.

In addition, the extent to which dissociation products can exist in solution as a function of pH can be calculated from the solubility product, K_{sp}. Thus, the maximum concentration of a given dissociation product in solution is controlled by pH. The reaction for this experimental example was stabilised at pH 8.6. The solubility, S, of the final product can be calculated thus:

$$S = [Pb^{2+}] = \sqrt{K_{sp}\left(1 + \frac{[H^+]}{K_{a2}}\right)} \qquad \textbf{6-12}$$

Given $K_{sp} = 7.14\text{x}10^{-14}$, K_{a2} for $CO_3^{2-} = 4.8\text{x}10^{-11}$ and pH 8.6, $[H^+] = 2.5\text{x}10^{-9}$ the solubility of the synthesized $PbCO_3$ at pH 8.6 would therefore be $2\text{x}10^{-6}$ M. Since $PbSO_3$ has a mass of 267.21 g/mol, the solubility can be written as 0.0005 g/L which is consistent with results published by Clever and Jonhston[143] on investigations into $PbCO_3$ using CO_2.

The final product from this experimental procedure in generating $PbCO_3$ from lead citrate is therefore expected to be of a high purity with very little waste by-products in the filtrate, which can be reused. Indeed, the experimental output compares favourably to the expected amounts from molar calculations as predicted from the solubility calculations shown in Table 6-5.

***Table 6-5**: An example reaction using $PbSO_4$ with $NaHCO_3$ with a 1:11 molar ratio in 300 ml solution*

Reagent	Reagent Mass (g)	pH and Temp (°C)	Physical Characteristic	Product Mass (g)	Expected Mass (g)	Conversion (%)
$Pb(C_6H_6O_7)\cdot H_2O$	10	4.4	White			
NaOH	9.6	12.7/33 °C	<Turbidity			
$NaHCO_3$	30.4	9.6/23 °C	White			
$C_6H_8O_7$	18.5	7.2/16 °C	White			
				6.39	6.44	99

As Table 6-5 shows, the total by-product for this typical example experiment yielded 6.39 g of recoverable material. Assuming complete conversion from molar calculations of total Pb^{2+} ions present, the theoretical total $PbCO_3$ that can be obtained was 6.44 g. This gives a conversion percentage of approximately 99%.

The purity of the end product is reflected in the XRD analysis, which indicated a perfect match of all diffraction peaks associated with $PbCO_3$. The diffraction pattern is shown in Figure 6-24B.

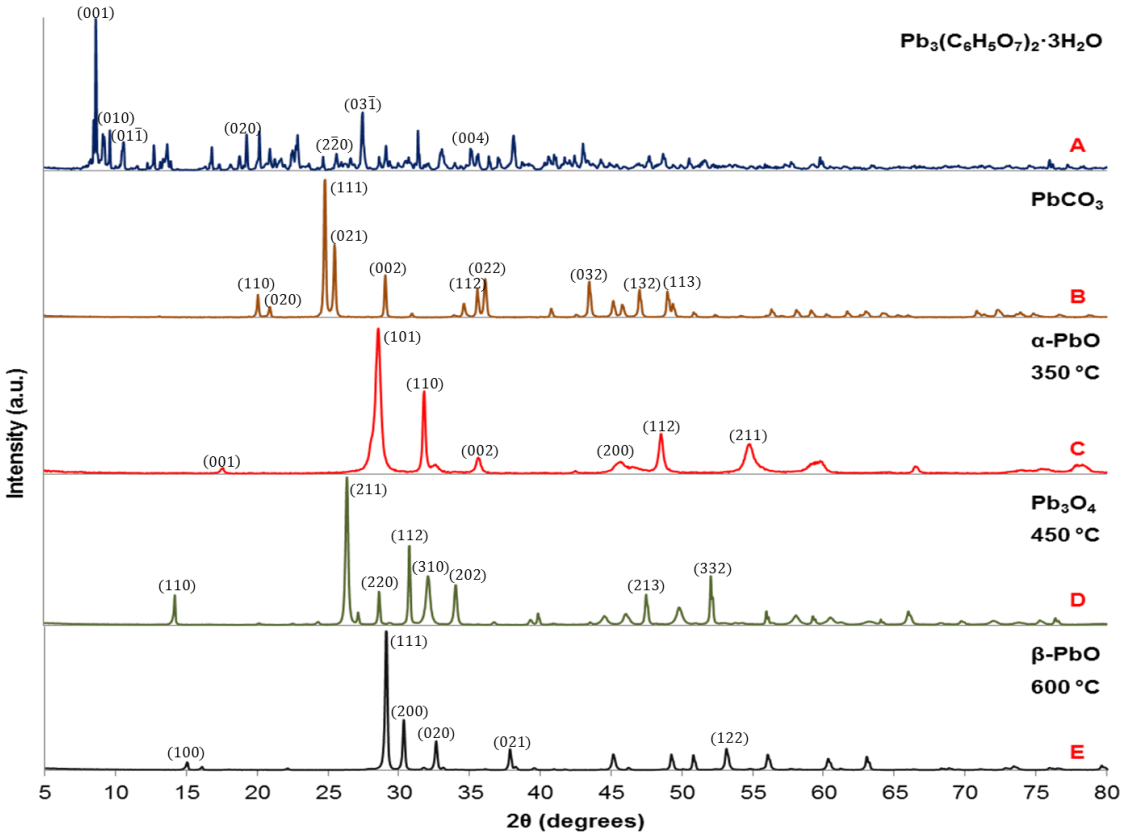

***Figure 6-24**: XRD diffraction patterns illustrating the sequence of chemical conversion of $Pb_3(C_6H_5O_7)_2 \cdot 3H_2O$ (A) to $PbCO_3$ (B). Calcination of $PbCO_3$ to pure α-PbO at 350 °C (C), Pb_3O_4 at 450 °C (D) and pure β-PbO at 600 °C (E)*

Figure 6-24A illustrates the starting compound, $Pb_3(C_6H_5O_7)_2 \cdot 3H_2O$, that was leached from a sample of depleted battery paste from industry. The compound was then converted to $PbCO_3$ in a procedure similar to the one outlined above with starting reagents slightly altered to take into account the extra Pb^{2+} in the compound.

Once the lead citrate was successfully chemically converted to $PbCO_3$ a series of calcination experiments was conducted similar to those by Sajadi et al[78]. This was to investigate the potential for a variety of useful by-products that can be generated via thermal decomposition as a function of temperature.

Figures 6-24C, D and E illustrates the XRD diffraction patterns of compounds calcined at 350, 450 and 600 °C respectively at 5 °C/min and held for one hour before being allowed to cool naturally. Analysis of the compound calcined at 350 °C demonstrated good agreement with that of α-PbO (ref. code: 03-065-0398) with no erroneous peaks.

Significantly, no free lead was detected in any of the samples as the thermal decomposition was purely through calcination without any combustion. This was also the case for the compound analysed from a sample calcined at 600 °C. This sample was determined to be pure β-PbO (ref. code: 00-005-0570).

As with the previous examples of chemical conversion to generate pure α and β-PbO from lead citrate, $PbSO_4$ and commercial PbO outlined earlier, the absence of free metallic lead in any of these samples may preclude their use in LABs as the apparent reactivity with the electrolyte is significantly reduced compared to the state of the art.

However, they may find use in Schottky-type photovoltaic devices as it has been demonstrated that they can be used in the photoactive layer[144, 145]. It has been further shown that β-PbO can be used as a surface modification layer in inverted polymer solar cells for lowering work function[146]. The band-gap of α-PbO of 1.9 eV[147, 148] is of particular interest in photovoltaic applications[149].

The significance to LABs of these experiments is the manufacture of Pb_3O_4 from the calcination of $PbCO_3$ at 450 °C. This is confirmed by XRD analysis as shown in Figure 6-24D. The diffraction pattern is a perfect match for Pb_3O_4 (ref. code: 00-041-1493). Figure 6-25 illustrates a powder sample of $PbCO_3$ (A) before and after calcination at 450 °C (B)

***Figure 6-25**: $PbCO_3$ (A) from $Pb_3(C_6H_5O_7)_2 \cdot 3H_2O$ calcined at 450 °C to form Pb_3O_4 (B)*

As shown in Figure 6-25B, the calcination of $PbCO_3$ at 450 °C produced the distinctive orange crystalline compound, Pb_3O_4. The use of Pb_3O_4 is widespread in the LAB industry as it is more conductive than PbO due to its higher oxidation state and so facilitates the electrochemical formation of PbO_2[150]. It is also reported to improve the initial capacity performance of LABs and increase their cycle life[13]. An increase in acid absorption has also been attributed to presence of Pb_3O_4[14].

The microstructure of the chemically converted $PbCO_3$, thermally generated α-PbO, Pb_3O_4 and β-PbO were analysed using SEM and are shown in Figure 6-26A, B, C and D respectively.

The SEM images illustrate the changes in morphologies of the calcined products and the differences in the shape and size of each compound as a function of reaction temperature.

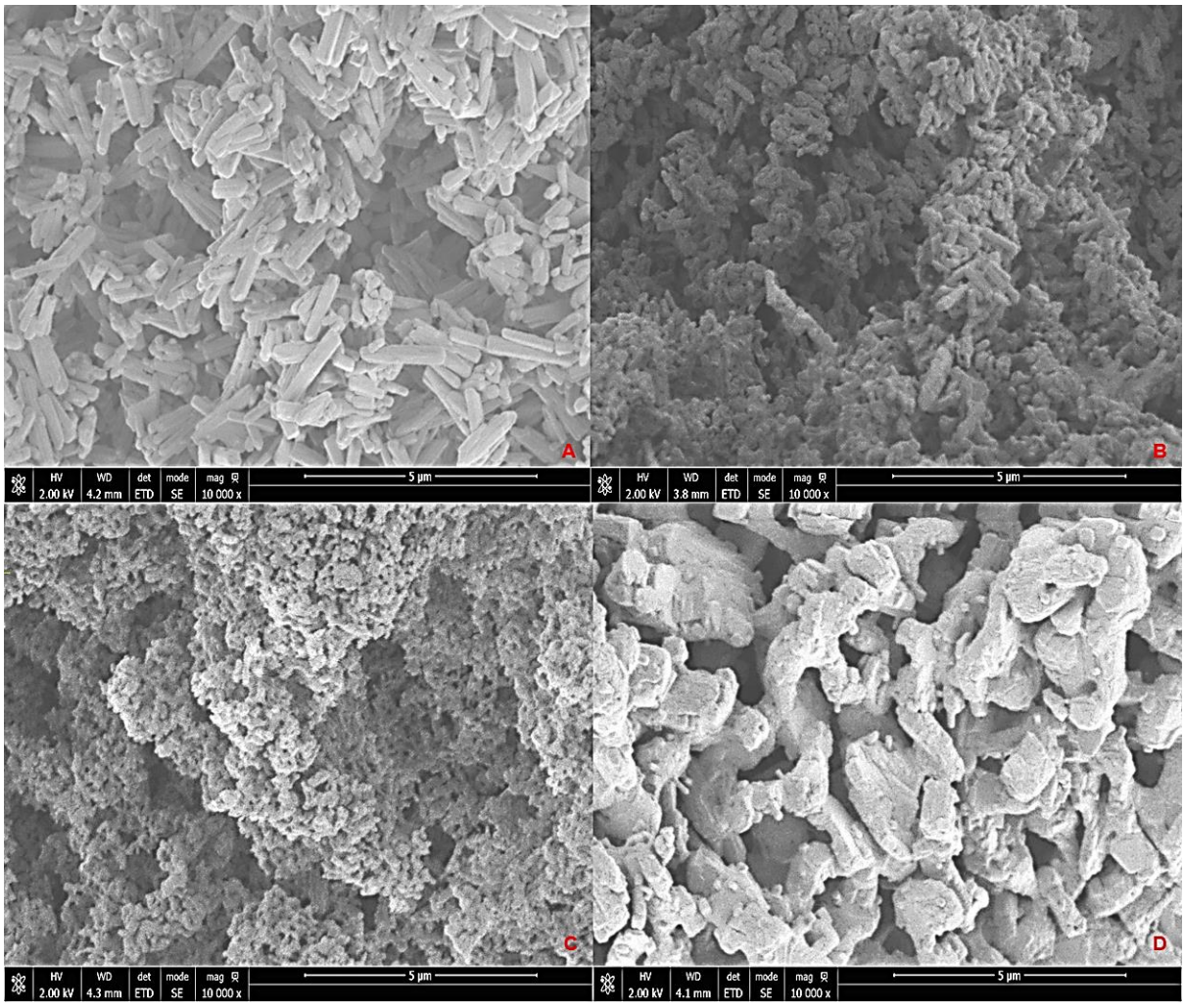

***Figure 6-26**: SEM imagery of $PbCO_3$ (A), chemically converted from $Pb_3(C_6H_5O_7)_2 \cdot 3H_2O$, and calcined to α-PbO at 350 °C (B), Pb_3O_4 at 450 °C (C) and β-PbO at 600 °C (D). All at x10,000 magnification for comparison*

The starting compound illustrated in Figure 6-26A shows a microstructure that is dominated by a series of randomly distributed and elongated particles that are 2-3 µm in length. The calcined product at 350 °C shown in Figure 6-26B demonstrates the breakup of the initial microstructure, forming smaller particles with some elongation still evident.

As the calcination temperature increased to 450 °C, the microstructure became more uniform with general particle size distribution becoming more homogenous. The particles became smaller and rounder with sizes in the 200-300 nm range. Some agglomeration is evident as inter-particulate coalescence begins to become visible.

Indeed, as the calcination temperature reached 600 °C larger particles have formed with large scale agglomeration clearly visible. As illustrated in Figure 6-26D, the elevated temperature has resulted in large interlocking particles with highly textured surfaces from incomplete inter-particulate coalescence.

6.7 Thermal Treatment of α-PbO and $PbCO_3$ with Glycerol

6.7.1 Introduction

Although both the chemically and thermally generated α and β-PbO may prove commercially and technologically useful in future photovoltaic devices, they have limited utility in their current form in LABs.

A series of experiments was conducted using glycerol ($C_3H_8O_3$) as a reducing agent mixed in either acetone (C_3H_6O) or isopropanol (C_3H_8O) of varying mass fractions between the principal reagent and the given delivery media. Mixtures of 1 to 7 wt. % glycerol were added to samples of α-PbO and magnetically stirred while under heating.

The use of glycerol as a reducing agent has been explored by many researchers for generating nanoparticles and commercially valuable compounds[151-154].

These experiments were designed to uniformly entrain the optimum amount of glycerol into the α-PbO in order to thermally reduce a sufficient volume fraction of a given compound to generate metallic lead with the intention of increasing its reactivity for use in a LAB as desired by industry for commercialisation.

6.7.2 Experimental

Laboratory grade acetone sourced from Sigma Aldrich was chosen as the primary delivery media for the glycerol due to its high vapour pressure at room temperature and relative low cost. The glycerol incorporated mixture was coated and absorbed into the α-PbO powder while under magnetic stirring as the heat from the hotplate evaporated the acetone leaving the glycerol entrained in the compound.

A 1 to 3 solid to liquid ratio with 5 wt. % glycerol in acetone and within a temperature range of 330-350 °C at 10 °C/min for 1 hour was found to be the optimum combination to generate PbO dominated by the tetragonal phase with metallic lead in the compound.

6.7.3 Results and Discussion

Figure 6-27 illustrates XRD patterns of a sample of α-PbO before and after glycerol induced thermal reduction of some of the compound.

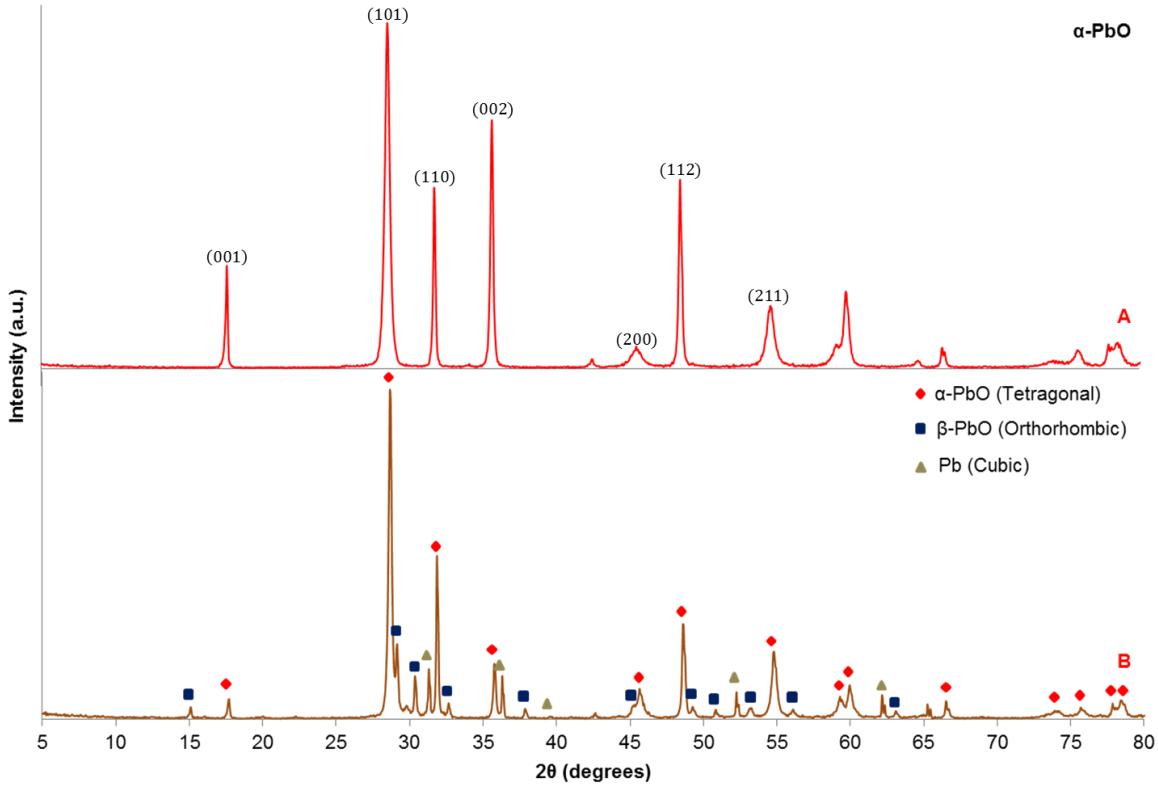

***Figure 6-27**: XRD patterns of chemically generated pure α-PbO (A) from $Pb_3(C_6H_5O_7)_2 \cdot 3H_2O$ to PbO with metallic Pb after combustion at 330 °C at 10 °C/min for 1 hour using 5 wt. % glycerol in acetone (B)*

Figure 6-27 shows a comparison of two XRD patterns demonstrating the change in phase composition as the result of glycerol partial thermal reduction of a sample of α-PbO (A) that had been chemically converted from $Pb_3(C_6H_5O_7)_2 \cdot 3H_2O$.

The sample was mixed with 5 wt. % glycerol in acetone. It was then dried and heated to 330 °C at 10 °C/min and held for 1 hour before being allowed to cool. As illustrated in Figure 6-27B, α-PbO was successfully partially reduced to generate metallic lead in the system, which also resulted in the formation of the orthorhombic crystal phase.

The experiment with glycerol was replicated with $PbCO_3$ to determine the effects of the reductant on the compound as it is heated to 350 °C where α-PbO is known to form. The glycerol mixture together with $PbCO_3$, while under magnetic agitation, was heated simultaneously to evaporate the acetone in order to leave the glycerol entrained in the compound. A 1 to 3 solid to liquid ratio with 5 wt. % glycerol in acetone was used in the experiment.

The dried compound was then calcined at a temperature of 350 °C at 10 °C/min for 1 hour. Figure 6-28 illustrates the XRD patterns of the sample of $PbCO_3$ (A) before and after calcination with glycerol (C). Figure 6-28B is a diffraction pattern of α-PbO calcined from $PbCO_3$ without glycerol for comparison.

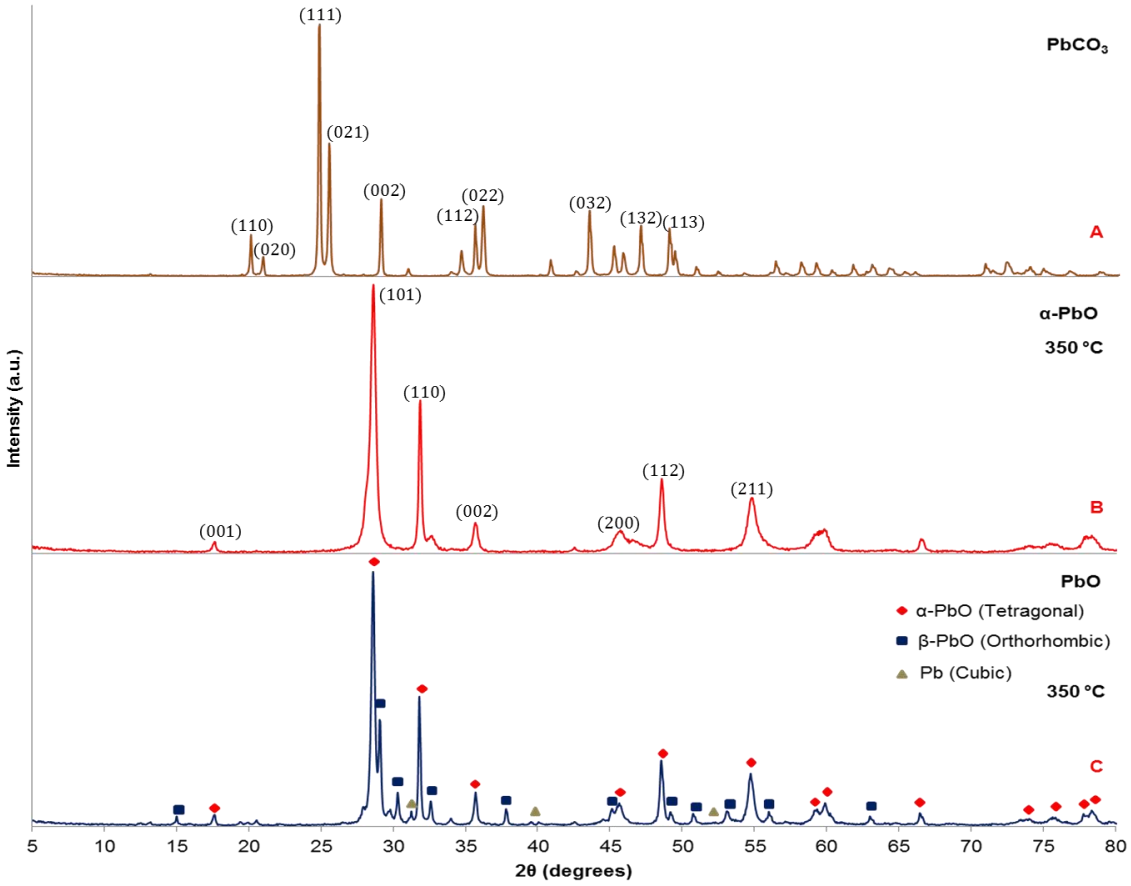

***Figure 6-28**: XRD patterns of chemically converted $PbCO_3$ (A) from $Pb_3(C_6H_5O_7)_2 \cdot 3H_2O$ combustion-calcination at 350 °C at 10 °C/min for 1 hour generating pure α-PbO (B) and with 5 wt. % glycerol in acetone generating PbO with metallic lead and minor β-PbO (C)*

As the XRD patterns in Figure 6-28 shows, the glycerol was successful in enabling a combustion-calcination reaction together with $PbCO_3$ (A) to generate α-PbO (C) containing metallic Pb at 350 °C. Figure 6-28B shows a diffraction pattern of a sample calcined from $PbCO_3$ without glycerol for comparison and illustrates the difference the phase proportion between the tetragonal and orthorhombic polymorphs as the direct result of the glycerol induced reduction.

A possible mechanism for this reaction might emanate from the release of hydrogen within the powder matrix from the reforming of glycerol[155]. The reforming of glycerol is represented as:

$$C_3H_8O_{3(l)} + 3/2O_{2(g)} \rightarrow 3CO_{2(g)} + 4H_{2(g)} \quad \textbf{6-13}$$

The rate of the heterogeneous gas-solid reaction may then be determined by the diffusion of the H_2 released from this reaction through the gas film at the exterior surface of the powder. As suggested by Culver et al[156] the reduction of PbO may be presumed to progress in the following manner:

- Activated adsorption of H_2 on the surface of PbO
- Surface reaction of the adsorbed H_2 to form Pb and H_2O
- Desorption of H_2O from the reaction interface

The overall reaction can be represented as:

$$PbO_{(s)} + H_{2(g)} \rightarrow Pb_{(s)} + H_2O_{(g)} \quad \textbf{6-14}$$

Another possibility, and the most likely is thermal reduction from the incomplete combustion of glycerol. This may arise from poor thermal input due to the insulation of the glycerol within the powder matrix. Incomplete combustion of glycerol within the powder matrix can lead to the production of carbon and carbon monoxide as reducing agents. These reactions can be represented as follows:

$$PbO_{(s)} + C_{(s)} \rightarrow Pb_{(s)} + CO_{(g)} \quad \textbf{6-15}$$

$$PbO_{(s)} + CO_{(g)} \rightarrow Pb_{(s)} + CO_{2(g)} \quad \textbf{6-16}$$

It is expected that both reactions would occur, with carbon first being partially oxidised to form CO as shown in eq **6-15**, and would then be involved in further reduction as represented in eq **6-16**. A mixture of gases would be expected with CO_2 being the dominate form.

Such reduction reactions with glycerol have been reported to generate nanoparticles[151, 154]. Indeed, from Figure 6-29 a comparison of two SEM images are illustrated between α-PbO before (A) and after (B) glycerol facilitated reactions, showing a greater distribution of nanostructured particles after reduction.

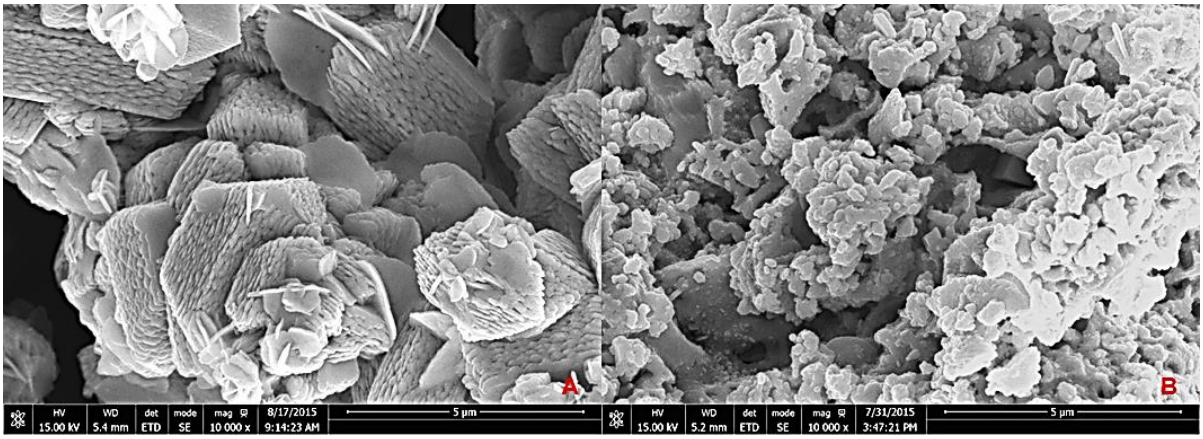

***Figure 6-29**: SEM imagery of chemically converted α-PbO (A) from $Pb(C_6H_6O_7)\cdot H_2O$ at x10,000 magnification before and after combustion at 330 °C at 10 °C/min for 1 hour with 5 wt. % glycerol in acetone (B)*

As shown in Figure 6-29 the partial thermal reduction of α-PbO has led to a general decrease in particulate size as illustrated between micrograph (A) to (B). This is likely due to surface reactions on the PbO with phase boundary responses occurring between adsorbed reducing agents and the compound.

These reactions would lead to an increase in the concentration of Pb ions and electrons resulting in the diffusion of Pb ions and electrons to Pb nuclei at the Pb/PbO interface. Phase boundary reactions at the Pb/PbO interface will occur as a result, where Pb ions and electrons are transferred into the metallic phase[156], thus creating smaller distinct new particles.

Figure 6-30 illustrates SEM imagery of the microstructure of $PbCO_3$ (A) compared to α-PbO (B) that was calcined without glycerol at 350 °C together with the calcination product heated at the same temperature with glycerol (C) which XRD identified as being PbO with a high α to β ratio containing metallic Pb.

Figure 6-30D illustrates an EDX map of a sample from (C) where the oxides are highlighted in red and lead in green.

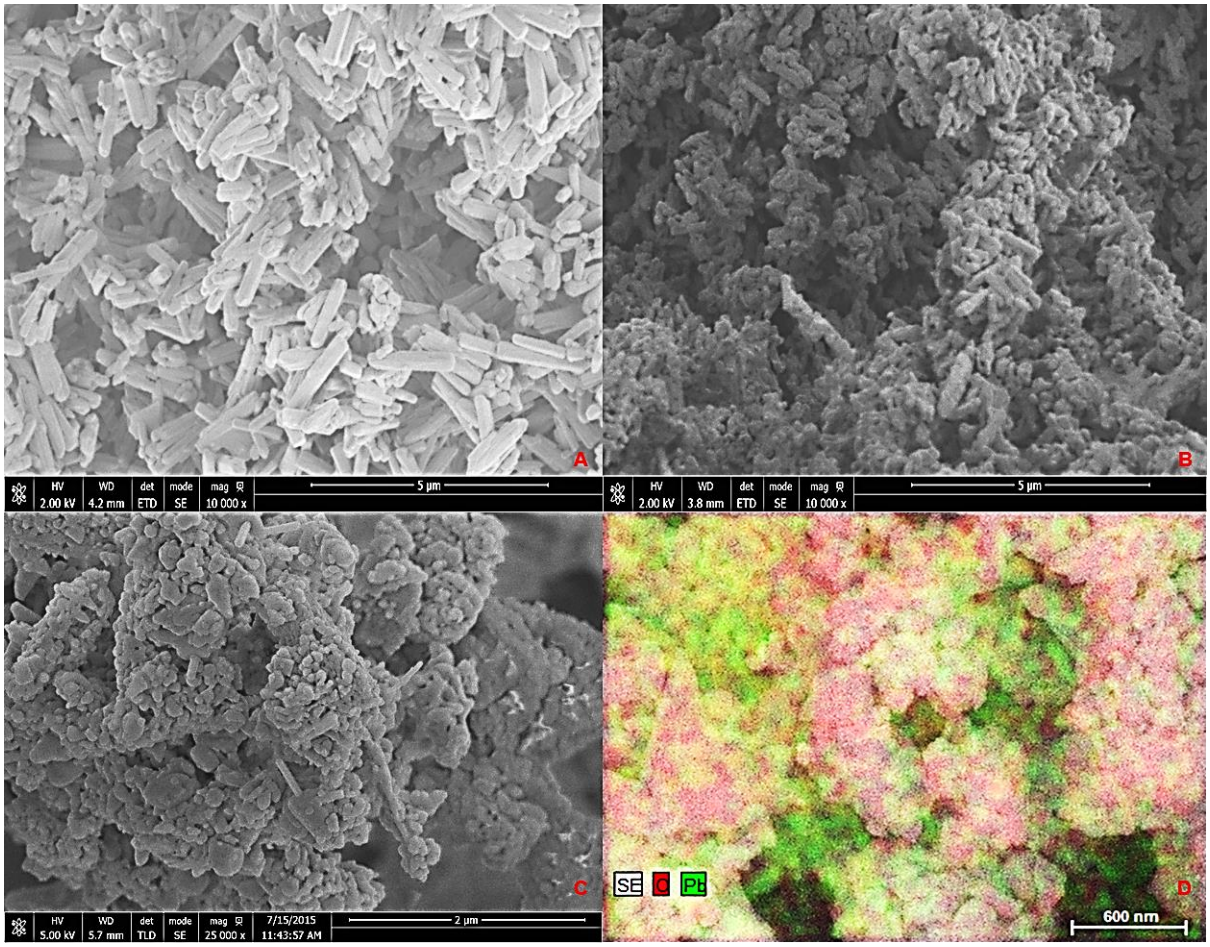

***Figure 6-30**: SEM imagery of chemically converted $PbCO_3$ (A,) from $Pb_3(C_6H_5O_7)_2 \cdot 3H_2O$, combustion-calcination at 350 °C at 5 °C/min for 1 hour generating pure α-PbO (B) and with 5 wt. % glycerol in acetone generating PbO with metallic Pb and minor β-PbO (C) with EDS mapping of sample (D)*

The combustion of the entrained glycerol combined with the calcination of $PbCO_3$ to PbO has resulted in generating a microstructure that appears to contain a greater proportion of rounded and spherical particles as illustrated in Figure 6-30C, compared to the microstructure of pure α-PbO calcined without glycerol as depicted in Figure 6-30B.

These rounded particles of various sizes ranging from tens of nanometres to hundreds, appear fused and agglomerated forming larger clusters. The general morphology appears more compact compared to that seen in B, while retaining some topological features seen in α-PbO, the microstructure observed here is similar to that seen in PbO generated from the combustion-calcination of lead citrate.

EDS mapping was used to analyse the thermally treated sample to determine the distribution of metallic lead relative to the oxide in the PbO system. As seen in Figure 6-30D the metallic Pb, shown in green, has formed distinct layers adjacent to the oxide. This may prove beneficial in serving as a conduction pathway in an electroactive paste.

To test the reactivity of the treated compounds, a series of titrations were conducted to measure the difference in the degree of interaction with H_2SO_4 of each sample. Table 6-6 illustrates a comparison of the acid reactivity of laboratory grade PbO with those generated from the current study with and without glycerol.

***Table 6-6**: Comparative reactivity between analytically pure PbO (A), chemically converted α-PbO (B), thermally partially reduced α-PbO using glycerol (C) and calcination of $PbCO_3$ with glycerol (D)*

Sample	**PbO (A)**	**α-PbO (B)**	**α-PbO (C)**	**PbO (D)**
Characteristic	Commercial	Chemically converted	330 °C w/t glycerol	350 °C from $PbCO_3$ w/t glycerol
Acid reactivity (mg/g)	105	114.3	99.1	121

As Table 6-6 shows, the chemical conversion from a commercially sourced sample of PbO (A) to pure α-PbO (B) had the effect of slightly increasing the reactivity of the compound. However, the partial thermal reduction of the same sample of α-PbO using glycerol (C), although had the desired consequence of introducing metallic lead into the system, resulted in lowering the reactivity.

A broader study will be required to determine whether this is a general trend or an artefact of this particular procedure of manufacture. The partial thermal reduction of α-PbO, though it generated smaller particles and therefore increased the surface area of the microstructure, may have decreased the absorption properties of the powder as a result of sintering from incomplete combustion of the entrained glycerol, thus acting as a barrier to absorption/reaction.

The increase in reactivity measured in the PbO generated from $PbCO_3$ shown in D, compared to sample C could be due to the combination of processes occurring in the $PbCO_3$.

A more complete combustion reaction from the entrained glycerol in $PbCO_3$, together with its calcination to PbO and partial reduction to metallic Pb, could have resulted in a more reactive compound. The difference in the two processes that may have resulted in the differing reactivity could be summarised by the nature of the reactions that dominated in the two respective routes to generating PbO; reduction-sintering in the α-PbO to PbO and calcination-reduction in the $PbCO_3$ to PbO.

This reinforces the observation made on other reactivity results throughout the current study; large variations can arise from the smallest changes in experimental procedure and therefore it is important to take into account the smallest alteration in manufacturing methods and the differences they create.

6.8 Summary

Pure α-PbO was generated from both forms of lead citrate, $Pb(C_6H_6O_7)\cdot H_2O$ and $Pb_3(C_6H_5O_7)_2\cdot 3H_2O$, synthesised in this study through disassociation reactions using NaOH. Pure β-PbO was also generated from $Pb(C_6H_6O_7)\cdot H_2O$ and $Pb_3(C_6H_5O_7)_2\cdot 3H_2O$ using NaOH, but through dissolution/re-precipitation reactions.

It was found that pure α-PbO could also be filtered out of micron sized PbO powders normally containing both the α and β phases using 0.67 M NaOH. The same dissolution/re-precipitation reaction that generated pure β-PbO from $Pb(C_6H_6O_7)\cdot H_2O$ and $Pb_3(C_6H_5O_7)_2\cdot 3H_2O$ using NaOH was also observed for $PbSO_4$. The microstructure of the β-PbO from lead citrate and $PbSO_4$ were noted to be very different in terms of particulate shape and size, but similar in terms of surface texture on particulate sheets that both have in common with.

$NaHCO_3$ was found to be successful in acting both as a source of carbonate ions and in maintaining reaction pH within the $PbCO_3$ stability region when used to leach $PbSO_4$. The reaction induced by $NaHCO_3$ within this stability region was attributed to the amphoteric nature of $NaHCO_3$ and resulted in a conversion percentage of approximately 99%.

$PbCO_3$ was also successfully generated from $Pb(C_6H_6O_7)\cdot H_2O$ and $Pb_3(C_6H_5O_7)_2\cdot 3H_2O$ using NaOH, $NaHCO_3$ and then an acid in a series of dissociation and reprecipitation reactions. The $PbCO_3$ was then used to thermally generate α and β-PbO as well as Pb_3O_4 by calcination at 350, 600 and 450 °C respectively. Glycerol was entrained in both $PbCO_3$ and α-PbO as an in-situ reducing agent to generate PbO containing metallic Pb.

7 Combustion Synthesis of PbO in Carbon Dioxide

7.1 Introduction

The current research aims to mitigate some of the major drawbacks of the LAB and is focused on the manufacture of nanostructured PbO from lead citrate derived from the low temperature hydrometallurgical process used in the leaching and recycling of spent LABs that has proven successful both here and elsewhere[76, 77].

During the plate formation process PbO is converted, via Pb, into basic $PbSO_4$. The type of basic $PbSO_4$ in the paste affects the structure of the active materials formed, especially of the PbO_2 active mass. The active mass structure in turn determines the charge/discharge cycling performance of the battery. Experience from industry has shown that for batteries produced with tribasic lead sulphate ($3PbO{\cdot}PbSO_4{\cdot}H_2O$) pastes, the maximum allowable content of β-PbO is 10 wt. %. If tetrabasic lead sulphate ($4PbO{\cdot}PbSO_4$) pastes are used, however, this upper limit is increased to 20 wt. %. The above limits hold for positive battery plates. The phase composition of the pastes for negative plates is of minor importance, because no $4PbO{\cdot}PbSO_4$ crystals are formed as $PbSO_4$ and basic lead sulphate are dissolved with the Pb^{2+} ions reduced to Pb. Here, the content of β-PbO should not exceed 15 wt. %[157].

Thus, control of the α-PbO to β-PbO ratio is of fundamental importance for the quality of the batteries[13]. The active mass obtained from $4PbO{\cdot}PbSO_4$ paste has led to increased cycle life compared to those produced from $3PbO{\cdot}PbSO_4{\cdot}H_2O$ paste[158]. This has been attributed to the discrete elongated $4PbO{\cdot}PbSO_4$ crystals of approximately 22 microns in length[159]. The larger crystal size compared to the $3PbO{\cdot}PbSO_4{\cdot}H_2O$ also give rise to a smaller pore surface in the active masses obtained from $4PbO{\cdot}PbSO_4$ pastes[160].

It was established that $4PbO{\cdot}PbSO_4$ paste could only be obtained from an initial three-component mix of $3PbO{\cdot}PbSO_4{\cdot}H_2O$ with β-PbO and α-PbO without organic capillary active substances. In addition, the presence of Pb_3O_4 facilitates the nucleation of $3PbO{\cdot}PbSO_4{\cdot}H_2O$ and in turn the nucleation of $4PbO{\cdot}PbSO_4$ crystals[160]. It has been determined in the current study as well as others [74, 83, 115, 116] that the combustion of lead citrate yields nanostructured PbO that contains a higher proportion of the β form than the α configuration. It would therefore be desirable to be able to control the α-PbO to β-PbO ratio to further optimise the utility of the citrate recycling route by producing the favoured basic $PbSO_4$ configuration to facilitate longer battery cycling-life.

Work previously conducted by Sajadi et al[78] has demonstrated that pure forms of the α and β PbO can be generated by the calcination of $PbCO_3$ at 350 and 600 °C respectively and has been demonstrated in the previous chapter.

However, unlike the combustion-calcination of lead citrate, the calcination of $PbCO_3$ does not produce any of the free metallic Pb required to form the necessary conductive skeletal structure needed in an effective battery paste.

In the current study, lead citrate is heated using a number of heating protocols under different concentrations of CO_2.

It is speculated that lead citrate can form $PbCO_3$ at a given concentration of CO_2 at a given temperature range. If correct, this gives rise to the possibility of combining the calcination of $PbCO_3$, as discussed above, with the combustion of lead citrate which could enable the synthesis of a PbO compound with a high proportion of the α polymorph. This process may furthermore allow for the control of the α:β ratio as a function of CO_2 concentration, while retaining the highly reactive pyrophoric lead produced through the citrate combustion mode.

7.2 Experimental

Lead citrate of the form $Pb_3(C_6H_5O_7)_2 \cdot 3H_2O$ was used in the following investigation into the use of CO_2 of various concentrations in combustion experiments in an attempt to control the α:β ratio in PbO. XRD was used to analyse all by-products.

Thermal analyses of lead citrate were performed in alumina crucibles by a TGA/DSC 1 from Mettler Toledo in static air, 10% and 50% CO_2 concentrations with gas flow of up to 100 ml/min. In the principal lead citrate experiments each sample was heated from 50 to 350 and 450 °C at a rate of 10 °C/min.

All samples were held at their respective temperatures for 30 minutes and were cooled in ambient atmosphere. A slower heating rate of 1 °C/min was also used over temperature ranges of interest. One sample was heated to 250 °C at 10 °C/min before the slower rate was initiated between 250-300 °C. This was replicated for the temperature range 300-350 °C. Both of these experiments were conducted in 50% CO_2.

A number of samples of $Pb_3(C_6H_5O_7)_2 \cdot 3H_2O$ were then used in a tube furnace in separate combustion experiments using industrial grade CO_2 under a variety of concentrations to simulate the applicability of industrial scale-up. SEM/EDS, BET, BJH, apparent density and titration measurements were used to determine any microstructural changes that may have occurred as a function of CO_2 concentration and their effects on the reactivity of the by-products.

7.3 Results and Discussion

7.3.1 Thermal Analysis

The thermal decomposition characteristics of lead citrate were analysed in air, 10% and 50% concentrations of CO_2. The thermogravimetric and corresponding heat flow data for a sample of lead citrate heated to 350 °C are displayed in Figure 7-1. The TG curves in Figure 7-1 illustrate very similar trends up to around 300 °C where the initial stages of weight loss appear in the 90-180 °C temperature range.

The weight loss in this region is around 4.5 to 5% and is assessed to be due to the dehydration of the citrate.

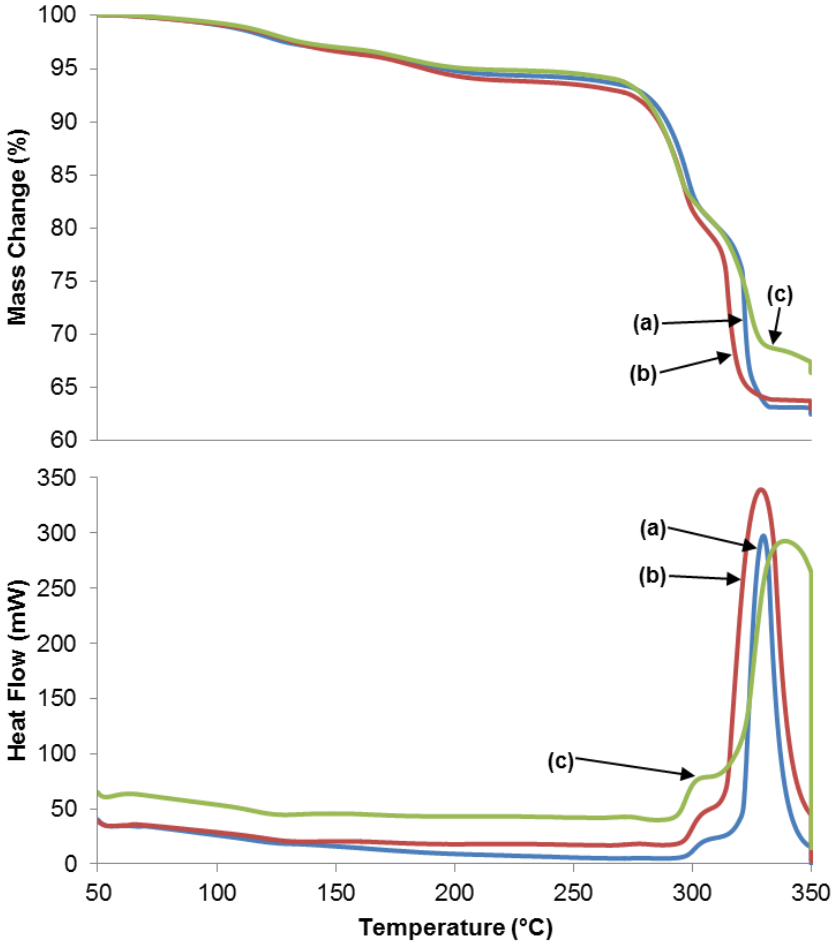

***Figure 7-1**: TGA and heat flow data from $Pb_3(C_6H_5O_7)_2 \cdot 3H_2O$ decomposition at 350 °C in air (a), 10% CO_2 (b) and 50% CO_2 (c)*

The general thermal characteristics observed in Figure 7-1 are also reflected in the data gathered in Figure 7-2 where both TG and heat flow information are shown for a sample of $Pb_3(C_6H_5O_7)_2 \cdot 3H_2O$ heated to 450 °C. Both sets of data display very similar decomposition characteristics with minor variations including in the overall difference in weight loss.

Both sets of data also illustrate further weight loss between 180-250 °C where dehydration appears to continue. By around 275 °C the heat flow data from both samples show a slight increase which is interpreted as the formation of C=C bonds from the transformation of some the citrate to aconitate. Immediately following this transformation, a significant increase in heat flow is observed in both samples with corresponding weight lost in the 280-350 °C temperature range. This is recognised as being due to the combustion of the citrate[161].

The significant increase in the heat flow suggests the compound is self-heating with variations in the magnitude, seen in both data sets, assessed to be due to different CO_2 concentrations and corresponding change in O_2 content. The various heat flow fluctuations from 270 °C onwards are attributed to the oxidation of carbon and hydrogen[161].

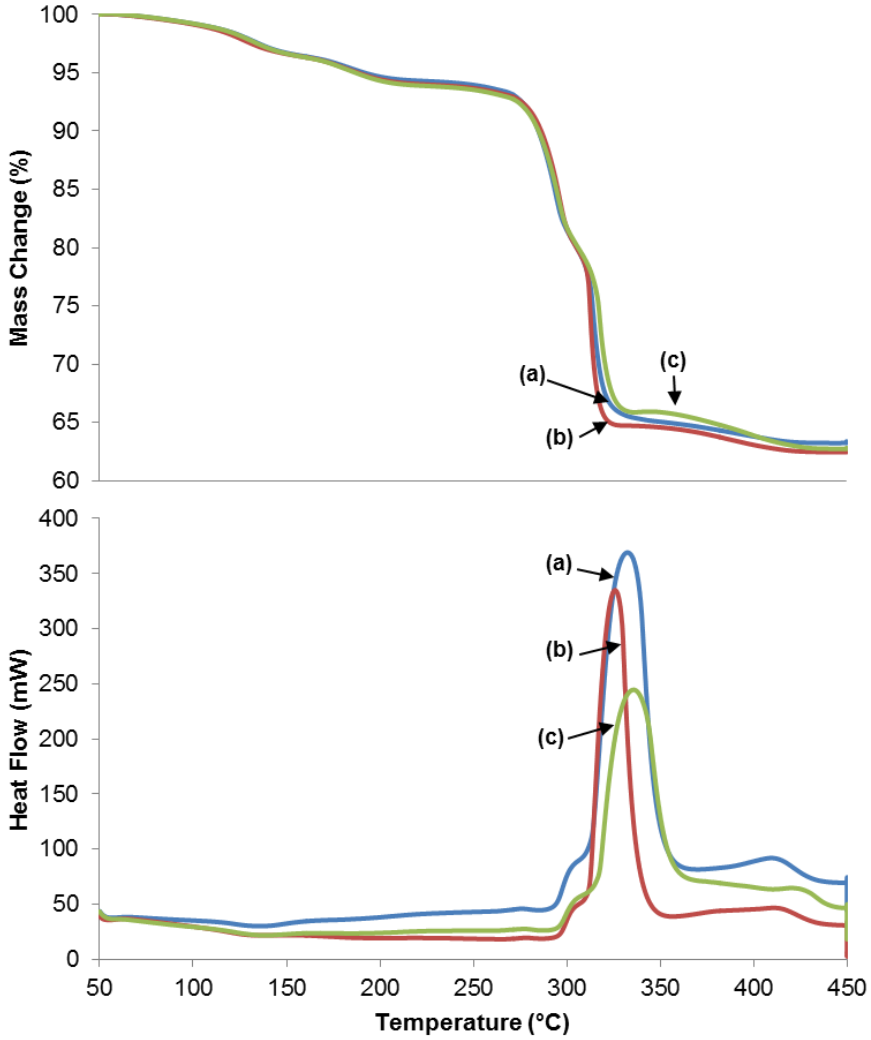

***Figure 7-2**: TGA and heat flow data from $Pb_3(C_6H_5O_7)_2 \cdot 3H_2O$ decomposition at 450 °C in air (a), 10% CO_2 (b) and 50% CO_2 (c)*

XRD analysis indicated the presence of some $PbCO_3$ peaks, as shown in Figures 7-5 and 7-6. $PbCO_3$ has been observed to form around 230-270 °C due to CO_2 and has been noted to be an intermediate compound prior to the formation of PbO[162].This is better illustrated by Figure 7-3, where the decomposition was analysed in 50% CO_2 to facilitate the analysis of $PbCO_3$ formation in this temperature range.

A sample of $Pb_3(C_6H_5O_7)_2{\cdot}3H_2O$ was heated to 250 °C at 10 °C/min before a slower rate of 1 °C/min was initiated until 300 °C to analyse this temperature region more closely.

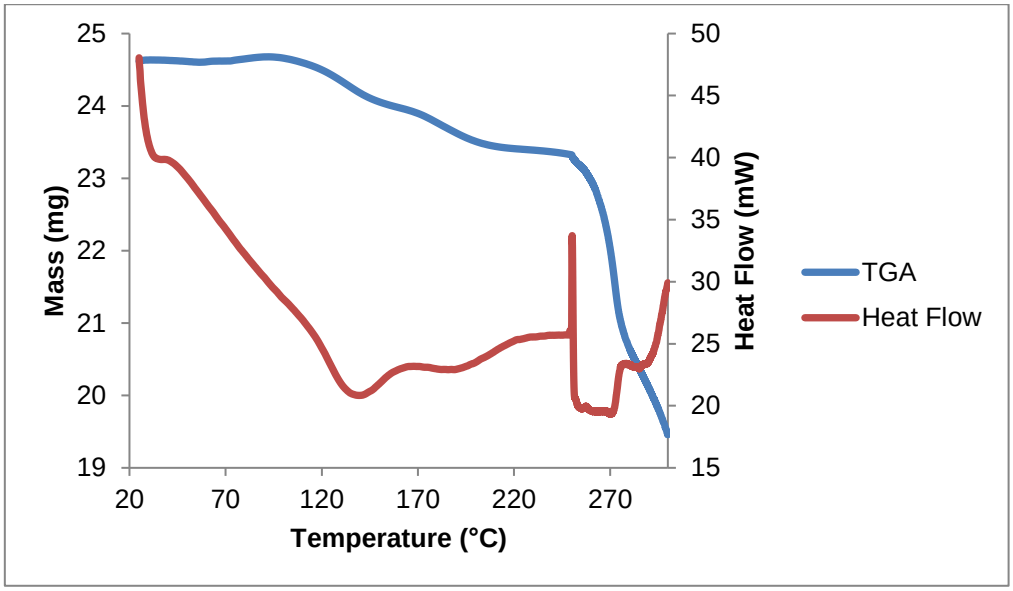

***Figure 7-3**: TGA and heat flow data from $Pb_3(C_6H_5O_7)_2{\cdot}3H_2O$ heated between 250-300 °C at 1 °C per minute in 50% CO_2*

The sharp heat flow peaks illustrated in Figure 7-3, in the 230-300 °C range, correspond well to where $PbCO_3$ is known to form and begin to decompose to $PbO{\cdot}PbCO_3$[162, 163] before generating PbO at higher temperatures. This is significant as it is a strong indication that $PbCO_3$ has been formed from the $Pb_3(C_6H_5O_7)_2{\cdot}3H_2O$. Other carbonate intermediate phases have also been reported at temperatures higher than 300 °C.

In addition, heat flow data from the 350 and 450 °C decomposition experiments, from Figures 7-1 and 7-2, illustrate marked elongations as a function of CO_2 concentration in the 300-350 °C range. Therefore, a sample of $Pb_3(C_6H_5O_7)_2{\cdot}3H_2O$ was heated to 300 °C at 10 °C/min before a slower rate of 1 °C/min was initiated until 350 °C to analyse this temperature range more closely. Figure 7-4 illustrate results obtained from the 300-350 °C temperature range in 50% CO_2.

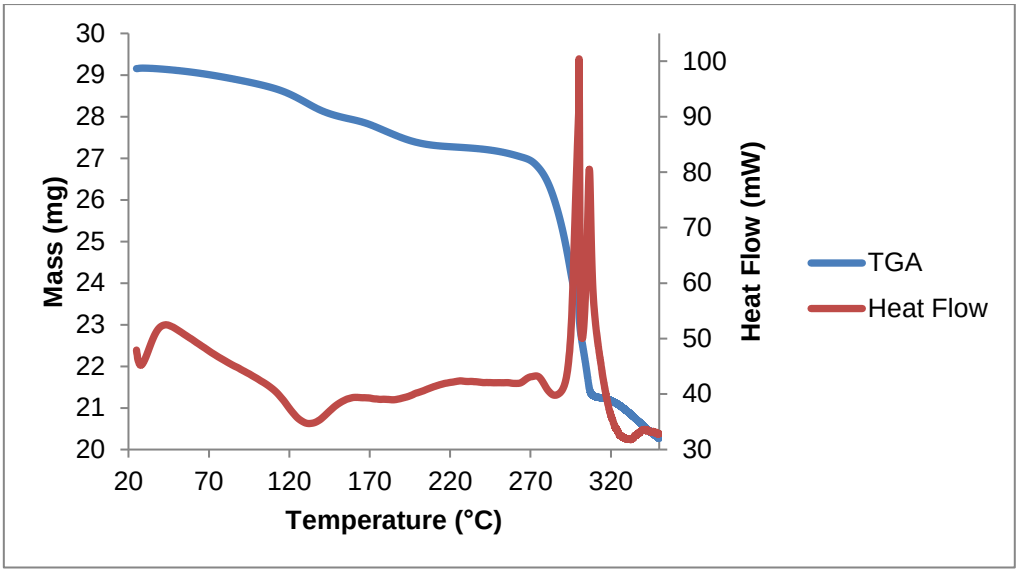

***Figure 7-4**: TGA and heat flow data from $Pb_3(C_6H_5O_7)_2 \cdot 3H_2O$ heated between 300-350 °C at 1 °C per minute in 50% CO_2*

The heat flow peaks, shown in Figure 7-4, in the 300-315 °C temperature range corresponds well to where $PbCO_3 \cdot 2PbO$ is known to form[163]. This is consistent with the XRD pattern shown in Figure 7-10 which matches well with the $PbCO_3 \cdot 2PbO$ diffraction pattern (reference code: 00-019-0681). The low heat flow seen in Figure 7-4 compared to decomposition experiments conducted in air points to a combustion process that is dominated by pyrolysis.

Assuming the final thermal decomposition product to be PbO, the results indicate that the calculated total percentage weight loss, from the chemical formula, for the complete combustion of $Pb_3(C_6H_5O_7)_2 \cdot 3H_2O$ is 36.5. This is consistent with the results obtained from TG analysis displayed in Table 7-1.

The total weight loss for those samples decomposed under a stable heating regime up to 350 and 450 °C varies somewhat due to decomposition under different CO_2 conditions, but is largely consistent with what is expected from the complete decomposition of $Pb_3(C_6H_5O_7)_2 \cdot 3H_2O$ to PbO.

***Table 7-1**: Percentage weight loss as a function of thermal decomposition conditions compared with calculated weight loss for complete decomposition of $Pb_3(C_6H_5O_7)_2 \cdot 3H_2O$*

Decomposition conditions	% Mass loss
350 °C in static air (10 °C/min)	37.5
350 °C in 10% CO_2 (10 °C/min)	37.1
350 °C in 50% CO_2 (10 °C/min)	33.6
450 °C in static air (10 °C/min)	36.6
450 °C in 10% CO_2 (10 °C/min)	37.4
450 °C in 50% CO_2 (10 °C/min)	37.2
250 – 300 °C in 50% CO_2 (1 °C/min)	21
300 – 350 °C in 50% CO_2 (1 °C/min)	30.5
Calculated mass loss for complete combustion of $Pb_3(C_6H_5O_7)_2 \cdot 3H_2O$	36.5

The rate of water release was similar in the current study to that observed for the carbonation of $Mg(OH)_2$ to produce $MgCO_3$ under CO_2[164]. The decomposition in that instance is 350 °C[165] to MgO and is the same as the initial decomposition of lead citrate and $PbCO_3$ to PbO. Interestingly, the hydrates of the salts also lose water at different temperatures during decomposition[166].

For example, in the trihydrate, $Mg(HCO_3)(OH) \cdot 2(H_2O)$, from which $MgCO_3$ can also be prepared, the dehydration steps occur at 157 and 179 °C. This is very similar to the dehydration steps found for the lead citrate where the dehydration steps were observed to be between 90 to 180 °C in the current and previous studies[110].

It therefore may be of interest to follow some of the established protocols for the carbonation of $Mg(OH)_2$ to $MgCO_3$ as a basis for further investigation into the carbonation of $Pb_3(C_6H_5O_7)_2 \cdot 3H_2O$ to carbonate and finally to the oxide.

7.3.2 XRD Analysis

The XRD patterns for the products from TG analysis are shown in Figures 7-5, 7-6, 7-9 and 7-10. The XRD patterns for samples heated to 350 °C in air, 10%, and 50% CO_2 are shown in Figure 7-5.

As seen in Figure 7-5, all three diffraction patterns displayed a good match with that of PbO showing the presence of both the α and β polymorphs (ref. code: 01-085-1288 and 00-005-0507 respectively) in addition to metallic Pb (ref. code: 03-065-2873). Furthermore, the intensity of peaks associated with the α polymorph is observed to increase as a function of CO_2 concentration.

The diffraction pattern of the decomposition product from the sample heated to 350 °C in 50% CO_2 displays additional diffraction peaks that correspond to $PbCO_3{\cdot}2PbO$ (ref. code: 00-019-0681). This finding also corroborates the experimental weight loss of 33.6% found with the calculated weight loss of $Pb_3(C_6H_5O_7)_2{\cdot}3H_2O$ to $PbCO_3{\cdot}2PbO$ of 33.8%.

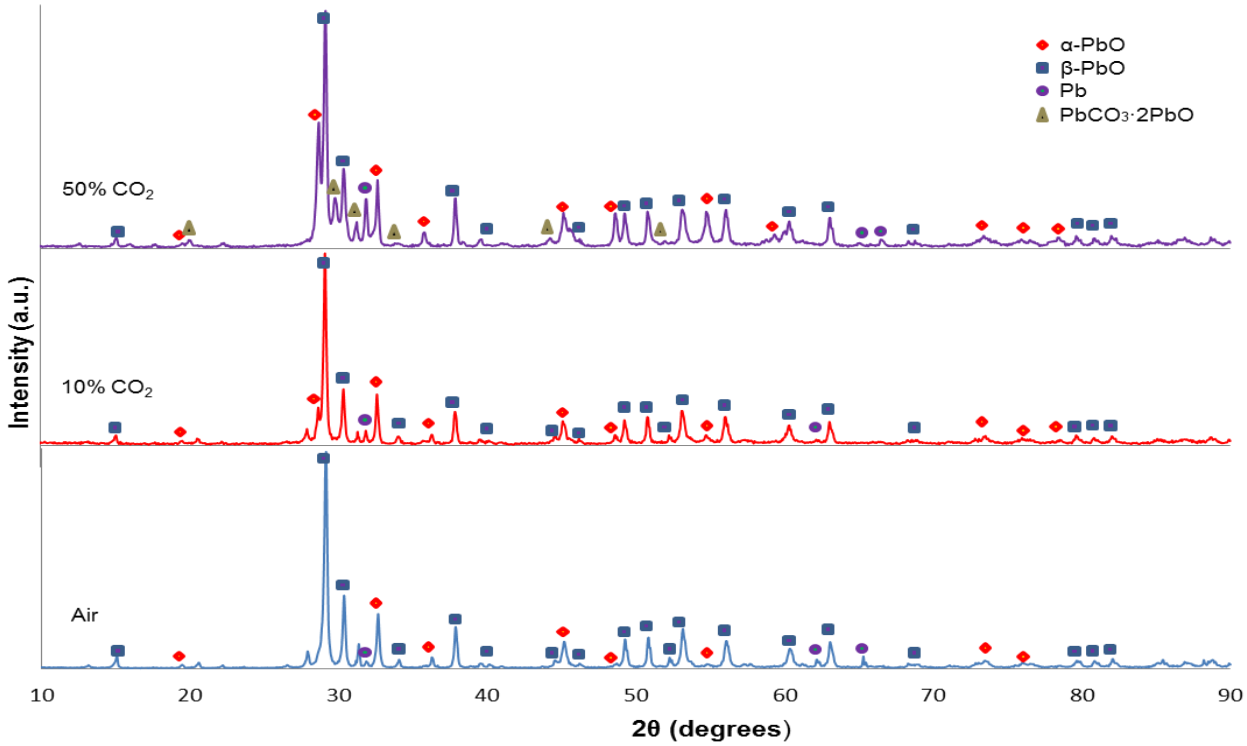

***Figure 7-5**: XRD patterns of samples heated to 350 °C in air, 10% and 50% CO_2*

$PbCO_3{\cdot}2PbO$ is a known intermediate product of the thermal decomposition of $PbCO_3$ to PbO[167]. The initial stages of decomposition are known to include the transition $PbCO_3$ – $Pb_2O(CO_3)$ – $PbCO_3{\cdot}2PbO$[168]. The presence of $PbCO_3{\cdot}2PbO$ not only indicates the initial formation of $PbCO_3$ from lead citrate, but also points to the incomplete combustion of the analyte to PbO by 450 °C observed in Figure 7-6. Therefore, future works with higher reaction temperatures may generate pure PbO with metallic Pb.

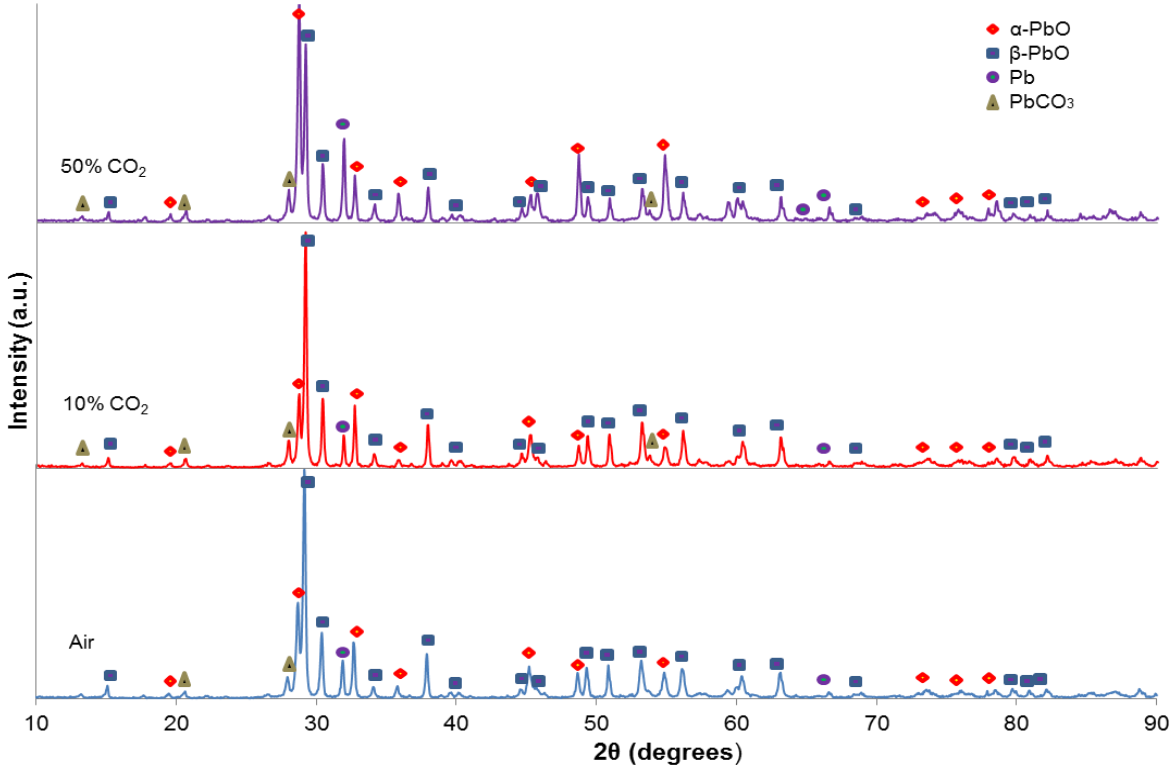

***Figure 7-6**: XRD patterns of samples heated to 450 °C in air, 10% and 50% CO_2*

As Figure 7-6 illustrates, in the same manner as that observed in Figure 7-5, the combustion product of samples heated to 450 °C consists of PbO with varying degrees of its constituent α and β polymorphs together with metallic Pb and peaks associated with $PbCO_3$. Furthermore, as observed previously with samples heated to 350 °C, the α to β-PbO ratio appears to have been influenced by the CO_2 concentration with the intensity of the α peak increasing due to elevated CO_2.

As displayed in Figure 7-6, the higher decomposition temperature of 450 °C appears to have the effect of greatly increasing the α peak intensity over that of the β as seen in the diffraction pattern for 50% CO_2.

To better illustrate the increase in the α to β-PbO ratio as a function of CO_2 content, figures 7-7 and 7-8 have been constructed from the two prominent X-ray peaks of α and β, from 28.7 and 29.2 2θ respectively. The ratios of these 2 peaks were calculated for ambient (indicated as “0” on each graph), 10 and 50 CO_2 percentage content in the reaction vessel at 350 and 450 °C.

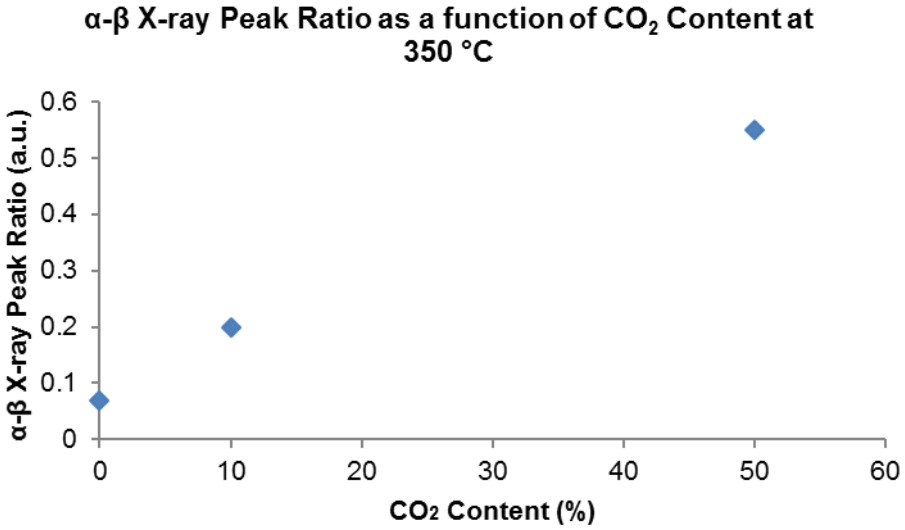

***Figure 7-7**: α-β X-ray peak ratio as a function of CO_2 content at 350 °C*

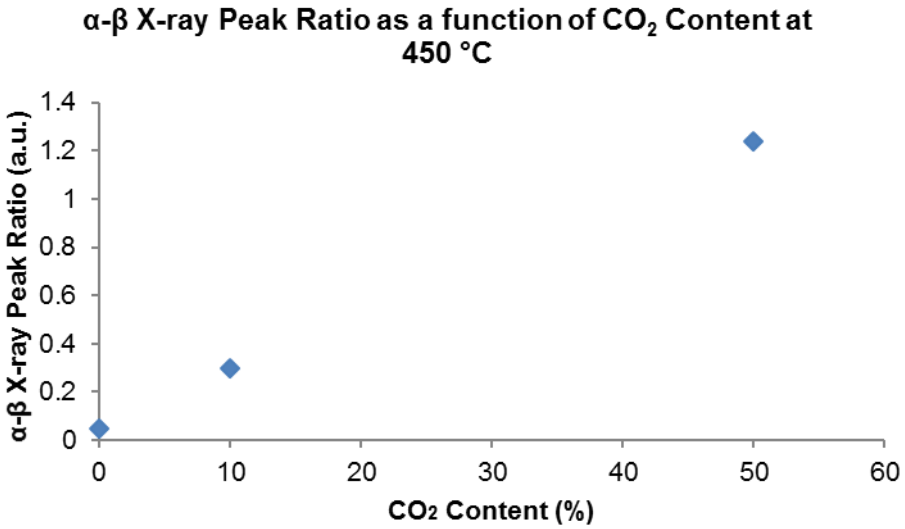

***Figure 7-8**: α-β X-ray peak ratio as a function of CO_2 content at 450 °C*

As illustrated in both Figures 7-7 and 7-8, the α-β ratio of PbO from samples combusted at 350 and 450 °C respectively have been observed to increase from ambient to 50% CO_2 content. The steepest increase of the two investigations was observed for the sample reacted at 450 °C where the ratio surpassed one.

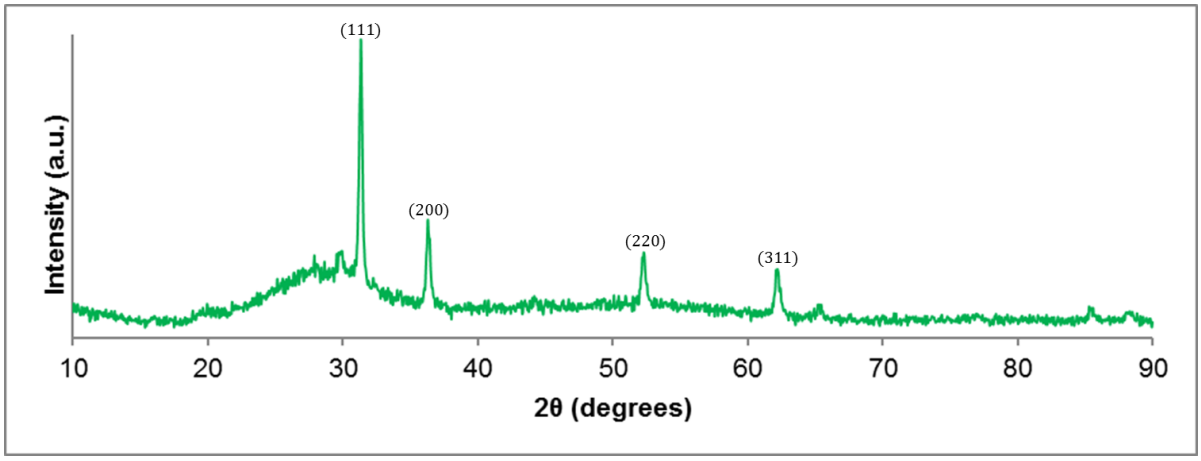

***Figure 7-9**: XRD pattern of sample heated between 250-300 °C at 1 °C/minute in 50% CO_2*

The high heat flow seen in the TG data, indicating self-sustained combustion, is consistent with previous work on lead citrate combustion[169] where an active pyrophoric material was generated when decomposed in the 300-600 °C temperature range. The pyrophoric lead produced from the citrate was found to be highly reactive at temperatures above 350 °C. As with other studies on pyrophoric materials[170] this study observed the first-order uptake of oxygen.

Furthermore, a varying degree of carbonaceous material is observed to be present depending on the mode of heating which is also in line with the other combustion experiments in the current study. This is particularly evident in the slow heating rate a sample between 250-300 °C. The by-product was highly carbonaceous with no visible sign of PbO.

This observation is reflected in the XRD pattern for the sample shown in Figure 7-9. The diffraction pattern gives a strong indication of an amorphous material with peaks matching metallic lead (ref code: 00-004-0686). The slow rate of heating, coupled with the high CO_2 content may have facilitated the formation of $PbCO_3$ to PbO and then its reduction by the carbon to generate metallic Pb within that narrow heating range.

The high observed carbon content is consistent with the low percentage weight loss seen in Table 7-1, where the experimental weight loss from the TGA was found to be 21%.

The strong presence of carbon in this and subsequent reactions is significant as it seems to facilitate the formation of pyrophoric lead at temperatures above the melting point of lead without any coalescence of the metal.

The lead appears to be adsorbed on a carbon matrix, which acts to insulate the lead particles from coalescence. The reaction proceeds to form a combination of PbO and carbonate as illustrated in Figures 7-5 and 7-6 at a higher rate of heating.

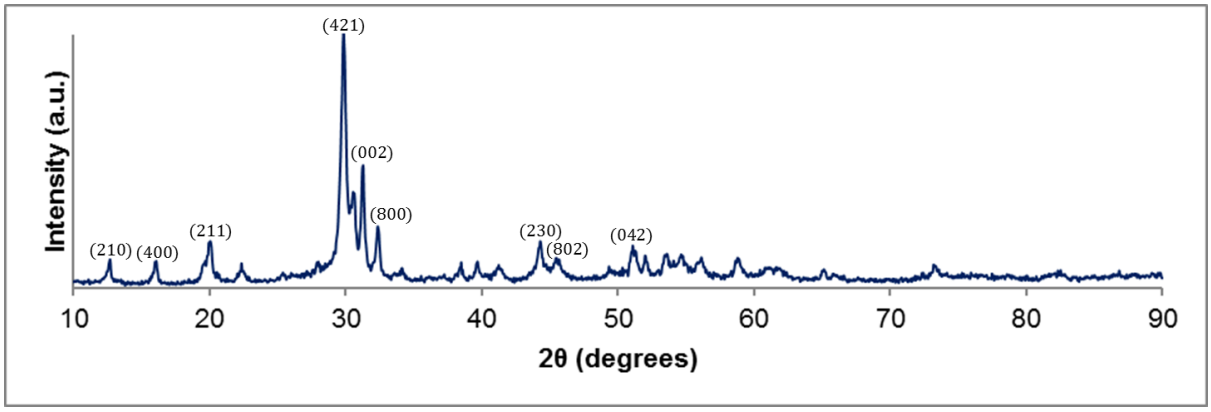

***Figure 7-10**: XRD pattern of sample heated between 300-350 °C at 1 °C/minute in 50% CO_2*

As Figure 7-10 illustrates, the XRD diffraction pattern for the by-product of a sample heated at a rate of 1 °C/min between 300-350 °C matches well with $PbCO_3 \cdot 2PbO$ (ref code: 00-019-0681).

The lower rate of heating coupled with lower O_2 content may account for the lower heat flow seen in Figure 7-4. This is approximately a factor of 3 lower than the rate observed in decomposition experiments conducted in air.

This would have the effect of suppressing the combustion of the citrate and preventing the decomposition outcome normally seen at this temperature to form PbO. The experimental percentage weight loss of 30.5%, seen in Table 7-1 for this experiment also matches well with the calculated weight loss of 33.8% for the decomposition of $Pb_3(C_6H_5O_7)_2 \cdot 3H_2O$ to $PbCO_3 \cdot 2PbO$.

7.3.3 Possible $Pb_3(C_6H_5O_7)_2 \cdot 3H_2O$ to $PbCO_3$ Mechanisms

CO_2 reaction with $Pb(OH)_2$

The formation of carbonates has been observed at relatively low temperatures of less than 40 °C by Isahak et al[171]. In their study, they reported that the production of carbonate was accelerated by the formation of a hydroxide phase in the presence of water at low levels.

This is significant because a hydroxide phase such as $Pb(OH)_2$ could form in the early stages of decomposition of the citrate complex, thereby facilitating carbonate production. Indeed, work by Garenne et al[172] found that the gas-solid carbonation of calcium hydroxide can be achieved at temperatures below 30 °C in the presence of adsorbed water. In a similar manner, if $Pb(OH)_2$ were to form, the following reaction could be feasible:

$$Pb(OH)_{2(s)} + CO_{2(g)} \rightarrow PbCO_{3(s)} + H_2O_{(v\text{-}l)} \quad \textbf{7-1}$$

This would have been made possible through the production of CO_3^{2-} via the following reaction:

$$CO_{2(g)} + H_2O \text{ (absorbed)} \rightarrow CO_3^{2-} + 2H^+ \quad \textbf{7-2}$$

This would have been required to form a carbonate layer around the $Pb(OH)_2$ particles. Carbonate formation could also be explained by the dissociation/disproportionation of CO_2 through interactions with O^{2-} and OH^- ions forming CO_3^{2-} and HCO_3^-[173].

Nucleophilic/Electrophilic substitution reaction

CO_2 possesses several coordination sites and exhibits diverse coordination ability with various metals and is thus able to form many complexes with a great variety of coordination modes. CO_2 presents two different reaction sites:

1: The carbon atom (LUMO orbitals) exhibits a Lewis acid character and can be defined as an electrophilic centre.

2: The oxygen (HOMO orbitals) is a weak Lewis base and can act as a nucleophilic centre.

Most of the catalytic reactions involving CO_2 require simultaneous acid-base activation, implying that the carbon atom and one of the oxygen atoms interact with the metal at the same time.

In addition, π electrons in the two double C = O bonds can interact with d electrons of transition metals. When the LUMO orbitals of CO_2 are occupied (via electron transfer), the lowest energy state corresponds to a bent geometry. For example, the radical anion $CO_2^{-\bullet}$ is a bent molecule with an equilibrium angle of 134°. Therefore, any interaction of CO_2 with a metal will induce a loss of its linearity(174).

There are four basic modes of CO_2 coordination: (a) η^1-C, (b) η^2(C,O) (side-on), (c) η^1-O (end-on) and (d) η^2-O,O. For the η^1 - C coordination mode there is a strong charge transfer between a d_z^2 metal orbital and the anti - bonding π* orbital of CO_2.

This bonding mode is preferred with electron - rich metals, and may be facilitated by an additional weak interaction between one or two oxygen atoms of CO_2 with a Lewis acid centre located in the coordination sphere of the metal. In the η^2 (C,O) bonding mode, there is a double bonding scheme with a σ bond from the π orbital of CO_2 to an empty d_z^2 metal orbital, together with a "back - bonding" from a filled d_{xy} metal orbital to the empty π* CO_2 orbital.

The η^1 (O) end - on coordination mode is preferred with electron - poor metals, and the CO_2 molecule can remain linear or be weakly bent. The η^2 (O,O) coordination mode can be described as a metal carboxylate with an ionic bond $M^+CO^-_2$ and is often encountered with alkali or alkaline - earth metals or, in the case of CO_2 adsorption, with metal surfaces(164). In this example the most likely mode of CO_2 coordination with the lead citrate complex would be the η^2 (O,O). A schematic of this is shown in Figure 7-11.

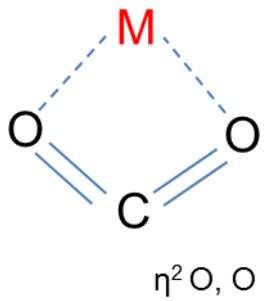

***Figure 7-11**: Possible coordination mode for lead-CO_2 complex*

In the example given in Figure 7-11, the M = Pb and an additional reaction would occur where an O^- ion would interact with the carbon to form $PbCO_3$.

Another possible route of formation is through the cleavage of CO bonds. Metal oxides yielded through such a mechanism can react further with CO_2 leading to a net conversion of two CO_2 molecules to CO and CO_3^{2-} which then may interact further to form $PbCO_3$. The same conversion can occur via the intermediate coupling of two CO_2 molecules at a metal centre. Coordinated CO_2 exhibits an enhanced reactivity at oxygen towards electrophiles, leading to metallacarboxylic acids and their derivatives.

Electrophilic attack at oxygen is also the prevalent reactivity of η^1 - CO_2 complexes and CO_2 - bridged complexes with alkali cations. Many stoichiometric and most catalytic reactions involving CO_2 activation proceed via the formal insertion of CO_2 into highly reactive M – L bonds, with the formation of new C– L bonds (where L = ligand).

These reactions might not necessarily require strong coordination of CO_2, but are generally initiated by a nucleophilic attack of L at the Lewis acidic carbon atom of CO_2. A weak interaction between the metal and the lone pairs of one oxygen atom or the π - C = O bond of CO_2 may also play a role in supporting the insertion process.

It has been reported that the geometry around Pb^{2+} in the lead citrate structure appears to be distorted trigonal bipyramidal with Pb-O distances ranging from 2.397(7) to 2.527(6) Å and the lone pair on Pb^{2+} occupying one of the three basal plane positions. Further, the citrate binds the Pb^{2+} forming rhomboidal Pb_2O_2 units, while it subtends its terminal carboxylate onto a proximal Pb^{2+}, thus linking adjacent Pb_2O_2 units into a chain along the *a* axis.

The involvement of citrate in hydrogen bonds with water molecules and abutting Pb–citrate moieties leads to a stable structure[109]. The coordinated Pb^{2+} forms dimeric units, which are interconnected through the terminal carboxylate group leading to an infinite chain[110].

The concerted utilization of the central carboxylate and hydroxyl units of citrate in the formation of a chelate metal-containing ring has been observed in other cases of metal–citrate complexes as well. In three dimensions, the structural cohesiveness of the coordinated complex emerges as a result of an extensive hydrogen-bonding network. CO_2 is classified as an inorganic carbonyl compound.

Oxygen is more electronegative than carbon, and thus draws electron density away from carbon to increase the bond's polarity. Therefore, the carbon becomes electrophilic. It can therefore be attacked by nucleophiles or a negatively charged part of another molecule. During such a reaction, the carbon-oxygen double bond is broken and the carbonyl group may experience additional reactions. Also, the electronegative oxygen can react with an electrophile.

It is proposed that a reaction might be possible along the dimeric units formed of coordinated Pb^{2+} with CO_2 whereby the oxygen anion (nucleophilic) interacts with CO_2 (electrophilic) to form the carbonate anion, which is converted into the carbonate. Such an occurrence has been observed in other works and is therefore considered a possibility[175]. A schematic of this potential reaction is shown in Figure 7-12, where part of the Pb^{2+} dimer is shown and attacked by an incoming CO_2 molecule.

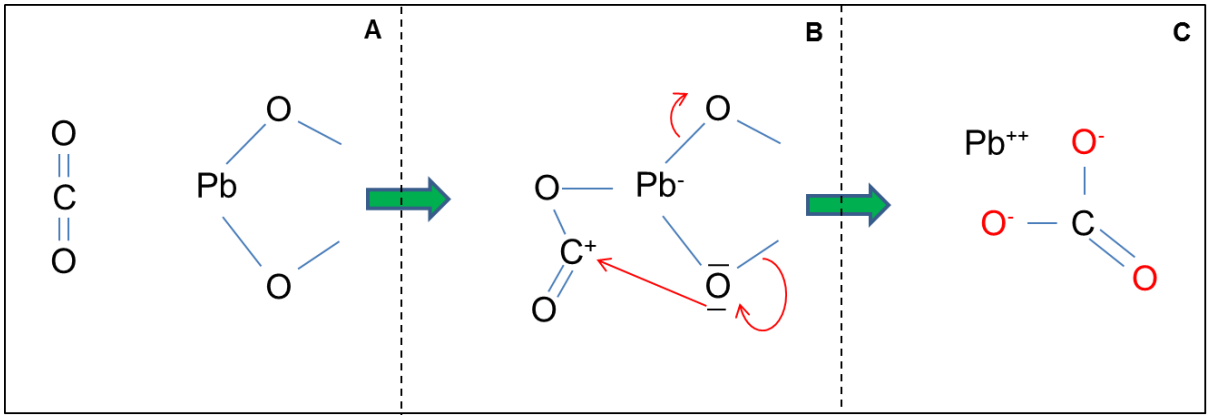

***Figure 7-12**: Schematic of possible reaction of $Pb_3(C_6H_5O_7)_2 \cdot 3H_2O$ with CO_2*

In this example, illustrated by Figure 7-12, the low electron density on the metal complex facilitates the initial nucleophilic attack on the Pb^{2+} ion. While this attack takes place, the adjacent oxygen is drawn to the carbon electrophile. This can be viewed as an electrophilic attack by the carbon on the ligand.

Alternatively, it could be that the coordinated CO_2 acts as a ligand where the oxygen of the η2- or η1-bonded coordinated CO_2 can bind onto the complex[164] which then forms PbO when the combustion temperature is reached[174].

7.3.4 SEM/EDS Analysis

Images obtained from SEM were used to analyse the microstructure of the by-products of decomposition at different atmospheres and temperatures. A FEI Nova NanoSEM was used to image the powdered samples.

Figure 7-13 illustrates 4 secondary electron images with A and B of 10,000 and 25,000 times magnifications respectively depicting the microstructure of $Pb_3(C_6H_5O_7)_2 \cdot 3H_2O$ samples that were heated to 350 °C in air. Images C and D portray samples of the same corresponding magnifications as A and B for direct comparison that were heated to 350 °C in 50% CO_2 and air.

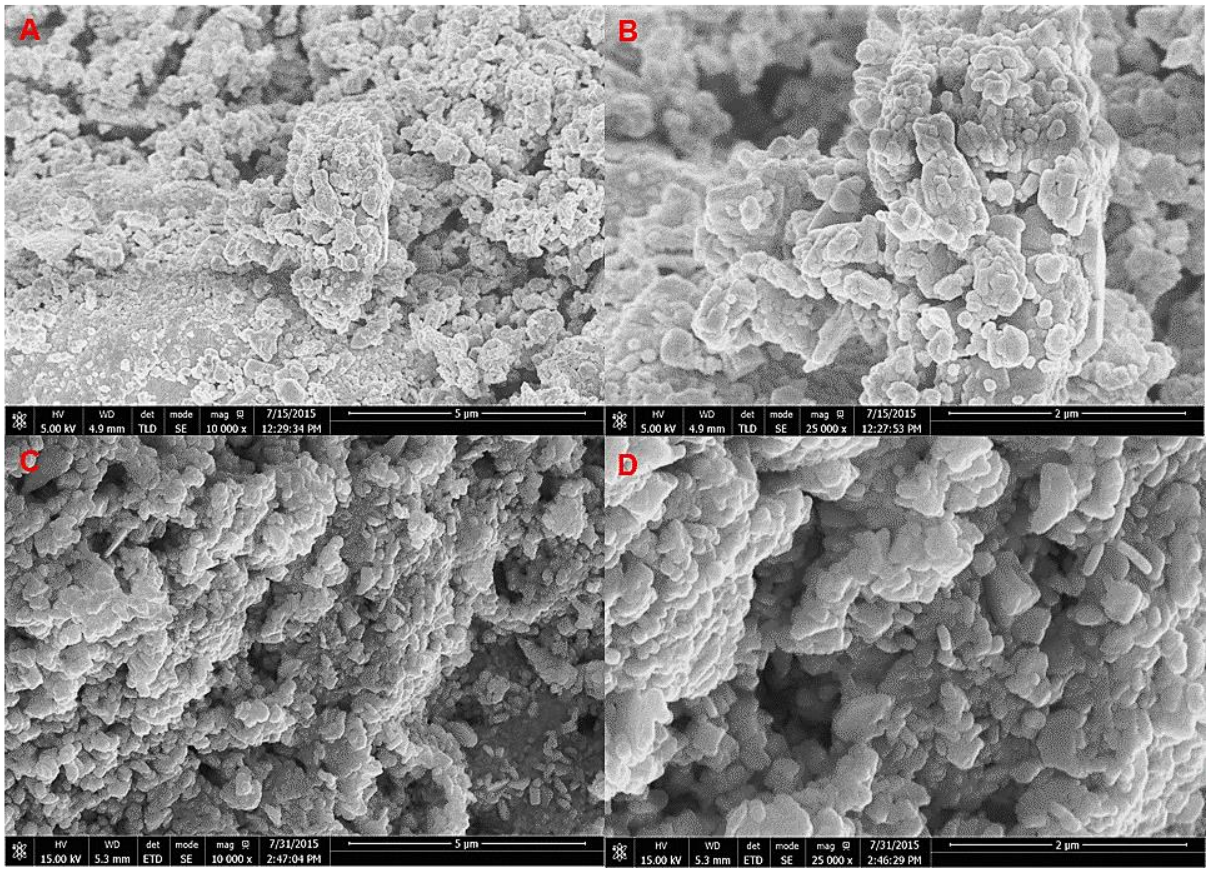

***Figure 7-13**: A and B are SEM images of samples heated to 350 °C in air and C and D were in 50% CO_2*

As the micrographs in Figure 7-13 illustrate, the decomposition products heated to 350 °C in air and 50% CO_2 contain a variety of shapes and sizes. The particulate size distribution within each sample ranges from tens to a few hundred nanometres.

Both decomposition products display a number of different shapes with examples of spheres, with various degrees of sphericity, elongated and irregular particles observed. These particles appear to overlap and sometimes stack on top of each other on the surfaces of the crystallites and appear to be randomly distributed.

Quantitative area analysis with energy dispersive X-ray was conducted, in the form of elemental mapping on the samples to investigate the oxide and free lead distribution in a given area.

Figure 7-14 shows a SEM image with the corresponding elemental mapped area with lead (in red) and oxide (in green) overlaid to illustrate a good oxide to free lead distribution. In addition, the corresponding x-ray spectra generated from the scanned area is displayed on the bottom left.

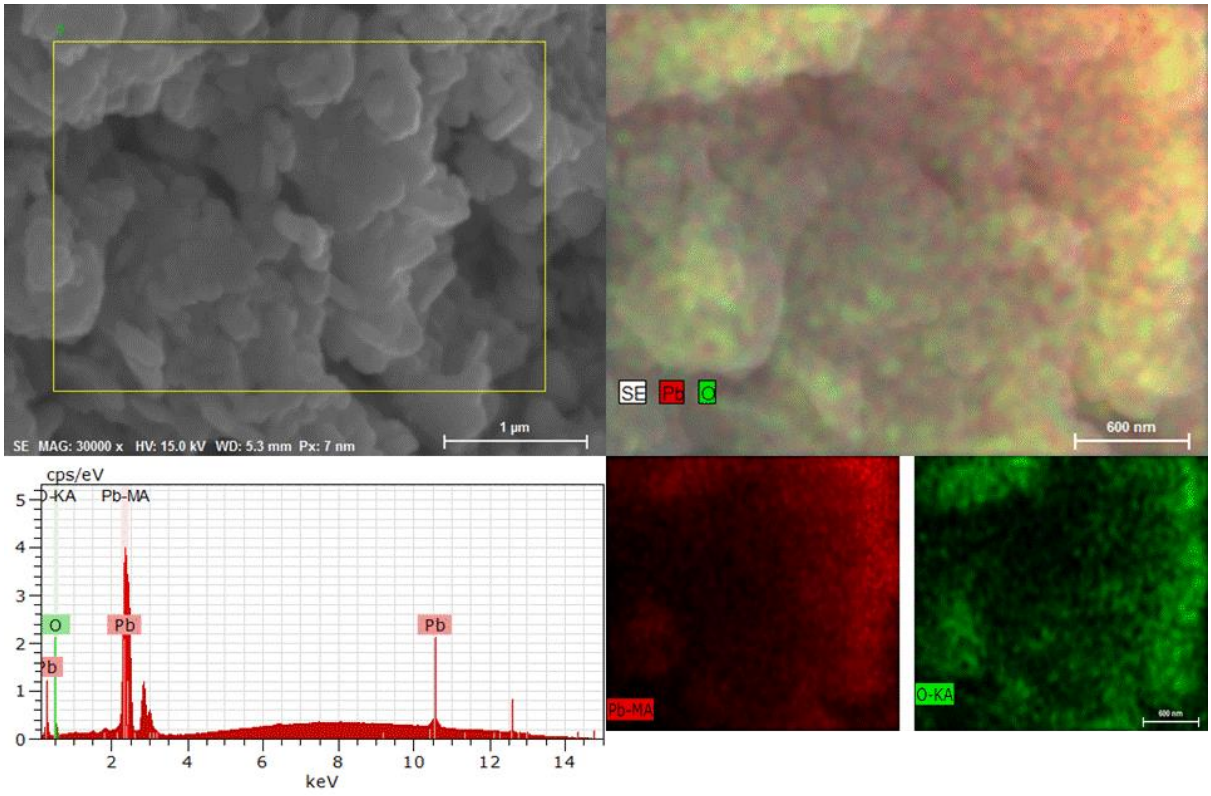

***Figure 7-14**: SEM image with EDS trace and elemental mapping of $Pb_3(C_6H_5O_7)_2 \cdot 3H_2O$ heated to 350 °C in 50% CO_2*

The elemental maps in Figure 7-14 displays the distribution and relative proportion of the defined elements over a given area of a sample decomposed at 350 °C in 50% CO_2. The relative proportions of free lead and oxide are indicated by the intensity of the respective colours displayed on the bottom right. As seen in the overlay in the top right, both the free lead and oxide are well distributed with the proportion of the oxide dominating overall as expected.

Figure 7-15 illustrates 4 secondary electron images with A and B, of 10,000 and 25,000 times magnifications respectively, depicting the microstructure of $Pb_3(C_6H_5O_7)_2 \cdot 3H_2O$ samples that were heated to 450 °C in air. Images C and D portray samples of the same corresponding magnifications as A and B for direct comparison. These were heated to 450 °C in 50% CO_2.

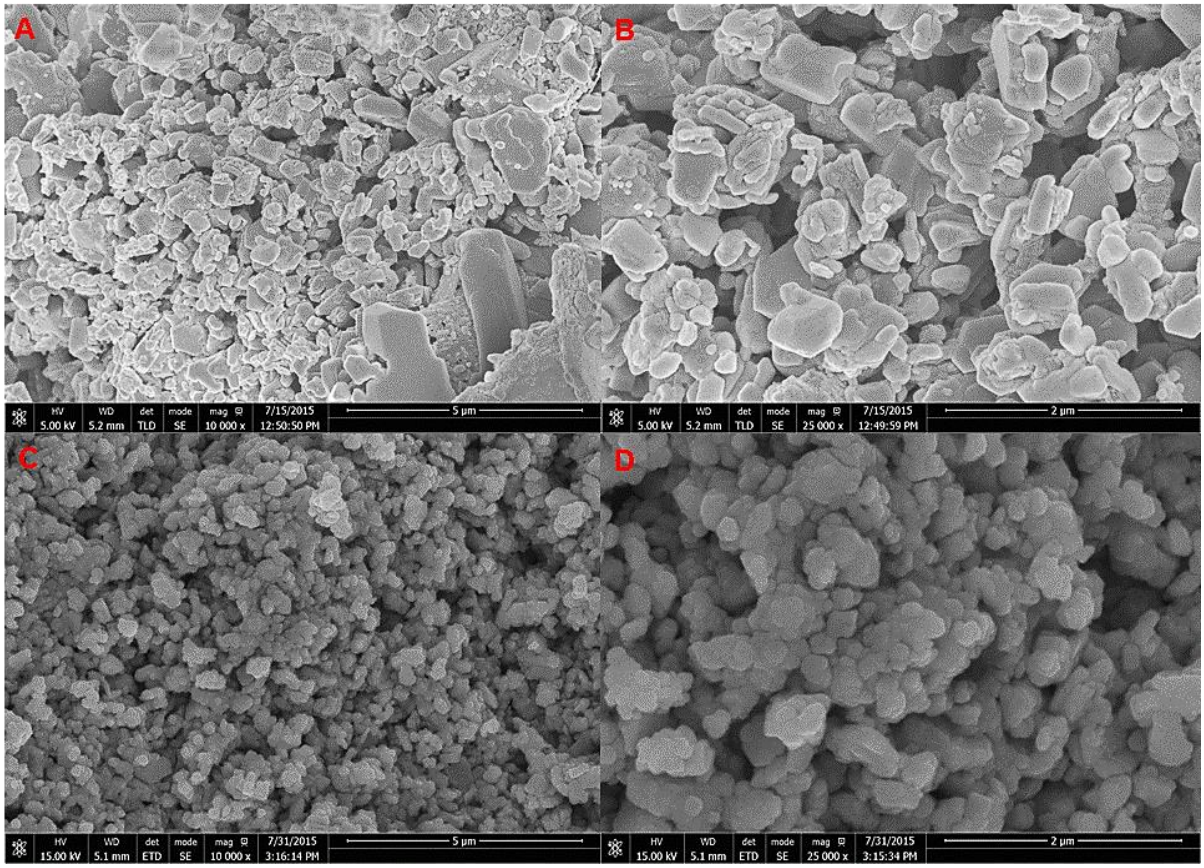

***Figure 7-15**: A and B are SEM images of samples heated to 450 °C in air and C and D were in 50% CO_2*

As the micrographs in Figure 7-15 illustrate, the decomposition products from samples heated to 450 °C in air and 50% CO_2 both contain a variety of shapes and sizes similar to those observed in the sample decomposed at 350 °C. The particulate size distribution within the sample decomposed in air ranges from tens to a few hundred nanometres, whereas the sample exposed to 50% CO_2 appears to have a narrower range of sizes in the tens of nanometres.

Both decomposition products display a number of different shapes with examples of spheres, of various degrees of sphericity, and elongated and irregular particles. Larger blocks are observed in the air sample indicating sintering and partial inter-particulate coalescence.

Although a range of shapes is observed in the sample exposed to 50% CO_2, similar to that seen in Figure 7-13, the sample is dominated by spherical particles. As observed previously, these particles appear to overlap and sometimes stack on top of each other on the surfaces of the crystallites and appear to be randomly distributed.

The general disorder in the particulate distribution together with the similar final primary particle size observed in both the principle experiments indicate a rapid growth of nuclei in all directions and orientations.

The amount of surface revealed from all decomposition reactions, and especially that of the sample decomposed to 450 °C in 50% CO_2, appears to be high.

The quantitative area analysis with energy dispersive X-ray for this sample is illustrated in Figure 7-16. In the same layout as previously shown, a SEM image with the corresponding elementally mapped area with lead (in red) and oxide (in green) is displayed.

The overlaid maps of lead and oxide shown in the top right of Figure 7-16 illustrate areas where lead is dominant; forming what can be described as conductive pathways.

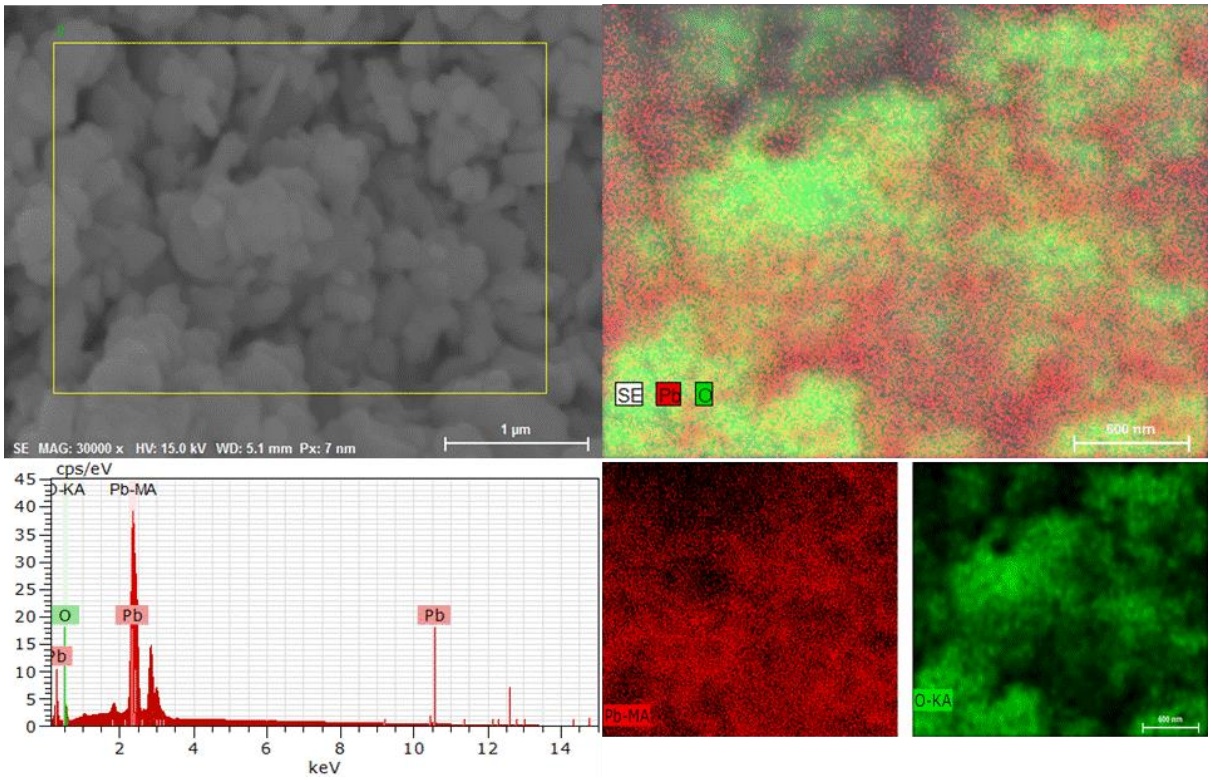

***Figure 7-16**: SEM image with EDS trace and elemental mapping of $Pb_3(C_6H_5O_7)_2 \cdot 3H_2O$ heated to 450 °C in 50% CO_2*

The individual maps for lead and oxide indicate a well-distributed system throughout the scanned area. As observed in both the X-ray spectra (shown on the bottom left of Figure 7-16) and XRD analysis, the intensity of the oxide trace in the mapped area is much higher than that for the lead, indicating a higher relative proportion.

7.3.5 BET/BJH, Apparent Density and Acid Reactivity Analysis

A number of experiments were conducted using industrial grade CO_2 in a tube furnace with small differences in the heating temperature and atmosphere. This was to determine whether the microstructural and chemical changes from the combustion-calcination of $Pb_3(C_6H_5O_7)_2 \cdot 3H_2O$ in CO_2 had any direct impact on the acid reactivity on the reacted samples. The small changes in the combustion-calcination parameters was to gauge any potential trend that may result and for industrial scale-up.

To test the reactivity of the treated compounds a series of titrations were conducted to measure the difference in the degree of interaction with H_2SO_4 of each sample. BET/BJH and density measurements were also conducted on some of the samples to compare the differences in the results and these parameters. Absorption tests were also conducted on some of the samples to directly compare them with data from industry, illustrated in Table 7-2.

***Table 7-2**: Characteristics of Barton Pot leady oxide for different battery applications[14]*

Characteristic	Automotive Batteries	Industrial Batteries
Free Lead (wt. %)	18-24	22-28
Apparent density (g/ml)	7-9.4	9-11.4
Acid absorption (mg/g)	170-210	130-155

In addition to the information gathered from industry, the results detailed in Table 7-3 also contain experimental data from the current study for direct comparison, listed as samples 1 to 6. Samples 1 to 4 are results obtained from controlled combustion-calcination experiments at various target temperatures under different heating rates from chapter 5.2. Results listed in sample 5 are those from the self-sustained combustion experiment from chapter 5.3 and sample 6 is from chapter 6.7 of a sample of pure α-PbO heated with glycerol.

Results detailed under samples 7 to 12 are of those reacted in CO_2 and were all heated at the same rate of 10 °C/min and held for 30 minutes at the stated temperature.

***Table 7-3**: BET surface area, BJH pore volume and size, apparent density and acid reactivity/absorption comparison of lead citrate combustion-calcination in air and CO_2*

Reaction Temperature (°C) (Sample)	**350 (1)**	**400 (2)**	**410 (3)**	**430 (4)**	**270 (5)**	**α-PbO 330 (6)**
Heating Rate (°C/min)	5	50	30	30	smoulder	10
Atmosphere	Air	Air	Air	Air	Air	Air/Gly
BET surface area (m^2 g^{-1})	1.3	1.6	2.7	3.4	0.74	1.26
BJH cumulative pore volume between 1.7 nm and 300 nm (ml/g)	0.018	0.013	0.014	0.015	0.054	0.016
BJH average pore diameter (nm)	45.1	33.8	23.2	19.2	159.1	41
Apparent Density (g/ml)	8.2	5.3	6.9	6.5	9.6	9.6
Acid Reactivity/ Absorption (mg/g)	128/168.2	43.2/-	78.5/-	38.3/-	111.3/-	99.1/-
Reaction Temperature (°C) (Sample)	**~460 (7)**	**~460 (8)**	**~460 (9)**	**~470 (10)**	**~360 (11)**	**~410 (12)**
Heating Rate (°C/min)	10	10	10	10	10	10
Atmosphere	~56% CO_2	~50% CO_2	~54% CO_2	~55% CO_2	~48% CO_2	~47% CO_2
BET Surface Area (m^2 g^{-1})	2.15	2.14	1.53	1.56	-	-
BJH cumulative pore volume between 1.7 nm and 300 nm (ml/g)	0.19	0.02	0.012	0.1	-	-
BJH average pore diameter (nm)	166.4	40	26	152.7	-	-
Apparent Density (g/ml)	8.2	8.8	8.6	8.9	-	-
Acid Reactivity/ Absorption (mg/g)	270.8/290.4	238/-	211/240	220/254	253.8/-	331.9/-

As the reactivity and absorption results from samples 7 to 12 show, the combustion-calcination of $Pb_3(C_6H_5O_7)_2 \cdot 3H_2O$ in CO_2 had generated PbO samples that were highly reactive compared to samples simply reacted in air. Some of the results demonstrated at least a 2-fold increase in reactivity compared to air reacted samples. When comparing the BET/BJH data, it is observed, as before, that there is no correlation between reactivity and surface area of a given sample. Indeed, these results further the observation and work done by Boden[14] that the total pore volume and median size plays a far more significant role in potential performance characteristics of generated PbO. Another factor in the improved reactivity could be attributed to the greater shape and size uniformity seen in the microstructure of the samples reacted in CO_2. The interplay between all these factors will need to be examined in greater detail to determine whether a single attribute or, more likely, a combination of a given number of features hold the key in truly controlling and predicting the reaction characteristics of generated PbO.

The overall results of these experiments have pointed to a process that has the potential to significantly improve the reaction characteristics of PbO from the citrate recycling process. These results have shown to be equal to, and in some cases, better than those obtained from industry for both automotive and industrial batteries in terms of acid absorption. Together with the data gathered on the microstructure, the overall recycling and combustion-calcination processes outlined here have demonstrated to be very promising in future LAB applications.

7.4 Summary

The synthesis of nanostructured PbO with different ratios of α to β polymorphs was achieved through the decomposition of $Pb_3(C_6H_5O_7)_2 \cdot 3H_2O$ in CO_2 content up to 56% by volume. The ratio of α to β-PbO was observed to increase as a function of CO_2 concentration and temperature, while maintaining the presence of metallic Pb within the powder matrix.

A slow rate of heating coupled with a high CO_2 (lower O_2) content was observed to supress the normally violent combustion of the hydrogen and carbon in the organic intermediate of the citrate thereby lowering the characteristic intense exothermic phenomenon. SEM analyses indicate a well distributed array of particles revealing a high degree of surface grown in three-dimensions. The corresponding EDS analyses show that both the lead and oxide in this three-dimensional array are well-distributed, with the metallic Pb forming a conductive skeletal structure surrounded by PbO.

Acid reactivity and absorption results have shown to be equal to, and in some cases, better than those obtained from industry for both automotive and industrial batteries.

8 Conclusions and Recommendations for Future Works

8.1 Conclusions

The aim of this thesis was to investigate a hydrometallurgical recycling process using citric acid to leach used LAB pastes. The by-products from this process were characterised to determine their potential use in new LABs. The by-products and processes from this study were then optimised and explored further to generate components related to the operations of LABs. The main conclusions from this work are summarised here.

Initial leaching experiments conducted with waste simulants using analytically pure compounds for PbO demonstrated the importance of the initial reaction environment in determining the dominant reactive species available to generate the final product. The final product of either form of lead citrate benefited from a S:L ratio of 1:5 with a molar ratio of 1:3 and 1:2 for PbO to $C_6H_8O_7.H_2O$ and NaOH respectively in terms of maintaining a processing time <1 hour and generating an analytically pure compound.

It was found that the pH of reaction played a vital role in reaction kinetics. Increasing the pH, using NaOH, resulted in an increase in the rate of reaction and greater utilisation of the $C_6H_8O_7 \cdot H_2O$. This was due to an increase in OH^- favouring the formation of chelate complexes between $C_6H_8O_7 \cdot H_2O$ and the metal cations. Furthermore, $C_6H_5O_7^{3-}$ was found to be the stronger complexing agent compared to the other two citrate species, which can speed up the complex-crystallization reaction.

As a result, the minimum moles of H_2O_2 solution required for leaching pure PbO_2 to generate $Pb_3(C_6H_5O_7)_2 \cdot 3H_2O$ was found to be 1 when reacted with 2 and 4 moles of $C_6H_8O_7 \cdot H_2O$ and NaOH respectively, per mole of PbO_2.

It has been demonstrated that $PbSO_4$ can be successfully leached using NaOH and $C_6H_8O_7 \cdot H_2O$ to form different lead citrate complexes as a function of NaOH molar concentration. As a result of these investigations the molar concentrations, with a S:L ratio of 1:5, of 2.5 M H_2O_2, 3.2 M $C_6H_8O_7 \cdot H_2O$, and 3.5 M NaOH were used to leach depleted LAB paste and shedding material from industry and were successful in synthesising $Pb_3(C_6H_5O_7)_2 \cdot 3H_2O$ after less than an hour of reaction time.

The individual leaching procedures for the positive and negative paste materials could also be used as the option exists where plate materials can be treated like for like, according to their specific chemistries, to avoid the excess use of reagents that will be required for combined leaching of the negative and positive paste materials.

8 Conclusions and Recommendations for Future Works

The combustion-calcination of $Pb_3(C_6H_5O_7)_2 \cdot 3H_2O$ was successful in generating PbO containing both forms of the polymorph α and β together with metallic Pb. The manner in which the heating regime was implemented had a direct effect on the microstructure generated, which demonstrates the degree to which the final PbO product can be potentially manipulated to preferentially produce a desirable by-product to cater for specific end use in a variety of LAB applications.

A novel method to generate PbO from lead citrate was found through a self-sustaining combustion route where the leached waste materials from LABs were preheated to 270 °C for ~15 minutes. A self-sustaining smouldering reaction to produce PbO with a predominately β phase containing metallic Pb was elicited when an external heat source was introduced. The method points to a potential application where a continuous and energy efficient method could be introduced to the manufacturing of PbO from recycled waste materials from LABs. Furthermore, results obtained from acid reactivity measurements showed no direct relationship between the surface area of materials and the degree of reactivity of a given sample. The results point to a more complex combination of factors including pore volume and size to be the main contributing features to the reactivity of PbO.

Electrochemical analysis of PbO from $Pb_3(C_6H_5O_7)_2 \cdot 3H_2O$ demonstrated the viability in the by-product to be used in an electroactive paste in new LABs. A direct relationship between the microstructure of PbO derived from the heat treatment of $Pb_3(C_6H_5O_7)_2 \cdot 3H_2O$ has been shown. This alterability in the microstructure of PbO demonstrates the potential to control the end product and thus meet the demands from industry for active materials for a variety of battery types.

Pure α-PbO was generated from both forms of lead citrate, $Pb(C_6H_6O_7) \cdot H_2O$ and $Pb_3(C_6H_5O_7)_2 \cdot 3H_2O$, synthesised in this study through dissolution reactions using NaOH. Pure β-PbO was also generated from $Pb(C_6H_6O_7) \cdot H_2O$, $Pb_3(C_6H_5O_7)_2 \cdot 3H_2O$ and $PbSO_4$ using NaOH, but through dissolution/reprecipitation reactions.

It was found that pure α-PbO could also be filtered out of micron sized PbO powders normally containing both the α and β phases using 0.67 M NaOH. The same dissolution/re-precipitation reaction that generated pure β-PbO from $Pb(C_6H_6O_7) \cdot H_2O$ and $Pb_3(C_6H_5O_7)_2 \cdot 3H_2O$ using NaOH was also observed for $PbSO_4$. The microstructure of the β-PbO from lead citrate and $PbSO_4$ were noted to be very different in terms of particulate shape and size, but similar in terms of surface texture on particulate sheets that both have in common.

$NaHCO_3$ was found to be successful in acting both as the source of carbonate ions and in maintaining reaction pH within the $PbCO_3$ stability region when used to leach $PbSO_4$. The reaction induced by $NaHCO_3$ within this stability region was attributed to the amphoteric nature of $NaHCO_3$ and resulted in a conversion percentage of approximately 99%.

$PbCO_3$ was also successfully generated from $Pb(C_6H_6O_7)\cdot H_2O$ and $Pb_3(C_6H_5O_7)_2\cdot 3H_2O$ using NaOH, $NaHCO_3$ and then an acid in a series of dissociation and re-precipitation reactions. The $PbCO_3$ was then used to thermally generate α and β-PbO as well as Pb_3O_4 by calcination at 350 °C, 600 °C and 450 °C respectively. Glycerol was entrained in both $PbCO_3$ and α-PbO as an in-situ reducing agent to generate PbO containing metallic Pb.

The synthesis of nanostructured PbO with different ratios of α to β polymorphs was achieved through the decomposition of $Pb_3(C_6H_5O_7)_2\cdot 3H_2O$ in various CO_2 enriched atmosphere. The ratio of α to β-PbO was observed to increase as a function of CO_2 concentration and temperature, while maintaining the presence of metallic Pb within the powder matrix.

A slow rate of heating coupled with a high CO_2 (lower O_2) content was observed to supress the normally violent combustion of the hydrogen in the organic intermediate of the citrate thereby lowering the characteristic intense exothermic phenomenon. SEM analyses indicate a well distributed array of particles revealing a high degree of surface grown in three-dimensions. The corresponding EDS analyses show that both the lead and oxide in this three-dimensional array are well-distributed, with the metallic Pb forming a conductive skeletal structure surrounded by PbO.

Acid reactivity and absorption results have shown to be equal to, and in some cases, better than those obtained from industry for both automotive and industrial batteries. This demonstrates significant promise in the use of this recycling process in generating more efficient electroactive materials for new LABs.

8.2 Future Works

The current study has provided new insight into improving the LAB, from recycling to reuse. To further develop the technology, the following areas for future research are suggested:

- Modifications to the processing of PbO powders could be further explored to determine potential benefits they may impart on the porous active mass.
- Changes in atmosphere, heating and cooling rate may contribute to varied physical changes to the PbO microstructure.
- An in-depth analysis between the interplay between total pore volume, median pore size, surface area, apparent density and particulate distribution of shape and size may prove significant in determining and further enhancing PbO reaction characteristics.
    - Multivariate or neural network methods can be used to determine potential correlations between the above characteristics and the performance of the end product.
- Altering the primary precursor paste material of PbO, the changes to the physical characteristics of the porous active mass forming the working electrode can be significant. Therefore, changes to the types of carbon used in the facilitation of electrical conduction across the active mass can be explored to gauge their effects in battery performance in conjunction with modified PbO.
- Carbon nanotubes as well as other functionalised carbons and graphene can be used to determine possible improvements to the overall performance of LABs.
- Further alterations can be made to the paste formulation in conjunction with the changes in curing conditions. Different curing conditions can also be used to explore the effect of temperature, humidity and time on the surface area as well density and electrochemical characteristics of paste mixtures.
- Investigations can be carried out into the replacement of plate materials with alternative light modern advanced materials such as foams, conductive ceramics, composites or coatings. This is aimed at eliminating the need for heavy lead grids, which only serve to hold the paste and conduct current and will significantly decrease the overall weight of the LAB.
- Having demonstrated the potential viability of the manufactured nanostructred PbO in the working electrode of half electrochemical cells, impedance spectroscopy and further battery testing will be needed to demonstrate proof of concept in developing a fully operational LAB for future industry use.

9 References

1. Pan J, Zhang C, Sun Y, Wang Z, Yang Y. A new process of lead recovery from waste lead-acid batteries by electrolysis of alkaline lead oxide solution. Electrochemistry Communications. 2012;19:70-2.
2. Laboratory NHMF. Plante Battery Tallahassee 2010. Available from: http://www.magnet.fsu.edu/education/tutorials/museum/plantebattery.html.
3. Genaidy AM, Sequeira R, Tolaymat T, Kohler J, Rinder M. An exploratory study of lead recovery in lead-acid battery lifecycle in US market: An evidence-based approach. Science of the Total Environment. 2008;407(1):7-22.
4. Ellis TW, Mirza AH. The refining of secondary lead for use in advanced lead-acid batteries. Journal of Power Sources. 2010;195(14):4525-9.
5. Kreusch MA, Ponte MJJS, Ponte HA, Kaminari NMS, Marino CEB, Mymrin V. Technological improvements in automotive battery recycling. Resources, Conservation and Recycling. 2007;52(2):368-80.
6. Compton RG, Sanders GHW. Electrode Potentials: University of Oxford Press; 1996. 96 p.
7. Linden D, Reddy TB. Hand Book of Batteries. 3rd ed: McGraw-Hill; 2002. 1454 p.
8. Bullock KR. Lead/acid batteries. Journal of Power Sources. 1994;51(1-2):1-17.
9. Moseley PT, Rand DAJ. Changes in the demands on automotive batteries require changes in battery design. Journal of Power Sources. 2004;133(1):104-9.
10. McAllister SD, Patankar SN, Cheng IF, Edwards DB. Lead dioxide coated hollow glass microspheres as conductive additives for lead acid batteries. Scripta Materialia. 2009;61(4):375-8.
11. Battlebury DR. A high performance lead-acid battery for EV applications. Journal of Power Sources. 1999;80(1-2):7-11.
12. Prout L. Aspects of lead/acid battery technology 8. Battery oxide. Journal of Power Sources. 1994;47(1-2):197-217.
13. Pavlov D. Lead-Acid Batteries: Science and Technology. A handbook of lead-acid battery technology and its influence on the product. First ed. Oxford: ELSEVIER; 2011.
14. Boden DP. Improved oxides for production of lead/acid battery plates. Journal of Power Sources. 1998;73(1):56-9.
15. Corino GL, Hill RJ, Jessel AM, Rand DAJ, Wunderlich JA. A Study of the phase composition, crystallinity, morphology, porosity and surface area of leady oxides used in lead/acid battery plates. Journal of Power Sources. 1985;16(2):141-68.
16. Shin J-H, Kim K-W, Ahn H-J. Preparation of leady oxide for lead-acid battery by cementation reaction. Journal of Power Sources. 2000;89(1):46-51.
17. Mayer MG, Rand DAJ. Leady oxide for lead/acid battery positive plates: scope for improvement? Journal of Power Sources. 1996;59(1-2):17-24.
18. Gillian WF, Hardman AM, Kiessling R, Lambert DWH, Manders JE, Rand DAJ. Technical and research aspects of lead/acid battery production. Journal of Power Sources. 1989;28(1-2):217-35.
19. Dengke Q. Changes in the structure of active materials in lead-acid batteries. Journal of Power Sources. 1999;78(1-2):88-93.
20. Chahmana N, Matrakova M, Zerroual L, Pavlov D. Influence of some metal ions on the structure and properties of doped beta-PbO_2. Journal of Power Sources. 2009;191(1):51-7.
21. Moseley PT. Consequences of including carbon in the negative plates of Valve-regulated Lead-Acid batteries exposed to high-rate partial-state-of-charge operation. Journal of Power Sources. 2009;191(1):134-8.
22. Wagner R. High-power lead-acid batteries for different applications. Journal of Power Sources. 2005;144(2):494-504.
23. Kamenev Y, Lushina M, Yakovlev V. New lead-acid battery for submersible vehicles. Journal of Power Sources. 2009;188(2):613-6.

24. Hernández JC, Soria ML, González M, García-Quismondo E, Muñoz A, Trinidad F. Studies on electrolyte formulations to improve life of lead acid batteries working under partial state of charge conditions. Journal of Power Sources. 2006;162(2):851-63.
25. Ltd WC. Battery and Energy Technologies Chester 2010 Available from: http://www.mpoweruk.com/chemistries.htm.
26. Prout L. Aspects of lead/acid battery technology 7. Separators. Journal of Power Sources. 1993;46(1):117-38.
27. Wagner R. Secondary Batteries - High Temperature Systems | Flooded Batteries. Encyclopedia of Electrochemical Power Sources. Amsterdam: Elsevier; 2009. p. 677-92.
28. May GJ, Lenain P. Gelled-electrolyte lead/acid batteries for stationary and traction applications. Journal of Power Sources. 1992;40(1-2):187-93.
29. Soria ML, Valenciano J, Ojeda A, Raybaut G, Ihmels K, Deiters J, et al. Development of high power VRLA batteries using novel materials and processes. Journal of Power Sources. 2003;116(1-2):61-72.
30. Simarro R. Synthetic fibre reinforcement of absorptive glass-mat separators for valve-regulated lead-acid batteries. Journal of Power Sources. 1999;78(1-2):65-7.
31. Darling D. The Encyclopedia of Alternative Energy and Sustainable Living 2010 Available from: http://www.daviddarling.info/encyclopedia/L/AE_lead-acid_battery.html.
32. Keim TA. Systems for 42 V mass-market automobiles. Journal of Power Sources. 2004;127(1-2):16-26.
33. Bullock KR. Lead-acid battery research and development--a vital key to winning new business. Journal of Power Sources. 2003;116(1-2):8-13.
34. Cooper A. Development of a high-performance lead-acid battery for new-generation vehicles. Journal of Power Sources. 2005;144(2):385-94.
35. Moseley PT, Nelson RF, Hollenkamp AF. The role of carbon in valve-regulated lead-acid battery technology. Journal of Power Sources. 2006;157(1):3-10.
36. Calábek M, Micka K, Krivák P, Baca P. Significance of carbon additive in negative lead-acid battery electrodes. Journal of Power Sources. 2006;158(2):864-7.
37. Shiomi M, Funato T, Nakamura K, Takahashi K, Tsubota M. Effects of carbon in negative plates on cycle-life performance of valve-regulated lead/acid batteries. Journal of Power Sources.64(1-2):147-52.
38. Wagner R. Failure modes of valve-regulated lead/acid batteries in different applications. Journal of Power Sources. 1995;53(1):153-62.
39. Miraglio R, Albert L, El Ghachcham A, Steinmetz J, Hilger JP. Passivation and corrosion phenomena on lead-calcium-tin alloys of lead/acid battery positive electrodes. Journal of Power Sources. 1995;53(1):53-61.
40. Bui N, Mattesco P, Simon P, Steinmetz J, Rocca E. The tin effect in lead-calcium alloys. Journal of Power Sources.67(1-2):61-7.
41. Prengaman RD. Lead-acid technology: a look to possible future achievements. Journal of Power Sources. 1999;78(1-2):123-9.
42. Hollenkamp AF, Baldsing WGA, Hamilton JA, Rand DAJ. Advanced lead/acid batteries for stand-alone power-supply systems. Journal of Power Sources. 1990;31(1-4):329-36.
43. Juergens T, Nelson RF. A new high-rate, fast-charge lead/acid battery. Journal of Power Sources. 1995;53(2):201-5.
44. Bhardwaj RC. Constant and pulse power capabilities of lead-acid batteries made with thin metal film (TMF®) for different applications. Journal of Power Sources. 1999;78(1-2):130-8.
45. Valeriote EM. Resistance of expanded grids and high-rate plate performance: preliminary results. Journal of Power Sources. 1989;28(1-2):93-104.
46. Meissner E. Calculation of potential distribution and voltage drop at electrodes on high-rate discharge: literature survey and computer-aided approach. Journal of Power Sources. 1993;42(1-2):103-18.

47. Barkleit G, Grahl A, Maccagni M, Olper M, Scharf P, Wagner R, et al. Electrodeposited, dispersion-hardened, lightweight grids for lead-acid batteries. Journal of Power Sources. 1999;78(1-2):73-8.
48. Soria ML, Fullea J, Sáez F, Trinidad F. Lead-acid batteries with polymer-structured electrodes for electric-vehicle applications. Journal of Power Sources. 1999;78(1-2):220-30.
49. Trinidad F, Gimeno C, Gutiérrez J, Ruiz R, Sainz J, Valenciano J. The VRLA modular wound design for 42 V mild hybrid systems. Journal of Power Sources. 2003;116(1-2):128-40.
50. Valenciano J, Trinidad F, Fernández M. The influence of different negative expanders on the performance of VRLA batteries. Journal of Power Sources. 2003;113(2):318-28.
51. Bode H. Lead-acid Batteries. 1st ed: Wiley - Interscience; 1977. 381 p.
52. Pavlov D. A theory of the grid/positive active-mass (PAM) interface and possible methods to improve PAM utilization and cycle life of lead/acid batteries. Journal of Power Sources. 1995;53(1):9-21.
53. Dreier I, Saez F, Scharf P, Wagner R. Investigation on soaking and formation of lead/acid battery plates with different mass structure. Journal of Power Sources. 2000;85(1):117-30.
54. Prout L. Aspects of lead/acid battery technology I. Pastes and paste mixing. Journal of Power Sources. 1993;41(1-2):107-61.
55. Prout L. Aspects of lead/acid battery technology 3. Plate curing. Journal of Power Sources. 1993;41(1-2):185-93.
56. Yolshina LA, Malkov VB, Yolshin AN. The influence of formation conditions on the electrochemical behavior of lead oxide in sulfuric acid solution. Journal of Power Sources. 2009;191(1):36-41.
57. Wang J, Zhong S, Wang GX, Bradhurst DH, Ionescu M, Liu HK, et al. Electrochemical performance of nanocrystalline lead oxide in VRLA batteries. Journal of Alloys and Compounds. 2001;327(1-2):141-5.
58. Cruz M, Hernán L, Morales J, Sánchez L. Spray pyrolysis as a method for preparing PbO coatings amenable to use in lead-acid batteries. Journal of Power Sources. 2002;108(1-2):35-40.
59. Karami H, Karimi MA, Haghdar S, Sadeghi A, Mir-Ghasemi R, Mahdi-Khani S. Synthesis of lead oxide nanoparticles by Sonochemical method and its application as cathode and anode of lead-acid batteries. Materials Chemistry and Physics. 2008;108(2-3):337-44.
60. Karami H, Karimi MA, Haghdar S. Synthesis of uniform nano-structured lead oxide by sonochemical method and its application as cathode and anode of lead-acid batteries. Materials Research Bulletin. 2008;43(11):3054-65.
61. Salavati-Niasari M, Mohandes F, Davar F. Preparation of PbO nanocrystals via decomposition of lead oxalate. Polyhedron. 2009;28(11):2263-7.
62. Sun X, Yang J, Zhang W, Zhu X, Hu Y, Yang D, et al. Lead acetate trihydrate precursor route to synthesize novel ultrafine lead oxide from spent lead acid battery pastes. Journal of Power Sources. 2014;269:565-76.
63. Sadeghzadeh H, Morsali A, Yilmaz VT, Büyükgüngör O. Synthesis of PbO nano-particles from a new one-dimensional lead(II) coordination polymer precursor. Materials Letters. 2010;64(7):810-3.
64. Zhu X, Li L, Sun X, Yang D, Gao L, Liu J, et al. Preparation of basic lead oxide from spent lead acid battery paste via chemical conversion. Hydrometallurgy. 2012;117–118:24-31.
65. Ferracin LC, Chácon-Sanhueza AE, Davoglio RA, Rocha LO, Caffeu DJ, Fontanetti AR, et al. Lead recovery from a typical Brazilian sludge of exhausted lead-acid batteries using an electrohydrometallurgical process. Hydrometallurgy. 2002;65(2-3):137-44.
66. Chen TT, Dutrizac JE. The mineralogical characterization of lead-acid battery paste. Hydrometallurgy. 1996;40(1-2):223-45.
67. Andrews D, Raychaudhuri A, Frias C. Environmentally sound technologies for recycling secondary lead. Journal of Power Sources. 2000;88(1):124-9.
68. Smith GR. Lead Recycling in The United States in 1998 (Flow Studies For Recycling Metal Commodities in the United States). Journal of Hazardous Materials 2009. 2009;161.

69. Sobanska S, Ricq N, Laboudigue A, Guillermo R, Brémard C, Laureyns J, et al. Microchemical investigations of dust emitted by a lead smelter. Environmental Science and Technology. 1999;33(9):1334-9.
70. Lyakov NK, Atanasova DA, Vassilev VS, Haralampiev GA. Desulphurization of damped battery paste by sodium carbonate and sodium hydroxide. Journal of Power Sources. 2007;171(2):960-5.
71. Zhu X, He X, Yang J, Gao L, Liu J, Yang D, et al. Leaching of spent lead acid battery paste components by sodium citrate and acetic acid. Journal of Hazardous Materials. 2013;250–251:387-96.
72. Chen HY, Li AJ, Finlow DE. The lead and lead-acid battery industries during 2002 and 2007 in China. Journal of Power Sources. 2009;191(1):22-7.
73. Zhu XF, Liu WC, Yang HY, Li L, Yang JK. Preparation of ultrafine PbO powders from lead paste in spent lead acid battery. Zhongguo Youse Jinshu Xuebao/Chinese Journal of Nonferrous Metals. 2010;20(1):132-6.
74. Li L, Zhu X, Yang D, Gao L, Liu J, Kumar RV, et al. Preparation and characterization of nano-structured lead oxide from spent lead acid battery paste. Journal of Hazardous Materials. 2012;203–204:274-82.
75. Maruthamuthu S, Dhanibabu T, Veluchamy A, Palanichamy S, Subramanian P, Palaniswamy N. Elecrokinetic separation of sulphate and lead from sludge of spent lead acid battery. Journal of Hazardous Materials. 2011;193:188-93.
76. Sonmez MS, Kumar RV. Leaching of waste battery paste components. Part 1: Lead citrate synthesis from PbO and PbO_2. Hydrometallurgy. 2009;95(1-2):53-60.
77. Sonmez MS, Kumar RV. Leaching of waste battery paste components. Part 2: Leaching and desulphurisation of $PbSO_4$ by citric acid and sodium citrate solution. Hydrometallurgy. 2009;95(1-2):82-6.
78. Sajadi SAA, Alamolhoda AA. Synthesis and properties of lead oxide carbonate. Inorg Mater. 2006;42(10):1099-103.
79. Gong Y, Dutrizac JE, Chen TT. The conversion of lead sulphate to lead carbonate in sodium carbonate media. Hydrometallurgy. 1992;28(3):399-421.
80. Gong Y, Dutrizac JE, Chen TT. The reaction of anglesite ($PbSO_4$) crystals with sodium carbonate solutions. Hydrometallurgy. 1992;31(3):175-99.
81. Arai K, Toguri JM. Leaching of lead sulphate in sodium carbonate solution. Hydrometallurgy. 1984;12(1):49-59.
82. Ramus K, Hawkins P. Lead/acid battery recycling and the new Isasmelt process. Journal of Power Sources. 1993;42(1-2):299-313.
83. Yang D, Liu J, Wang Q, Yuan X, Zhu X, Li L, et al. A novel ultrafine leady oxide prepared from spent lead pastes for application as cathode of lead acid battery. Journal of Power Sources. 2014;257:27-36.
84. Kety SS. The lead citrate complex ion and its role in the physiology and therapy of lead poisoning. Journal of Biological Chemistry. 1942;142(1):181-92.
85. Scintag, Inc. Basics of X-ray Diffraction. Bubb Road, Cupertino, CA 95014 U.S.A. Available from: http://www.geo.umass.edu/courses/geo311/xrdbasics.pdf
86. Cullity BD, Stock SR. Elements of x-ray diffraction. New Jersey, USA 2001.
87. Hindeleh AM, Johnson DJ. An empirical estimation of Scherrer parameters for the evaluation of true crystallite size in fibrous polymers. Polymer. 1980;21.
88. Patterson AL. The Scherrer Formula for X-Ray Particle Size Determination. Physical Review. 1939;56:978-82.
89. Jenkins R, Snyder RL. Introduction to X-Ray Powder Diffraction: John Wiley & Sons Inc; 1996.
90. Burton AW, Ong K, Rea T, Chan IY. On the estimation of average crystallite size of zeolites from the Scherrer equation: A critical evaluation of its application to zeolites with one-dimensional pore systems. Microporous and Mesoporous Materials. 2009;117:75 - 90.

91. Reed SJB. Electron Microprobe Analysis and Scanning Electron Microscopy in Geology. Cambridge, Second Edition. 2005.
92. Jansen W, Slaughter M. Elemental mapping of minerals by electron microprobe. American Mineralogist. 1982;67:521-33.
93. Brunauer S, Emmett PH, Teller E. Adsorption of Gases in Multimolecular Layers. Journal of the American Chemical Society. 1938;60(2):309-19.
94. Barrett EP, Joyner LG, Halenda PP. The Determination of Pore Volume and Area Distributions in Porous Substances. I. Computations from Nitrogen Isotherms. Journal of the American Chemical Society. 1951;73(1):373-80.
95. Parfitt GD, Sing KSW. Characterization of powder surfaces with special reference to pigments and fillers. London; New York : Academic Press. 1976:1-50.
96. Rouquerol R, Rouquerol J, Sing KSW. Adsorption by Powders and Porous Solids Principles, Methodology and Applications. Elsevier Science. 1998:204-6.
97. Kruk M, Jaroniec M. Gas Adsorption Characterization of Ordered Organic-Inorganic Nanocomposite Materials. Chemistry of Materials. 2001;13(10):3169-83.
98. Sing KSW, Everett DH, Haul RAW, Moscou L, Pierotti RA, Rouquerol J, et al. Reporting Physisorption Data for Gas Solid Systems with Special Reference to the Determination of Surface-Area and Porosity (Recommendations 1984). Pure Appl Chem. 1985;57(4):603-19.
99. Anderson RB. Pore Distributions from Desorption Isotherms. Journal of Catalysis. 1964;3:50-6.
100. Shull CG. The Determination of Pore Size Distribution from Gas Adsorption Data. 1948;70:1405-10.
101. Skinner LM, Sambles JR. The Kelvin Equation--A Review. Aerosol Science. 1972;3:199-210.
102. Chen M-m. Chapter 12 - Thermal Analysis A2 - Inagaki, Michio. In: Kang F, editor. Materials Science and Engineering of Carbon: Butterworth-Heinemann; 2016. p. 249-72.
103. Gallagher PK. Chapter 4 - Thermogravimetry and Thermomagnetometry. In: Michael EB, editor. Handbook of Thermal Analysis and Calorimetry. Volume 1: Elsevier Science B.V.; 1998. p. 225-78.
104. Compton RG, Banks CE. Understanding Voltammetry: University Oxford Press. 360 p.
105. Fisher AC. Electrode Dynamics: University of Oxford Press; 1996. 91 p.
106. Carpente MK, Bernardi DM, Wertz JA. The use of Hg/Hg_2SO_4 reference electrodes in valve-regulated lead/acid cells. Journal of Power Sources. 1996;63(1):15-22.
107. Kissinger PT, Heineman WR. Cyclic voltammetry. Journal of Chemical Education. 1983;60(9):702-null.
108. Ferg EE, Phangalala T, Van Dyl T. A new look at determining acid absorption of lead oxide used in the manufacturing of Pb-acid batteries. Journal of Applied Electrochemistry. 2010;40(2):383-91.
109. Kourgiantakis M, Matzapetakis M, Raptopoulou CP, Terzis A, Salifoglou A. Lead–citrate chemistry. Synthesis, spectroscopic and structural studies of a novel lead(II)–citrate aqueous complex. Inorganica Chimica Acta. 2000;297(1–2):134-8.
110. Zhang W, Yang J, Zhu X, Sun X, Yu W, Hu Y, et al. Structural study of a lead (II) organic complex – a key precursor in a green recovery route for spent lead-acid battery paste. Journal of Chemical Technology & Biotechnology. 2015.
111. Zhang Y, Fu B, Hong M, Xiang M, Liu Z, Liu H, et al. Effects of pH on the crystal structure, morphology and microwave dielectric properties of $Bi_{12}TiO_{20}$ ceramics synthesized by citrate sol–gel method. Journal of Materials Science: Materials in Electronics. 2015;26(5):3179-85.
112. Bottari E, Vicedomini M. On the complex formation between lead(II) and citrate ions in acid solution. Journal of Inorganic and Nuclear Chemistry. 1973;35(4):1269-78.
113. Bottari E, Vicedomini M. On the complex formation between lead(II) and citrate ions in alkaline solution. Journal of Inorganic and Nuclear Chemistry. 1973;35(7):2447-53.
114. Myer MG, Rand DAJ. J Power Sources. 1996;59(17).

115. Li L, Hu Y, Zhu X, Yang D, Wang Q, Liu J, et al. Lead citrate precursor route to synthesize nanostructural lead oxide from spent lead acid battery paste. Materials Research Bulletin. 2013;48(4):1700-8.
116. Yang J, Kumar RV, Singh DP. Combustion synthesis of PbO from lead carboxylate precursors relevant to developing a new method for recovering components from spent lead–acid batteries. Journal of Chemical Technology & Biotechnology. 2012;87(10):1480-8.
117. Speakman SA. Estimating Crystallite Size Using XRD Boston: MIT; Available from: http://prism.mit.edu/xray.
118. Jones FW. The Measurement of Particle Size by the X-Ray Method. Proceedings of the Royal Society of London Series A, Mathematical and Physical Sciences. 1938;166(924):16-43.
119. Singh AV, Gollner MJ. Experimental Methodology for Estimation of Local Heat Fluxes and Burning Rates in Steady Laminar Boundary Layer Diffusion Flames. Journal of Visualized Experiments : JoVE. 2016(112):54029.
120. Ohlemiller TJ. Modeling of smoldering combustion propagation. Progress in Energy and Combustion Science. 1985;11(4):277-310.
121. Ohlemiller TJ. Smoldering combustion propagation through a permeable horizontal fuel layer. Combustion and Flame. 1990;81(3):341-53.
122. Ohlemiller TJ, Lucca DA. An experimental comparison of forward and reverse smolder propagation in permeable fuel beds. Combustion and Flame. 1983;54(1):131-47.
123. Saraswati Auto Allied. Available from: www.Saraswatiautoallied.com. 2012
124. Pavlov D, Kapkov N. Lead-acid battery pastes containing $4PbO \cdot PbSO_4$ and Pb_3O_4. Journal of the Electrochemical Society. 1990;137(1):16-21.
125. Ferg EE, Loyson P, Rust N. Porosity measurements of electrodes used in lead-acid batteries. Journal of Power Sources. 2005;141(2):316-25.
126. Kwestroo W, Huizing A. The preparation of ultra pure lead oxide. Journal of Inorganic and Nuclear Chemistry. 1965;27(9):1951-4.
127. Perry DL. Synthesis of High-Purity alpha-and beta-PbO and Possible Applications to Synthesis and Processing of Other Lead Oxide Materials. 2011.
128. Jensen WB. Holleman-Wiberg's Inorganic Chemistry (edited by Wiberg, Nils). Journal of Chemical Education. 2002;79(8):944.
129. Wang C, Hou Y-D, Ge H-Y, Zhu M-K, Yan H. Crystal structure and orthorhombic–tetragonal phase transition of nanoscale $(Li_{0.06}Na_{0.47}K_{0.47})NbO_3$. Journal of the European Ceramic Society. 2009;29(12):2589-94.
130. Wang J, Fan W, Yang J, Da Z, Yang X, Chen K, et al. Tetragonal–Orthorhombic–Cubic Phase Transitions in Ag_2Se Nanocrystals. Chemistry of Materials. 2014;26(19):5647-53.
131. Douillard L, Gautier-Soyer M, Duraud JP, Fontaine A, Baudelet F. Time resolved XAS study of a phase transition: The polymorphic transformation of tetragonal to orthorhombic PbO. Journal of Physics and Chemistry of Solids. 1996;57(4):495-501.
132. Gavrilkin SM, Kopaneva LI, Batsanov SS. Anomalous Phase Transition in Shock-Compressed PbO. Combustion, Explosion and Shock Waves. 2003;39(6):723-6.
133. Yurkinskii VP, Sokolova NV, Popov VA. Effect of Lead(II) Complexation on Solubility of β-PbO in Alkaline Solutions in the Presence of Certain Alcohols. Russian Journal of Applied Chemistry. 2001;74(3):427-9.
134. Ziemniak SE, Palmer DA, Bénézeth P, Anovitz LM. Solubility of Litharge (α-PbO) in Alkaline Media at Elevated Temperatures. Journal of Solution Chemistry. 2005;34(12):1407-28.
135. Saal C, Petereit AC. Optimizing solubility: Kinetic versus thermodynamic solubility temptations and risks. European Journal of Pharmaceutical Sciences. 2012;47(3):589-95.
136. Bhattachar SN, Deschenes LA, Wesley JA. Solubility: it's not just for physical chemists. Drug Discovery Today. 2006;11(21–22):1012-8.

137. Box KJ, Völgyi G, Baka E, Stuart M, Takács-Novák K, Comer JEA. Equilibrium versus kinetic measurements of aqueous solubility, and the ability of compounds to supersaturate in solution—a validation study. Journal of Pharmaceutical Sciences. 2006;95(6):1298-307.
138. Yanakieva VP, Haralampiev GA, Lyakov NK. Desulphurization of the damped lead battery paste with potassium carbonate. Journal of Power Sources. 2000;85(1):178-80.
139. Ridgwell A, Zeebe RE. The role of the global carbonate cycle in the regulation and evolution of the Earth system. Earth and Planetary Science Letters. 2005;234(3–4):299-315.
140. Zeebe RE. An explanation of the effect of seawater carbonate concentration on foraminiferal oxygen isotopes. Geochimica et Cosmochimica Acta. 1999;63(13–14):2001-7.
141. Maynard JB. Overview of Lead Scale Formation and Solubility. University of Cincinnati. 2008.
142. Shirota Y, Niki K, Shindo H. Stabilities of crystal faces of aragonite-type strontianite ($SrCO_3$) and cerussite ($PbCO_3$) compared by AFM observation of facet formation in acid. Journal of Crystal Growth. 2011;324(1):190-5.
143. Clever HL, Johnston FJ. The solubility of some sparingly soluble lead salts: An evaluation of the solubility in water and aqueous electrolyte solution. Journal of Physical and Chemical Reference Data. 1980;9(3):751-84.
144. Droessler LM, Assender HE, Watt AAR. Thermally deposited lead oxides for thin film photovoltaics. Materials Letters. 2012;71:51-3.
145. Cattley CA, Stavrinadis A, Beal R, Moghal J, Cook AG, Grant PS, et al. Colloidal synthesis of lead oxide nanocrystals for photovoltaics. Chemical Communications. 2010;46(16):2802-4.
146. Zhang H, Ouyang J. High-performance inverted polymer solar cells with lead monoxide-modified indium tin oxides as the cathode. Organic Electronics: physics, materials, applications. 2011;12(11):1864-71.
147. Veluchamy P, Minoura H. Simple electrochemical method for the preparation of a highly oriented and highly photoactive α-PbO film. Applied Physics Letters. 1994;65(19):2431-3.
148. Schottmiller JC. Photoconductivity in tetragonal and orthorhombic lead monoxide layers. Journal of Applied Physics. 1966;37(9):3505-10.
149. Poll CG, Payne DJ. Electrochemical Synthesis of PbO_2, Pb_3O_4 and PbO Films on a Transparent Conducting Substrate. Electrochimica Acta. 2015;156:283-8.
150. Joey Jung LZ, Jiujun Zhang. Lead-Acid Battery Technologies: Fundamentals, Materials, and Applications: CRC Press; 2015. 365 p.
151. Kim M, Son W-S, Ahn KH, Kim DS, Lee H-s, Lee Y-W. Hydrothermal synthesis of metal nanoparticles using glycerol as a reducing agent. The Journal of Supercritical Fluids. 2014;90:53-9.
152. Díaz-Álvarez AE, Cadierno V. Glycerol: A promising Green Solvent and Reducing Agent for Metal-Catalyzed Transfer Hydrogenation Reactions and Nanoparticles Formation. Applied Sciences. 2013;3:55-69.
153. Garcia N, Garcia-Garcia P, Fernandez-Rodriguez MA, Garcia D, Pedrosa MR, Arnaiz FJ, et al. An unprecedented use for glycerol: chemoselective reducing agent for sulfoxides. Green Chemistry. 2013;15(4):999-1005.
154. Kou J, Bennett-Stamper C, Varma RS. Green Synthesis of Noble Nanometals (Au, Pt, Pd) Using Glycerol under Microwave Irradiation Conditions. ACS Sustainable Chemistry & Engineering. 2013;1(7):810-6.
155. Vaidya PD, Rodrigues AE. Glycerol reforming for hydrogen production: A review. Chemical Engineering and Technology. 2009;32(10):1463-9.
156. Culver R, Matthew I, Spooner E. The Kinetics of the Reduction of Lead Monoxide by Hydrogen. Australian Journal of Chemistry. 1962;15(1):40-55.
157. Manders JE, Lam LT, Peters K, Prengaman RD, Valeriote EM. Lead/acid battery technology. Journal of Power Sources. 1996;59(1-2):199-207.
158. Biagetti RV, Weeks MC. Lead-Acid Battery: Tetrabasic Lead Sulfate as a Paste Material for Positive Plates. Bell System Technical Journal. 1970;49(7):1305-19.

159. Culpin B. The role of tetrabasic lead sulphate in the lead/acid positive plate. Journal of Power Sources. 1989;25(4):305-11.
160. Rand DAJ, Pavlov D, Kapkov N. Proceedings of the International Conference on Lead/Acid Batteries: LABAT'89 Lead/acid battery positive plates manufactured from $4PbO{\cdot}PbSO_4$ pastes prepared from leady oxide and red lead. Journal of Power Sources. 1990;31(1):189-201.
161. Brown ME. Thermal decomposition of lead citrate. Journal of the Chemical Society, Faraday Transactions 1: Physical Chemistry in Condensed Phases. 1973;69(0):1202-12.
162. Peretti EA. Thermal Decomposition of Lead Carbonate. Journal of the American Ceramic Society. 1957;40(5):171-3.
163. Živković Ž. Kinetics and mechanism of thermal decomposition of lead carbonate. Journal of Thermal Analysis and Calorimetry. 1979;16(1):3-11.
164. Aresta M, Wiley I. Carbon dioxide as chemical feedstock [electronic resource]. Weinheim :Chichester: Wiley-VCH ;John Wiley [distributor]; 2010. p. 1 online resource (394 p.).
165. Weast RC. CRC Handbook of Chemistry and Physics CRC Press. 1978;(59th ed.):p. B-133.
166. Vágvölgyi V, Hales M, Frost RL, Locke A, Kristóf J, Horváth E. Conventional and controlled rate thermal analysis of nesquehonite $Mg(HCO_3)(OH){\cdot}2(H_2O)$. Journal of Thermal Analysis and Calorimetry. 2008;94(2):523-8.
167. Krivovichev SV, Burns PC. Crystal chemistry of basic lead carbonates. III. Crystal structures of $Pb_3O_2(CO_3)$ and $NaPb_2(OH)(CO_3)_2$. Mineralogical Magazine,. December 2000;Vol. 64(6), pp. 1077–1087(Department of Civil Engineering and Geological Sciences, 156 Fitzpatrick, University of Notre Dame, Notre Dame IN 46556-0767 USA).
168. Krivovichev SV, Burns PC. Crystal chemistry of basic lead carbonates. I. Crystal structure of synthetic shannonite, $Pb_2O(CO_3)$. Mineralogical Magazine. December 2000;Vol. 64(6), pp. 1063–1068(Department of Civil Engineering and Geological Sciences, 156 Fitzpatrick, University of Notre Dame, Notre Dame IN 46556-0767, USA).
169. Charles J, Kopf PW, Toby S. The Reaction of Pyrophoric Lead with Oxygen. The Journal of Physical Chemistry. 1966;70(5):1478-82.
170. Gorrie TM, Kopf PW, Toby S. Kinetics of the reaction of some pyrophoric metals with oxygen. The Journal of Physical Chemistry. 1967;71(12):3842-5.
171. Isahak WNRW, Ramli ZAC, Ismail MW, Ismail K, Yusop RM, Hisham MWM, et al. Adsorption–desorption of CO_2 on different type of copper oxides surfaces: Physical and chemical attractions studies. Journal of CO_2 Utilization. 2013;2:8-15.
172. Garenne A, Montes-Hernandez G, Beck P, Schmitt B, Brissaud O, Pommerol A. Gas–solid carbonation as a possible source of carbonates in cold planetary environments. Planetary and Space Science. 2013;76:28-41.
173. Dropsch H, Baerns M. CO adsorption on supported Pd catalysts studied by adsorption microcalorimetry and temperature programmed desorption. Applied Catalysis A: General. 1997;158(1–2):163-83.
174. Liu A-H, Gao J, He L-N. Chapter 4 - Catalytic Activation and Conversion of Carbon Dioxide into Fuels/Value-Added Chemicals Through CC Bond Formation. In: Suib SL, editor. New and Future Developments in Catalysis. Amsterdam: Elsevier; 2013. p. 81-147.
175. Wan Isahak WNR, Che Ramli ZA, Mohamed Hisham MW, Yarmo MA. The formation of a series of carbonates from carbon dioxide: Capturing and utilisation. Renewable and Sustainable Energy Reviews. 2015;47:93-106.